**Title**

Femtoscale MEMS Controlled Solar Sail Spacecraft for Asteroidal Imaging and Cometary Sample Capture



**ISBN**

9798189270079

**Author**

Alvara, Alexander Nicholas

**Publication Date**

2026-05-01

Peer reviewed|Thesis/dissertation

# Femtoscale MEMS Controlled Solar Sail Spacecraft for Asteroidal Imaging and Cometary Sample Capture

By

Alexander Nicholas Alvara

A dissertation submitted in partial satisfaction of the

requirements for the degree of

Doctor of Philosophy

in

Engineering -- Mechanical Engineering

in the

Graduate Division

of the

University of California, Berkeley

Committee in charge:

Professor Kristofer S.J. Pister, Co-Chair
Professor Liwei Lin, Co-Chair
Professor Oscar D. Dubon
Professor Dorian Liepmann

Spring 2026

Femtoscale MEMS Controlled Solar Sail Spacecraft for Asteroidal
Imaging and Cometary Sample Capture



by

Alexander Nicholas Alvara

Abstract

Femtoscale MEMS Controlled Solar Sail Spacecraft for Asteroidal Imaging and Cometary Sample Capture

by

Alexander Nicholas Alvara

Doctor of Philosophy in Mechanical Engineering

University of California, Berkeley

Professor Kristofer S.J. Pister, Co-Chair

Professor Liwei Lin, Co-Chair

The continuing miniaturization of commercial electronics, micro-electromechanical systems (MEMS), and low-mass spacecraft hardware has created an opportunity to reconsider how interplanetary science missions can be designed, manufactured, and deployed. Conventional spacecraft have enabled extraordinary planetary-science returns, but their high cost, long development cycles, and large system masses limit the number of targets that can be explored. This dissertation presents a MEMS-enabled femtoscale solar-sail spacecraft architecture intended to support low-cost asteroidal imaging, small-body reconnaissance, and future cometary sample-capture missions.

The central spacecraft concept developed in this work is the Berkeley Low-cost Interplanetary Solar Sail (BLISS), a nearly 10 g solar-sail spacecraft that uses a roughly 1 $m^2$ reflective sail, commercial-off-the-shelf electronics, onboard imaging, optical communication, and MEMS-based mechanical steering. The BLISS architecture uses solar radiation pressure as its primary propulsion source and relies on controlled displacement of sail-support tethers to modify the relative geometry between the sail and spacecraft body. Earth-escape and interplanetary trajectory studies show that a BLISS-class spacecraft can, in principle, spiral out from near-Earth orbit, perform heliocentric transfers, and rendezvous with near-Earth objects such as Bennu on mission timescales relevant to small-body exploration.

This dissertation further develops the MEMS actuation and microrobotic systems

needed to support that spacecraft-level architecture. The MEMS Actuators for control of Solar-sail Tethers (MAST) are presented as the steering and tether-control mechanism for BLISS. MAST devices use MEMS inchworm motors and gap-closing actuators to displace carbon-fiber tether elements, thereby enabling control of sail attitude through center-of-pressure and center-of-mass offset. The Self-righting Quadrupedal Inchworm Driven Spacewalker (SQuIDS) is developed as a candidate microrobotic rover payload that a BLISS-class spacecraft could carry for on-asteroid or small-body surface exploration. SQuIDS addresses the need for local mobility, surface interaction, and self-righting in low-gravity environments where landing orientation and ground contact are uncertain.

The actuator-level foundation for future versions of these systems is provided by the Transmission Gap Closing Actuator (TGCA) and $\mu\Delta$ motor work. TGCA-based motors are designed to extend conventional MEMS inchworm actuation by introducing bidirectional, transmission-capable, and variable-output behavior. In the long term, this actuator architecture is intended to replace the more conventional inchworm motors used throughout BLISS, MAST, and SQuIDS, creating a common MEMS motor platform for sail steering, tether control, rover locomotion, and small-body interaction.

Taken together, this dissertation presents a linked research program rather than a single isolated device. BLISS defines the spacecraft and mission architecture, MAST provides the solar-sail steering mechanism, SQuIDS extends the mission concept to surface exploration, and TGCA provides a future motor technology for unifying actuation across the platform. The work remains intentionally foundational: several subsystems require additional fabrication refinement, environmental testing, closed-loop control, and integrated validation before flight use. Nevertheless, the designs, models, simulations, fabrication processes, and experimental results presented here establish a coherent path toward MEMS-controlled femtoscale spacecraft and microrobotic explorers for distributed interplanetary science.

***Dedicated to my family (in no particular order):***

*Mom, for always being my mom. Nana, for always listening. Tata, for being so consistent. Mock, for always being supportive. Evie, for always being so loving. Marcie, for always being my stone and my comfort. Joe, for being so dry and funny while staying true to yourself. Pumpkin, for always understanding even when you didn't. Frank, for being a great example and friend. Lori, for being so positive and stable. Monique, for showing us how to find our way. Daniel, for being a great friend. Alf, for showing us how to change our lives for the better. Stormy, for being so free and yet so grounded. Joseph, for being so kind. Adrian for being so easy-going. Jacob, for being so thoughtful and caring. Lisa, for being so smart and tough. Stephen, for being the grown up many of us still don't know how to be and for being my little big brother. Phyllis, for being so responsible. Roxy, for being such a good mother. Johnny, for being such a good man. Martin, for being the father none of us had. Desire, for being such a strong woman and mother. Mel, for being so careful and loving with your heart. To all your significant others, for their dedication and love of the highest caliber, because each of you deserve it and owe it to our younger selves to make sure we get that love and give it where we can. And to all your kids, may they look up to you and see more than your belly and your nose hairs. Crystal, for showing me there is a path forward and for being side-by-side with me through the worst of it.*

## Acknowledgments

I can never hope to truly communicate how much I appreciate every person who took part in my journey, nor could I ever hope to understand the ways in which their actions and contributions truly impacted me. However, this will not stop me from trying to do both. So... first, thank you all very very much.

To my advisors who were there for me in all the ways I did not know I needed:

- Kristofer S. J. Pister for his help in discussions, fabrication funding, and double checking all back of the envelope calculations and writing. Thank you for your many lessons and detailed conversations. Your expertise and insight were awe inspiring and your dedication to the craft still inspires me every time I do work. I am sincerely grateful for your patience and time. May you never have to deal with another student like me.

- Liwei Lin for his help in conceptualization, mentor support, processing understanding and troubleshooting, and simplification of experimentation. Thank you for your faith in my work and that the process will do its work on me. Your support and guidance were indispensable at many times where I lost my faith in the process and myself.

- Oscar D. Dubón for his help in mentor support, fabrication funding, and processing understanding. Thank your for bringing me into the fold of your group and for giving me so much time, care, and support. Your words, actions, and input were always comforting. Your continued faith in me and the contributions to my progress were incredibly edifying and still live in my mind and heart as motivating factors. Without your help, I do not know where I would be today. You continue to be a shining example for the rest of us Latinx students and in particular your career and dedication to the students as a whole is what I am striving to be.

- Dorian Liepmann for his guidance, perspective, and insight into MEMS, microfluidics, and the broader practice of engineering research. Thank you for the conversations that helped me think more clearly about devices, fabrication, and the relationship between technical detail and useful engineering outcomes. Your perspective helped ground parts of this work in a larger tradition of Berkeley MEMS research, and I am grateful for the time, care, and encouragement you gave me along the way.

- Andrew J. Westphal for his help in mission conceptualization, scientific framing, cometary and asteroidal sample-return context, and the broader vision that helped connect this work to planetary science. Your ability to connect technical details to mission-scale purpose helped lift my eyes beyond the immediate engineering obstacles. I am deeply grateful for your generosity, insight, and willingness to treat speculative ideas as things worth refining rather than dismissing.

All of my works would not have been possible without the financial support and funding from various sources, including:

- UC Berkeley Chancellor's Fellowship;
- National Science Foundation Graduate Research Fellowship Program (NSF-GRFP);
- Ford Foundation Predoctoral Fellowship;
- UC President's Pre-Professoriate Fellowship; UC Berkeley Chancellor's Fellowship;
- Professor Oscar D. Dubón Research and Fabrication Funding;
- Castellino Fellowship;
- Lin Fellowship with the Space Sciences Laboratory;
- UC Berkeley Basic Needs Emergency Fund; and
- UC Berkeley Emergency Loan;

Due to spacing, the acknowledgments are continued in Appendix C.

# Contents

# List of Figures

# List of Tables

# Table of Nomenclature

| Symbol | Description | SI Units | Defining Equation/Context |
|---|---|---|---|
| $\vec{a}$ | Acceleration vector | $m/s^2$ | Newton's Second Law |
| $\vec{a}_{\text{srp}}$ | SRP acceleration | $m/s^2$ | $\vec{F}_{\text{srp}}/m$ |
| $a_c$ | Characteristic acceleration | $m/s^2$ | At 1 AU, sail normal to Sun |
| $A$ | Sail area | $m^2$ | Geometric parameter |
| $\alpha$ | Sail cone angle | rad | Angle between sail normal and Sun-line |
| $\beta$ | Lightness number | dimensionless | SRP acc. / solar gravity acc. |
| $c$ | Speed of light | $m/s$ | $\approx 2.998 \times 10^8$ |
| $\delta$ | Sail clock angle | rad | Orientation around Sun-line |
| $\vec{e}$ | Eccentricity vector | dimensionless | From apoapsis to periapsis |
| $\vec{e}_\rho, \vec{e}_\phi, \vec{e}_z$ | Cylindrical unit vectors | dimensionless | Coordinate directions |
| $\vec{e}_r, \vec{e}_\theta, \vec{e}_\phi$ | Spherical unit vectors | dimensionless | Coordinate directions |
| $\epsilon$ | Quaternion vector part | dimensionless | $\epsilon = [q_1, q_2, q_3]^T$ |
| $\eta$ | Quaternion scalar part | dimensionless | $\eta = q_4$ |
| $\vec{F}$ | Force vector | $N$ | Newton's Second Law |
| $\vec{F}_g$ | Gravitational force | $N$ | Newton's Law of Gravitation |
| $\vec{F}_{\text{srp}}$ | SRP force | $N$ | SRP on sail |
| $G$ | Gravitational constant | $m^3/kg/s^2$ | $\approx 6.674 \times 10^{-11}$ |
| $\vec{h}$ | Angular momentum | $m^2/s$ | $\vec{r} \times \vec{v}$ |
| $h$ | Magnitude of $\vec{h}$ | $m^2/s$ | $\lvert\vec{h}\rvert$ |
| $H$ | Hamiltonian | $J$ | Total system energy |
| $I$ | Inertia tensor | $kg \cdot m^2$ | Rotational dynamics |

**Table of Nomenclature (Continued)**

| **Symbol** | **Description** | **SI Units** | **Defining Equation/Context** |
|---|---|---|---|
| $m$ | Mass | $kg$ | System parameter |
| $M_\oplus$ | Mass of Earth | $kg$ | $\approx 5.972 \times 10^{24}$ |
| $\mu$ | Earth gravitational parameter | $m^3/s^2$ | $GM_\oplus$ |
| $\mu_s$ | Sun grav. parameter | $m^3/s^2$ | $GM_\odot$ |
| $\vec{n}$ | Sail normal unit vector | dimensionless | Defines sail attitude |
| $P_{\text{srp}}$ | Solar radiation pressure | $N/m^2$ | Force per area |
| $p$ | KS quaternion | $m^{1/2}$ | Regularized coords |
| $q$ | Attitude quaternion | dimensionless | $[\epsilon; \eta]$ |
| $\vec{r}$ | Position vector | $m$ | From Earth center |
| $r$ | Magnitude of $\vec{r}$ | $m$ | $\|\vec{r}\|$ |
| $\vec{r}_{cp}$ | CoM to CoP vector | $m$ | For torque calc. |
| $\vec{r}_{sun}$ | Sun's position vector | $m$ | Direction of sunlight |
| $\hat{r}_s$ | Sun-sail unit vector | dimensionless | $\vec{r}_{sun}/\|\vec{r}_{sun}\|$ |
| $\rho$ | Cylindrical radial coord | $m$ | State variable |
| $\rho_a, \rho_d, \rho_s$ | Reflectivity coeffs | dimensionless | Optical properties |
| $s$ | Fictitious time (KS) | $m \cdot s$ | Regularized dynamics |
| $\sigma$ | Sail loading | $kg/m^2$ | $m/A$ |
| $\vec{T}$ | Torque vector | $N \cdot m$ | Rotational dynamics |
| $t$ | Time | $s$ | State variable |
| $\theta$ | Polar angle | rad | State variable |
| $\phi$ | Azimuthal angle | rad | State variable |
| $\vec{v}$ | Velocity vector | $m/s$ | $\dot{\vec{r}}$ |
| $\vec{\omega}$ | Angular velocity | $rad/s$ | Rotational rate |

# Chapter 1

# The Mission: An Introduction to Small Scale Solar Sail Spacecraft for Interplanetary Exploration

## 1.1 Motivation

As spaceflight grows from its beginnings as democratized government-funded science in search of truth to its now industrialized and subsidized privatized position, the extent to which innovation is supported might be up for debate, however, some things will remain the same in spaceflight considerations:

- trips to space are needed for planetary, economic, and scientific exploration and expansion;
- space debris is a deterrent to achievable spaceflight and observation;
- costs for space exploration will always need to be reduced;
- space is an extreme environment that requires specialized hardware, mission design, and operational planning.

The rapid miniaturization of commercial-off-the-shelf (COTS) electronics, driven in recent years by the emergence of smartphones and the Internet of Things, has made many of the components used in spacecraft available in very small, low-cost, low-power packages. This trend has inspired the CubeSat [17], and, subsequently, ChipSat [18] and later the Kicksat [19], concepts—the idea of building chip-scale satellites with the same devices and processes used in the consumer electronics industry. While much of the development in this area has focused on expanding access to low-Earth orbit (LEO) for educational and hobbyist use, this dissertation extends the concept to address a different frontier: interplanetary science.

While industry is fighting at the top, with its commercial suborbital tourism and privately subsidized launch models, the truth can still be said as it was before,

> *"[t]here is plenty of room at the bottom."* - Richard Feynman [20]

and while we sit idly by, proving one great thinker right, why not prove another great mind wrong by finding out if it can still be said in a hundred years that,

> *"[t]he Earth is the only world known so far to harbor life."* - Carl Sagan [21]

Despite decades of exploration, relatively few missions have returned physical samples or close-flyby imagery from small bodies.

It stands to reason then that a less costly, negligibly debris producing, method for maneuvering the space environment is needed to continue the planetary, financial, and scientific interests of peoples, governments, and corporations.

It is safe to say that the general historical trend for launching rockets has been steadily increasing over time [1]. However, the technology aboard the rockets themselves has seen a trend downward in mass, volume, and in some cases, cost [22].

In this regard, high-value discoveries or explorations are without a doubt those which bring actual materials or new found information from the visited target to Earth for study. Of the many thousands of missions launched into space, it is estimated that over 17,000 [23], about 402 have brought 676 humans to space (including those not passing the Karman line) [24], nearly 445 spacewalks [25], and of all of these only 11 missions have brought materials back from a celestial body [26], the majority of which have lunar rocks and soil. Only four missions have brought back material from something other than our moon: OSIRIS-REx [27], Hayabusa [28] & Hayabusa2 [29], and the Stardust [30] have returned materials from bodies other than our Moon, returning approximately $121.6g$, $1mg$, $5.4g$, and $0.3mg$, respectively. With the two smaller returned sample masses being microscopic in nature as even individual dust particles were counted for Hayabusa and Stardust missions, this ostensibly makes these materials the most exotic and expensive, by cost-to-mass ratio, known to the human world.

However, traditional, massive spacecraft are prohibitively expensive and require long development cycles, limiting the number of targets that can be explored. A New Frontiers-class mission, for example, costs approximately $1 billion and, even on an aggressive schedule, would not return cometary samples before the mid-2040s.1 This paradigm creates a bottleneck in planetary science, where the rate of discovery is limited by mission cost and complexity rather than scientific curiosity. This research posits that a new class of science missions, built around large ensembles or "swarms" of gram-scale "femto-spacecraft," can overcome these limitations. Such an architecture could enable the rapid optical reconnaissance of thousands of asteroids and the return of samples from dozens of comets, allowing thousands of data points to be collected simultaneously over vast regions of the inner solar system and multiplying scientific returns far beyond what is possible with a single large probe.

The primary motivation behind small-scale solar sails is that practical, $10-100\ g$ solar sail spacecraft remain difficult to build [31--33]. Transit times increase linearly with sail mass loading, so any design significantly above $10\,\mathrm{g/m^2}$ leads to mission times which are on the order of dozens of years. The high cost of depositing such a sail outside the Hill sphere of Earth is another limitation and the selection of Earth escape trajectories is also limited by sail mass loading in that most proposed trajectories require relatively fast maneuvers to maintain heading. At a sail mass loading of $10\,\mathrm{g/m^2}$, leaving Earth orbit and transiting to near-Earth objects (NEOs) both require roughly a year [34, 35]. Such a mass loading also allows for more agile maneuvers. Unfortunately, achieving such a low mass loading is a severe challenge for conventional spacecraft. Even CubeSats, among the smallest of spacecraft, require hundreds of square meters of sail area to achieve a mass loading of $10\,\mathrm{g/m^2}$. Missions like New Horizons and OSIRIS-REx had a dry mass of hundreds of kilograms and would require sail areas in the tens of thousands of square meters, the area of many football fields, to achieve the desired mass loading [27, 36]. Sails of this size require sophisticated deployment design, and the difficulty of developing low-mass sail-deployment hardware has played a role in their lack of use to date. The low mass of consumer electronics enables a new class of spacecraft driven by solar radiation pressure. These new capabilities have the potential to dramatically lower cost and decrease mission duration for inner solar system reconnaissance and sample return.

Demonstration of the potential of the new small-scale spacecraft development will proceed in phases. The first science mission we propose will be to image tens to hundreds of NEOs. The second will be to collect pristine cometary materials from thousands of Jupiter-family comets.

Missions to many celestial objects are within the capability of our 10 g robot, but for an initial demonstration, choosing targets with orbits close to 1 astronomical unit (AU) from the Sun simplifies the design of the power and thermal systems on the spacecraft. There are roughly 20,000 known NEOs, roughly 1,000 of which are believed to be asteroids greater than 1 km in diameter. Only 10 of these NEOs have been visited by spacecraft.

Beyond NEO reconnaissance, there are many potential applications of BLISS in solar system exploration and planetary science. Swarms of approximately 10 g interplanetary spacecraft would enable rapid sample return from dozens of Jupiter-family comets. Comets contain the building blocks of the solar system, preserved in deep freeze for 4.6 billion years. Sample return of pristine cometary material was identified as a high priority in the most recent Planetary Decadal Survey [37], and a comet sample return mission --- from a single comet --- was one of two finalists in the most recent New Frontiers (1B-class) competition [38]. Even with an aggressive schedule, cometary samples would be expected no earlier than the mid-2040's with a New Frontiers approach. However, a fleet of 10 g interplanetary spacecraft has the potential to collect cometary samples from dozens of Jupiter-family comets within the next decade. Because cometary materials are complex on the submicron scale, large samples are not required for cometary sample return: the thousands of $\sim$10 $\mu$m rocks and abundant organic materials would keep the cosmochemistry community busy for decades.

## 1.2 Unifying Architecture and Research Intent

The projects presented in this dissertation are not intended to stand as isolated MEMS devices or independent spacecraft concepts. Rather, they form a single research direction centered on the question of whether MEMS mechanisms can provide direct mechanical functionality for femtoscale interplanetary spacecraft. In this framework, the Berkeley Low-cost Interplanetary Solar Sail (BLISS) is the spacecraft architecture. It provides the mission context, the solar-sail propulsion platform, the low-mass spacecraft body, and the system-level motivation for using MEMS actuation in space.

Within that architecture, the MEMS Actuators for control of Solar-sail Tethers (MAST) serve as the steering and tether-control mechanism for BLISS. The MAST devices are designed to displace the carbon-fiber tether elements connected to the solar-sail frame, thereby changing the relative geometry of the sail and spacecraft body. This motion provides a means of shifting the relationship between the center of pressure and the center of mass, allowing the spacecraft to generate steering torques under solar radiation pressure. Thus, MAST is not merely a separate MEMS actuator demonstration; it is the mechanical steering interface of the BLISS spacecraft.

The Self-righting Quadrupedal Inchworm Driven Spacewalker (SQuIDS) extends the same architecture from spacecraft-level transport to surface-level exploration. In the intended mission concept, a BLISS-class solar-sail spacecraft could carry a SQuIDS rover as a microrobotic payload for on-asteroid or small-body exploration. Whereas BLISS enables low-cost transport through the inner solar system and MAST provides sail steering, SQuIDS addresses what happens after arrival at a small body: local mobility, surface interaction, and recovery from uncertain landing orientations. The SQuIDS work therefore represents a first step toward pairing femtoscale spacecraft transport with MEMS-based in-situ exploration.

The Transmission Gap Closing Actuator (TGCA) work provides a longer-term actuation path that connects these systems at the motor level. The BLISS, MAST, and SQuIDS concepts all depend on compact MEMS motors capable of producing controlled displacement and useful force within severe mass, volume, and power constraints. The TGCA architecture is intended to replace the conventional inchworm motors used in these systems in a future design generation by providing bidirectional, transmission-capable, and variable-output MEMS actuation. In this sense, TGCA is both a motor contribution and a unifying actuator technology for the broader platform.

Taken together, BLISS, MAST, SQuIDS, and TGCA define a linked MEMS-enabled exploration architecture. BLISS is the spacecraft, MAST is the steering controller for the solar-sail tether system, SQuIDS is the intended microrobotic rover payload for asteroid-surface exploration, and TGCA is the next-generation motor technology that could eventually replace and improve the motors throughout the system. The work presented here establishes the mechanical concepts, models, fabrication approaches, and preliminary demonstrations needed to support that architecture. However, several parts of the complete system remain intentionally open-ended: BLISS requires further spacecraft-level integration and environmental qualification; MAST requires additional tether-loaded and vacuum testing; SQuIDS requires further assembly, locomotion, and deployment validation; and TGCA requires additional refinement before it can replace the conventional inchworm motors throughout the platform. Thus, this dissertation should be read both as a set of technical contributions and as a roadmap for future work. A central purpose of the dissertation is to define a coherent path that future students can continue toward an integrated MEMS-controlled solar-sail spacecraft and microrobotic exploration platform.

## 1.3 Contributions

This dissertation describes a linked architecture for low-cost interplanetary missions based on femto-scale solar sail spacecraft and MEMS-enabled mechanical control. The central spacecraft is BLISS, which uses MAST as its tether-control and steering mechanism and is intended to support small microrobotic payloads such as SQuIDS for on-asteroid exploration. The TGCA work provides a future actuation path for replacing the conventional inchworm motors used across these systems with a more versatile transmission-capable MEMS motor architecture. The major contributions are:

1. The design and implementation of a steerable interplanetary femto-spacecraft architecture, BLISS, using COTS components and solar-sail propulsion.
2. A mission architecture, including trajectory design and control laws, for low-cost NEO imaging and cometary sample return.
3. The development of a novel, transmission-capable MEMS actuator architecture intended to enable bidirectional, multi-modal force and displacement outputs.
4. The design and analysis of SQuIDS, a self-righting quadrupedal microrover intended as a possible BLISS-carried payload for surface exploration in micro-gravity environments.
5. The design and analysis of MAST, a MEMS inchworm-motor tether-control system for direct actuation and steering of the BLISS solar sail.

## 1.4 Outline

Each chapter in this dissertation builds toward the same integrated concept: a femtoscale solar-sail spacecraft that can steer itself using MEMS tether actuation, carry MEMS microrobotic payloads for small-body exploration, and eventually use transmission-capable MEMS motors as a common actuation technology across the spacecraft and rover systems.

Chapter 2 discusses the prior literature, historical cases, and contemporary advances of similar work. This chapter reviews emphasized and similar works in the sub-field of solar sails and chip-scale spacecraft.

Chapter 3 presents the design, fabrication, and dynamics of the Berkeley Low-cost Interplanetary Solar Sail (BLISS) spacecraft, a nearly 10-gram vehicle built from COTS components. It details the hardware architecture, including the integration of computation, power, imaging, and propulsion subsystems, and establishes the physical principles governing its motion along with the mechanical and thermal performance.

Chapter 4 presents the first of the MEMS-specific technical contributions, a novel MEMS-based transmission for solar sail actuation. This chapter details the theory, design, and experimental characterization of a bidirectional, transmission-capable Gap Closing Actuator (TGCA) that provides the precise control authority required for solar sailing.

Chapter 5 presents the second MEMS-specific technical contribution: the Self-righting Quadrupedal Inchworm Driven Spacewalker (SQUIDS). This chapter describes the design and analysis of a MEMS-based microrover capable of locomotion and self-righting in microgravity environments found on asteroids and comets, enabling in-situ surface science.

Chapter 6 represents the third MEMS-specific technical contribution: the MEMS Actuators for control of Solar-sail Tethers (MAST). This chapter describes the design and analysis of a MEMS actuator for direct steering of the BLISS spacecraft.

Chapter 7 provides a final summary, synthesizing the key findings and contributions of the preceding chapters. It reiterates the potential for MEMS use in femto-spacecraft to transform planetary science and discusses future directions for research in this emerging field.

Because the full BLISS--MAST--SQuIDS--TGCA architecture is larger than any single dissertation-scale demonstration, the chapters that follow should be understood as connected stages of a broader research program rather than as a completed flight-ready system.

# Chapter 2

# Literature Review

## 2.1 Small Spacecraft: The Frontier of Spacecraft Miniaturization

The evolution of spacecraft over the past several decades has been marked by a sustained trend toward miniaturization. What began as a transition from large, monolithic spacecraft to smaller and more modular platforms has accelerated into a broader redefinition of what constitutes a viable space system. This progression extends beyond the now-mature CubeSat standard and into increasingly compact classes of spacecraft, including picosatellites, femtosatellites, and attosatellites [39--41]. At these scales, spacecraft design is no longer governed solely by conventional mass reduction; rather, it increasingly depends on new manufacturing paradigms, new subsystem integration strategies, and new mission philosophies.

This trend toward ultra-small spacecraft is not merely an exercise in miniaturization for its own sake. Instead, it reflects a fundamental shift in the economics and architecture of spaceflight. The availability of highly integrated, low-cost commercial electronics has enabled functions that once required multiple dedicated spacecraft subsystems to be condensed into single boards, flexible circuits, or chip-scale packages [39]. As a result, classes of spacecraft that were once conceptual now occupy a credible region of the design space, particularly for distributed sensing, short-duration technology demonstration, and low-cost access-to-space missions.

At the same time, miniaturization changes the governing engineering constraints. As spacecraft shrink, form factor and manufacturing method become increasingly inseparable from system architecture. Planar fabrication methods such as printed circuit board manufacturing, flexible substrate integration, and MEMS-compatible processing do not simply reduce cost; they impose geometric constraints that influence power generation, communications, structural behavior, and attitude control. Consequently, the study of ultra-small spacecraft requires not only a mass-based taxonomy, but also a classification by form factor and physical architecture.

## 2.1.1 The Path Forward

### 2.1.1.1 The COTS Revolution as the Primary Enabler

The gram-scale spacecraft revolution is almost entirely dependent on the availability and performance of low-cost, highly integrated Commercial-Off-The-Shelf (COTS) components [42, 43]. The development trajectory of these platforms is fundamentally intertwined with the consumer electronics industry. An analysis of key projects reveals that their core technologies are not products of bespoke aerospace research but are rather opportunistic adoptions of components---microcontrollers, sensors, radios, and power systems---originally developed for terrestrial mass markets such as mobile phones, automotive systems, and the Internet of Things (IoT) [42, 43]. This symbiotic relationship creates an agile but technologically dependent innovation cycle, where advances in space capability are directly tied to the release schedules of commercial hardware. This reliance on COTS technology introduces a critical duality. On one hand, it radically lowers the financial and technical barriers to entry for space access, enabling academic institutions, small companies, and even individuals to develop and launch space missions for costs that are orders of magnitude lower than traditional programs [19, 39, 42]. On the other hand, it imports the inherent vulnerabilities of non-space-grade hardware, particularly susceptibility to the harsh radiation environment of space, which can lead to premature component degradation and mission-ending failures.

### 2.1.1.2 Literature Review Scope and Structure

This section provides a technical review of solar sail spacecraft and related chip-scale platforms developed or conceptualized for use in space. It begins by establishing a clear taxonomy for this emerging class of spacecraft. It then presents a comparative analysis of key projects, detailing their technical specifications, mission objectives, and flight heritage. Following this, the report explores visionary concepts for interplanetary and interstellar applications that motivate much of the research in this field. This review does not present a fully comprehensive analysis of the enabling COTS technologies or claim to present a definitive analysis of which architecture is preferable for a given use case. Rather, it presents the prior works in their representative categorizations as a catalog of the historical background of solar sails and chip-scale platforms to give context for the gap in technology that many others might benefit from by filling that gap. It presents questions to be answered in many ways and poses the question to the reader, where future contributions in this regard best benefit humanity?

In doing so, the author hopes to present the technological background in such a way as to help the reader better answer the question and to help the reader see how the author attempted to answer this question in his own right.

### 2.1.2 New Mission Philosophies

The emergence of gram-scale and ultra-small spacecraft has enabled mission concepts that are impractical or uneconomical with conventional spacecraft. Because these platforms can often be produced at far lower cost and in much greater number than traditional satellites, they support a different philosophy of mission assurance. Rather than relying on the near-zero-failure expectation associated with large flagship missions, ultra-small-spacecraft missions may instead tolerate substantial unit-level failure while achieving system-level success through redundancy, multiplicity, and distribution [39]. In this framework, mission success is no longer defined solely by the survival of each individual spacecraft, but by the collective performance of a population.

Instead of the "zero-failure" tolerance required for a multi-billion-dollar flagship mission, gram-scale missions can be designed with an expected high failure rate, relying on mass redundancy to achieve collective objectives [39]. The successful KickSat-2 mission, which deployed 105 ChipSats, and the conceptual Breakthrough Starshot project, which envisions a fleet of a thousand interstellar probes, exemplify this philosophy [19, 44, 45]. This statistical approach to mission assurance allows for architectures that are collectively robust, opening possibilities for high-risk, high-reward missions in hazardous environments, such as atmospheric entry probes or planetary impactors, where individual survival is unlikely [39]. Furthermore, these platforms are ideal for creating massively distributed sensor networks capable of making simultaneous, multi-point measurements of phenomena like space weather or planetary gravity fields, providing a level of spatial and temporal resolution that a single satellite cannot achieve [46]. Additionally, the decrease in mass and volume drastically cuts down on the prevalence of space debris, allowing for a cleaner and more predictable future of spaceflight. Previous missions were inundated with concerns about decommissioning and secondary use as the debris cloud could become larger than the volume occupied by the deployed launch vehicle and its payload adapters where smaller craft exist in the size regime of their individual debris components [47]. Individual particulate scale debris can cause catastrophic damage to any spacecraft or satellite and debris trajectories are often irregular and unpredictable and rely on statistical models to characterize their spatial density [47--50].

Distributed missions also enable scientific capabilities that are difficult to achieve with a single spacecraft. Large numbers of small vehicles can provide simultaneous, multi-point measurements of spatially varying phenomena such as atmospheric structure, space weather, magnetic-field topology, or local gravity-field variations [46]. For hazardous or short-lifetime mission environments, this architecture is especially attractive because it allows high-risk measurements to be obtained without requiring each individual unit to survive for extended periods.

However, the same characteristics that make ultra-small spacecraft attractive also impose new limitations. Power generation scales unfavorably as characteristic size decreases, communications margins narrow rapidly, and reliance on COTS electronics increases vulnerability to radiation and other space-environment effects. Consequently, the transition from demonstration missions to operational or science-focused deployments depends not only on continued miniaturization, but also on improvements in subsystem reliability, fault tolerance, and low-power system design [39]. The long-term utility of these spacecraft therefore depends on the ability to convert low-cost hardware into architectures that remain credible under realistic mission environments.

### 2.1.3 Taxonomy of Small to Ultra-Small Spacecraft

A consistent classification scheme is necessary because the literature does not employ a single universal taxonomy for small and ultra-small spacecraft. Mass-based definitions vary somewhat across institutions, but NASA classifications and widely cited academic reviews provide a useful basis for synthesis [39--41, 51, 52]. In this work, the term *Smallsat* is used broadly for spacecraft below 500 kg, while *Ultra-SmallSat* is used to denote the lower end of that spectrum, especially picosatellites and below.

The following taxonomy is adopted primarily on the basis of wet mass:

- **Minisatellite (MiniSat):** spacecraft in the approximate range of 100 kg to 500 kg. These systems often support commercial constellations, remote sensing, or more capable scientific payloads, and occupy the upper end of the Smallsat regime [53, 54].
- **Microsatellite (MicroSat):** spacecraft in the range of 10 kg to 100 kg. This class often includes Earth-observation platforms, scientific missions, and advanced technology demonstrations, where greater subsystem capability is required than in CubeSat-scale architectures [55].

- **Nanosatellite (NanoSat):** spacecraft in the range of 1 kg to 10 kg. This category includes the canonical CubeSat regime and has become the most visible and widely adopted class within academic and commercial small-spacecraft development [17, 56].
- **Picosatellite (PicoSat):** spacecraft in the range of 100 g to 1 kg. This class includes architectures such as PocketQubes and ThinSats, and is often associated with low-cost technology demonstration, education, and early-stage subsystem validation [57, 58].
- **Femtosatellite (FemtoSat):** spacecraft in the range of 10 g to 100 g. This class is especially relevant to planar spacecraft, ChipSats, and other highly integrated demonstrators that push miniaturization into the gram-scale regime [39--41].
- **Attosatellite (AttoSat):** spacecraft in the range of 1 g to 10 g. This category represents the lower boundary of currently plausible functional spacecraft concepts and is associated with highly integrated, often experimental architectures [59, 60].
- **Zeptosatellite (ZeptoSat):** a currently theoretical category for spacecraft below 1 g [61]. At present, this regime is best understood as a conceptual extension of ultra-miniaturized spacecraft enabled by future developments in nanoscience, materials science, and extreme subsystem integration.

This mass-based taxonomy is useful for framing the scale of a spacecraft, but it is insufficient on its own. At the smallest scales, manufacturing approach and physical geometry become equally important descriptors. A femtosatellite based on stacked CubeSat-derived electronics differs fundamentally from a femtosatellite fabricated as a planar, PCB-based, or chip-scale device. For that reason, a second classification by form factor and architecture is also required.

This taxonomy is intended to define the mass regimes used throughout this dissertation. The categories are not universally applied in the literature, but they provide a practical framework for comparing spacecraft architectures across kilogram-, gram-, and sub-gram-scale systems.

### 2.1.4 Classification by Form Factor and Architecture

Beyond mass, ultra-small spacecraft can be classified by their physical architecture. This is especially important because, at small scales, spacecraft geometry is often a direct consequence of the manufacturing infrastructure used to produce it. In contrast to conventional spacecraft, which are generally assembled as three-dimensional structures from specialized aerospace subsystems, many ultra-small spacecraft derive their form directly from planar electronic manufacturing processes such as printed circuit board fabrication, flexible-film assembly, or MEMS-compatible lithographic methods.

These manufacturing choices are not merely economic. They define the structural and functional character of the spacecraft. Planar or quasi-planar spacecraft generally offer low cost, repeatability, and compatibility with mass production, but they also introduce new challenges in structural rigidity, thermal control, attitude determination and control, power generation, and packaging. Accordingly, form factor is not a superficial descriptor; it is a primary architectural variable that shapes subsystem performance and mission suitability.

#### 2.1.4.1 CubeSat: The Standardized Small Spacecraft Bus

The CubeSat standard remains the dominant small-spacecraft architecture in the nanosatellite regime. Based on modular units of approximately $10\,\mathrm{cm} \times 10\,\mathrm{cm} \times 10\,\mathrm{cm}$, CubeSats established a common mechanical, integration, and deployment framework that dramatically lowered barriers to access for universities, research groups, and emerging space companies [17, 56]. The availability of a standardized deployer, coupled with increasing access to low-cost launch opportunities, transformed CubeSats from educational tools into credible scientific and commercial platforms.

CubeSat units (U) generally have a $1\ kg$ weight and are $1,000\ cm^2$ stackable from $1-24\ U$ in general usage, with $3\ U$ being the most widely used ($SI64$) [62], for various proposed missions such as ionospheric sensing [63], asteroid close-proximity imaging [64], analysis of radiation effects on biological samples during deep space exploration [65], quantum communication [66], ice thaw mapping [67], and much more. Even with cost savings from COTS components, CubeSat development for specific mission uses usually ranges well above $\$10,000\ USD$ and takes years to develop [68].

The CubeSat ecosystem also normalized the use of COTS electronics in space-system development, a design pattern that later enabled even smaller PCB-based, ChipSat, and planar spacecraft architectures.

#### 2.1.4.2 ChipSat: The Integrated Planar Spacecraft

The term *ChipSat* refers to a spacecraft in which the majority of functional subsystems are integrated onto a single printed circuit board, flexible substrate, or chip-like platform, resulting in a flat and highly mass-efficient form factor. In the contemporary literature, the term is often most closely associated with the Sprite and Monarch lineages developed through Cornell-led efforts [59, 69]. These spacecraft represent a significant departure from the CubeSat approach: rather than miniaturizing a conventional bus architecture, they collapse much of the spacecraft into a nearly monolithic planar device.

ChipSats are significant because they expose the extent to which spacecraft can be reduced to a manufactured electronic object rather than an assembled vehicle. This shift has major implications for cost, scalability, and mission design. The rapid progression of gram-scale spacecraft is exemplified by the deployment and launch of 105 Sprite femtosatellites by the KickSat-2 mission by Manchester *et al.* at Cornell University [19, 45]. Manchester *et al.* [19] have deployed an orbital swarm of more than one hundred ChipSats, spacecraft at the size scale of a system-on-chip (often designed in the same processes as consumer electronics) weighing only a few grams each. This progress, driven almost exclusively by the leveraging of COTS microelectronics, has demonstrated the fundamental viability of building and operating functional spacecraft with masses measured in single grams. However, the transition from short-duration technology demonstrators to widespread deployment for complex science and commercial missions faces several significant hurdles that define the current research frontiers.

Despite this promise, ChipSats remain constrained by a set of tightly coupled subsystem limitations. Power is the most immediate of these. Because available surface area scales down more rapidly than many subsystem power requirements, ultra-small planar spacecraft face a persistent power-density challenge. Communications is closely related: transmitting useful data from low-power hardware with extremely limited antenna volume remains difficult even in Low Earth Orbit, and becomes far more restrictive in deep-space applications [43, 44]. Additional barriers include radiation tolerance, limited attitude control authority, thermal management, and the absence of mature propulsion systems suitable for the gram-scale regime.

Accordingly, the present state of the field is best understood as a transition from proof-of-concept demonstration to architecture maturation. The physical feasibility of gram-scale spacecraft has been established, but their expansion into long-duration, high-value science or commercial roles depends on the maturation of power systems, communications strategies, radiation robustness, and low-mass control or propulsion technologies.

#### 2.1.4.3 Notable Related Architectural Concepts

Several related terms appear in the literature and are useful for clarifying the architectural landscape surrounding ChipSats and planar spacecraft.

**PCBSat (Printed Circuit Board Satellite):** PCBSat is a broader architectural category for spacecraft built primarily on standard printed circuit boards. The concept emphasizes the use of industrial PCB manufacturing infrastructure to produce low-cost, mass-replicable space systems. Whereas the term ChipSat often implies an extreme degree of planar integration and very low mass, PCBSat may refer to a wider range of architectures built around one or more boards with minimal structural overhead [46].

**PlanarSat (Planarized and Multi-Chip Based Satellites:** PlanarSat is a useful descriptive term for spacecraft with very large surface-area-to-thickness ratios. This geometry is characteristic of many PCB-based, flexible, and chip-scale spacecraft, and it introduces subsystem challenges that differ from those of compact three-dimensional buses. For example, power generation becomes highly surface constrained, thermal gradients can become pronounced, and attitude-control solutions must often be adapted to a geometry with limited out-of-plane moment arms [42, 70].

**DustSats (Smart Dust-derived spacecraft):** The term "DustSat" is not a formally recognized class of spacecraft but is introduced here to represent the "space-based Smart Dust" swarm concept. The term "Smart Dust" originated in the 1990s from DARPA-funded research into terrestrial wireless sensor networks, describing a system of tiny, millimeter-scale MEMS sensors, or "motes," distributed in an environment to collect data [71]. In the context of space applications, the term has been adopted to describe a conceptual, often propellantless femtosatellite. This "space-based Smart Dust" would have a high area-to-mass ratio, allowing it to use external forces like solar radiation pressure for propulsion and maneuvering, typically as part of a communicating swarm [72, 73]. The conceptual foundation for autonomous planetary swarms was largely established by Barker [74], after the initial proposed use cases by Warneke [75, 76]. These concepts are especially relevant to future work in distributed sensing, swarm autonomy, and ultra-low-mass sailcraft.

The significance of these related terms is that they show the field is not converging on a single ultra-small-spacecraft architecture. Instead, it is diversifying into multiple lineages defined by manufacturing strategy, form factor, and mission philosophy. CubeSats, PCBSats, ChipSats, planar spacecraft, and Smart Dust-derived concepts should therefore be understood not as competing labels for the same object, but as overlapping categories that reflect different architectural priorities.

### 2.1.5 Architectural Implications for Ultra-Small and Planar Spacecraft

Taken together, the preceding taxonomies show that spacecraft miniaturization is not governed by mass alone. As systems move from the kilogram scale toward the gram scale, architecture becomes increasingly dominated by form factor, manufacturing process, and distributed mission philosophy. This is particularly important for planar spacecraft, where the same geometric features that simplify fabrication also intensify engineering challenges in power, communications, structural reliability, and control.

These trends are especially relevant to solar-sail and other area-dominated spacecraft concepts. Planar and chip-scale spacecraft naturally possess large surface-area-to-mass ratios, making them promising candidates for architectures in which propulsion, structure, and geometry are tightly coupled. In such systems, the spacecraft bus is no longer merely a platform to which propulsion is attached; rather, the physical form of the spacecraft may itself become the dominant propulsive and structural element. This observation motivates a more detailed examination of small solar sails, where deployment mechanism, stiffness source, sail area, and steering approach collectively define the relevant architecture. See Fig. 2.1 for a comparison chart that summarizes relative sizes, masses, operating orbits, and subsystem characteristics of representative planar spacecraft.

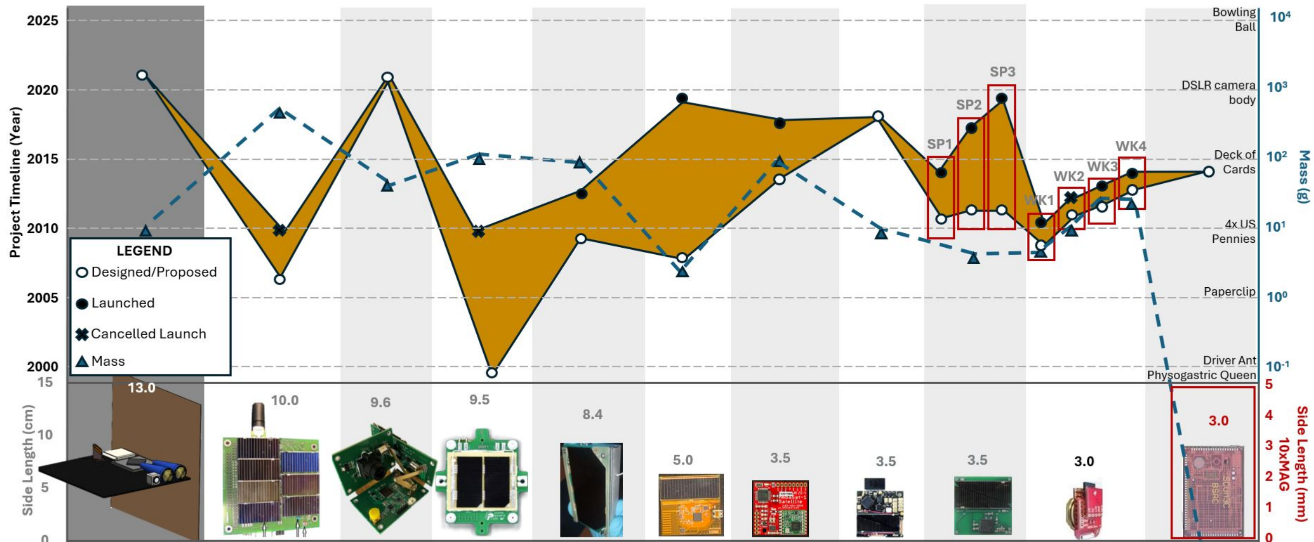


| | BLISS | PCBSat | f-PCBSat | RyeFemSat | p-PUCP | Monarch | AmbaSat-1 | SpinorSat | Sprite | WikiSat1 | SCuM |
|---|---|---|---|---|---|---|---|---|---|---|---|
| Steering | MEMS+IMU+SS | - | IMU+MT-MM | - | - | - | - | Torque Coils | - | IMU+MT | - |
| Oper. Orbit | IP | LEO | LEO | LEO(400-800km) | LEO | LEO | LEO (300km) | LEO | LEO | LEO(250km) | - |
| DIM (cm) | 13x13x8 | 10x10x2.5 | 9x9.6x1.6 | 9x9.5x1.0 | 8.4x4.85x1.64 | 5x5x0.1 | 3.5x3.5x0.2 | 3.5x3.5x0.1 | 3.5x3.5x0.2 | 3x2.5x0.2 | 0.3x0.2x0.03 |
| Mass (g) | 9.8 | 300 | 70 | 100 | 97 | <3 | <100 | <10 | 5.0 | 7.6 | 5e-3 |
| COMM TX | 10mW Laser+FL | 2.4 GHz, 60 mW RF | CC1101 RF | 2.4-2.5 GHz | 10mW CW OOK | 2.4 GHz | UHF dwnlnk | UHF / BPSK | 437.325 MHz, 10mW | 2.4 GHz ISM | 2.4 GHz ISM |
| COMM RX | SPAD+FL | - | - | - | 437.2 MHz | - | LP LoRa btwn | - | Coiled Nitinol | Ceramic Ant | - |
| Power | SC+LiPo BAT | GaAs SC+LiPo BAT | Si SC+LiPo BAT | SC+LiPo BAT | CaInP/GaAs/Ge SC | SC | 5 1U SAUs | 17cm RF | SC 60 mA at 2.2 V | 3.3V LiPo+GaAs SC | 1.0-1.2 V |
| Imaging | 16 Mpxl | 640x480 CMOS | 2 MP CMOS | 640x480 CMOS | - | SR & 3D-MT | * | PCB-MT | - | 1.3 Mpx HD | * |

Figure 2.1: Chart of ChipSats, PCBSats, and PlanarSats describing the approximate relative sizing, where ordering on the horizontal axis is by side-length or diameter from largest to smallest. The vertical axes are shared, where the left-hand side depicts year of project start and finish/cancel and the right-hand side depicts mass of the spacecraft. Acronyms for Steering row are: inertial measurement unit (IMU), micro electro-mechanical systems (MEMS), solar sail (SS), magnetorquers (MT), magnetometers (MM), where '-' means that the systems themselves were either passive or non-controlled. Acronyms for Operating Orbit row are: inter-planetary orbit (IP), low-earth orbit (LEO), with some having their orbit distance called out. In the Imaging row, '-' indicates no imaging or sensing capabilities were known at the time of writing this and '*' is used to indicate that the systems employ a range of optional sensing capabilities however none include imaging capabilities.

### 2.1.6 Propellantless Spaceflight: Small Solar Sails

Propellantless propulsion remains highly attractive for spaceflight because it decouples total delivered impulse from carried propellant mass. Although a range of concepts have been proposed under the broader umbrella of propellantless or quasi-propellantless flight, solar sailing remains the most mature and repeatedly flight-demonstrated architecture for sustained propellant-free spacecraft propulsion using solar radiation pressure [1, 77]. The practical significance of this capability is especially strong for small spacecraft, where onboard propellant mass and tankage volume can dominate the system-level design space.

In parallel with the broader miniaturization of spacecraft, solar sail systems have also undergone substantial reductions in mass, stowed volume, and subsystem complexity. This trend has enabled a growing set of small solar sail missions and technology demonstrations, ranging from CubeSat-scale boom-deployed sails to more scalable spin-tensioned concepts [78--80]. However, the design space is not well represented by a simple chronological list of missions. A more useful literature-review framework is to classify solar sail architectures according to four coupled engineering considerations: *structural stiffness*, *sail area*, *steering mechanism*, and *deployment mechanism* [1].

These four considerations are not independent. The deployment mechanism determines how the membrane is released, tensioned, and packaged. That choice strongly constrains the source of structural stiffness, whether the deployed sail is supported by booms, by centrifugal tension, or by a hybrid solution. The stiffness architecture then limits the feasible sail area through buckling, thermal distortion, wrinkle growth, and flexible-body dynamics. Finally, the steering mechanism must operate within the structural and dynamic envelope created by the first three choices. Accordingly, deployment and stiffness are the most upstream architectural decisions, while sail area and steering are more mission-facing variables selected within those upstream constraints [1, 78].

#### 2.1.6.1 Taxonomy by Stiffness Mechanism

The first major discriminator in solar sail architecture is the source of deployed structural stiffness. At the highest level, small solar sails can be grouped into **structurally stiffened**, **centrifugally stiffened**, and **hybrid** architectures. This distinction is fundamental because stiffness is not merely a structural property; it governs membrane shape fidelity, wrinkle suppression, flexible mode content, thermal sensitivity, and control bandwidth.

**Structurally stiffened sails (typically three-axis stabilized):** These sys-

Table 2.1: Solar Sail Form Factor Classification

| Form Factor | Typical Bus | Sail Area | Architecture | Material Constraint |
|---|---|---|---|---|
| ChipSat | MEMS/ Femto | $cm^2 - m^2$ | Monolithic | **Stiction & Lithography:** Sail is often the substrate itself. Requires MEMS actuators for steering (e.g., electrochromic pixels). [81] |
| CubeSat | 3U - 12U | $10m^2 - 100m^2$ | Boom-Supported | **Stowage Efficiency:** Membrane thickness ($< 5\mu m$) and boom packing efficiency are critical. Booms often bistable composites. [79] |
| SmallSat | ESPA Class | $100m^2 - 1000m^2$ | Boom or Spinner | **Buckling Load (Booms):** Booms require high cross-sectional inertia (TRAC booms) to resist solar pressure without buckling. [82] |
| Large-Scale | Custom Bus | $> 2000m^2$ | Heliogyro / Disk | **Tensile Strength (Root):** Centrifugal loads dominate. Material must withstand high tensile stress at the root/hub interface. [1] |

tems rely on deployable booms or masts to support the membrane and maintain geometric tension. This is the dominant architecture for CubeSat-scale and near-term small-spacecraft missions because it is compatible with three-axis attitude control, deterministic pointing, and conventional payload operations [79, 80, 83].

In this regime, the sail behaves as a pre-tensioned membrane supported by long, slender deployable members. The central engineering challenge is that the deployed structure must remain sufficiently stiff to control out-of-plane deformation while remaining light enough to preserve a favorable area-to-mass ratio. As the sail size increases, boom mass, boom stability, thermal distortion, and post-deployment flexible dynamics can become the dominant scaling constraints rather than membrane mass alone [78, 82, 84].

These systems are therefore typically favored for missions in which pointing, communications geometry, science observation, or navigation place a premium on stable, non-spinning operation. In such cases, stiffness and steering are strongly coupled, because the usable control authority depends directly on the structural fidelity of the deployed sail.

**Centrifugally stiffened sails (typically spin stabilized):** These systems generate membrane tension through rotation and centripetal loading rather than through long compression-bearing booms. This architecture is especially attractive for larger sails because it avoids many of the mass and buckling penalties associated with cantilevered support members [77, 85].

Two important subclasses are commonly discussed:

- **Spinning disk sails:** A continuous membrane is tensioned by spacecraft spin, often with distributed masses or peripheral devices. The canonical demonstration is *IKAROS*, which used centrifugal deployment and maintained sail shape through rotation [77].

- **Heliogyros:** Rather than one continuous membrane, these systems employ long, narrow blades deployed from a rotating hub. The heliogyro architecture is attractive because it can reduce packaging complexity and, in principle, provide rapid steering through blade-pitch variation, though it introduces tightly coupled blade dynamics and control challenges [85].

In this class, stiffness is effectively replaced by rotationally generated tension. This improves scalability in sail area, but at the cost of tighter coupling between structural support, spacecraft angular momentum, and steering strategy.

**Hybrid or gradient-stiffness architectures:** A third class spans concepts that combine deployable structural members with rotational tensioning, variable-stiffness elements, or other distributed load-sharing approaches. These architectures are often proposed to bridge the gap between the operational stability of boom-supported sails and the scalability of spin-tensioned sails. Although less mature than the two principal regimes above, they are important in the literature because they expose the fact that stiffness is not a binary design choice but a continuum of load-path and shape-control strategies [82, 84].

From a systems perspective, the most important conclusion is that **stiffness is more upstream than steering and closely coupled to deployment**. Once the source of deployed stiffness is selected, the available sail sizes, control bandwidths, and mission-compatible pointing modes become substantially constrained.

#### 2.1.6.2 Taxonomy by Sail Area

Sail area is the most visible performance parameter in solar sail design, but it should not be treated in isolation. The true mission-relevant quantity is the effective area-to-mass ratio, since solar radiation pressure acceleration depends jointly on reflective area and total spacecraft mass [1]. Increasing sail area raises the available thrust force, but it also amplifies packaging difficulty, deployment risk, membrane wrinkling, boom loading, thermal sensitivity, and attitude-control complexity.

For this reason, sail area is best treated as a **downstream consequence** of the selected deployment and stiffness architecture. Boom-supported three-axis systems have historically occupied the small-to-moderate sail area regime, where structural control and deployment reliability remain manageable. By contrast, spin-supported architectures are more naturally extensible to larger sail areas because they avoid long compression-bearing booms and instead use rotational tension to maintain membrane shape [77, 85].

At small scale, modest sail areas can be favored for robustness and operational simplicity, particularly in technology demonstrations and Earth-orbit missions. At larger scale, the design challenge shifts toward membrane flatness, boom or blade stability, and tolerance to manufacturing and deployment asymmetries. Thus sail area is not simply a sizing parameter; it is a systems-level stressor that reveals the limits of the chosen stiffness and deployment approach [78, 83].

#### 2.1.6.3 Taxonomy by Steering Mechanism

Steering mechanisms provide the operational link between solar-sail architecture and mission objectives. In practice, steering approaches may be grouped into several recurring families: conventional spacecraft attitude actuators, center-of-mass / center-of-pressure offset methods, tip-vane or flap-based control, and modulation of sail optical properties.

- **Conventional actuator-assisted steering:** Small boom-supported sails frequently rely on reaction wheels, magnetorquers, or small thruster systems to maintain or reorient attitude. This is common when the sailcraft must support conventional communications pointing, observation geometry, or navigation operations [79, 80].

- **Center-of-mass / center-of-pressure offset control:** A widely studied method is to shift the spacecraft center of mass relative to the sail center of pressure, thereby generating controllable solar torque. This approach is especially attractive because it uses the sail force itself as the source of control torque [80].

- **Tip-vane or flap control:** Small aerodynamic-analog appendages or vanes can locally modify solar torque and allow steering without large bus reorientation. These methods are particularly relevant for larger sails, though they introduce additional deployables and hinge-like subsystems.

- **Reflectivity-control devices:** *IKAROS* demonstrated steering via liquid-crystal reflectivity control devices embedded in the sail, showing that optical-property modulation can provide torque without conventional moving appendages [77].

Of the four classification variables considered here, steering is the most strongly tied to mission-specific requirements such as maneuverability, target tracking, communications geometry, and permissible settling time. However, it is not fully independent: the effectiveness of any steering law depends on structural stiffness, membrane shape stability, and the deployment-induced symmetry of the sail. For that reason, steering should be understood as a **downstream architectural choice constrained by stiffness and deployment**, rather than as a primary independent driver.

#### 2.1.6.4 Taxonomy by Deployment Mechanism

The deployment mechanism is the most upstream of the four principal considerations because it defines how the launch-packaged system becomes a flight structure. It determines the initial release sequence, the method of membrane extraction, the buildup of sail tension, the deployment transients, and the stowed-volume efficiency of the system.

At the broadest level, solar sail deployment methods can be divided into **boom-driven deployment** and **centrifugal deployment**. Boom-deployed systems use stored-strain or mechanically driven deployable members to extend the sail corners or edges outward from the spacecraft bus. These systems are generally favored for missions requiring non-spinning operation, but they face strong engineering constraints in boom packaging, friction management, synchronization, and reliable one-time release [79, 80, 83].

Centrifugal deployment instead uses spacecraft spin to extract and tension the membrane. This can reduce the need for long, highly loaded structural members and is attractive for larger sail geometries. However, it also couples deployment directly to the spacecraft rotational state and can complicate payload operations, communications, and post-deployment maneuvering [77, 85].

For small solar sails, deployment reliability is often one of the dominant mission risks because the sail system is highly packaged, mechanically nonlinear, and only deployed once in flight. Consequently, deployment and stiffness are the most strongly correlated of the four major considerations. In practice, the deployment mechanism largely selects the admissible stiffness regime, which in turn bounds sail area and steering options. This is why deployment is best treated as the most upstream architectural choice in a subsystem-centered taxonomy of small solar sails.

#### 2.1.6.5 Notable Mentions

**Planet Labs** has shown that hundreds of 3 L spacecraft can support commercial Earth-observation use cases and that spacecraft assembled using consumer-electronics standards can survive in low Earth orbit (LEO).

**The Breakthrough Starshot** initiative hopes to show that similar spacecraft can go to the nearest stars and return image data [86]. While many works detail the use of solar sails, the continued use of specialized equipment that remains expensive and massive contributes to a high moment of inertia restricting the possibility of high agility maneuvers which remains a technological challenge.

Other work has described a smaller and similarly capable concept for deploying the ubiquitous SmartDust [73, 75] as a femtosatellite, ChipSat, propelled by SRP as described by Niccolai et al. [87] where the SmartDust femtosatellite is simulated as a sun-facing particle of orbital dust using an Electrochromic Coating System (ECS) for attitude control in various mission possibilities with onboard camera, solar cells, computation, antennas, and batteries.

Fig. 2.2 compares the size regimes of solar sails and related technology. In particular the selections are chosen for their range of unique demonstrative missions and physical characteristics as well as their chosen technology.

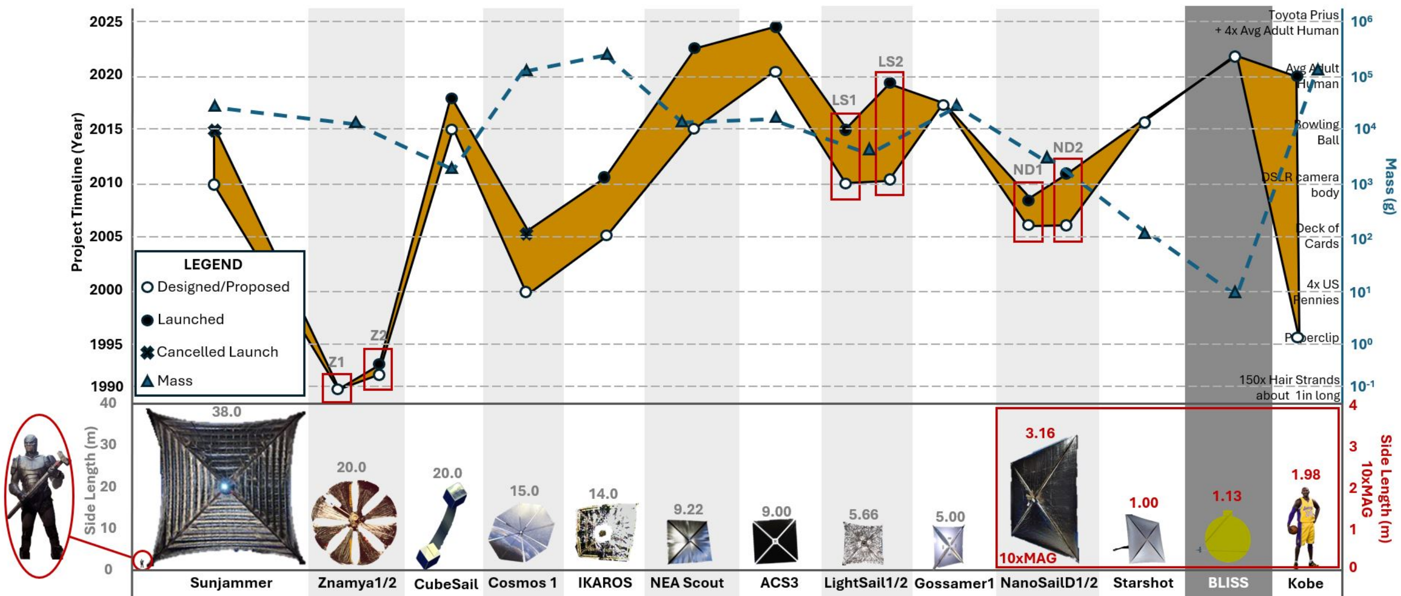


| | Sunjammer | Znamya1/2 | CubeSail | Cosmos 1 | IKAROS | NEA Scout | ACS3 | LightSail1/2 | Gossamer1 | NanoSailD1/2 | Starshot | BLISS | Kobe |
|---|---|---|---|---|---|---|---|---|---|---|---|---|---|
| **Active Sailing** | Y | N | N | Y | Y | Y | N | Y | N | N | N | Y | Y |
| **Sail Shape** | Square | Circular | Ribbon | Circular | Square | Square | Square | Square | Square | Square | Square | Circular | Sphere |
| **Steering Tech** | RW & DCV | N/A | N/A | RW & APA | LCVR | RW | RW & MT | RW & MT | N/A | N/A | N/A | MEMS | Mamba |
| **Deployment Method** | Inflatable Rigid Composite Booms | Centrifugal-deploy Mesh | Heliogyro | Spring-launched Booms | Spin-deploy Tension Booms | Mini-coil CFRP Booms | Roll Polymer-Composite Booms | Tape Spring Booms | Crossed Beam Booms | Tape Spring Booms | Tape Spring Booms | Carbon Fiber Rods | Zapata-Mobiles |
| **Mission Goal** | Large-scale SS prop. for DS miss. | Passive space mirror | Validate Ribbon | Rotating sail panel demo. | JAXA Venus Probe | Recon. NEA by SRP only | 12U CS | LEO demo | Passive tension demo | Sail self deploy (rapid) demo | Laser driven accel. demo | Inter-planetary exploration | Three-Peat Champ |

Figure 2.2: Chart describing the approximate relative sizing, where ordering on the horizontal axis is by side-length or diameter from largest to smallest. The vertical axes are shared, where the left-hand side depicts year of project start and finish/cancel and the right-hand side depicts mass of the spacecraft. On the far left-hand side in the red circle is a miniaturized image of NBA legend Shaquille O'Neal as depicted in the DC movie, Steel, and on the far right of the horizontal axis is an image of the NBA legend Kobe Bryant for scale comparisons. The acronyms for the Steering Tech row are as follows: rotating-wheel (RW), direct control vanes (DCV), adjustable panel angles (APA), liquid crystal variable reflectivity (LCVR), magneto-torques (MT), and micro electro-mechanical systems (MEMS), N/A means the systems were either passive or non-controlled.

# Chapter 3

# The Spacecraft: Berkeley Low-cost Interplanetary Solar Sail (BLISS)

## 3.1 Abstract

Leveraging advancements in micro-scale technology, we propose a fleet of autonomous, low-cost, small solar sails for interplanetary exploration. The Berkeley Low-cost Interplanetary Solar Sail (BLISS) project aims to utilize small-scale technologies to create a fleet of tiny interplanetary femto-spacecraft for rapid, low-cost exploration of the inner solar system. This paper describes the hardware required to build a $\sim$10 g spacecraft using a 1 $m^2$ solar sail steered by micro-electromechanical systems (MEMS) inchworm actuators. The trajectory control to a NEO, here 101955 Bennu, is detailed along with the low-level actuation control of the solar sail and the specifications of proposed onboard communication and computation. Two other applications are also briefly considered: sample return from dozens of Jupiter-family comets and interstellar comet rendezvous and imaging. The paper concludes by discussing the fundamental scaling limits and future directions for steerable autonomous miniature solar sails with onboard custom computers and sensors.

## 3.2 The Spacecraft

### 3.2.1 Structure and Function

This is where the structural considerations are introduced and levied against the mission goals. Later we discuss the structural capabilities (after we have introduced

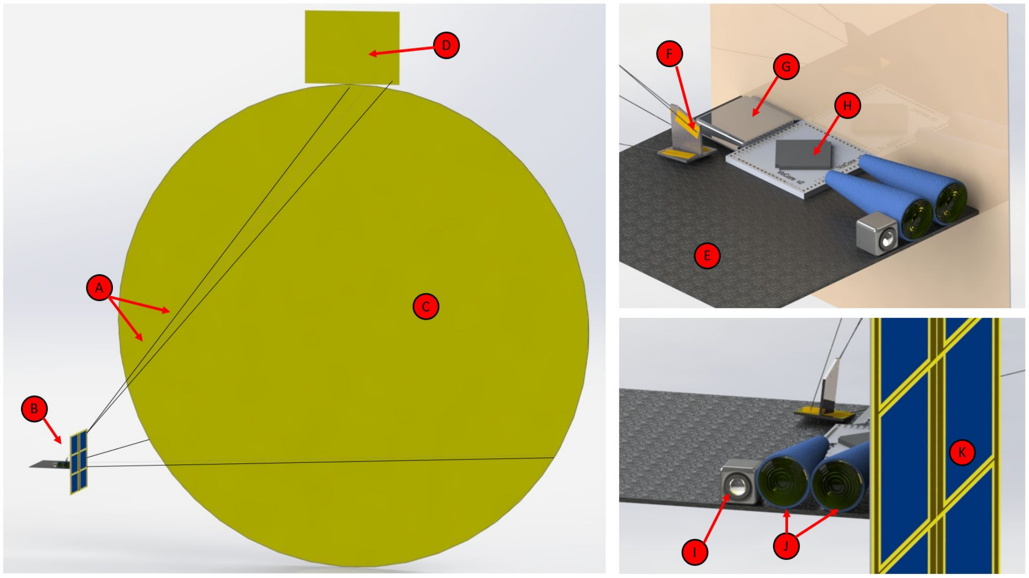


Figure 3.1: Rendering of the BLISS spacecraft. *Left*: isometric view of the solar sail craft with A) carbon fiber rods, B) spacecraft body, C) mylar main sail, and D) mylar roll sail. *Right-top*:spacecraft body with E) HOPG radiator fin, F) MEMS motor actuators, G) LiPo battery, and H) VoCore2 CPU. *Right-bottom*: spacecraft body with I) smartphone-grade CMOS image sensor, J) optical 853nm Tx/Rx, and K) solar panels.

the general structure itself and given some validation to why we chose that structure and not some other one).

The proposed components for the BLISS spacecraft are listed in Table 3.1 along with their masses and an illustration highlighting the components and their relative positions is shown in Fig. 3.20. None of the components listed have masses more than a few grams, and most, such as the battery and motors, are a small fraction of a gram.

With the core of the spacecraft weighing roughly 10 g and costing less than $1,000 USD, there are not many options for propulsion with the same order of magnitude in size and cost. Traditional chemical propulsion does not scale well to small sizes due to surface to volume issues with heat loss and low propellant burn rates [88]. Electric thrusters such as ion engines and electrospray engines are very promising, but are still orders of magnitude too large [88]. Until some other technique can be reduced to a mass of grams, the best propulsion for a 10 g spacecraft is a solar sail. The fundamental limits to this scaling are discussed in Sec. 3.7. While Lozano et al. has demonstrated spacecraft capabilities at the cm scale for 480 emitters using their

| Component | mass(g) |
|---|---|
| Mylar Sail | $< 2$ |
| MEMS Motors + IMU | $< 0.3$ |
| Optical Tx/Rx | 2 |
| HOPG Radiator | 1 |
| LiPo Battery | 0.33 |
| Camera | $< 1$ |
| VoCore2 PC | 2.4 |
| Alta Solar Cells | 2 |
| **Total** | $< 11.03$ |

Table 3.1: List of Component Masses

electrospray devices [49, 88, 89], their work shows that the necessary thrust to mass ratio is relatively higher than that of the solar sail described here while the power utilization to thrust is still undefeated for the solar sail case, where the solar sails power utilization is essentially infinite.

### 3.2.2 Solar Sail Sizing and Packaging

With this mass, a solar sail that is just over a meter in diameter is needed to accomplish a sail loading of $10\,\mathrm{g/m^2}$. Aluminized mylar is available in $1.5\,\mu\mathrm{m}$ thickness, weighs $2\,\mathrm{g/m^2}$, and yet is strong enough to be handled, cut, folded, and thermally bonded. A carbon fiber rod can be bent into a ring on the perimeter of the aluminized mylar sail and is sufficiently flexible to be bent into a multi-turn flattened disk, and sufficiently stiff to pop back to regular shape after release on orbit. Folds of three and five would allow a square meter sail to be carried inside a 9U or perhaps 3U CubeSat for early technology demonstrations [17, 90]. In addition to the main sail, we will append a small sub-sail called the *roll sail* to one edge of the main sail to achieve control authority about all body axes. For a launch with one thousand spacecraft after the technology has been proven, the sails may be stored stacked on top of each other, with the spacecraft bodies arrayed around the perimeter. One thousand spacecraft of this type will weigh roughly 10 kg, and the stack of sails could be only a few millimeters thick.

## 3.3 Dynamics

In this section we detail the physical mechanisms that control the small solar sail through its spaceflight.

### 3.3.1 Light Pressure

Photons have energy $E = hc/\lambda$, and momentum $p = h/\lambda = E/c$. A flux of photons with power $P$ being absorbed by a surface imparts a force equal to the change in momentum, $F_{\text{photon}} = P/c$.

A perfectly reflective flat sail of area $A$ at an angle $\alpha$ from the solar flux of $G_{\text{sc}} = 1.361\text{kW}/\text{m}^2$ experiences a normal force of:

$$F_N = 2\frac{G_{sc}}{c}A\cos^2(\alpha) \approx (9\ \mu N/m^2)A\cos^2(\alpha) \tag{3.1}$$

This is the same as the gravitational attraction between the sail and the Sun at a distance of 1 AU if the mass loading of the sail is roughly $1.6\,\text{g}/\text{m}^2$. Real sails will have a reflection coefficient less than 1, some Lambertian reflection, and pressure from black body emission from the back side, making the peak normal force somewhat lower [1].

The radial ($F_r$), tangential ($F_t$), and normal ($F_h$), components of the force then become:

$$F_r = F_N\cos(\alpha), \tag{3.2}$$
$$F_t = F_N\sin(\alpha)\sin(\delta), \tag{3.3}$$
$$F_h = F_N\sin(\alpha)\cos(\delta). \tag{3.4}$$

Taking $\delta$ to be $\frac{\pi}{2}$, it can be observed that the behavior in the plane of the ecliptic gives $F_t = F_N\sin(\alpha)$ & $F_h = 0$.

The tangential force is maximized at an angle $\sin^{-1}(1/\sqrt{3})$ ≈0.6 rad, giving a maximum tangential force of roughly $0.39F_N$. For near-circular orbits this is the force that maximizes the rate of change of orbital energy.

For a 10 g spacecraft with a $1\,\text{m}^2$ sail at 1 AU, this maximum force corresponds to an acceleration of roughly $0.3\,\text{mm}/\text{s}^2$.

The sail force vector for an ideally reflective sail is always normal to the surface of a flat sail, and the radial component is always positive (away from the Sun). Nevertheless, a solar sail can still move toward the Sun by using the tangential force making its orbital energy more negative while the SRP force vector opposes the velocity vector while still increasing the amplitude of its tangential velocity

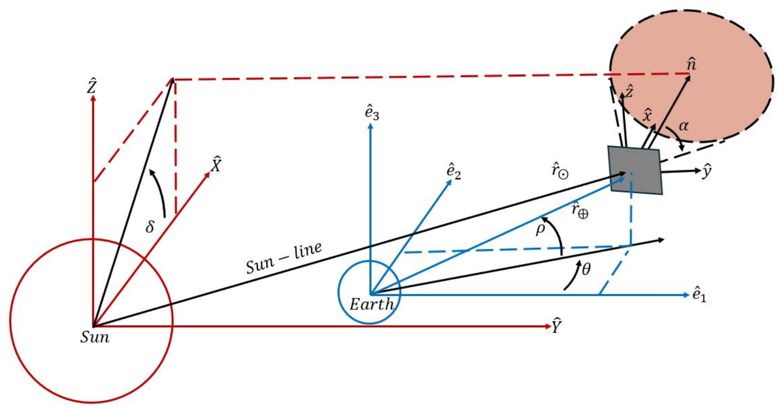


Figure 3.2: Diagram showing the relative coordinate system used for the Sun-Earth orbit over the earth escape trajectory showing coordinate, vector, and angle definitions.

component [31]. In a nautical analogy, the spacecraft tacks into the solar photon flux by dipping its keel into the sun's gravitational well. For elliptical orbits, the desired force will vary in angle relative to the sun line. In general, the force in a particular direction relative to the Sun line is maximized by a sail cone angle ($\alpha$) of roughly one third of the desired angle [1], see Fig. 3.2.

### 3.3.2 Rotation and Steering

Achieving the desired cone angle requires utilizing shifts in the center of mass (COM) relative to the SRP pointing vector creating a torque about the COM.

The main sail and the roll sail will be connected to the spacecraft body with four carbon fiber rods, here labeled a-d, roughly 0.3 mm in diameter and 2 m long.

The rods *a*-*c* will be connected at one end to the main sail with *a* designated as the stationary rod and attached at the opposing end to the main body structure. Rods *b* and *c* are attached at their opposing end to MEMS linear inchworm motors adjusting length to control the relative position and orientation of the main sail to the spacecraft main body. Rod *d* will control the roll sail's relative motion and is affixed at one end to the roll sail and the other end to MEMS motors similar to the previous two driven rods, *b* and *c*. The MEMS motors will be placed on the spacecraft body, as seen in Fig. 3.20 [91]. A schematic depicting the axis and relative positions of the main sail, roll sail, carbon fiber rods, and the spacecraft body can be seen in Fig. 3.3, not to scale.

Parallel and differential actuation of the first and second carbon fiber rods will move the main sail relative to the craft's payload, offsetting the COM from the SRP

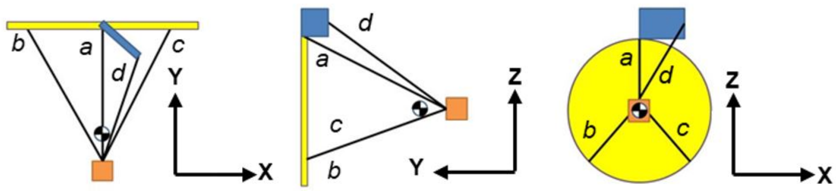


Figure 3.3: Illustrating the BLISS body centered reference frame and approximate center of mass. Lengths not to scale. *Left*: x-y plane, *Middle*: y-z plane, and *Right*: z-x plane.

pointing vector providing a moment about the COM of the system, allowing control of rotation about $x$-axis (pitch) and about $z$-axis (yaw). A fourth rod, with the third motor, will control the roll sail to generate a moment about the y-axis (roll). Here, a decoupled rotation approach is chosen where the rotations about the $x$- and $z$- axes neglect the contribution of torque due to the roll flag in the calculations below.

Coordinating movement of the inchworm motors gives an input acting on the main body of the femto-spacecraft as:

$$\vec{q} = \begin{matrix} q_{\mathrm{a}} & q_{\mathrm{b}} & q_{\mathrm{c}} & q_{\phi} \end{matrix} . \tag{3.5}$$

where $q_i$ represents a linear movement, caused by the MEMS inchworm motors, of the carbon fiber rod attached to the roll sail. Whereas $q_{\mathrm{b}}$ and $q_{\mathrm{c}}$ represent the linear movement of rods b and c which induces a positional change on the payload relative to the center-line of the main solar sail; the axes are shown in Fig. 3.3. Such movement will create a mirrored motion of the sail relative to the origin at the COM. Note, the sail positions ($x_{\mathrm{ss}}$, $y_{\mathrm{ss}}$, $z_{\mathrm{ss}}$) and payload positions ($x_{\mathrm{p}}$, $y_{\mathrm{p}}$, $z_{\mathrm{p}}$) are all functions of the inputs, $\vec{q}$. Still, the notation is simplified for clarity to be distances in their relative direction from the COM.

MEMS electrostatic inchworm motors have a step size that is typically designed to be on the order of 1 µm, with a speed on the order of $1\,\mathrm{mm\,s^{-1}}$ [91], and Teal *et al.* [92] has shown a range that has been demonstrated at nearly 8 cm. For this work, an actuation range of $\leq \pm 10$ cm, a speed of $1\,\mathrm{mm\,s^{-1}}$, and a step size of 2 µm is simulated in Sect 3.6. The inchworm motors are powered by capacitive gap-closing actuator (GCA) arrays and push a centrally aligned spine and pawl with high frequency, electrically induced steps [93]. Applied to the meter-scale shroud lines of the sail, this will generate an angular change in the sail center-line of roughly one microradian (0.2 arc seconds) per step. There may be significant low-frequency dynamics excited by an abrupt step, so caution in motor design is necessary.

In the body-centered frame the principal mass moments of inertia are:

$$\begin{aligned}\mathrm{I}_1 = &\frac{1}{4}m_{\mathrm{ss}}r_{\mathrm{ss}}^2 + m_{\mathrm{ss}}({y_{\mathrm{ss}}}^2 + {z_{\mathrm{ss}}}^2)\\&+ \mathrm{I}_{\mathrm{mp,xx}} + m_{\mathrm{p}}({y_{\mathrm{p}}}^2 + {z_{\mathrm{p}}}^2)\\&+ m_{\mathrm{ss}}^{\phi}({x_{\mathrm{ss}}^{\phi}}^2 + {y_{\mathrm{ss}}^{\phi}}^2)\end{aligned} \tag{3.6}$$

$$\begin{aligned}\mathrm{I}_2 = &\frac{1}{2}m_{\mathrm{ss}}r_{\mathrm{ss}}^2 + m_{\mathrm{ss}}({x_{\mathrm{ss}}}^2 + {z_{\mathrm{ss}}}^2)\\&+ \mathrm{I}_{\mathrm{mp,yy}} + m_{\mathrm{p}}(x_{\mathrm{p}}^2 + z_{\mathrm{p}}^2)\\&+ m_{\mathrm{ss}}^{\phi}{r_{\mathrm{ss}}^{\phi}}^2\end{aligned} \tag{3.7}$$

$$\begin{aligned}I_3 = &\frac{1}{4}m_{\mathrm{ss}}r_{\mathrm{ss}}^2 + m_{\mathrm{ss}}({x_{\mathrm{ss}}}^2 + {y_{\mathrm{ss}}}^2)\\&+ I_{\mathrm{mp,zz}} + m_{\mathrm{p}}(x_{\mathrm{p}}^2 + y_{\mathrm{p}}^2)\\&+ m_{\mathrm{ss}}^{\phi}({x_{\mathrm{ss}}^{\phi}}^2 + {y_{\mathrm{ss}}^{\phi}}^2)\\&+ I_{\mathrm{zz},\phi}\end{aligned} \tag{3.8}$$

where $I_{\mathrm{mp,xx}}$, $I_{\mathrm{mp,yy}}$, and $I_{\mathrm{mp,zz}}$ are the inertial moment of mass for the spacecraft body COM used to indicate positions of components within the spacecraft as related to the parallel axis theorem in the $\hat{x}$, $\hat{y}$, and $\hat{z}$ body centered coordinate system. Other cross terms exist and are negligible, but for early experiments these represent the principal moments of inertia used in Sec. 3.6.1.

If the sail normal is moved about 1 mm from the COM in the $\hat{x}$-direction, the resulting pitch or yaw moment will be a torque of around 60 nNm, and an angular acceleration of:

$$\ddot{\alpha} = \frac{\tau_{\mathrm{z}}}{I_{\mathrm{zz}}}, \tag{3.9}$$

roughly $1 \times 10^{-6}\mathrm{rad/s^2}$ if we take into account only the main sail giving a rough estimate for $I_{\mathrm{zz}} \approx I_{\mathrm{ss,zz}}$. Note, due to the symmetry shown in Eq. 3.6 and Eq. 3.8, the rotation about the $\hat{z}$ axis behaves similarly to the rotation about the $\hat{x}$ axis. Rotations about the $\hat{y}$ axis are substantially slower due to lower peak torque from the smaller roll sail, but motions in this axis are primarily for thermal regulation and data collection. These present a much smaller set of problems with much longer timescales of motion than when compared to maneuvers needed to escape geosynchronous orbit (GEO).

## 3.4 Mission profile

The mission profile entails orientation following an en masse launch, spiraling out from GEO, interplanetary trajectory optimization, NEO approach, imaging, and return to Earth for data transmission. Assuming that the spacecraft will be released near GEO, atmospheric drag will be negligible, as any orbit with a perigee above roughly $1,000$ $km$ [94] is high enough that the energy gained per orbit from the sail is greater than the energy lost due to atmospheric drag. The return to Earth mirrors the procedure to the interstellar object.

### 3.4.1 De-tumble and Orient

After release from the launch vehicle, the spacecraft will need to kill any residual rotation imparted by release.

Orientation control of the spacecraft is provided by MEMS inchworm motors pulling on shroud lines on the sail.

For rotation rates above $1\,^\circ\,\mathrm{s}^{-1}$, the on-board IMU will inform the control system's decisions. Low-cost MEMS gyros have thermal-noise-limited resolution and bias drift of a small fraction of a degree per second. Below that rate, the camera will be used in a time lapse exposure to find the axis of rotation and rotation rate. Once the rotation rate is sufficiently low, a standard "lost in space" algorithm will be run on the star images to accurately determine orientation [95]. If there is sufficiently low magnitude and duration of tumbling on release, the IMU itself may be able to provide fairly accurate initial orientation estimates. During this initial phase, communication between spacecraft and the launch vehicle will be possible to a distance of a few hundred meters using the integrated WiFi radio available in almost all embedded LINUX platforms.

### 3.4.2 Spiral out

Once oriented, the spacecraft will begin the process of increasing its orbital altitude until it crosses out of the Earth's sphere of influence, utilizing a trajectory in the Sun-Earth orbital plane.

A conservative estimate for escape time is given by [1]:

$$t_{\mathrm{escape}} = \frac{2800\ \mathrm{days}}{\beta\sqrt{6371 + h}}, \tag{3.10}$$

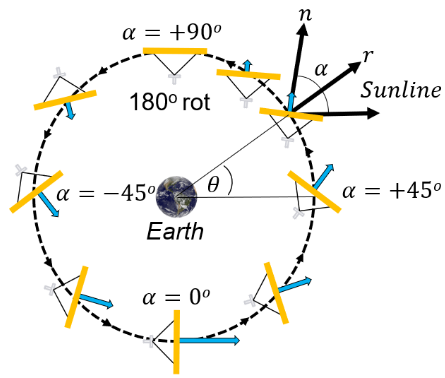


Figure 3.4: McInnes orbit rate steering law showing direction of sail normal throughout a full circular orbit around Earth. Adapted from [1]. Not to scale.

where $h$ is the initial orbital altitude in km, and $\beta$ is the sail lightness number, the ratio of the maximum light pressure acceleration to the solar gravitation, which to first order is independent of distance from the Sun.

For a sail mass loading of $10\,\mathrm{g/m^2}$, $\beta \approx 0.16$. Starting from GEO this process takes about three months. Imaging the Earth, moons, and stars provides the necessary position input for the attitude control system to calculate the necessary sail angle during this process. The chosen in-plane spiral-out trajectory is one adapted from McInnes [1], where the cone angle ($\alpha$) traverses from 0° to 90° monotonically with the mean anomaly ($\theta$), switches relatively quickly from 90° to −90° at the 'top' of the orbit, and then proceeds monotonically sweeping from −90° to 0° throughout the course of each orbit, as seen in Fig. 3.4, more in Sec. 3.6.1. During this phase of the mission, the spacecraft can be in periodic communication with ground stations on Earth using its primary optical communication system.

### 3.4.3 Localization and Matching Orbits

There is a wide variety of NEO orbits, the majority of which will take between a few months and two years to match given our sail mass loading [96] During this time, the spacecraft may be in communication with many of its neighbors, and able to use a combination of triangulation and optical time-of-flight (TOF) to determine its location in the solar system as other works have shown is possible [97]. Round trip TOF with a 1 Mbps optical communication system can easily achieve range errors of less than a kilometer at distances of at least one million kilometers, and small fractions of that error are possible with specialized hardware development. Pointing accuracy in the communication system should provide angular position measurements of roughly 0.1 mrad, or 100 km lateral accuracy at $1 \times 10^6$ km range, with errors accumulating the more hops the spacecraft is from a known reference point. If a fleet of spacecraft leaves the range in which communication with Earth is possible, it may have a reasonably accurate picture of the relative position of each member of the fleet (kilometers of error or less), but a very poor estimate of where the fleet is in the solar system (one hundred thousand kilometers).

For those spacecraft without communication to their neighbors, they will rely on triangulation using the location of the planets against the stellar background. Unmodified cell phone cameras are able to take pictures of stars down to visual magnitude 5 through Earth's atmosphere. With minimal effort the inner six planets can be located in these images with an accuracy of roughly one milliradian. This will allow a spacecraft to localize itself in interplanetary space to within a few hundred thousand kilometers at a single point in time using several photographs. With better image processing algorithms and fusion of sensor data taken over many days, it is likely that this accuracy will improve by at least one order of magnitude. In either case, once it is close to the target NEO the spacecraft will use its camera to do terminal guidance.

### 3.4.4 NEO Approach, Image, and Return

The mission objective of asteroid imaging requires a down-selection to decide on an asteroid for case study that can act as a representative example for the benefits of the BLISS system in operation. As such, selection will be narrowed to include only near-Earth asteroids with diameters of 1 to 2 km. There are roughly 400 asteroids of 1 to 2 km diameter in near-Earth orbits [96, 98]. Of these, the 101955 Bennu asteroid is taken as a prime example of state-of-the-art asteroid rendezvous recently accomplished. Images will be taken of Bennu from a parking orbit of $1-3$ km from the surface. After the spacecraft has determined that it has sufficient images of the NEO, it will begin the return trip to Earth, following inverse order outlined for the trajectories specified in this paper. After the return trip, BLISS will transmit its data down to receivers on Earth from GEO.

## 3.5 Components off the Shelf (COTS)

### 3.5.1 Imaging

Imaging will be accomplished with a cell phone camera from within 1 km, so that the asteroid fills the field of view (from an approximately 60 degree field of view angle the ideal distance away to fill the aperture is $\sqrt{3} \cdot r_{\mathrm{NEO}}$). This will provide imaging with resolution on the order of $1-10\,\mathrm{cm}$, enough to differentiate regolith or other surface types on asteroids.

### 3.5.2 Communications

Communication between a spacecraft and earth will be achieved by a semiconductor laser transmitter with a diffraction-limited 1 cm aperture, and a modestly sized single photon avalanche detector (SPAD) array with a receive aperture with a 10 cm diameter. This same hardware will allow peer-to-peer communication between spacecraft at more than one million kilometers, enabling a mesh network to pass data around the inner solar system.

Digital processing and storage will consist of an off-the-shelf VoCore2 embedded LINUX computer running custom software. A micro-electromechanical system (MEMS) inertial measurement unit (IMU) will provide high-rate rotation sensing, and the CMOS camera will provide low-rate rotation sensing, star tracking, attitude determination, and rough localization. Propulsion will be provided by a roughly $1\,\mathrm{m}^2$ solar sail, with MEMS motors controlling the sail and spacecraft orientation in 3 axes. Power will be provided by a $10 \times 10\,\mathrm{cm}^2$ primary solar panel, a small rechargeable lithium battery, and a few small solar cells distributed around the structure to maintain power during maneuvers. Thermal control will be accomplished by control of the orientation relative to the Sun of the primary solar cells, a small solar reflector, and a highly-oriented pyrolytic graphite (HOPG) radiator fin, in addition to management of the electronics power consumption.

### 3.5.3 Computation and Storage

Cell phones and the internet of things have led to a wide range of choices in energy efficient, physically small computation platforms [99, 100]. The candidate platform should have the computational capabilities to store and process high resolution images. Other storage and processing requirements, such as guidance navigation and control, and communication processing, place significantly lower demands on processing and storage. Even the image processing task has relatively low requirements, with allowable processing times on the order of minutes or perhaps even hours.

To solve this, the VoCore2 PC [101]is a \$50 computer that runs Linux on a 580 MHz MIPS 24K processor with 128 MB of RAM and 16 MB of flash is selected. The entire computer weighs 2.5 g, including connectors for camera and power, empty board space, and a microSD card slot. Adding a 512 GB card to store images and other data increases the system weight by roughly 0.25 grams. The processor burns roughly 1W peak, and has many power control modes and has a temperature operating range from 0°C to 85°C.

Similar computational capability in a carefully designed board with commercial off-the-shelf components could weigh roughly a gram, and operate from −40°C to 85°C. Custom designed silicon would drop the mass to well under a gram and increase the allowed temperature range while allowing radiation hardening by design.

## 3.6 Trajectories

This section addresses trajectory considerations but does not claim to be a comprehensive analysis of all solar sail trajectories, particularly those controlled by MEMS Inchworm Motors. It is meant to address a portion of the considerations and troubleshooting largely associated with Solar sail as well as provide a discussion around the specific uses for this style of femto-spacecraft.

### 3.6.1 Earth Orbit Maneuvers

The modified orbit rate steering law (MORSL) will be used to accomplish Earth escape, which is adapted from McInnes [1], see Fig. 3.4. In the original McInnes orbit rate steering law (OgMORSL), described as an orbit in the plane of the ecliptic, the spacecraft cone angle follows monotonically the mean anomaly in a prograde orbit about Earth. The orbit, idealized as circular at onset, begins at the 3 o'clock position in a 45° cone angle, where 12 o'clock is the direction of Earth orbit in the projected heliocentric coordinate system. At the 12 o'clock position, the spacecraft flips orientation, executing a rapid transition that is effectively instantaneous relative to the orbital period and thereafter continues its cone angle rotation again matching monotonically to mean anomaly. The crucial low-level control maneuver for a solar sail orbiting around Earth in the plane of the ecliptic is the rapid switch of orientation to maintain the required orientation of the reflective side of the sail facing the Sun, assuming the 3 o'clock position is directly in the Earth's shadow as the Sun will be at the 9 o'clock position. Ideally, upon reaching the apogee, an ideal solar sail must switch from a cone angle of +90° to −90° [1] as indicated in Fig. 3.4. Fig. 3.2 details the coordinate system used for the Earth Escape Trajectory with initial conditions listed in Tab. 3.2.

#### 3.6.1.1 Adjusted McInnes Orbit Rate Steering Control Law

Using the ODE45 solver in MATLAB/SIMULINK, the set up for the problem is offered in Eq. 3.11, transformed into the derivative form of the state space in Eq.

Table 3.2: Initial conditions used for the Earth escape trajectory.

| ICs | Value | Units |
|---|---|---|
| $\alpha$ | 0.8613 | rad |
| $\dot{\alpha}$ | 3.6459 $\times 10^{-}5$ | rad $s^{-1}$ |
| $r$ | 42164 | km |
| $\dot{r}$ | 0.0000 | km $s^{-1}$ |
| $\theta$ | 0.1519 | rad |
| $\dot{\theta}$ | 7.2919 $\times 10^{-}5$ | rad $s^{-1}$ |

3.12, and cast into the $s_i$ format that is required for the ODE45 solver in Eq. 3.13.

$$[s] = \begin{bmatrix} r \\ \dot{r} \\ \theta \\ \dot{\theta} \\ \alpha \\ \dot{\alpha} \end{bmatrix} = \begin{bmatrix} s_1 \\ s_2 \\ s_3 \\ s_4 \\ s_5 \\ s_6 \end{bmatrix} \xrightarrow{d/dt} [\dot{s}] = \begin{bmatrix} \dot{s_1} \\ \dot{s_2} \\ \dot{s_3} \\ \dot{s_4} \\ \dot{s_5} \\ \dot{s_6} \end{bmatrix} = \begin{bmatrix} \dot{r} \\ \ddot{r} \\ \dot{\theta} \\ \ddot{\theta} \\ \dot{\alpha} \\ \ddot{\alpha} \end{bmatrix} = \begin{bmatrix} s_2 \\ \dot{s_2} \\ s_4 \\ \dot{s_4} \\ s_6 \\ \dot{s_6} \end{bmatrix} \tag{3.11}$$

$$[\dot{s}] = \begin{bmatrix} \dot{r} \\ \ddot{r} \\ \dot{\theta} \\ \ddot{\theta} \\ \dot{\alpha} \\ \ddot{\alpha} \end{bmatrix} = \begin{bmatrix} \frac{f_0[\cos^3(\alpha)\cos(\theta)+\cos^2(\alpha)\sin(\alpha)\sin(\theta)]}{m} - \frac{\mu}{r^2+\theta^2} \\ \dot{\theta} \\ \frac{f_0[-\cos^3(\alpha)\sin(\theta)+\cos^2(\alpha)\sin(\alpha)\cos(\theta)]}{m}\frac{1}{r} - 2\dot{r}\dot{\theta}\frac{1}{r} \\ \ddot{a} \\ \frac{f_0\cos^2(\alpha)\cdot x}{I(x)} \\ \frac{f_0\cos^2(\alpha)\cdot x}{I(x)} \end{bmatrix} \tag{3.12}$$

$$[\dot{s}] = \begin{bmatrix} \frac{f_0[\cos^3(s_5)\cos(s_3)+\cos^2(s_5)\sin(s_5)\sin(s_3)]}{m} - \frac{\mu}{s_1^2+s_1 s_4^2} \\ s_4 \\ \frac{f_0[-\cos^3(s_5)\sin(s_3)+\cos^2(s_5)\sin(s_5)\cos(s_3)]}{m}\frac{1}{s_1} - 2s_2s_4\frac{1}{s_1} \\ s_6 \\ \frac{f_0\cos^2(s_5)\cdot x}{I(x)} \\ \frac{f_0\cos^2(s_5)\cdot x}{I(x)} \end{bmatrix} \tag{3.13}$$

where $r = s_1, \dot{s}_1 = \dot{r} = s_2; \theta = s_3, \dot{s}_3 = \dot{\theta} = s_4;$ and $\alpha = s_5, \dot{s}_5 = \dot{\alpha} = s_6$. For rotation rates above $1^o/s$, the on-board IMU will inform the control system's decisions.

The original McInnes Orbit Rate Steering Law [1] was used as a starting point for the trajectory algorithm here. The original trajectory description can be seen in Fig. 3.5 and Fig. 3.6 where the idealized in-plane 2D formulation began with a simple instantaneous "flip" of $180^o$ to track the solar sail with a monotonic function about the Earth formulated in Eq. 3.14.

The orbital rate control law from McInnes [1] is used with a modification to limit the maximum cone angle to $+/-70^o$ so that the spacecraft can always maintain control authority ( Fig. 3.5), above $||70^o||$ the SRP drops below 10% of the maximum. The crucial low-level control maneuver for a solar sail orbiting around Earth in the plane of the ecliptic is the rapid switch of orientation to maintain the required orientation of the reflective side of the sail facing the Sun, a maneuver that would be difficult for larger spacecraft due to high moments of inertia. Constraints on the angular acceleration of the spacecraft body and the drop-off in force on a solar sail with the sine of the cone angle, as well as motor speed, step size, and displacement range are incorporated Fig. 3.7. With these constraints in mind, the flip is no longer considered instantaneous and therefore must be re-evaluated for viability within the confines of the orbital energy constraints, too low and the spacecraft will have a premature landing and is also therefore renamed as a “Transition Slope” (Eq. 3.15).

$$\alpha(\theta) = \begin{cases} Orig1: \dfrac{\pi}{4} + \dfrac{\theta}{2}, & 0 \leq \theta < \dfrac{\pi}{2}, \\ Flip: -\dfrac{\pi}{2}, & \theta = \dfrac{\pi}{2}, \\ Orig2: \dfrac{\pi}{4} + \dfrac{\theta}{2} - \pi, & \dfrac{\pi}{2} < \theta < 2\pi. \end{cases} \tag{3.14}$$

$$\alpha(\theta) = \begin{cases} Orig1: \dfrac{\pi}{4} + \dfrac{\theta}{2}, & \theta < 2\ \alpha_{\text{sat}} - \frac{\pi}{4}\ , \\ Slope1: \alpha_{\text{sat}}, & 2\ \alpha_{\text{sat}} - \frac{\pi}{4}\ \leq \theta < \frac{\pi}{2} - \theta_{\text{offset}}, \\ Flip: -\dfrac{\alpha_{\text{max}} - \alpha_{\text{min}}}{\theta_{\text{max}} - \theta_{\text{min}}}\ \theta - \theta_{\text{min}}\ + \alpha_{\text{max}}, & \frac{\pi}{2} - \theta_{\text{offset}} \leq \theta \leq \frac{\pi}{2} + \theta_{\text{offset}}, \\ Slope2: -\alpha_{\text{sat}}, & \frac{\pi}{2} + \theta_{\text{offset}} \leq \theta < \pi - 2\ \alpha_{\text{sat}} - \frac{\pi}{4}\ , \\ Orig2: \dfrac{\pi}{4} + \dfrac{\theta}{2} - \pi, & \pi - 2\ \alpha_{\text{sat}} - \frac{\pi}{4}\ \leq \theta < 2\pi. \end{cases} \tag{3.15}$$

Based on preliminary tuning of the PD system and its effect on the stability of the trajectory mapping we will take the upper limit of $\tau_{spin} = 60s$, where $\tau_{spin}$ is the time that the spacecraft spends during the $180^o$ flip maneuver. The PD response is tuned to maintain that the "real" time spent during the flip maneuver is below the desired

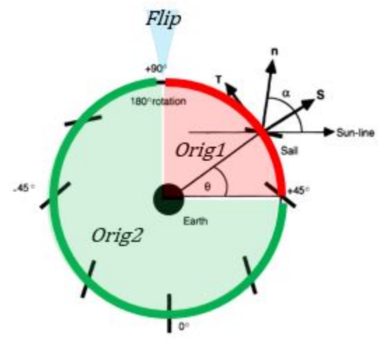


Figure 3.5: Diagram of the conceptual orbit geometry / original McInnes flip maneuver. The diagram shows the approximate angle, not to scale, that the three phases occur in. The three distinct segments are indicated as the first part of the original trajectory (Orig1), the $180^o$ instantaneous "flip" maneuver (Flip), and the second part of the original trajectory (Orig2).

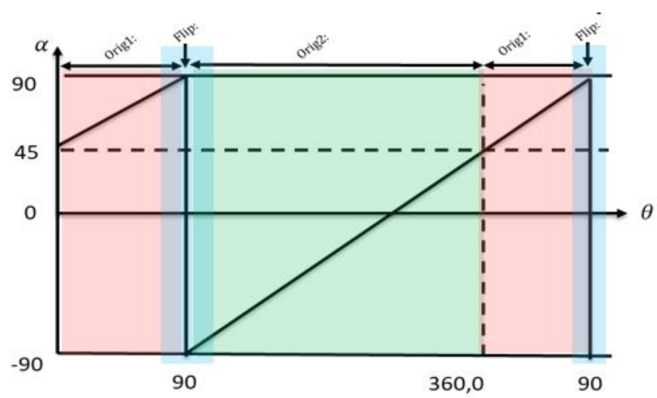


Figure 3.6: Diagram of the cone-angle schedule for the original McInnes orbit-rate steering law. Shows trajectory with three distinct segments indicated as the first part of the original trajectory (Orig1), the $180^o$ instantaneous "flip" maneuver (Flip), and the second part of the original trajectory (Orig2).

upper limit (i.e., $\tau_{spin} > \tau_{spin,real}$). Through this tuning the effect on the overall sail trajectory and orbital energy losses are small enough to consider the trajectory viable with the given solar sail configuration, control stiffness, and damping.

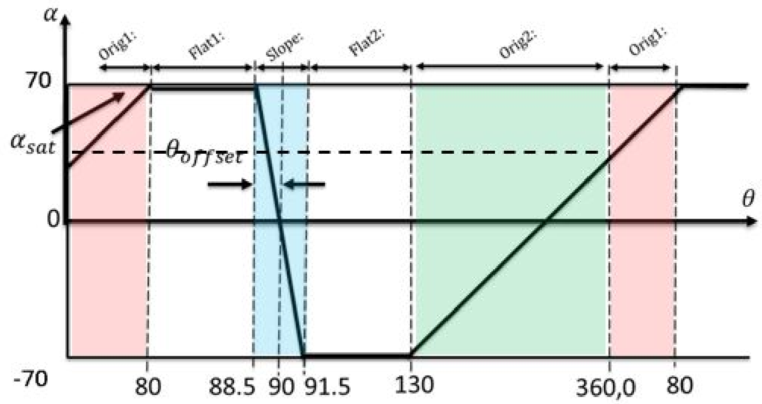


Figure 3.7: Diagram of the adjusted/saturated cone-angle schedule with finite transition slope. Shows trajectory with four distinct segments indicated as the first part of the original trajectory (Orig1); maintaining constant attitude with $\alpha = 70^o$ (Flat1); finite transition slope to the $180^o$ orientation (Slope); maintaining constant attitude with $\alpha = -70^o$ (Flat2); and the second part of the original trajectory (Orig2).

#### 3.6.1.2 Parameterization

This section presents a parametric analysis of the low-level control strategy used by the BLISS femto-scale solar sail spacecraft to achieve Earth-escape trajectories. The spacecraft is assumed to use MEMS inchworm motors to manipulate carbon-fiber tethers connecting the sail to the spacecraft main body. Changes in tether length modify the relative position of the sail and body, thereby changing the spacecraft pitch and yaw angles and allowing the sail cone angle to follow a prescribed steering law. Because the effectiveness of this strategy depends on both solar-sail performance and initial Earth-orbit geometry, the analysis sweeps three primary parameters: the lightness number, $\beta$; the initial angular position about Earth, $\theta_0$; and the initial orbital radius or altitude parameter, $h_{\text{init}}$.

Two trajectory models are compared throughout this parameter study. The first is the nominal McInnes-style orbit-rate steering law, in which the sail orientation follows an idealized prescribed trajectory and the transition maneuver is treated as effectively instantaneous. The second is the augmented, or ‘‘Ideal,’’ trajectory model used in this work, which includes the non-instantaneous 180° transition maneuver, PD-controlled cone-angle response, MEMS motor speed and step-size limits, and non-harmonic carbon-fiber tether flexing and bowing. All other swept parameters are held the same between the two models so that the plotted differences isolate the effect of adding these low-level actuation and structural constraints.

The resulting parameter space is summarized in Figs. 3.8--3.11. Figures 3.8 and 3.10 show fine-grained sweeps of the scalar performance metrics, while Figs. 3.9 and 3.11 show representative trajectory histories selected from those sweeps. In the fine-grained plots, the black curve reports the ratio of the augmented trajectory escape time to the McInnes trajectory escape time. Values below unity indicate that the augmented trajectory is faster than the McInnes case, while values above unity indicate a longer escape time. The red curves report the absolute escape time in years on the right-hand axis, with the solid red curve corresponding to the augmented trajectory and the dashed red curve corresponding to the McInnes trajectory.

Figure 3.8 shows the effect of initial angular position, $\theta_0$, for four fixed values of lightness number at $h_{\text{init}} = 4.5 \times 10^4$ km. Each subplot sweeps $\theta_0$ from 0° to 359° in 1° increments. The figure shows that the relative benefit or penalty of the augmented steering law is not uniform over initial angular position. Instead, the escape-time ratio exhibits localized peaks and dips that depend on the initial phasing of the sail trajectory relative to the Sun--Earth geometry. These variations are expected because the finite transition maneuver can either align favorably or unfavorably with the orbital energy-gain portion of the trajectory.

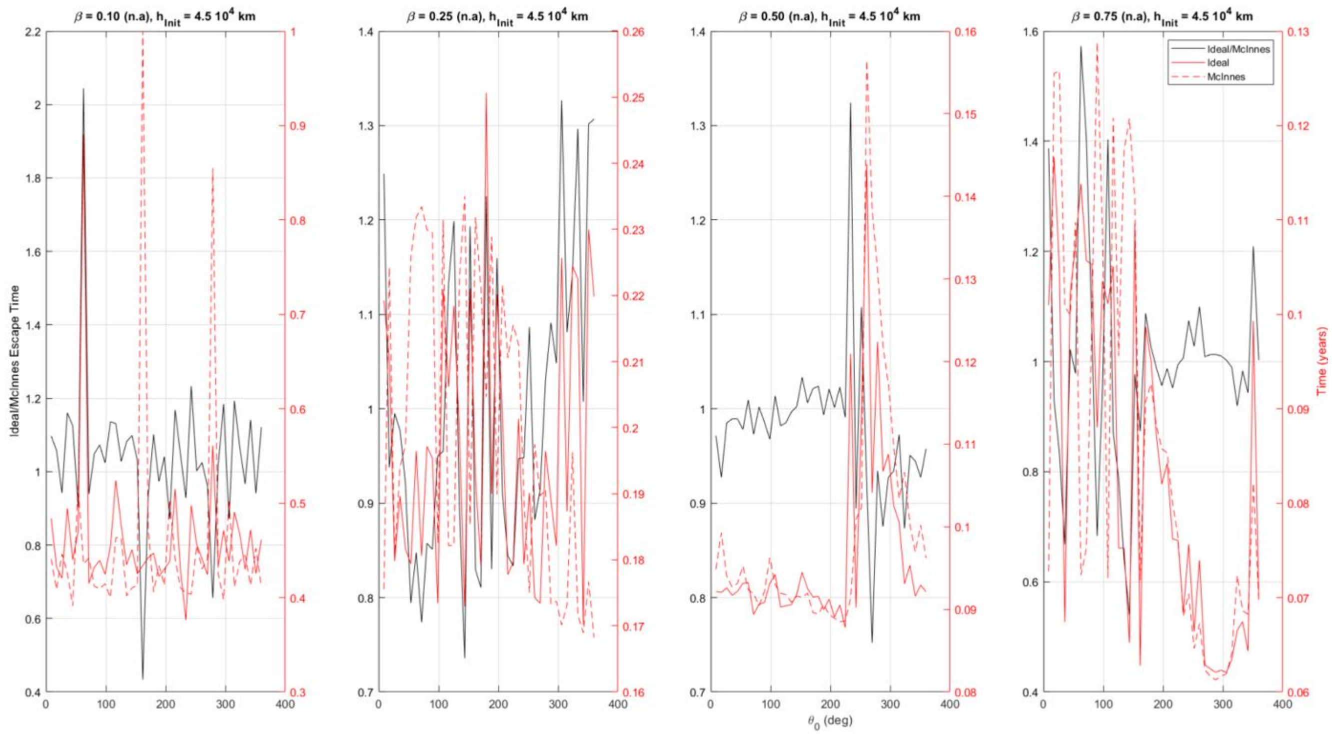


Figure 3.8: Fine-grained sweep of Earth-escape performance as a function of initial angular position, $\theta_0$, for four fixed lightness numbers, $\beta$, at $h_{\text{init}} = 4.5 \times 10^4$ km. The horizontal axis in each subplot is the initial angular position about Earth. The black curve uses the left axis and gives the ratio of the augmented trajectory escape time to the McInnes trajectory escape time. The red curves use the right axis and show absolute escape time in years, with the solid red curve corresponding to the augmented trajectory and the dashed red curve corresponding to the McInnes trajectory. Values of the black curve below unity indicate cases where the augmented trajectory escapes faster than the McInnes reference, while values above unity indicate a longer escape time.

Figure 3.9 shows representative trajectory histories corresponding to selected points from the angular-position sweep. Each column corresponds to a different lightness number, $\beta$, and each row corresponds to a selected initial angular position, $\theta_0$, with $h_{\text{init}}$ fixed at $4.5 \times 10^4$ km. The red curves show the augmented trajectory and the gray curves show the McInnes trajectory. The plotted paths show the spacecraft spiraling outward from the initial Earth orbit and then escaping along a solar-sail-driven trajectory. Increasing $\beta$ generally produces stronger solar-radiation-pressure acceleration, reducing the number of spiral-out loops required before escape. The comparison also shows that the augmented trajectory can diverge noticeably from the McInnes trajectory for some initial angular positions, especially where the finite transition maneuver occurs at a dynamically important point in the orbit.

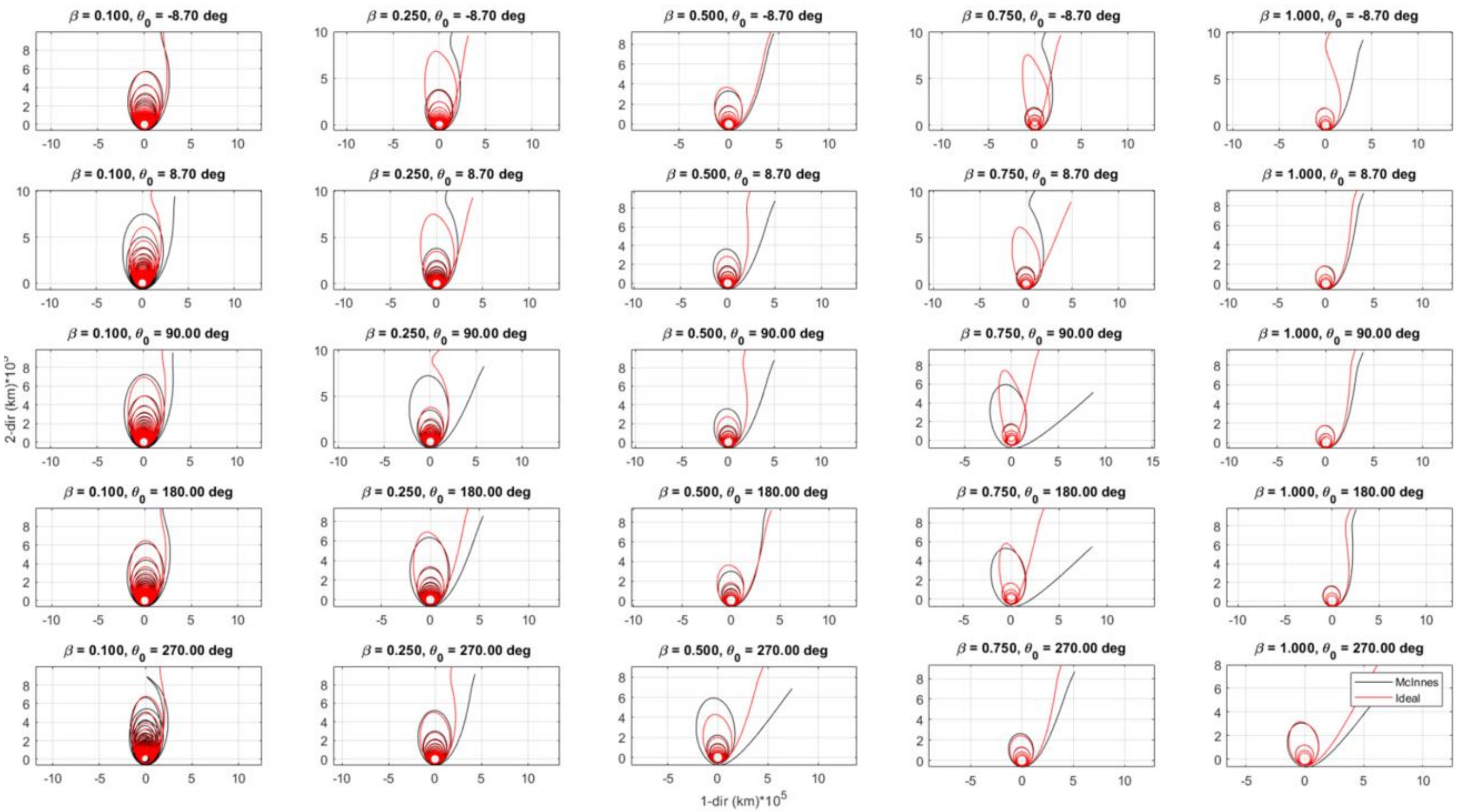


Figure 3.9: Representative Earth-escape trajectories selected from the angular-position sweep in Fig. 3.8. Each column corresponds to a different lightness number, $\beta$, and each row corresponds to a selected initial angular position, $\theta_0$, with $h_{\text{init}} = 4.5 \times 10^4$ km. Red curves show the augmented trajectory including finite transition and MEMS actuation effects, while gray curves show the McInnes reference trajectory. The plots illustrate how increasing $\beta$ reduces the number of spiral-out loops required for escape and how the augmented trajectory can deviate from the idealized reference depending on initial orbital phasing.

Figure 3.10 shows the effect of lightness number for three fixed initial orbital radii or altitude parameters. In these plots, $\beta$ is swept from 0.1 to 1 using a logarithmic horizontal axis while $\theta_0$ is held fixed. As expected, increasing $\beta$ decreases the absolute time to Earth escape because the sail experiences greater acceleration from solar radiation pressure. However, the black escape-time ratio also shows that the augmented model does not scale as a simple constant offset from the McInnes model. Instead, the finite steering transition, tether response, and motor-limited actuation introduce localized deviations in performance, producing regions where the augmented trajectory is comparable to, better than, or worse than the idealized McInnes case.

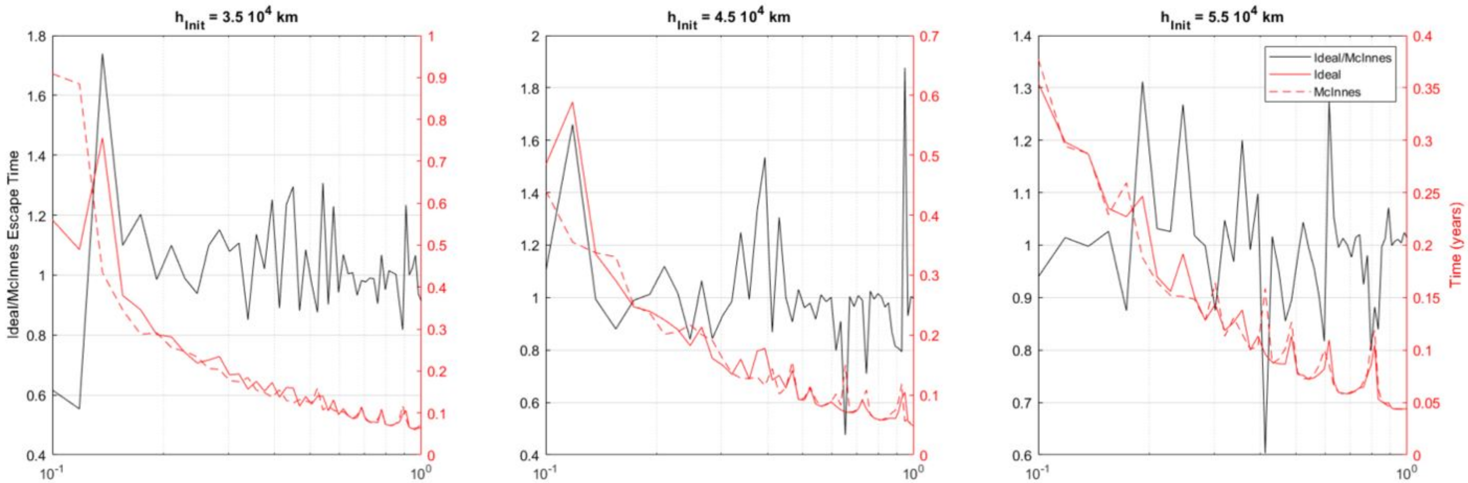


Figure 3.10: Fine-grained sweep of Earth-escape performance as a function of lightness number, $\beta$, for three fixed values of $h_{\text{init}}$. The horizontal axis is $\beta$ on a logarithmic scale. The black curve uses the left axis and gives the ratio of the augmented trajectory escape time to the McInnes trajectory escape time. The red curves use the right axis and show absolute escape time in years, with the solid red curve corresponding to the augmented trajectory and the dashed red curve corresponding to the McInnes trajectory. Increasing $\beta$ generally decreases escape time, while deviations in the black ratio curve show where actuator-limited steering and finite transition dynamics change the relative performance of the augmented trajectory.

Figure 3.11 shows representative trajectory histories corresponding to selected points from the radius--lightness sweep. Each column corresponds to a different value of $\beta$, while each row corresponds to a different value of $h_{\text{init}}$. The red curves again indicate the augmented trajectory, and the gray curves indicate the McInnes trajectory. The figure illustrates the coupled influence of initial orbital size and sail acceleration on the Earth-escape path. Lower-$\beta$ cases require longer spiral-out arcs before escape, while higher-$\beta$ cases escape more directly. Larger initial orbits generally reduce the required orbit-raising burden, although the detailed path remains sensitive to the interaction between cone-angle timing, transition maneuver duration, and orbital phasing.

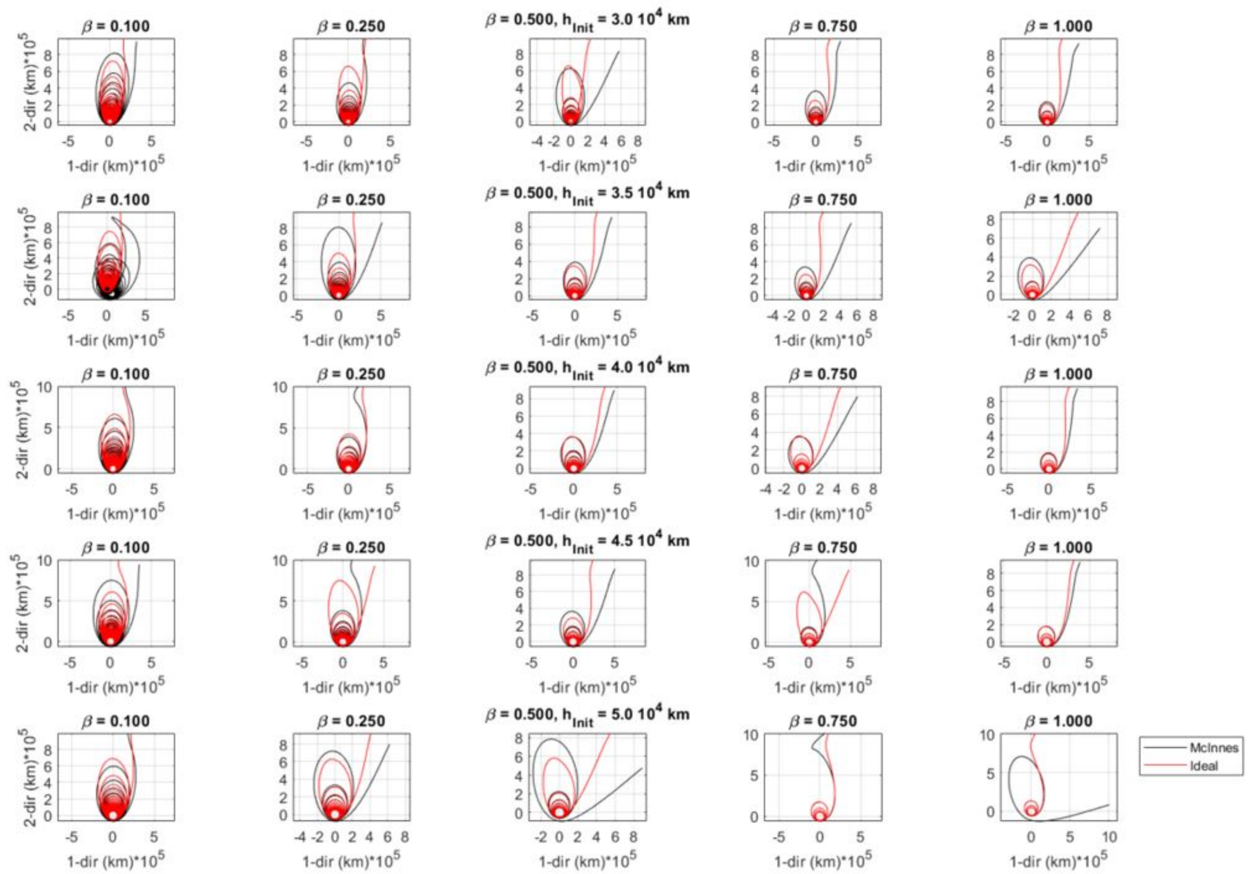


Figure 3.11: Representative Earth-escape trajectories selected from the radius--lightness sweep in Fig. 3.10. Each column corresponds to a different lightness number, $\beta$, and each row corresponds to a different value of $h_{\text{init}}$. Red curves show the augmented trajectory including finite transition and MEMS actuation effects, while gray curves show the McInnes reference trajectory. The figure shows the combined effect of sail acceleration and initial orbital radius on the spiral-out path: lower-$\beta$ cases require longer orbit-raising arcs, while higher-$\beta$ cases escape more directly.

Taken together, these parameter sweeps show that the BLISS Earth-escape trajectory is sensitive not only to sail performance, represented by $\beta$, but also to the initial orbital geometry and the practical limits of the MEMS tether-actuation system. The expected global trend is recovered: increasing $\beta$ generally reduces escape time. However, the local variations in escape-time ratio indicate that low-level actuation dynamics can affect trajectory performance in ways that are not captured by an instantaneous ideal steering law. This result motivates retaining actuator-limited steering behavior in future BLISS trajectory studies rather than treating the sail attitude as an immediately commanded state.

#### 3.6.1.3 Results

Given the angular-acceleration constraints of the spacecraft body outlined in Sec. 3.3.2, and the reduction in usable solar-radiation-pressure (SRP) force as the cone angle approaches $\pm 90°$, the cone angle is limited to maintain practical trajectory-control authority. As the cone angle approaches $\pm 70°$, the effective SRP force approaches approximately 10 % of its nominal value, which is used here as the saturation limit for commanded steering. The transition from $+70°$ to $-70°$ near the upper portion of the Earth orbit is therefore a critical maneuver: it allows the sail to preserve the desired sign of tangential work while avoiding both loss of control authority and excessive orbital-energy loss.

The selected Earth-escape case is summarized in Figs. 3.12--3.16. Figure 3.12 shows the projected spiral-out trajectory over the full Earth-escape phase. Figure 3.13 shows the corresponding time histories of the main orbital state variables. Figures 3.14 and 3.15 show the low-level actuator command and resulting sail cone-angle command over the full trajectory. Finally, Fig. 3.16 shows a one-day window that resolves the finite transition maneuver and the corresponding motor displacement.

The downstream effect of inserting these practical non-idealities is an initially slower and more eccentric spiral-out trajectory than the idealized McInnes orbit-rate steering law. The augmented maneuver does not instantaneously reverse the sail orientation; instead, it requires finite motor motion, finite angular acceleration, and a controlled transition between the positive and negative cone-angle saturation limits. This causes the spacecraft using the modified orbit-rate steering law (MORSL) to trail the original McInnes orbit-rate steering law (OgMORSL) by approximately 47 days during the Earth-escape portion of the trajectory. Although this represents a measurable loss in Earth-orbit-raising performance, it remains a relatively small penalty in the context of the complete interplanetary mission and is overcome once the spacecraft leaves the dominant influence of Earth's gravity.

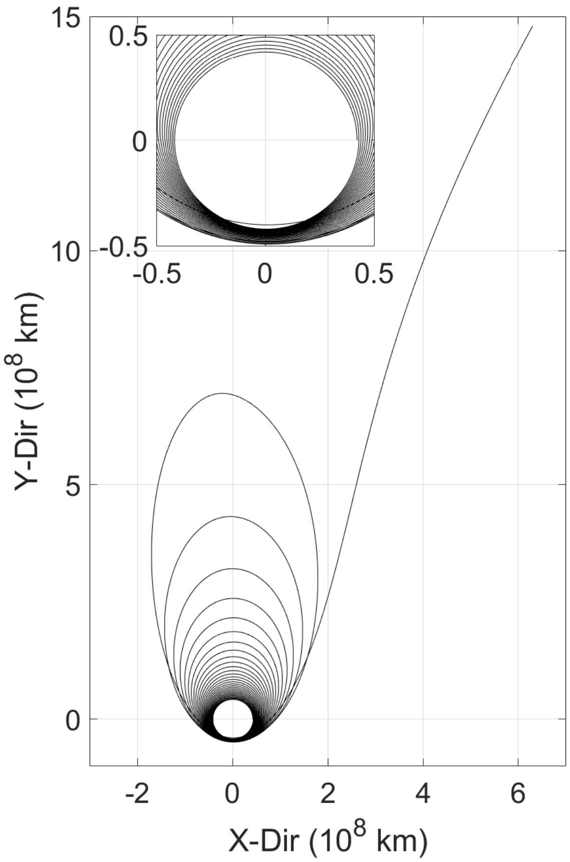


Figure 3.12: Projected Earth-escape spiral-out trajectory for the selected 125-day BLISS case. The main plot shows the spacecraft trajectory in the $x$--$y$ plane over the full escape maneuver, with axes scaled by $10^8$ km. The inset magnifies the early Earth-bound portion of the trajectory, where the repeated loops show the gradual orbit-raising process before final escape. The increasing separation between successive loops reflects the accumulation of orbital energy from solar-radiation pressure under the modified steering law.

## 3.7 Technology Trends

The capabilities showcased here highlight the potential for swarms of low-cost spacecraft in the tens-of-grams mass range to perform observation, reconnaissance, and possibly sample-return missions using primarily commercial-off-the-shelf (COTS) components. In the Earth-escape trajectory presented above, the time to escape from

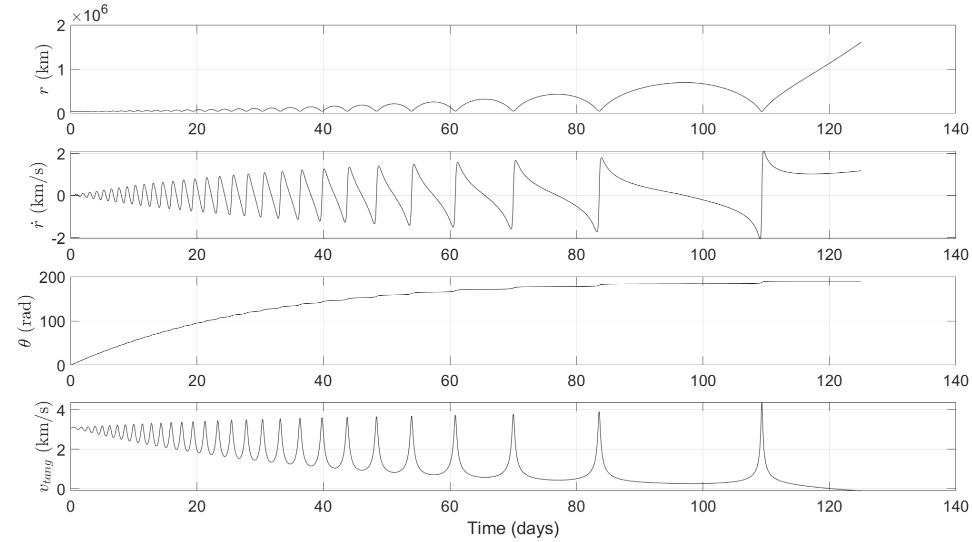


Figure 3.13: Orbital state histories for the selected 125-day Earth-escape trajectory. From top to bottom, the plots show radial distance from Earth, $r$; radial velocity, $\dot{r}$; accumulated angular position, $\theta$; and transverse velocity, $v_{\text{tang}}$, as functions of time. The radial distance increases gradually during the early spiral-out phase and then grows rapidly as the spacecraft transitions to escape. The oscillations in $\dot{r}$ and $v_{\text{tang}}$ correspond to repeated Earth-orbit passes during which solar-radiation pressure alternately adds or redistributes orbital energy depending on the sail orientation and orbital phase.

near-Earth orbit is approximately 120--125 days. After escape, the spacecraft can use the same solar-sail steering concept to perform interplanetary transfer maneuvers. A representative Bennu transfer is summarized in Figs. 3.17--3.19, which show the required cone-angle history, the corresponding trajectory state variables, and the Sun--Earth-frame rendezvous geometry.

For the representative Bennu case, the spacecraft reaches approximately 2 AU in less than one year and completes the outbound interplanetary travel to intercept Bennu near 1.3 AU in approximately 640 days. After a notional 346-day observation period, comparable to the orbital observation period of OSIRIS-REx around Bennu, the return to Earth orbit takes a similar amount of time. This gives a total round-trip mission duration of approximately 5.1 years, or 1,866 days. Although OSIRIS-REx included substantial additional time for proximity operations, site selection, sample acquisition, and return-capsule operations, it remains a useful benchmark because it represents the current state of practice for a near-Earth-asteroid sample-return

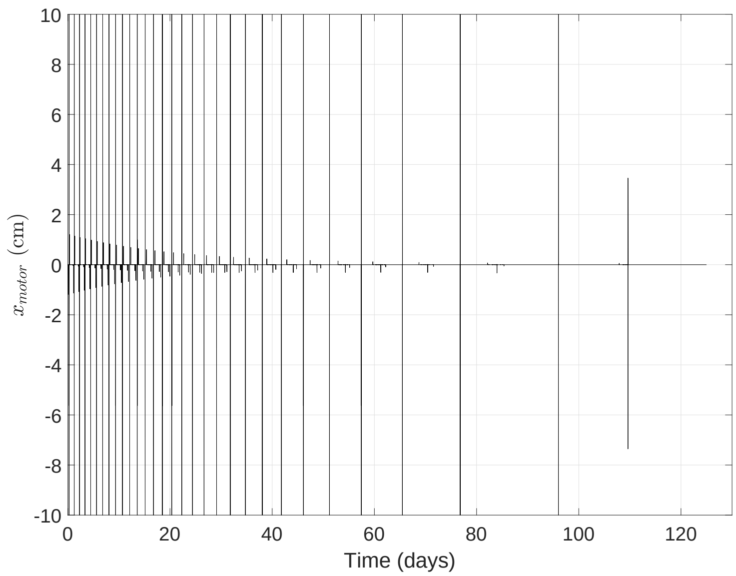


Figure 3.14: MEMS motor displacement command over the 125-day Earth-escape trajectory. The commanded motor position, $x$, represents the tether-control displacement required to generate the prescribed sail cone-angle history. Large changes in motor position occur during the finite transition maneuvers between the positive and negative cone-angle saturation limits, while smaller changes correspond to gradual steering during the orbit-raising portions of the trajectory.

mission.

Figure 3.17 shows the cone-angle command required for the interplanetary sail transfer. The cone angle remains within physically realizable bounds while changing sign and magnitude as needed to shape the heliocentric trajectory. Figure 3.18 shows the corresponding state evolution, including heliocentric radius, radial velocity, tangential velocity, and angular position. Figure 3.19 shows the resulting trajectory geometry in the Sun--Earth reference frame. Taken together, these figures show that the same low-mass sailcraft architecture used for Earth escape can also support interplanetary transfers when the sail attitude is controlled over mission-relevant timescales.

For a spacecraft that returns to Earth orbit to communicate, the ultimate lower limit on spacecraft size may be approximately an order of magnitude smaller than the BLISS architecture proposed here. Major subsystems such as the camera, computation and storage, communication, and power system can plausibly be engineered toward masses on the order of 0.1 g each. For a total spacecraft mass near 1 g, a sail area

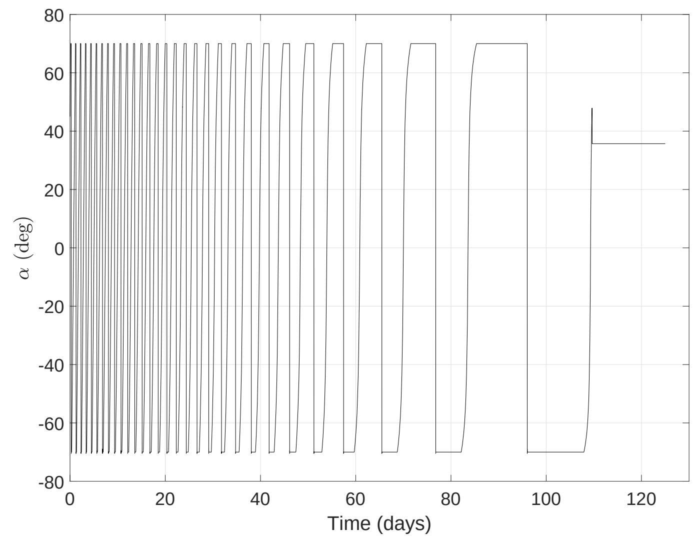


Figure 3.15: Sail cone-angle command, $\alpha$, over the full 125-day Earth-escape trajectory. The cone angle is bounded at approximately $\pm 70^o$ to preserve usable SRP control authority and avoid the near-zero effective force condition that occurs as the sail approaches $\pm 90^o$. The repeated transitions between positive and negative cone angle correspond to the steering-law reversals needed to maintain favorable tangential work over successive Earth orbits.

of approximately $0.1\,\mathrm{m}^2$, with sail mass near $0.1\,\mathrm{g}$, would provide an area-to-mass ratio suitable for rapid solar-sail maneuvering. This points toward a future class of highly agile, low-cost spacecraft that could be customized for specific imaging, sensing, reconnaissance, or sample-capture objectives.

Direct spectrography and microanalysis have long been central tools for understanding material composition. To that end, this work also proposes that BLISS-class spacecraft could eventually retrieve cometary samples for analysis on Earth. Inner-solar-system comets such as 107P/Wilson--Harrington are promising targets for such missions, and the transfer geometry would be similar in structure to the near-Earth-asteroid rendezvous case described above. The principal difference is that the science value of even microscopic returned material is high, meaning that gram-scale sailcraft may be able to provide useful sample-return capability without requiring the large returned masses associated with conventional spacecraft missions.

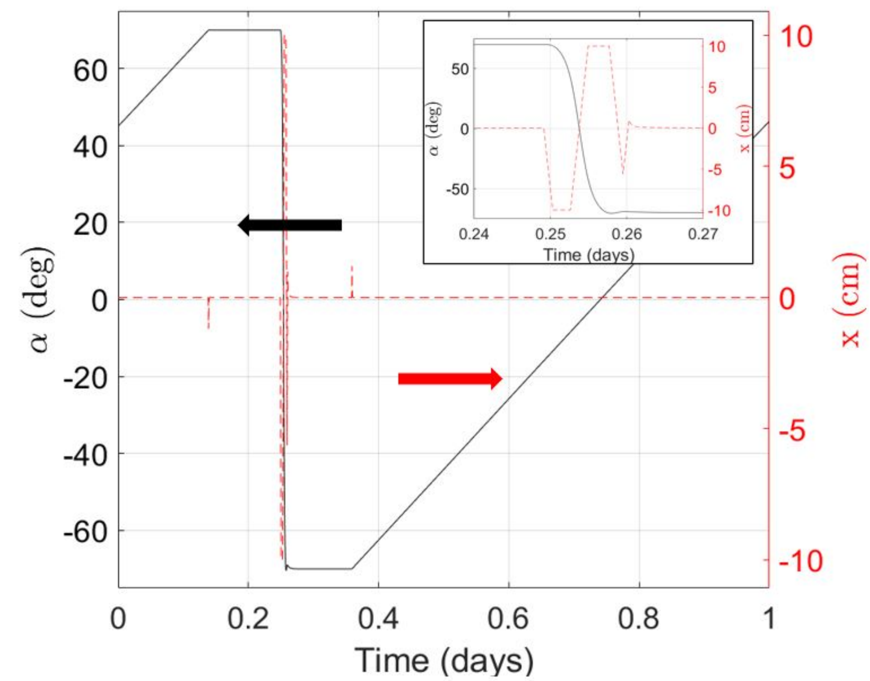


Figure 3.16: One-day time history of the sail cone angle and MEMS motor displacement during the Earth-escape trajectory. The black curve uses the left axis and shows the commanded cone angle, $\alpha$, in degrees. The red dashed curve uses the right axis and shows the motor displacement, $x$, in centimeters. The inset magnifies the finite transition maneuver near the cone-angle reversal, showing that the commanded sail angle changes from the positive saturation limit to the negative saturation limit over a finite time rather than instantaneously. The red motor-position response during this interval represents the tether displacement required to drive the sail through the transition.

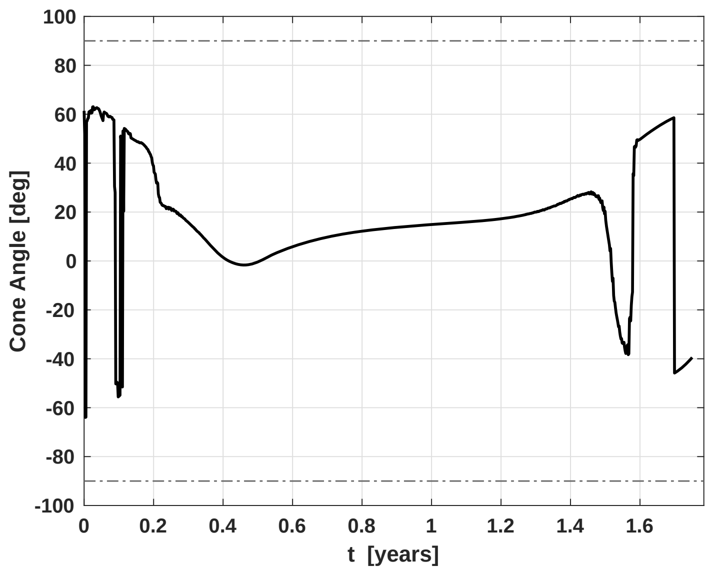


Figure 3.17: Cone-angle command for the BLISS interplanetary transfer to Bennu, reproduced with permission from [2]. The plot shows the commanded sail cone angle, $\alpha$, as a function of mission time in years. Changes in $\alpha$ modify the direction of the solar-radiation-pressure acceleration relative to the Sun--spacecraft line, allowing the spacecraft to shape its heliocentric orbit during the outbound transfer. The bounded cone-angle profile reflects the practical requirement that the sail maintain usable thrust and control authority throughout the maneuver.

## 3.8 Conclusion

This work presents a vision for the Berkeley Low-cost Interplanetary Solar Sail spacecraft using micro-scale actuators and small solar sails to explore NEOs. The initial actuation, control, communication, and computation tools required to realize the BLISS project rely on privatization of spaceflight and the consumerization of micro-technologies. The tools presented in this work represent the initially available mechanisms, and with specific research the parameters for the spacecraft can be improved substantially, which would move the progress of the project towards first launch and allow exploration of more ambitious profiles for future missions. In providing a large base of results demonstrating the feasibility of such technologies, we hope that this opens further investigation into novel spacecraft and mission profiles.

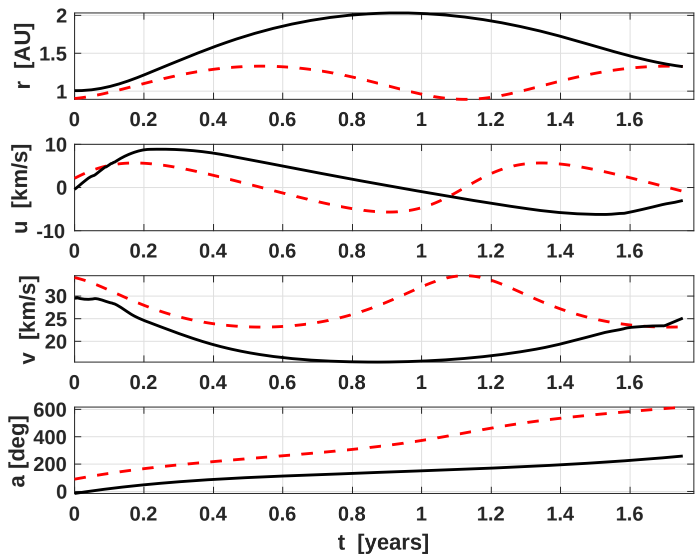


Figure 3.18: State history for the BLISS interplanetary transfer to Bennu, reproduced with permission from [2]. From top to bottom, the plots show heliocentric radius, $r$; radial velocity, $u$; tangential velocity, $v$; and angular position, $a$, as functions of mission time. The solid and dashed curves compare the BLISS trajectory state with the target/reference trajectory state used for the Bennu rendezvous analysis. The evolution of $r$, $u$, and $v$ shows how solar-sail steering changes both the orbital energy and angular phasing of the spacecraft so that it can approach the target orbit.

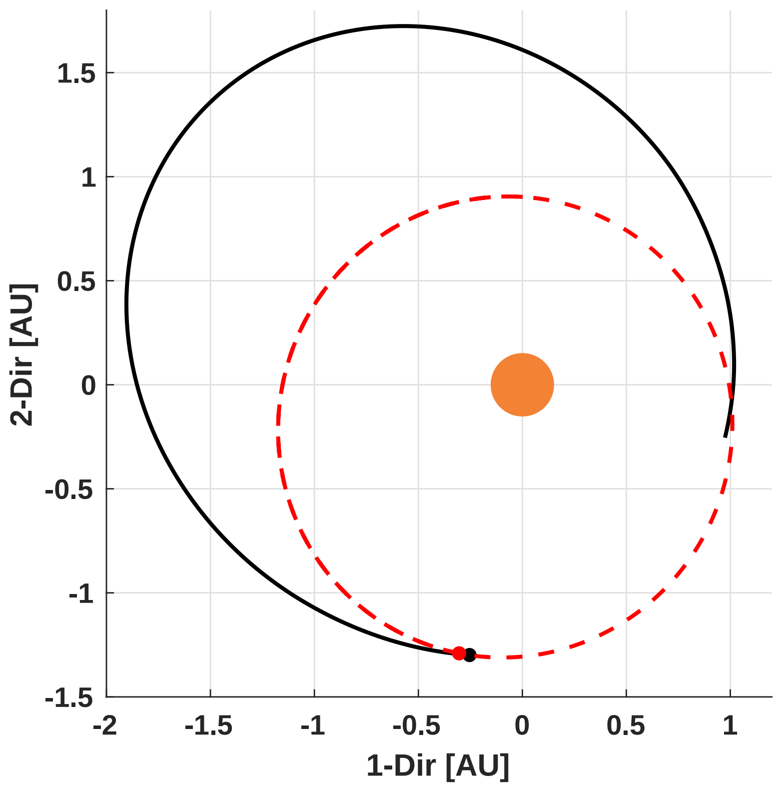


Figure 3.19: Sun--Earth-frame trajectory geometry for the BLISS transfer to Bennu, reproduced with permission from [2]. The plot shows the heliocentric path of the sailcraft relative to the target/reference trajectory in astronomical-unit coordinates. This view illustrates the large-scale orbital phasing problem that the sail must solve: the spacecraft must use continuous low-thrust SRP acceleration to change its heliocentric radius, angular position, and velocity state until it reaches the desired Bennu-intercept geometry.

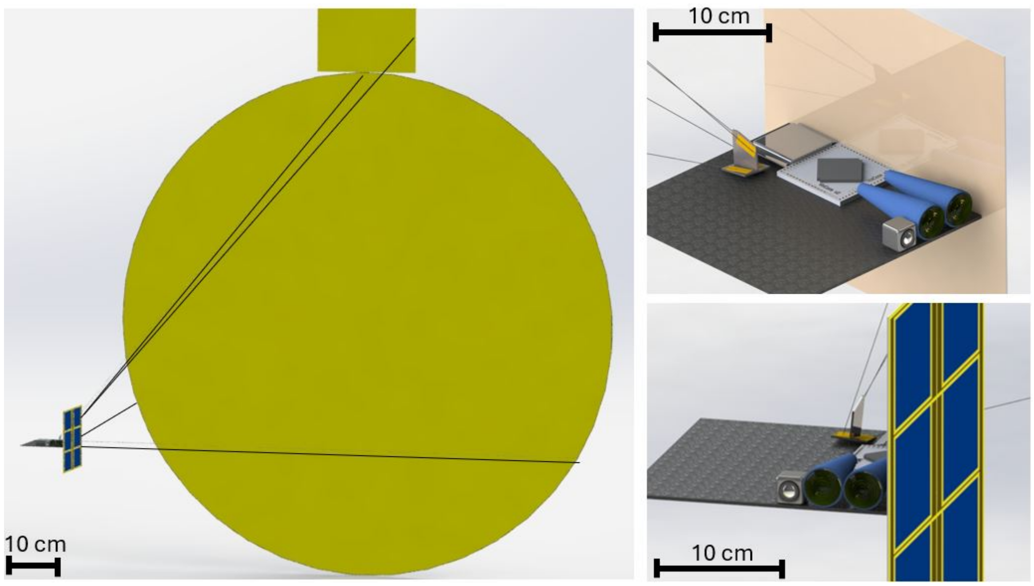


Figure 3.20: Rendering of the BLISS spacecraft showing (Left) isometric view of the solar sail craft; (Right-top) spacecraft body as viewed from top-left; (Right-bottom) spacecraft body as viewed from rear-right.

# Chapter 4

# The Motor: Transmission Gap Closing Actuators

## 4.1 Abstract

The $\mu\Delta$ Motors are a type of MEMS motor that are powered by Transmission-capable Gap Closing Actuators (TGCAs), designed to shift between predefined gear shift inputs, or positions within the reconfigurable morphology. The $\mu\Delta$ motors, a sub-class of TGCAs presented here, are designed to produce varied force, velocity, and distance outputs that are selectable and controllable.

The primary design features responsible for the motion of these motors are the clutch, multi-modal pawls, spine, and GCA fingers. The clutch is designed to reach a range of gear positions. The multi-modal pawls are designed to make gearing and reverse capabilities possible. The spine is designed to transfer the force without deformation from the fingers to the pawls. The GCA fingers are designed to produce force through capacitive electrical input.

There are four dual-sided multi-modal pawl designs: slide-slot, rotary-slot, frictional-rotation, and compliant mechanism.

The TGCA arrays demonstrate these capabilities at a small cost to footprint and input power that is still less than that needed for previous standard solutions. Previous standard solutions considered include but are not limited to doubling the motor array, reversing it, and adding it in series with the original to offer the reverse option. The $\mu\Delta$ Motors offer a significant increase in variety of optional outputs for a single design.

This work presents the first bidirectional transmission motor using a MEMS gap-closing actuator with a simple compliant beam bending mechanism. A continuous

range of forward and reverse motions have been achieved by bending the pawl of the mechanism with a force exerted perpendicular to a spine structure via the compliant cantilever input gear shift, $\Delta$. A study of the static loading and beam bending in the critical stages of motor actuation is conducted to confirm the motor performance criteria. Experimental results show an ability to impart output shuttle motion in the range of $[1.5, 9.5]\mu m$/step and $[-2.9, -5.9]\mu m$/step for a $\lambda = 25^o$ configuration and $[4.2, 12.2]\mu m$ and $[-1.5, -6.6]\mu m$/step for a $\lambda = 47.5^o$ configuration, with an input force of $0.9375mN$ for a $4.7\mu$ m/step motor input and are corroborated by ANSYS simulation.

The $\mu\Delta$'s increase the capability to engage multimodal actuation utilizing simple changes to the design of Gap Closing Actuators directly changing the single-mode motor to a true geared transmission motor with the same optimal outputs and a whole range of high force, high speed, and increased range of actuation.

## 4.2 Introduction

In spaceflight, every gram matters. Reducing size and mass are design and manufacturing goals that have produced entire fields of study on their own and indeed entire industrial benefits necessitating expertise and innovation where any improvement might lead to the cutting edge. The same is true in femtoscale spacecraft design, and to some extent might be considered more considerably weighted (pun intended). Similarly, in MEMS actuation, significant technological advantage is placed on the ability to produce high force density, low power, inexpensive units that often serve a specific single purpose in a small package. Through this MEMS is both highly efficient at reaching production in applications for particular use and achieving such at scale. In this way, MEMS has often secured a position as the firmware of actuators, in that it serves exactly the use case it is designed for with embedded speed and force as outputs for its current and voltage inputs often with little relative spread in its designated and calibrated use range. Giving a MEMS controlled spacecraft a way to steer in both directions while reducing the mass and size of the device itself would be highly sought after in any other methodology and the same is true here.

### 4.2.1 Background

The field of electrostatic MEMS actuators is a relatively young one with a deep roster of advancements in the 20th century and broad range of applications. Microelectromechanical systems (MEMS) have revolutionized numerous technological fields through their ability to integrate mechanical elements [102], sensors [103],

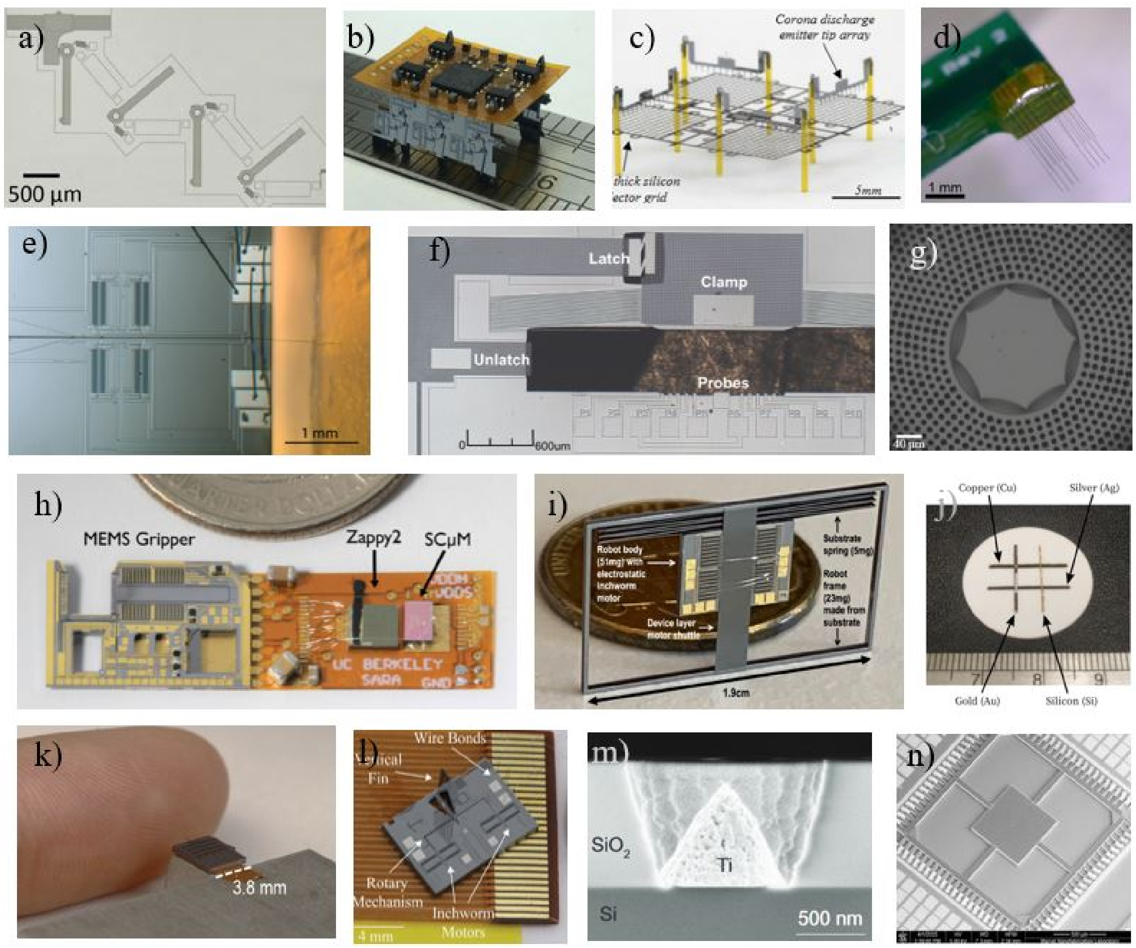


Figure 4.1: Representative works from the Pister Group. a) Joseph Greenspun's energy storage and self-destructing MEMS multi-stage hammer [3]; b) Daniel Contreras' hexapod walking microrobot [4]; c) Daniel Drew's flying microrobot with no moving parts, the Ionocraft [5]; d) Oliver Chen's microelectrode array's [6]; e) Rachel Zoll's carbon fiber pushers; f) Hani Gomez's zero insertion force latches [7]; g) Mauricio Bustamante's rotary inchworm for underwater propulsion [8]; h) Alex Moreno's integration of wireless systems with IoT sensors and microrobots [9]; i) Craig Schindler's jumping microrobot [10]; j) Daniel Teal's multimaterial printing via charged nanoparticle deposition [11]; k) Dillon Acker-James' micro-taction device [12]; l) Brian Kilberg's MEMS aerofoil [13]; m) Nishika Deka's portable field emission device [14]; and n) Yichen Liu's PV-powered MEMS differential capacitive sensor integration on CMOS [15].

actuators [104], and electronics [105] on a microscale, even branching to the nanoscale in many respects [106, 107]. As seen in Fig. 4.1, even within the Pister group, MEMS has been used in a variety of ways.

#### 4.2.1.1 Penskiy Motors

Electrostatic GCAs have a relatively large force but small displacement compared with comb-drive actuators. Electrostatic inchworm motors (EIMs) overcome the small displacement by taking multiple, usually consecutive, small steps. The force from the GCA is applied to a pawl which makes repeated contact with a shuttle, moving the shuttle a small amount each time the GCA closes.

The first EIMs used two GCAs: one to engage the pawl shoe with the shuttle, and one to drive the pawl forward [108]. Hollar et al. improved on this design by making the drive GCA bi-directional, allowing the EIM to move the shuttle either forward or backward using the same drive GCA [109]. Penskiy et al. improved on the original EIM by using an angled arm, or pawl, to support the shoe [110]. This removed the need for the pawl-engagement GCA, as the angled main drive GCA served to both engage the pawl and move the shuttle forward. This was an improvement in simplicity and reduced the number of control signals needed for the motor.

The main morphology of motor used for microrobots that the Pister Group works with are the original Penskiy inchworm motors. They include a GCA array, some alignment cantilever springs, closure stops, return stops, pawls, shuttle, shuttle return springs, alignment buffers, electrical paths, electrical pads, as well as sometimes a motion encoder, end-stop detector, and output end effector(s). These have the benefit of transferring a capacitive potential energy to a transverse kinetic energy. The angle of which was optimized by Penskiy as $67^o$ from the horizontal [110]. See Fig. 4.2 for the Penskiy-derived GCA structure.

### 4.2.2 Problem Statement

In general, many silicon-based monolithic motors and actuators exhibit similar practical limitations. They are often designed for a narrow set of predefined operating modes, with limited provision for reconfiguration into alternative mechanical behaviors that are not explicitly built into the electrical control scheme. In many cases, reverse actuation or bidirectional operation also requires added structural duplication or separate complementary mechanisms rather than arising from the native device architecture. As a result, these systems frequently perform best within a specific operating regime, while showing reduced capability outside that regime. Although such specialization is common in optimized devices, the first two limitations can

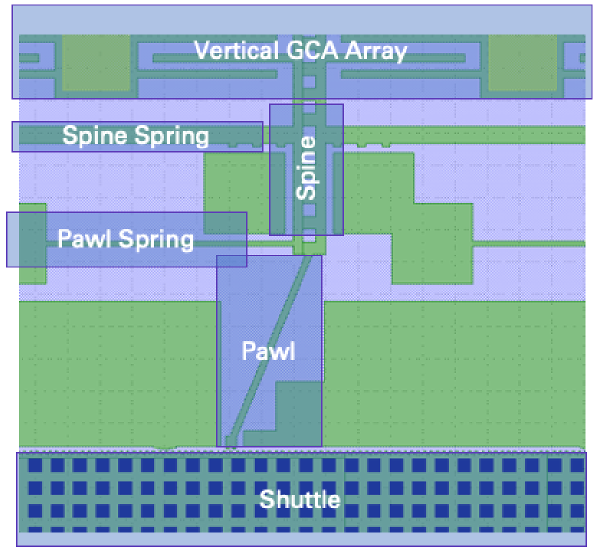


Figure 4.2: 2D design of the Penskiy-derived GCA structure used in the Pister group showing transparent overlay boxes indicating the respective components of the main pawl structure.

constrain broader design flexibility and complicate the mapping between intended tool function and achievable mechanical behavior.

As such, the stipulated goals of this work is to show:

- Bidirectional actuation.
- Variable selection of actuation gearing.
- Increased performance.

## 4.3 Theory

This analysis will provide a balanced examination of theoretical aspects, mechanical design considerations, simulation methodologies, and experimental results, offering insights into both current capabilities and future directions for MEMS motor technologies. This work aims to address the need for a compact bidirectional transmission actuator using the GCA system similar to that of Penskiy, see Fig. 4.3.

Among the most important developments in this domain are Gap Closing Actuator (GCA) motor arrays, representing a significant advancement in utilizing electrostatic

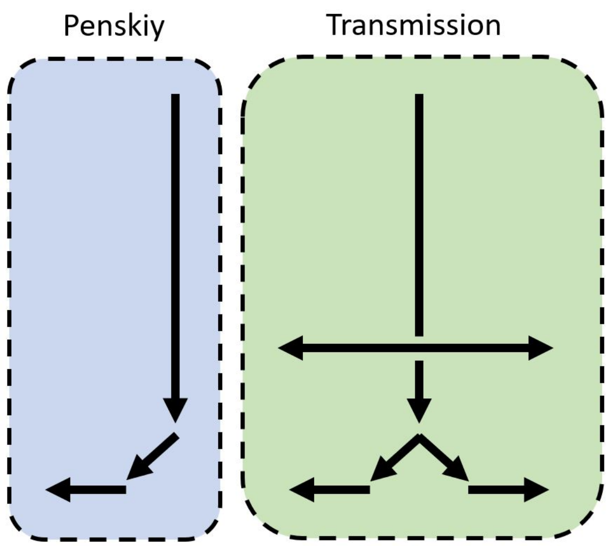


Figure 4.3: Depiction of the problem statement, showing on the left the prior Penskiy work indicating a single unidirectional output and on the right a transmission capable work indicating bidirectional and multi-modal continuous outputs.

attraction between charged Silicon beams to create motion in the perpendicular direction of the beam length. In nearly every iteration of the MEMS GCA use case, we find that as-fabricated performance is only controllable through the input Voltage ($V_{in}$), Current ($I_{in}$), and the dynamic control therein. Here we show that the range of motion ($RoM$), gear ratio ($G.R. = x_{out}/g_0$), and output force ($F_{out}$) are capable of being altered after fabrication with greater versatility than just that of $V_{in}$ and $I_{in}$ with minimal cost to planform area ($A_{plan}$) and efficiency ($\eta = P_{out}/P_{in}$).

The Transmission GCAs represent a fundamental shift from traditional actuation mechanisms.

TGCA systems operate via electrostatic attraction between parallel plate capacitors. When silicon beams are charged to the pull-in voltage ($V_{\mathrm{PI}}$), they attract each other, causing movement.

For a parallel-plate style gap-closing actuator, the most important quantities are the initial electrode gap $g_0$, the displacement of the moving electrode $x$, the instantaneous gap $g(x)$, the effective electrode area $A$, the applied voltage $V$, and the equivalent suspension stiffness $k$.

### 4.3.1 Gap Geometry and Kinematics

Let the instantaneous electrode gap be defined as

$$g(x) = g_0 - x \tag{4.1}$$

where $g_0$ is the initial gap and $x$ is the displacement of the moving electrode toward the fixed electrode. For an ideal parallel-plate configuration, the capacitance is

$$C(x) = \frac{\varepsilon A}{g_0 - x} \tag{4.2}$$

where $\varepsilon = \varepsilon_0 \varepsilon_r$ is the permittivity of the medium between the electrodes.

This capacitance relation is fundamental because it directly links actuator geometry to charge storage, electrostatic energy, and force generation.

### 4.3.2 Electrostatic Energy and Force

For voltage-driven operation, the electrostatic energy stored in the actuator is

$$U_{\text{es}}(x) = \frac{1}{2} C(x) V^2 \tag{4.3}$$

and the electrostatic force is obtained from the energy gradient,

$$F_{\text{es}}(x) = \frac{1}{2} V^2 \frac{dC}{dx} \tag{4.4}$$

which, for the ideal parallel-plate case, becomes

$$F_{\text{es}}(x) = \frac{1}{2} \frac{\varepsilon A V^2}{(g_0 - x)^2} \tag{4.5}$$

### 4.3.3 Mechanical Restoring Force and Suspension Stiffness

The electrostatic force must be balanced by the restoring force of the suspension. Under a linear spring approximation,

$$F_m = kx \tag{4.6}$$

where $k$ is the equivalent actuator stiffness. Static equilibrium is therefore governed by

$$kx = \frac{1}{2}\frac{\varepsilon A V^2}{(g_0 - x)^2} \tag{4.7}$$

The stiffness $k$ is determined by the suspension geometry and material properties. For bent clamped-clamped beams, as used in joiner members, the stiffness is

$$k_{spring} = 2Et(\frac{w}{L})^2 \tag{4.8}$$

where $E$ is Young's modulus, $t$ is the beam thickness into the plane, $w$ is the beam width, and $L$ is the beam length.

For bent cantilever beams, as used in GCA motors, the stiffness is

$$k_{spring} = \frac{Et}{4}(\frac{w}{L})^2 \tag{4.9}$$

For axial members,

$$k_{\text{axial}} = \frac{EA_s}{L} \tag{4.10}$$

where $A_s$ is the structural cross-sectional area.

### 4.3.4 Pull-In Instability

A defining feature of voltage-driven gap-closing actuators is pull-in instability. Stable equilibrium requires that the mechanical restoring stiffness exceed the magnitude of the electrostatic negative stiffness:

$$\frac{dF_m}{dx} > \frac{dF_{\text{es}}}{dx} \tag{4.11}$$

At the onset of pull-in,

$$k = \frac{dF_{\text{es}}}{dx} \tag{4.12}$$

For the ideal parallel-plate actuator, this yields the well-known pull-in displacement

$$x_{\text{PI}} = \frac{g_0}{3} \tag{4.13}$$

and the pull-in voltage

$$V_{\text{PI}} = \sqrt{\frac{8kg_0^3}{27\varepsilon A}} \tag{4.14}$$

### 4.3.5 Energy and Mechanical Work

An energy-based perspective is often helpful for comparing actuator architectures and estimating useful output. The electrostatic energy is

$$U_{\text{es}} = \frac{1}{2}CV^2 \tag{4.15}$$

while the mechanical strain energy stored in the suspension is

$$U_m = \frac{1}{2}kx^2 \tag{4.16}$$

The mechanical work delivered over a stroke is

$$W = \quad F\,dx \tag{4.17}$$

### 4.3.6 Scaling Relations and Design Tradeoffs

Several useful scaling relations follow directly from the governing equations. The electrostatic force scales as

$$F_{\text{es}} \propto \frac{AV^2}{g^2} \tag{4.18}$$

while the pull-in voltage scales as

$$V_{\text{pi}} \propto \sqrt{\frac{kg_0^3}{A}} \tag{4.19}$$

These relations show that smaller gaps strongly reduce the required actuation voltage, larger electrode areas also reduce the required voltage, and softer suspensions reduce voltage at the expense of robustness and resonant frequency. They also emphasize the strong sensitivity of actuator performance to fabrication tolerances in the initial gap.

### 4.3.7 Bidirectional Pawl

The upstream considerations for method of "gear" shifting is considered here.

Here the pawl itself was taken to be the same as that used within the Pister group [92, 111--113], derived from the Penskiy work [110]. The pawl position, general shape, thickness, and foot structure were not changed. Variations included length, relative angle, and number of pawls.

The goals for this work were to create a force transmission mechanism that was bidirectional, capable of multi-speed selections, capable of multi-force selections, and not much larger than the current structures already in use.

Having a pawl that is fully rotationally free would present a set of undesirable issues for a force transmitting component. As such, the pawl was set to be constrained within a range of motion and to achieve reversible force transmission from a vertical direction to either the forward horizontal or reverse horizontal within the plane of actuation. This constraint required that two opposing pawls were positioned at some angular separation as fabricated and it necessitated an upper bound for the pawl separation and relative shifting motion.

Additionally, it was surmised that there existed a singularity of angular orientation where the drive motion was directly in-line with the pawl angle, necessitating an angular offset. As such, the pawl was restricted from reaching this in-line orientation, thereby creating a minimum angular separation of pawls.

### 4.3.8 Pin Tab and Clutch

The method of actuation needed for moving from one gear to another is considered here. The 2D KLayout Rendering and the image from experimentation shows the Pin Tab in its intended use, see Fig. 4.7.

In initial designs, a manual gear selection method was chosen. Where a Pin Tab was designed as a rectangular shaped cantilever-suspended Silicon surface with a cut-out in it was selected. The Pin Tab is a structure that is connected to the pawl to engage the gear selection by moving the Pin Tab under mechanical application of force by probe tip. As such, the Pin Tab was sized to allow probe insertion. Through moving the probe in the direction of gear selection chosen and leaving the probe in that fixed position, the gear is fixed while the GCA engages.

In proceeding designs, the gear selection method was chosen to be a MEMS comb-drive motor to allow for the precise selection of motion in the plane. The shuttle of the comb-drive is then attached similar to the Pin Tab structure by a long-thin cantilever structure.

### 4.3.9 Gear Mechanisms

There were four concepts selected for the gear shifting technologies which were drawn upon from a large bank of possible morphologies, see Fig. 4.4 and Fig. 4.5. These four concepts represent a pared down categorical sum of the themes and approaches utilized in the banked morphologies and do not represent any optimal approach, only a selection based on what the mechanisms did at their fundamental core.

These designs are labeled as compliant mechanism (simple beam bending), Frictional Rotary Joint (Pinned Revolute Joint), Slot-Slide (Binary Keystone Prismatic Joint), and Rocker Smiley (combined approach).

**Compliant Mechanism** is a simple beam bending concept where the gear selection motion is obtained by bending a cantilever beam to a desired position by compression or tension on the driving beam.

**Frictional Rotary Joint** is a simple 2D pin-joint structure that uses friction, and the driving beam as a secondary support, to restrict free rotation essentially creating a lever action about the driving beam attachment joint to transmit force to the shuttle from the GCA spine.

**Slot-Slide** utilizes a slider that allows for the pawls to maintain alignment with the shuttle while enabling a key-stone structure, embedded into the pawl/gear shift cantilever, to engage the pawl only during GCA closure (actuation). This maintains the benefit of allowing the gear shift cantilever to remain as a monolithic structure. The drawbacks here are a reduction in selection options for the gearing.

**Rocker Smiley (Combined Rotary Joint/Slot-Slide)** is a combined approach that implements a rotary gear switching concept with a locking mechanism that is similar to the method used in the key-stone structure but with slide locking occurring at the pawl structure and constrained by the substrate by anchor pins. This approach implements lessons learned from the prior components in an attempt at reducing the drawbacks faced at each of the prior approaches. The implementation of springs at the interconnects of the pawl structure aimed at implementing the benefits of the compliant nature of the structures. The implementation of the pin joints acted to enable translation about an axis while keeping the structure from losing its position entirely. The implementation of the locking mechanisms is a direct call to the Slide-Slot approach but improved by affixing the pin-locks to the substrate.

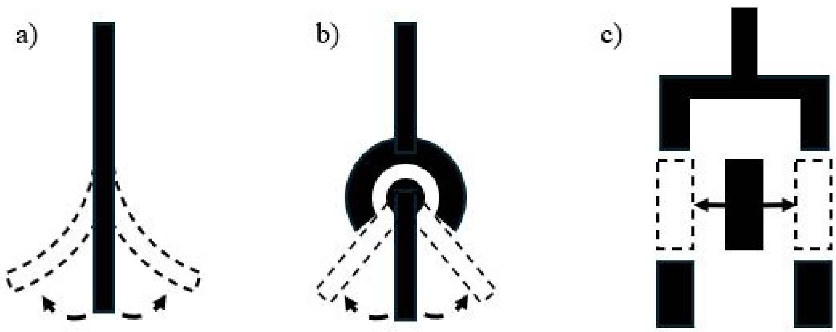


Figure 4.4: Diagram showing the basic mechanism of each of the conceptualized TGCA designs and their respective motion and engaging mechanism. a) depicts the basic concept of the Compliant Mechanism design, b) depicts the Frictional Rotary Joint design, and c) depicts the Slot-Slide design. The dotted lines represent engaged gears possible with the respective design.

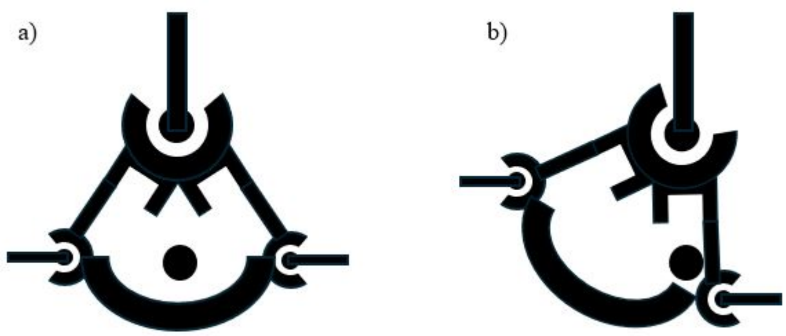


Figure 4.5: Diagram showing the basic mechanism of the Rocker Smiley concept for the TGCA design. a) shows the Rocker Smiley in neutral state and b) shows one aspect of the rotated/geared positions possible, another possible configuration would be to push the device such that it rotates and engages the opposite direction gearing.

The variation of sizes and tolerances made the Rocker Smiley difficult to etch with other designs, reducing the number of viably testable samples greatly. Similarly the necessity of the tight tolerances on the Rotary Joint concept to ensure proper rotation without the joint simply sliding out of place combined with the tight restriction on space at the pawl level made the likelihood of proper etching lower than the other approaches, again restricting the number of viable samples. The Slot-Slide concept lacked the functionality that was desired and was not used in future iterations. The main successor of this line of approaches was the Compliant Mechanism design, as discussed below. As a note, all designs above were designed, fabricated, and tested but only the Compliant Mechanism approach was favorable. See appendix for details on the other designs.

## 4.4 Mechanical Design

Fig. 4.6 shows that by first actuating the transverse gear shift, $\Delta$, the pawl structure can be angled relative to the shuttle in either the forward or the reverse direction. Then, while in this gear shifted configuration, the gap-closing actuator (GCA) can be engaged, driving the pawl foot into the shuttle. While the pawl foot and shuttle are interlocked by their respective interlocking teeth, the pawl arm undergoes elastic deformation and loads elastic energy as a spring, driving the shuttle in either the forward or reverse direction (depending on gear shifting) as the elastic energy from the pawl arm is released during the rest of the GCA force travel and displacement. Afterwards, the pawl springs back to its unactuated position, releasing the shuttle.

### 4.4.1 Compliant Structure Design

The effect of the corresponding compliances in the shape of the pawls can be seen in Fig. 4.10.

### 4.4.2 Configuration-Dependent Stiffness With Shuttle Contact

The linkage stiffness was modeled as a configuration-dependent tangent stiffness rather than as a single constant stiffness. This distinction is necessary because the mechanism is first displaced in the horizontal direction and is subsequently loaded in the vertical direction. The imposed horizontal displacement changes the linkage geometry, modifies the internal axial load state of each slender member, and therefore changes the incremental stiffness experienced during the later downward loading step. In the final contact-engaged state, the linkage is also constrained by a shuttle that is assumed to be compliant only in the horizontal direction and immovable in the vertical direction.

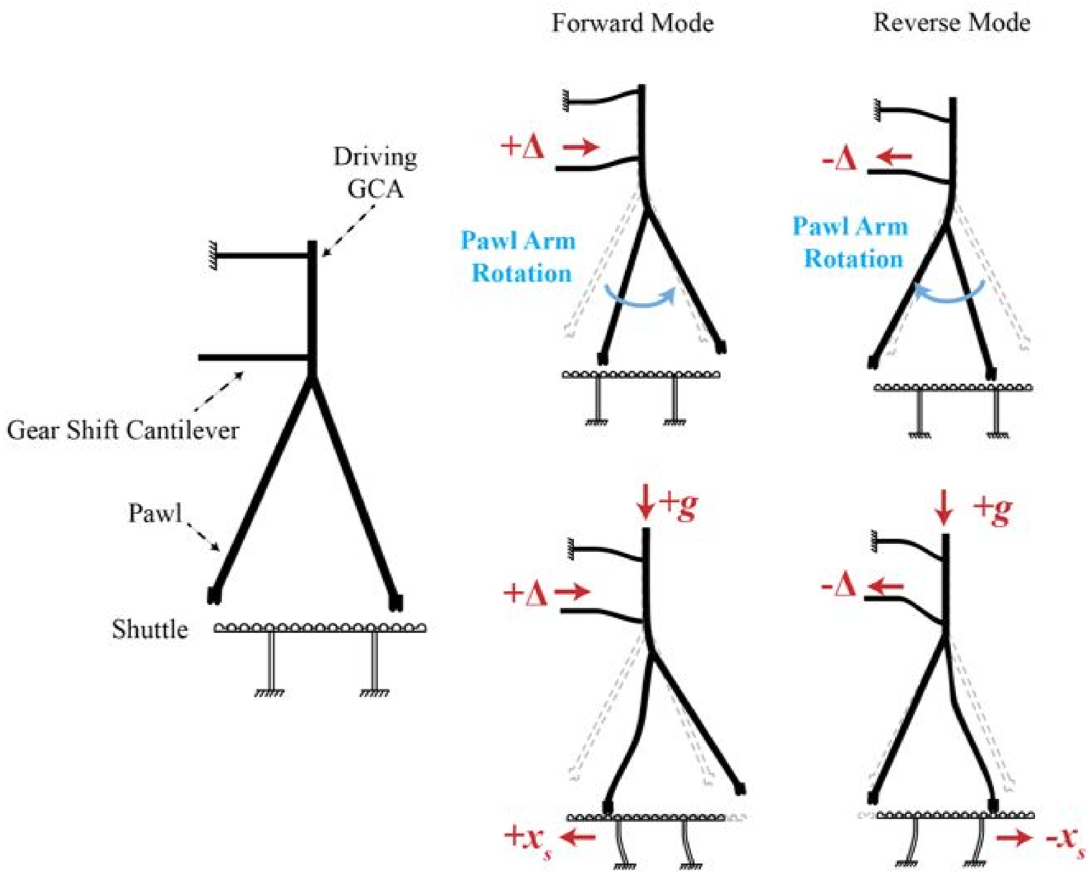


Figure 4.6: Diagram of the mechanics for the $\mu\Delta$ motor pawls with $\lambda = 25^o$. Top) demonstrates the initial state of the motor prior to actuation, Bottom-left) shows the gear shifted position at a given distance, $\Delta$, (orange arrow) with the deflection angular sweep, $\gamma$, (blue arrow). Bottom-right) demonstrates the GCA driving and shuttle motion step with the bending behavior of the pawl upon contact with the shuttle showing the force transmission from the axial direction (blue arrow) the orthogonal shuttle direction (red arrow). Indicated on top is the forward and the bottom the reverse gearing with bending indicated.

The loading sequence considered in this model is divided into four states:

$$\begin{aligned}
&\text{Step 1:} \quad \text{reference/unloaded configuration,} && (4.20)\\
&\text{Step 2:} \quad \Delta x \text{ applied, prior to downward force,} && (4.21)\\
&\text{Step 3:} \quad \Delta x \text{ held, downward force applied, prior to shuttle contact,} && (4.22)\\
&\text{Step 4:} \quad \Delta x \text{ held, downward force applied, shuttle contact engaged.} && (4.23)
\end{aligned}$$

Here, $\Delta x$ is the prescribed horizontal displacement applied to the input node. The downward force applied during Step 3 and Step 4 is denoted by

$$F_y = -3 \text{ mN}. \tag{4.24}$$

The shuttle is modeled as having a finite return stiffness only in the $x$ direction,

$$F_{s,x} = k_{\text{shuttle}} u_s, \tag{4.25}$$

where $u_s$ is the horizontal shuttle displacement and $k_{\text{shuttle}}$ is the shuttle return-spring stiffness. The shuttle is assumed to be vertically fixed, such that

$$v_s = 0. \tag{4.26}$$

#### 4.4.2.1 Element Geometry and Cross-Sectional Properties

For an element $e$ with undeformed nodal coordinates $(x_i, y_i)$ and $(x_j, y_j)$, the undeformed element length is

$$L_e = \sqrt{(x_j - x_i)^2 + (y_j - y_i)^2}. \tag{4.27}$$

The element orientation angle is

$$\phi_e = \tan^{-1}\left(\frac{y_j - y_i}{x_j - x_i}\right), \tag{4.28}$$

with direction cosines

$$c_e = \cos\phi_e = \frac{x_j - x_i}{L_e}, \tag{4.29}$$

$$s_e = \sin\phi_e = \frac{y_j - y_i}{L_e}. \tag{4.30}$$

For a rectangular MEMS beam with in-plane width $w_e$ and out-of-plane thickness $T$, the cross-sectional area and in-plane second moment of area are

$$A_e = w_e T, \tag{4.31}$$

$$I_e = \frac{T w_e^3}{12}. \tag{4.32}$$

The effective Young's modulus is written as

$$E^* = \frac{E}{1-\nu^2}, \tag{4.33}$$

where $E$ is the Young's modulus and $\nu$ is Poisson's ratio. This correction may be used when a plane-strain approximation is appropriate. The corresponding axial and flexural rigidities are

$$EA_e = E^* A_e, \tag{4.34}$$

$$EI_e = E^* I_e. \tag{4.35}$$

#### 4.4.2.2 Elastic Beam Stiffness

Each linkage member is modeled as a two-dimensional Euler--Bernoulli frame element. In the local coordinate system, the elastic element stiffness matrix is

$$\mathbf{k}^{\ell}_{e,\mathrm{el}} = \begin{bmatrix} \frac{EA_e}{L_e} & 0 & 0 & -\frac{EA_e}{L_e} & 0 & 0 \\ 0 & \frac{12EI_e}{L_e^3} & \frac{6EI_e}{L_e^2} & 0 & -\frac{12EI_e}{L_e^3} & \frac{6EI_e}{L_e^2} \\ 0 & \frac{6EI_e}{L_e^2} & \frac{4EI_e}{L_e} & 0 & -\frac{6EI_e}{L_e^2} & \frac{2EI_e}{L_e} \\ -\frac{EA_e}{L_e} & 0 & 0 & \frac{EA_e}{L_e} & 0 & 0 \\ 0 & -\frac{12EI_e}{L_e^3} & -\frac{6EI_e}{L_e^2} & 0 & \frac{12EI_e}{L_e^3} & -\frac{6EI_e}{L_e^2} \\ 0 & \frac{6EI_e}{L_e^2} & \frac{2EI_e}{L_e} & 0 & -\frac{6EI_e}{L_e^2} & \frac{4EI_e}{L_e} \end{bmatrix}. \tag{4.36}$$

The axial terms scale with $EA_e/L_e$, while the transverse bending terms scale with $EI_e/L_e^3$. This distinction is important for slender MEMS linkages because a change in geometry can shift the load path from bending-dominated to more axial-load-dominated behavior.

The local-to-global transformation matrix is

$$\mathbf{T}_e = \begin{bmatrix} c_e & s_e & 0 & 0 & 0 & 0 \\ -s_e & c_e & 0 & 0 & 0 & 0 \\ 0 & 0 & 1 & 0 & 0 & 0 \\ 0 & 0 & 0 & c_e & s_e & 0 \\ 0 & 0 & 0 & -s_e & c_e & 0 \\ 0 & 0 & 0 & 0 & 0 & 1 \end{bmatrix}. \tag{4.37}$$

The global elastic stiffness contribution of element $e$ is therefore

$$\mathbf{k}_{e,\mathrm{el}}^{g} = \mathbf{T}_e^T \mathbf{k}_{e,\mathrm{el}}^{\ell} \mathbf{T}_e. \tag{4.38}$$

#### 4.4.2.3 Geometric Stiffness From Axial Preload

After the imposed displacement $\Delta x$ is applied, each beam may carry an internal axial force. For element $e$, this axial force is denoted by $N_e$, where positive $N_e$ represents tension and negative $N_e$ represents compression. A convenient estimate of the axial force is

$$N_e = \frac{E^* A_e}{L_{e,0}} \left(L_{e,\mathrm{def}} - L_{e,0}\right), \tag{4.39}$$

where $L_{e,0}$ is the undeformed element length and $L_{e,\mathrm{def}}$ is the deformed element length,

$$L_{e,\mathrm{def}} = \sqrt{[x_j + u_j - (x_i + u_i)]^2 + [y_j + v_j - (y_i + v_i)]^2}. \tag{4.40}$$

The corresponding local geometric stiffness matrix is

$$\mathbf{k}_{e,\mathrm{geo}}^{\ell} = \frac{N_e}{30 L_e} \begin{bmatrix} 0 & 0 & 0 & 0 & 0 & 0 \\ 0 & 36 & 3L_e & 0 & -36 & 3L_e \\ 0 & 3L_e & 4L_e^2 & 0 & -3L_e & -L_e^2 \\ 0 & 0 & 0 & 0 & 0 & 0 \\ 0 & -36 & -3L_e & 0 & 36 & -3L_e \\ 0 & 3L_e & -L_e^2 & 0 & -3L_e & 4L_e^2 \end{bmatrix}. \tag{4.41}$$

This term captures the stress-stiffening or stress-softening contribution produced by the preloaded configuration. Tensile axial force increases the transverse tangent stiffness, whereas compressive axial force reduces it and may move the member closer to an instability condition.

The global geometric stiffness contribution is

$$\mathbf{k}_{e,\mathrm{geo}}^{g} = \mathbf{T}_e^T \mathbf{k}_{e,\mathrm{geo}}^{\ell} \mathbf{T}_e. \tag{4.42}$$

The global tangent stiffness of element $e$ is therefore

$$\mathbf{k}_{e,T}^{g} = \mathbf{k}_{e,\mathrm{el}}^{g} + \mathbf{k}_{e,\mathrm{geo}}^{g}. \tag{4.43}$$

#### 4.4.2.4 Shifting Behavior

In this work, we demonstrate that by introducing a second displacement input, $\Delta$, the angle of the pawl can be changed dynamically during motor operation. Penskiy showed that there was a trade-off between shuttle output force and shuttle displacement based on the angle of the pawl [110]. By changing the angle of the pawl, this work allows that trade-off to be made dynamically, similar in mechanism to shifting gears on a bike. In addition, we demonstrate that a dual-pawl head can be used on the GCA in Fig. 4.11, enabling both forward and reverse motion of the shuttle.

In the test chip case, the gear shift is maneuvered by a pin tab, as seen in Fig. 4.7, which is a structure that is meant to be shifted by a probe station probe. The gear shift cantilever travels transversely and bends the pawl cantilever around the spine structure, as seen in Fig. 4.6. This shows the basic geometric structure, where the $\Delta$ shift is highlighted by using a design with a pawl structure consisting of two cantilevers with a pitch angle, $\lambda$, of $47.5^o$ and $25^o$. An inverted "Y"-shaped holds a pair of pawls with notched teeth at their ends for forward and backward motions, respectively, while the other pawl idles.

Fig. 4.8a and Fig. 4.8b show the KLayout 2D model of the analog transmission GCAs using a Compliant Mechanism Cantilever as the shift capable morphology in the pawl-to-GCA connection. Fig. 4.8a shows a zoomed in perspective of the attachment at near the bottom of the connecting cantilever (top of the 2-pawl configuration), away from the pawls, which are arranged in the wider $67^o$ orientation. Fig. 4.8b shows a zoomed in perspective of the attachment at near the bottom of the connecting cantilever (top of the 2-pawl configuration) near where the pawls connect, which are arranged in the narrower $45^o$ orientation. Fig. 4.9 shows the 2D Klayout CAD with the components called out.

Here we present a monolithic actuator with embedded compliant structures that enable direct drive multi-force and -speed outputs in both forward and reverse directions. These actuators offer the capability for increased range in actuation displacement and output force for varied gear shift inputs. The sweep inputs, $\Delta$, can be shifted in micrometer ranges and the output shuttle movements have been characterized.

In this work, each motor device is actuated both in forward and in reverse and the data shown below reflects such actuation schemes and is confirmed by ANSYS simulation. Fig. 4.6 shows that through by first actuating the transverse gear shift, $\Delta$, the pawl structure can be angled relative to the shuttle in either the forward or the reverse direction. Then, while in this gear shifted configuration, the gap-closing actuator (GCA) can be engaged, driving the pawl foot into the shuttle. While the pawl foot and shuttle are interlocked by their respective interlocking teeth, the pawl arm undergoes elastic deformation and loads elastic energy as a spring, driving the shuttle in either the forward or reverse direction (depending on gear shifting) as the elastic energy from the pawl arm is released during the rest of the GCA force travel and displacement. Afterwards, the pawl springs back to its unactuated position,

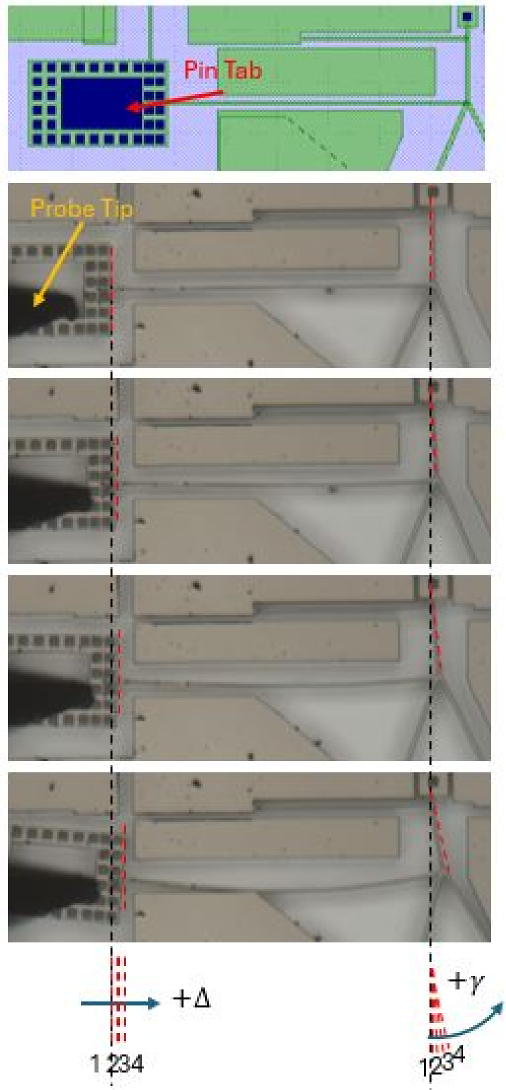


Figure 4.7: (Top) Klayout 2D CAD showing the location and use of the pin tab structure. (Middle) Four images showing the progression of the pin tab push by the probe tip at the probe station where the probe tip also applies a horizontal force and displacement in the $+\Delta$-direction causing a $+\gamma$ change in the pawl, which then imparts (when actuated) a $+\delta x$ change in shuttle motion where the $+\delta x$ is in the $-\Delta$ direction. The first of the four images shows the unshifted position but with the probe tip hovering just above the pin tab prior to actuation. The three following images show the probe tip engaging the pin tab and maneuvering it by applying a forced displacement. Guiding lines have been added in dashed red to assist the reader in viewing the changes in pin tab and pawl relative to their initial position, noted in black dashed line. (Bottom) Diagram showing the $+\Delta$ and $+\gamma$ changes aligned horizontally to depict their relative motion.

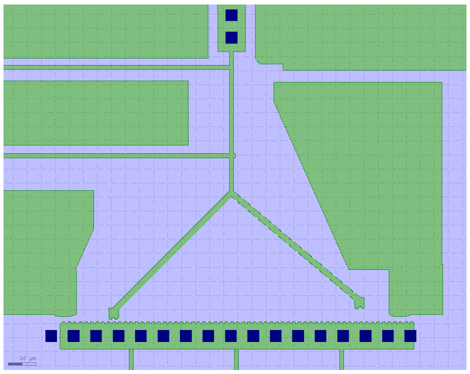

(a) Compliant Mechanism, Short Connecting Cantilever, Wide ($67^o$) Analog Transmission 2-Pawl Morphology.

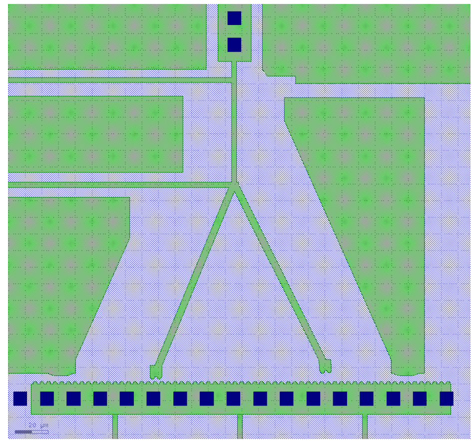

(b) Compliant Mechanism, Short Connecting Cantilever, Narrow ($45^o$) Analog Transmission 2-Pawl Morphology.

Figure 4.8: Figure showing the two compliant mechanism design morphologies.

releasing the shuttle. The main mechanical design challenge is finding methods of actuation that allow for gear shifting with minimal impact on the overall force transfer from vertical to horizontal while maintaining control over release and grip timing.

The shuttles have 3 cantilever springs together with $k_{sp,eff} = 0.928N/m$ as drawn. Each vertical gap closing array has 40 individual capacitive plate pairs attached to a single spine which together can produce approximately $0.9mN$ of force under an input bias voltage of $100V(N = 40, l_{OL} = 76.2\mu m, g_0 = 4.9\mu m)$ [113, 114].

Each of the following experience simple beam bending loaded conditions: gear shift, deflection, and pawl beams. The only beams which experience higher order bending is the gear shift horizontal alignment and the pawl and spine return beams, which are not discussed as they are simple bending beams which do not contribute directly to the main compliant structures which influence the transmission capability of the $\mu\Delta$-motors. Within the proper working range of normal prescribed function, simple beam bending can be expected in each of the components of the device.

## 4.5 Experimental Setup

The pin tabs are incorporated into the clutch mechanism as a method of manual positioning for initial as described above. These are also incorporated into the later devices and further iterations of the $\mu\Delta$ motors as a mode of manual start or mechanically forcing the gear shifts. The pin tabs are used to manually actuate the

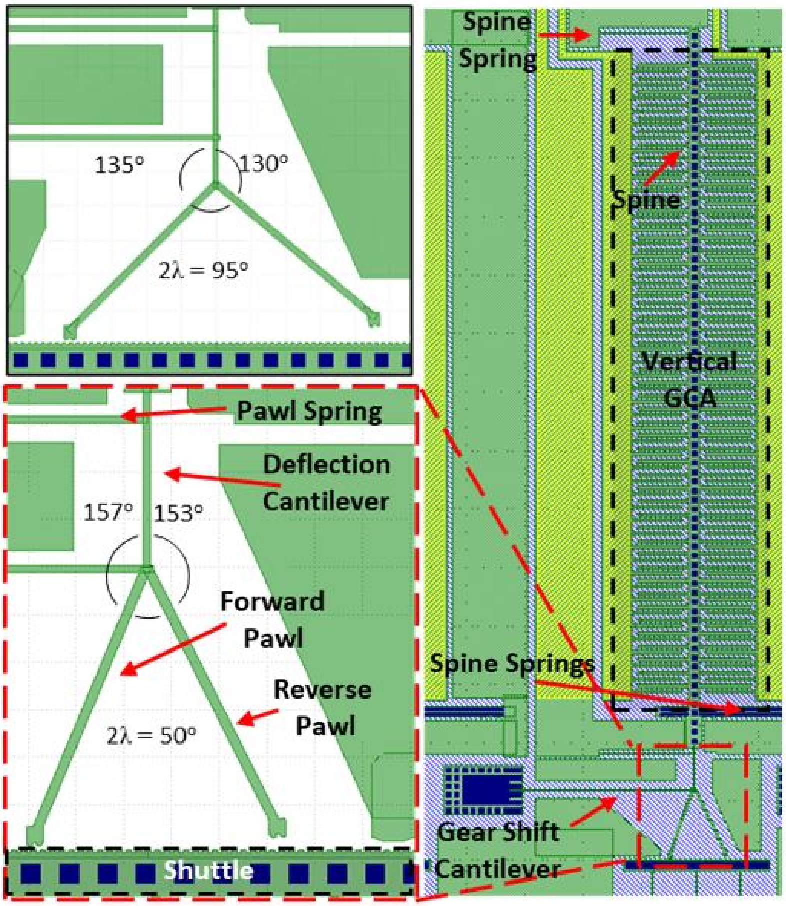


Figure 4.9: Diagram showing the $\mu\Delta$ motor (right). Left-top showing the pawl separation half-angle $\lambda = 47.5^o$ and left-bottom showing $\lambda = 25^o$. The forward pawl of the $\lambda = 25^o$ device has the same angular morphology of the Penskiy pawl with the noted difference of having a reverse pawl and a gear shift cantilever attached at the meeting of the forward and reverse pawls. The distance between the pawl top and the pawl spring has been elongated for the insertion of a deflection cantilever for rotation.

pawl through the sweep of $\partial\gamma$ as using the imparted motion of the probe, effectively described as $\Delta$.

Here the probe station is manipulated by micrometer stages with approximately $0.1\mu m$ resolution in their dial. While this is not the defining limit of the mechanism itself, for experimentation purposes, this is taken as the resolution for these experimental purposes.

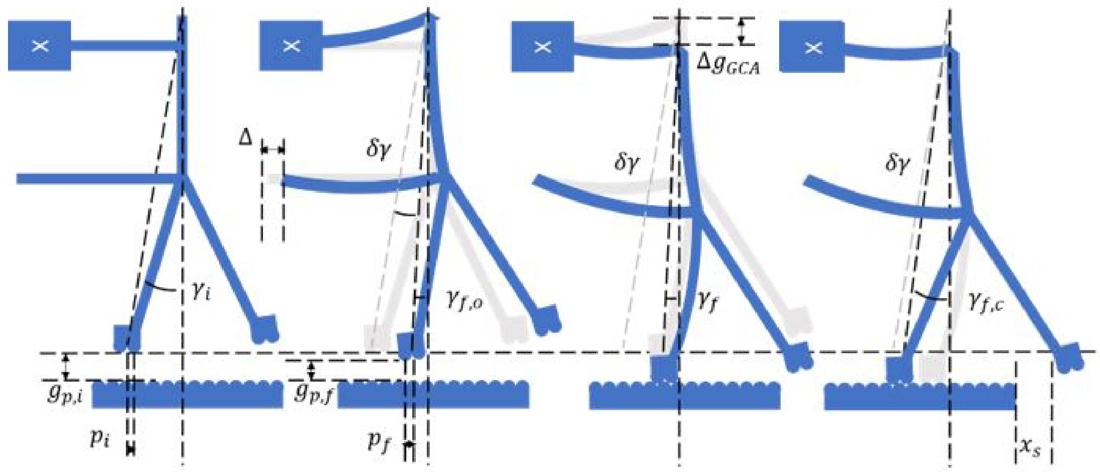


Figure 4.10: Diagram of small angle approximation for change in deflection angle, $\delta\gamma$ due to $\Delta$; the pitch offset, $p$, that contributes to pawl/shuttle tooth misalignment; pawl gap, $g_p$, which decreases with increasing $\delta\gamma$; and shuttle motion, $x_s$, which grows with increasing work done on the shuttle due to the decrease in $g_p$. From left to right is the progression actuation of as fabricated, gear shifted, GCA drive input, and shuttle motion. Not to scale. Interestingly at some $\gamma$'s the $x_s/\delta g_{GCA} > 1$. Shaded gray images correspond to the previous action for reference.

Pitch alignment offsets can impart misalignment that together with the spring load on the pawl contributes constructively or destructively to the overall compliance of the pawl structure. In most cases, this causes the compliance in the pawl structure to increase, in essence creating a stronger spring. Fig. 4.10 shows the pitch offset that contributes to the misalignment of the pawl tooth and the subsequent shuttle movement. As the pawl gap, $g_p$, increases with increasing $\Delta$, the work done on the spine (and pawl) by the GCA increases thereby increasing work done on the shuttle. When taken together with the information from Fig. 4.11, this implies that the $\mu\Delta$-motors increase the range of GCA action on the spine and therefore the pawl. Additionally the $\mu\Delta$-motors increased $\Delta$ causes the relative distance between the pawl foot and the shuttle teeth to decrease. This increases the range of motion that the pawl is in contact with the shuttle adding to the range of work done on the shuttle. These three mechanisms cause a byproduct of the overall action on the shuttle to be increased in three ways: stiffer spring force, longer GCA action, and increased pawl contact with shuttle. However, many of these byproducts can work against the direction of motion in the reverse case, indicating that the reverse direction actuation does not enjoy the benefits that we see in the forward direction gear selections.

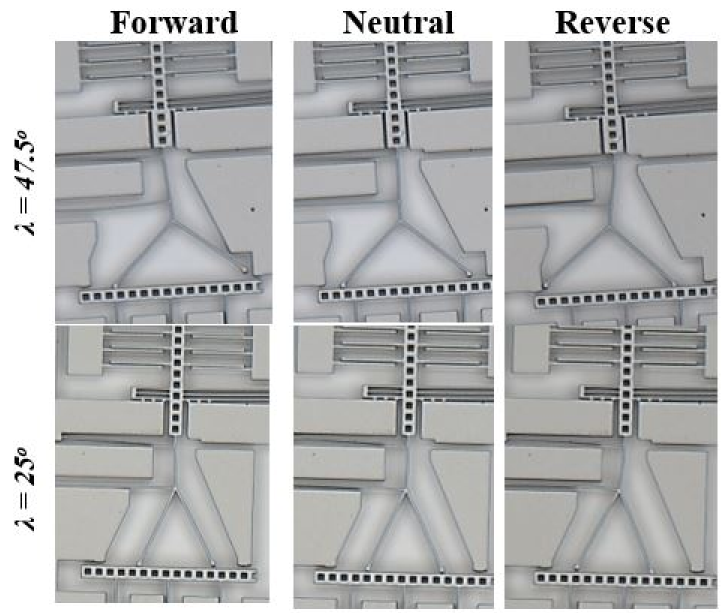


Figure 4.11: Optical images of fabricated devices in their actuated positions for representative display of the relative forward, neutral, and reverse positions for the $\lambda = 25^o$ and $\lambda = 47.5^o$ devices. In “forward gear”, the left pawl pushes the shuttle left. In “reverse gear”, the right pawl pushes the shuttle to the right.

Fig. 4.11 shows the impact of the pin tab action on the initial pre-GCA-actuation state of the $\mu\Delta$ motor. The two topologies show a range of capable gear selections with the wider $\lambda = 47.5^o$ structure having a smaller working range than the narrower $\lambda = 25^o$. The benefit of the wider topology is the reduced working stiffness through the actuation step than the narrower one which may in effect actually weaken the overall actuation power output.

For data collection, the main input variables were the indicated gear shift distance, $\Delta$, and the voltage, $V_{PI}$. First, a $V_{PI}$ was found for the Neutral case. Then, $\Delta$ was increased in the positive or negative direction until actuation halted. This halting point was considered the next "natural gear" for the device. From here, $V_{PI}$ was then found again by increasing voltage until actuation occurred again. This was repeated until the ultimate limit of the pawl was reached. The ultimate limit is determined to be the point at which the pawl comes into contact with the shuttle even before actuation takes place. There were no instances were the device fractured as a result of actuation or gear selection.

In some cases, such as the wider $\lambda = 4.5^o$, there is a gap near $\Delta = 2.5\mu m$ that is unattainable due to the collision of the pawl with the shuttle. This gap in the range was not present for the $\lambda = 25^o$ devices.

Theoretically, the devices do not have inherent gear selections as the incremental selection of positions is not inherent to the device itself but rather the resolution of input displacement. As such, the gear input, or $\Delta$, values were selected in such a way as to better understand the natural spacing of the possible individual gears. There are many different methods of choosing such a gear spacing and this work presents only some of the possible gear selection frameworks.

## 4.6 Results

Fig. 4.12 shows the ANSYS simulation results that correspond to the forward, between 1 to $10\mu m$, and parts of the reverse gear shifted, between 1 to $10\mu m$, actuation performance. The magnitude of the shuttle motion increases as the gear shifting displacement increases in both the forward and reverse directions. We observe an asymmetrical change in shuttle motion near zero input as the gear shift overcomes the as-fabricated forward state. Spine motion due to the rotation of the compliant structure with increasing gear shift changes the initial gap of the GCAs in a linear trend between 1 to $10\mu m$ of displacement with its corresponding pull -in voltage.

The video analysis results are indicated in Fig. 4.16, where the software, indicated in Fig. 4.15, is used to extract the relative positions of the individual components of the critical structure. The observed pull-in voltage and shuttle displacement agrees with the simulated value.

The GCA pull-in voltage variation is different for each $\Delta$ input, as seen in Fig. 4.18. This variation is attributed to the shift cantilever compliant mechanism, which increases the stiffness in the pawl imparting a decrease of GCA gap distance, gGCA, prior to actuation in the reverse and an increase in the forward direction.

Mechanical characterization, indicated in Fig. 4.17, shows a monotonic relationship between $\mu m$-scale deflection angle, $\gamma$, and the shuttle motion. While the shuttle does not constitute a force test, the distance the shuttle is pushed corresponds to range of output motion in the $\Delta$ shift for the given stiffness close to the no-load condition.

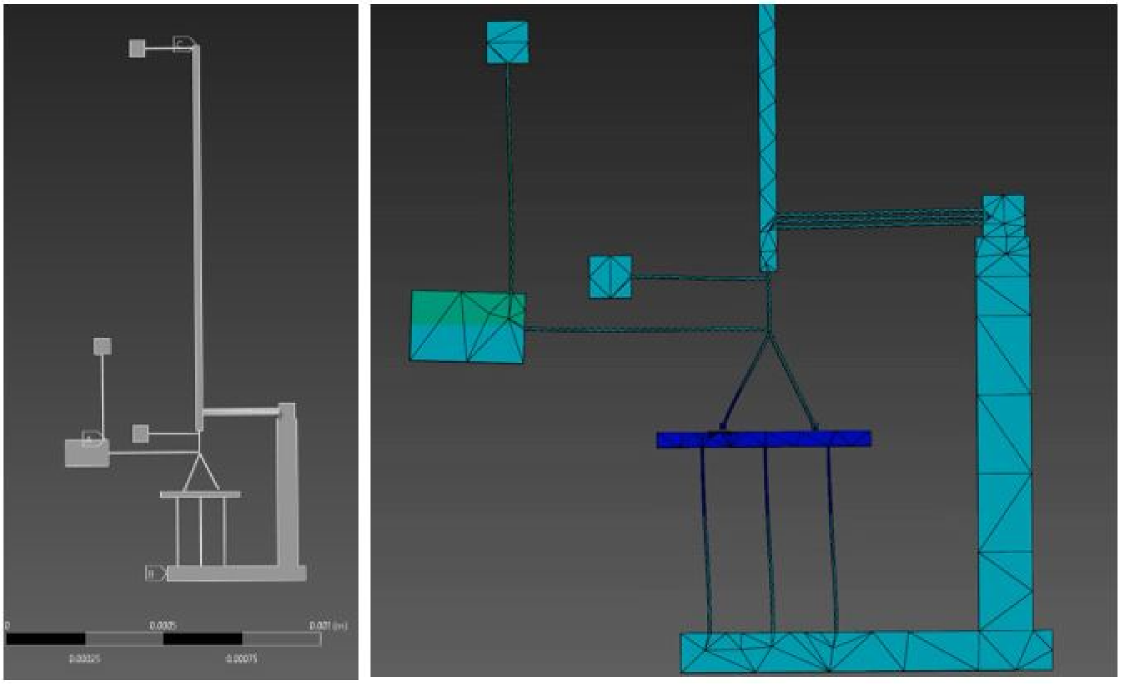


Figure 4.12: ANSYS simulation of the narrow $\lambda = 25^o$ compliant mechanism $\mu\Delta$Motor indicating the deflection magnitude in colormap.

### 4.6.1 ANSYS Simulations

Finite element analysis (FEA) using ANSYS represents a cornerstone of MEMS motor design and optimization, enabling detailed prediction of mechanical behavior, thermal characteristics, and electrostatic interactions. The simulation methodology typically follows a structured approach: The end.

We conduct a finite element analysis on the compliant structure comprising the gear shift cantilever, forward/reverse pawls, GCA spine, and shuttle system, illustrated in Fig. 4.10. In the first stage of the simulation, the gears shift cantilever displaces by $10\mu m$ with a step size of $1\mu m$, while the rest of the system remains anchored near the spine and pawl springs. The forward/reverse pawls deform under the static load induced by the gear shift cantilever displacement. Subsequently, the spine displaces by $3.8\mu m$ in the vertical direction and returns to its neutral state at each step of gear shifting displacement, simulating the GCA actuation. The forward pawl's tip moves toward the shuttle until contact occurs between the pawl teeth and shuttle teeth. The shuttle displacement serves as the output of the compliant structure.

First, we examine the response of the complaint structure with gear-shifting displacement only. As the input displacement increases at the end of the gear shift beam, the system rotates counterclockwise. As a result, the GCA spine displaces upward locally changing the effective initial gap and different pull-in voltage that is needed at the simulation step.

The complaint structure is connected to four clamp-clamped springs along y-axis in parallel: gear shifting beam, spine springs, and the pawl spring, as called-out in Fig. 4.9.

Therefore, the effective stiffness, $k_{eq}$, is the sum of the stiffness all four clamp-clamp spring systems where individual stiffness is described by Eq. 4.9. The resulting pull-in voltage versus input gear shifting displacement is shown in Fig. 4.18.

We then examine the system response to the GCA stride at each step of the gear shifting displacement. Both the initial distance and attack angle between the forward/reverse pawl and the shuttle change because of the gear shifting displacement. The initial distance between the pawl tip and shuttle determines the effective travel of the GCA that can contribute to the shuttle deformation. The attack angle determines the ratio of GCA output force to shuttle. This output force is divided between the components driving the shuttle along the x axis (transverse direction), the normal force (or holding force) perpendicular to the shuttle (parallel direction), and the friction force between the pawl tip and shuttle interface. As a result of both factors, the maximum distance the shuttle travels changes at each gear shifting displacement as shown in Fig. 4.13. When gear shifting angle input is low, shuttle displacement is dominated by the initial gap between the pawl tip and shuttle teeth; GCA displacement must overcome the large initial gap and not enough thrust is converted to shuttle displacement. At a large gear shifting angle input, however, the attack angle between pawl teeth and shuttle dominates the shuttle displacement. Additionally, at high attack angle input, the interacting pawl can come near a near perpendicular state with the shuttle which can cause non-stable bending in the pawl, creating a direct compression in the pawl and cause fracture to the pawl. Similarly, at very low attack angle or in a range of negative attack angle input there is a range where the interacting pawl can be too far from the shuttle to effectively interact with the shuttle and cause a dead zone.

Simulation results (Fig. 4.13) demonstrate a behavior that closely follows the simulated behavior. Experimental results show similar closely following behavior with fringe behavior near the large positive, low positive, low negative, and high negative edges of the attack angle input. This is likely a result of the trapezoidal shape of the pawls due to the DRIE which causes the bottom end of the etch to be wider than that of the top edge. These changes in shape, while not accounted for in the theory or simulation, are likely to be the source of unaccounted for torsion and mixed compression fractures or bending that occurs near the extremes of the actuation.

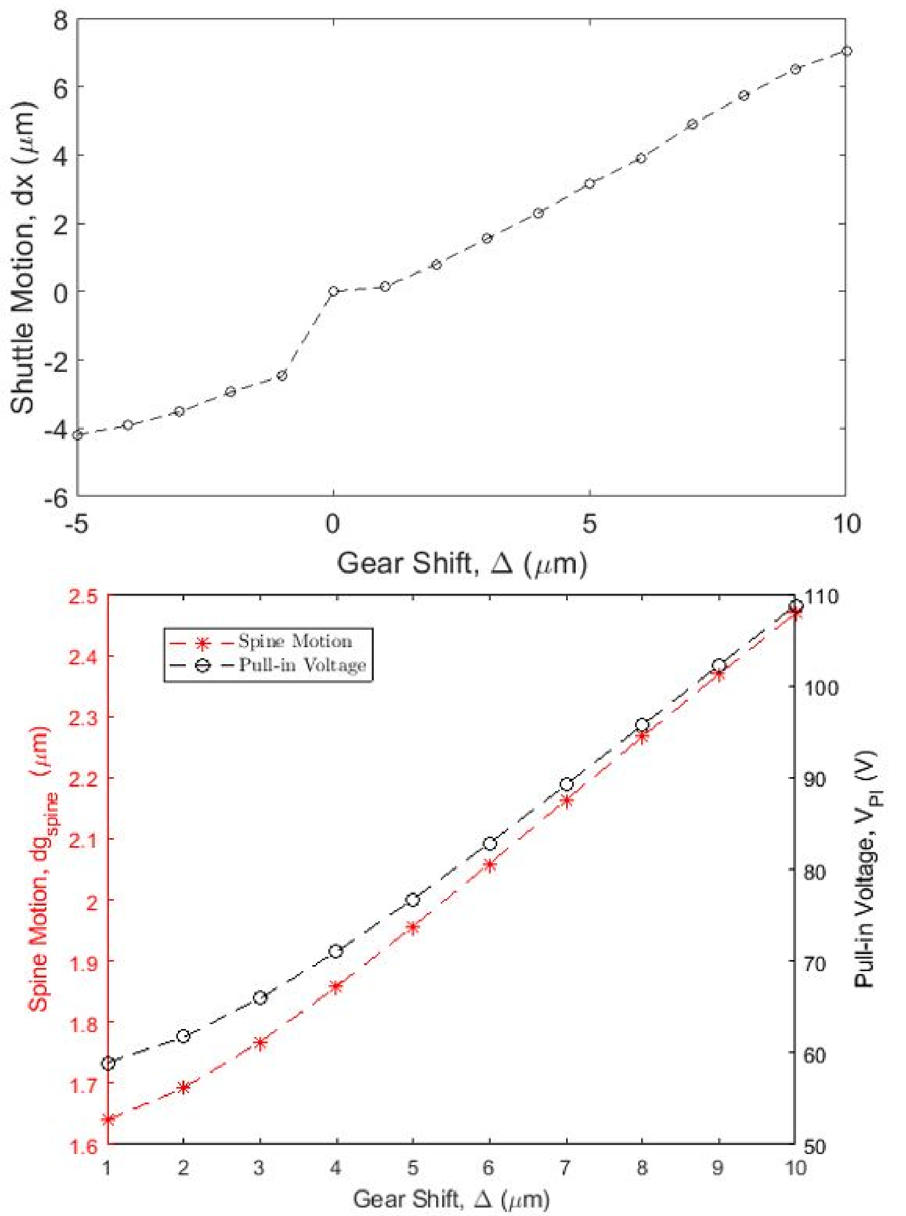


Figure 4.13: (Top) ANSYS simulation data of the shuttle motion with respect to the gear shift tab displacement. (Bottom) ANSYS simulation data of the spine motion shift (pre-actuation) on left axis and effective pull-in voltage on right both as a function of gear shift displacement.

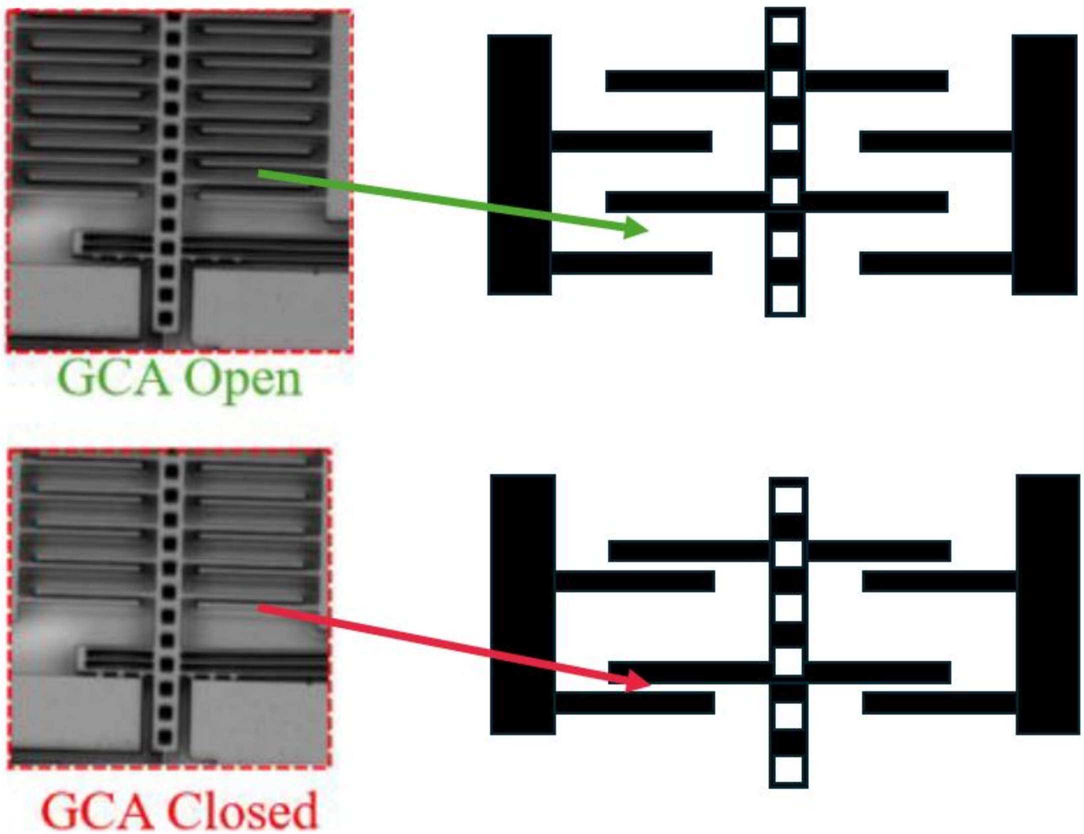


Figure 4.14: Zoomed in single frame images captured from video showing the open position of the GCA and the closed position of the GCA. Together with the diagrams depicting each for clarity.

### 4.6.2 Video Averaged Analysis

These experiments were derived in the same way as in Sec. 4.5. However, here the devices were allowed to run for eight minutes while video was taken.

Postprocessing of the videos occurred to evaluate the dynamic motion of the TGCA samples. A region of capture was manually selected by the user to indicate what region of the video motion analysis would be performed on, this was done to allow the software to more easily process the data available. Within the region of capture, the user set sample points of the image to monitor for motion and named each as well as indicating which direction within the given coordinate system, the software should monitor for specifically. A region of capture was set for the GCA

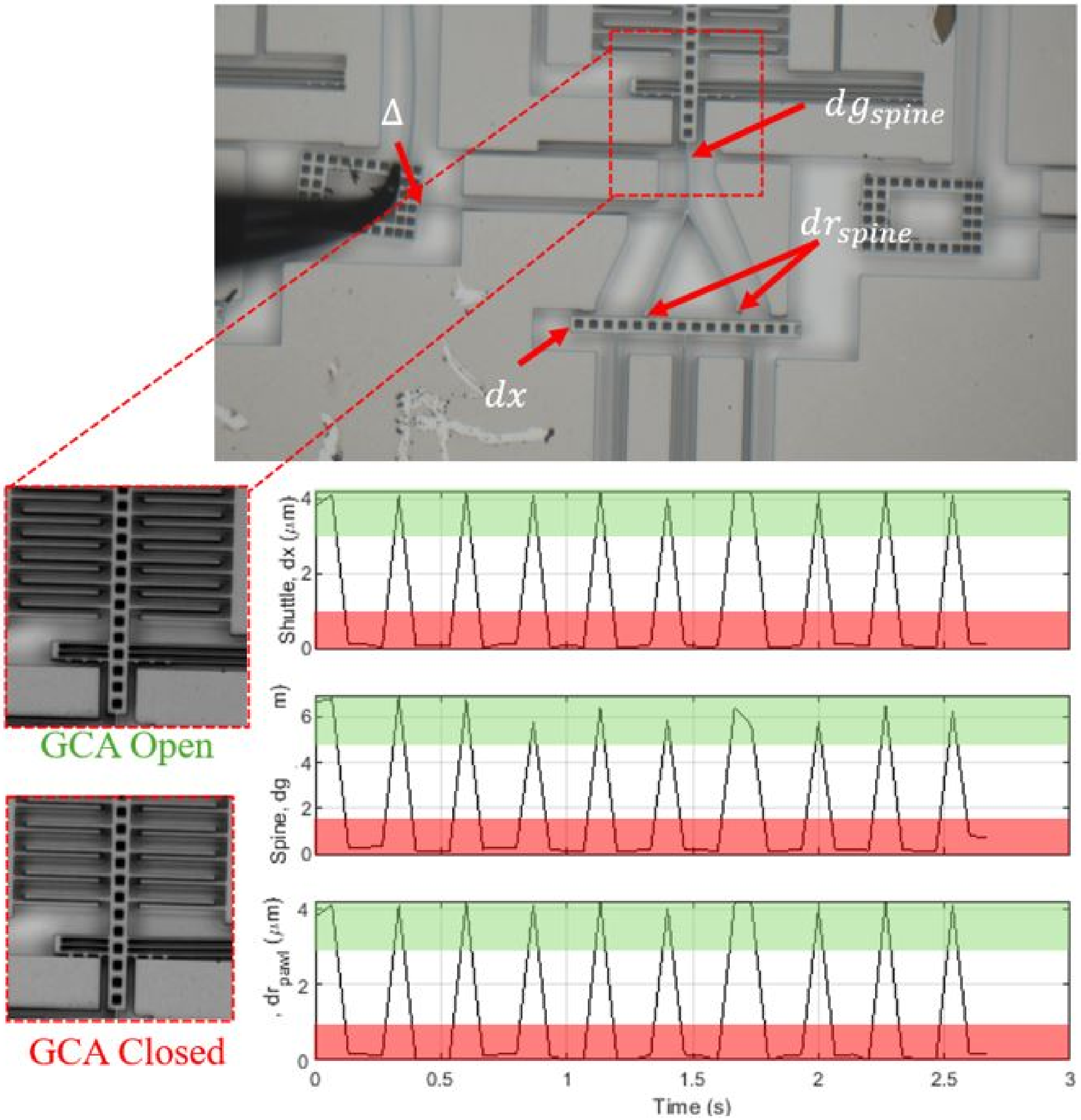


Figure 4.15: Single frame images captured from video of the narrow $\lambda = 25^o$ compliant mechanism $\mu\Delta$Motor with arrows indicating the pin-tab gear shift motion ($\Delta$), spine motion due to the closing gap of the fingers ($dg_{spine}$), the motion of the pawls ($dr_{pawl}$), and the displacement of the shuttle in the $x-$, or transverse-, direction ($dx$). Insets show the GCA in the open position and closed position with plots indicating the video captured motion of the spine, pawl, and shuttle. Green overlays are to indicate the automated region of capture where the "open" is considered a fully open GCA below in red is the indicated fully "closed" GCA motion.

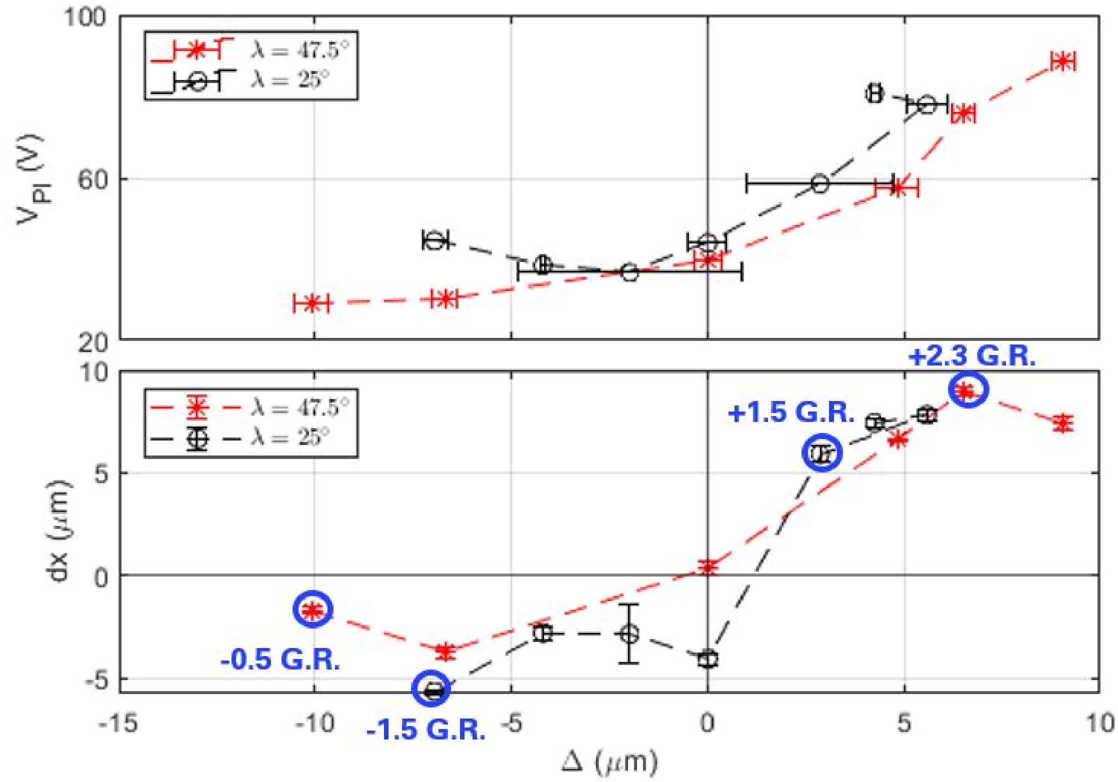


Figure 4.16: Plot showing the Video Averaged data of the $\mu\Delta$ Analog Transmission for both the $\lambda = 47.5^o$ and the $\lambda = 25^o$ designs in forward and reverse actuation. Indicated are selected Gear Ratio, $G.R. = x_s/g_o$

fingers, spine, connection point of both pawls, pawl feet, and shuttle to capture the behavior of each during the open and closed steps of the actuation phase, see 4.14 for an example of the open closed behavior of the GCA fingers and spine. See Fig. 4.15 for the data representation of the captured motion of the GCA fingers and spine.

Videos of the moving compliant system were captured for both narrow ($\lambda = 25^o$) and wide ($\lambda = 47.5^o$) devices. A probe station pin was employed to manually switch gears by displacing the gear shift cantilever. The vertical GCAs were driven at a frequency of 10 Hz, and the resulting shuttle displacement was recorded. Positions of points of interest were sampled for each device: the end of the gear shift cantilever, the shuttle, the tips of the forward and reverse pawls, the junction of the forward/reverse pawls, and the junction of spine deflection with the cantilever. See Fig. 4.16.

### 4.6.3 Single Stroke Analysis

These experiments were derived in the same way as in Sec. 4.5. However, while the Video Averaged Analysis used an average over numerous actuation cycles, the single stroke analysis used a hand tuned approach to verify the possibility of reaching higher gearing ratios by careful selection and trial and error. Here the same process was followed as above but instead of observing video of many actuation cycles, the actuation was limited to one closure to observe the static holding and range of the actuation cycle. Fig. 4.17 shows the results of this approach. A higher range of shuttle distances and achievable natural gears was observed.

Measurements of the pawl deflection angle ($\gamma$) are used as a measure of responsive compliance pre-actuation and post-actuation, shown in Fig. 4.18. Fig. 4.18 offers experimental analysis of the pawl gear change mechanism and its effect on the pawl compliance during the GCA actuation phase. Here, the analysis shows the deflection in the pawl both before (open) and after (closed) actuation and its relation to the shuttle motion ($\delta x$) output.

## 4.7 Conclusions

The implementation of the $\mu\Delta$ motors imparts three benefits to the overall motor performance.

1. **Gear Selection:** The compliant nature of the structure allows for selection of a range of gearing options that allow for forward and reverse transmission of force as well as a range of options for output displacement and force.

2. **Increase in $F_{out}$ and $ROM$:** Alternative configurations allow for higher force output and, for some, higher output ROM.

3. **Increase of work done to the shuttle:** Decrease in the effective distance between pawl and shuttle, thereby increasing the distance over which the pawl is in contact with the shuttle.

This work demonstrates the capabilities for an analog microscale transmission motor with the compliant beam-bending design. It presents a near-no-load condition for a mechanism to shift between geared positions for varied force and distance output. The output displacement of the shuttle is nearly three times that of the GCA travel and more than twice that of the original Penskiy motors, indicating that the overall gear shift mechanism has a high effective performance in the single-stroke case and the continuous operation case, as depicted in Fig. 4.19.

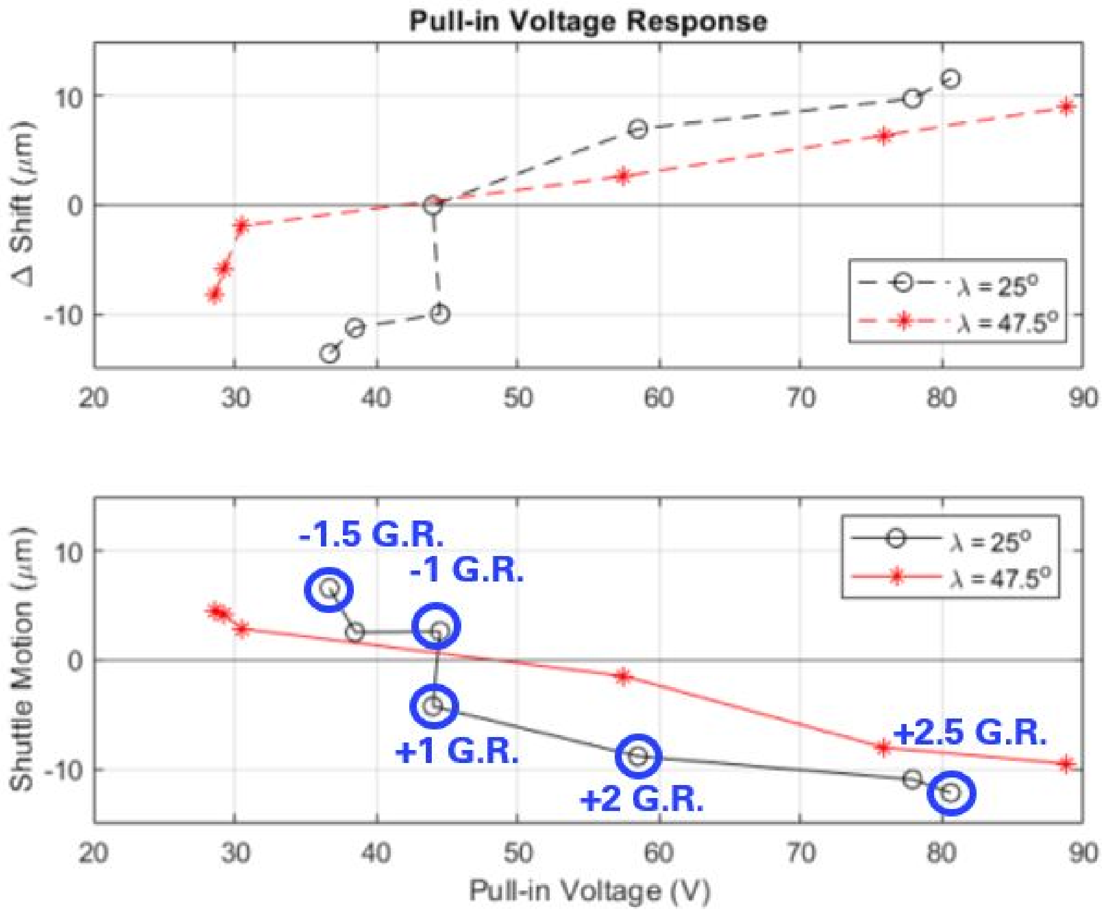


Figure 4.17: Plot of single-stroke data of (Top) gear shift position ($\Delta$) vs pull-in voltage ($V_{PI}$) and (Bottom) shuttle motion ($dx$) vs pull in voltage ($V_{PI}$) for the $\lambda = 47.5^o$ and $\lambda = 25^o$ devices. The trend for change in pull in voltage is observed to be influenced by the gear shifting motion. As the $\Delta$ increases, the compliant beam bending shifts the GCA fingers more in the reverse direction and opens them more in the forward direction.

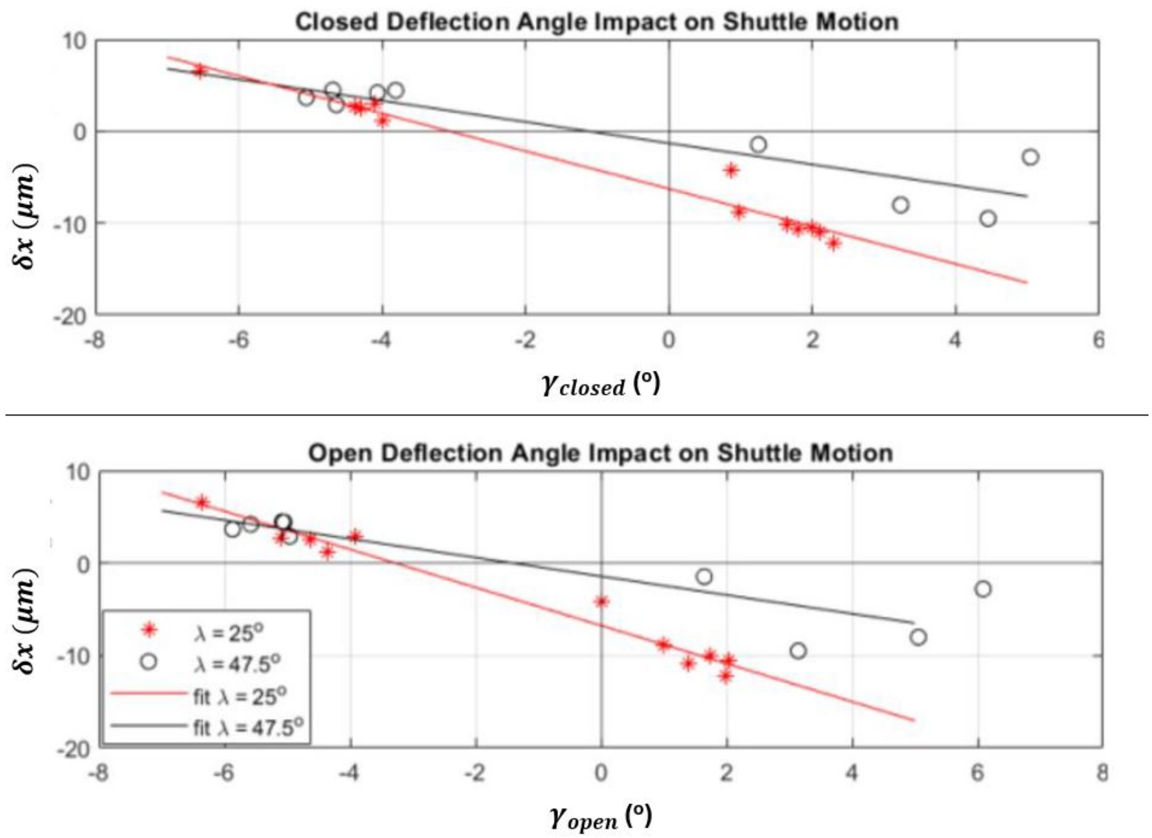


Figure 4.18: Plot of single-stroke experimental data of shuttle motion vs (Top) open and (Bottom) closed deflection angle, $\gamma$. The plots show the shift in $\delta x$ from the open to closed position of the GCA fingers owed to the bending in the compliant beams, showing the $\lambda = 25^o$ and $\lambda = 47.5^o$ configurations.

Fig. 4.20 shows the placement and relative sizes of each level of the spacecraft with scale bars for reference.

Future work will encompass dynamic analysis of the analog $\mu\Delta$-motors, a recently designed digital $\mu\Delta$-motor, and design which mixes elements of the two, termed the Digi-log $\mu\Delta$-motor. This work will also encompass microrobot integration and overall mechanical performance in an application specific goal-case.

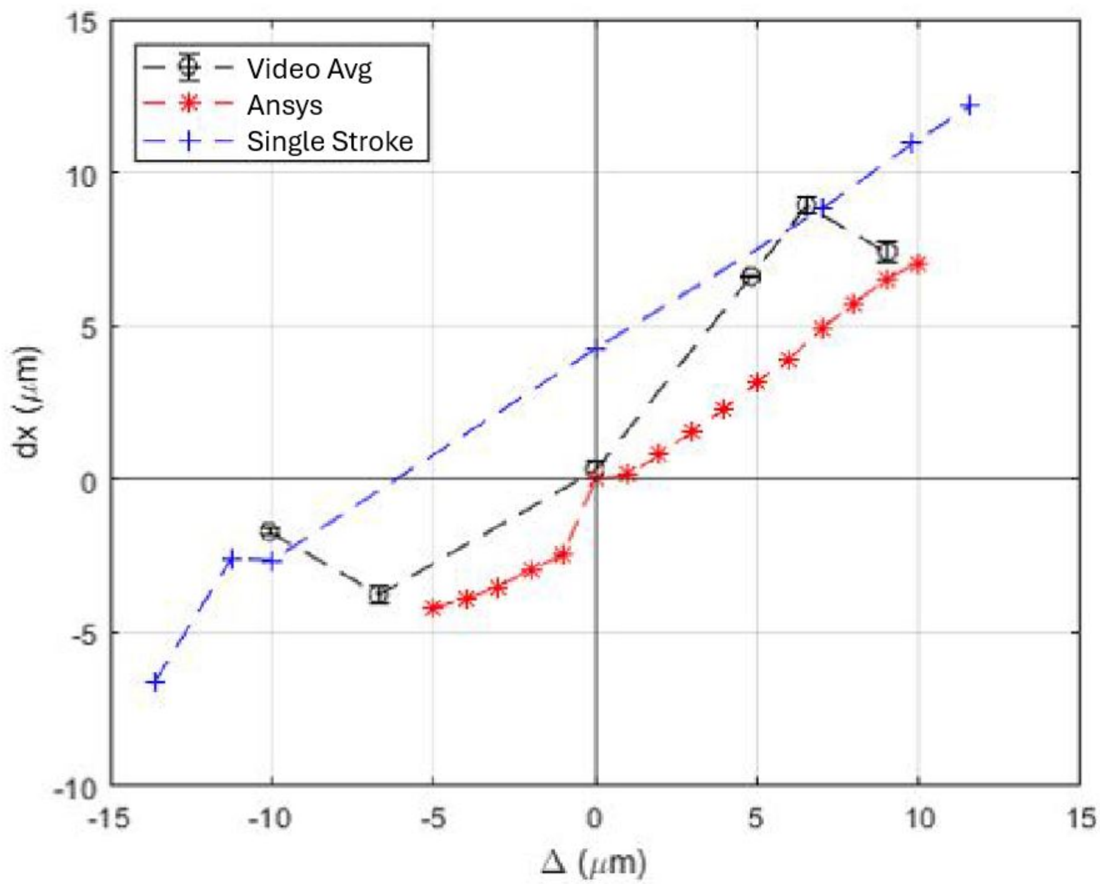


Figure 4.19: Combined data for ANSYS simulation, Video Averaged, and Single-Stroke Analyses.

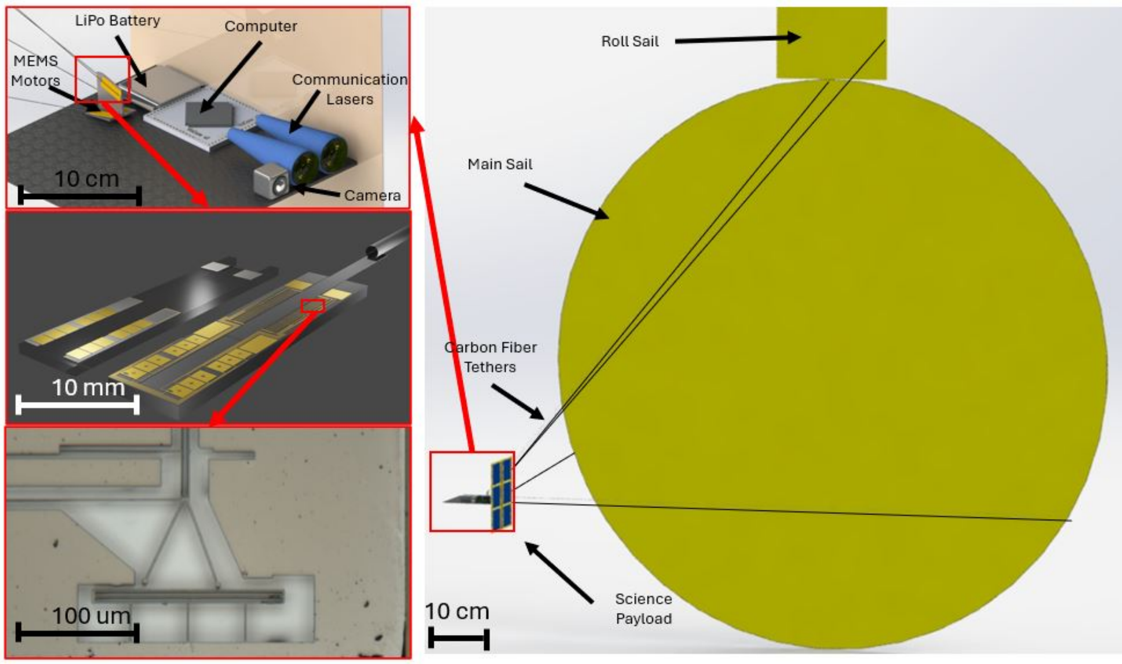


Figure 4.20: Diagram with optical images. Right) BLISS Solidworks 3D CAD showing relative size of modules with main body identified for inset and scale bar showing approximate 10$cm$ size on payload. Left Top) BLISS Main Body zoomed to show relative placements of components with 10$cm$ scale bar for reference (approximate) and MAST (MEMS for Actuation of Solar-sail Tethers) device identified for inset. Left Middle) MAST device Blender 3D CAD (compiled from KLayout 2D CAD layers) zoomed in and MEMS $\mu\Delta$ transmission motor pawl identified for inset with 10$mm$ scale bar for reference (approximate). Left Bottom) Optical image of TGCA on the $\mu\Delta$ motor zoomed in for reference with scale bar of 100$\mu m$ detailed (approximate).

# Chapter 5

# The Rover: Self-righting Quadrupedal Inchworm Driven Spacewalker (SQuIDS)

## Abstract

Millimeter-scale MEMS walking robots offer a path toward highly compact robotic systems, but previous silicon walker architectures have been limited by actuator count, assembly complexity, leg compliance, insufficient robustness, and the absence of recovery mechanisms after overturning. This chapter presents the design evolution of the Self-righting Quadrupedal Inchworm Driven Spacewalker (SQuIDS), a MEMS-based walker architecture developed to extend the functionality of prior Pister-group walking silicon robots while reducing mechanical and electrical complexity. The work is motivated by the broader design space of DARPA SHRIMP-scale microrobotics, where useful locomotion requires tight coupling between actuator force, linkage geometry, structural stiffness, ground contact, assembly strategy, and eventual autonomous recovery.

Several design paths are investigated. A cover-chip architecture is introduced to improve structural alignment and post-assembly electrical access. A dual three-bar linkage approach is then developed to reduce the number of motors required per leg by replacing independently actuated two-degree-of-freedom leg motion with a mechanically prescribed gait. Animal-inspired linkage variants are compared, and a crab-inspired mechanism is modeled using body-frame and world-frame kinematics, no-slip foot contact, frictionless body-floor contact, unilateral distal-joint behavior, and first-order force and torque estimates. Fabrication and testing of this design

demonstrated inchworm motor operation, but also revealed failure modes associated with pin-joint return springs, oxide removal, linkage sticking, and assembly fragility.

A simplified prismatic-leg design is then introduced to improve robustness and reduce linkage complexity. Substrate-layer and device-layer leg variants are evaluated through geometric modeling, contact-based locomotion simulation, analytical beam estimates, finite element analysis, and fabrication observations. These results show that substrate-reinforced legs can improve structural robustness, but also introduce center-of-mass and out-of-plane alignment challenges. Device-layer rectangular legs provide a reduced-complexity alternative while maintaining millimeter-scale compliance comparable to prior distal leg mechanisms.

A self-righting actuator concept is developed as a separate recovery mechanism for overturned microrobots. A planar linkage model is used to evaluate whether a single actuator-driven stroke can generate favorable body rotation under constrained ground contact. The chapter concludes with a reduced-size walker redesign that incorporates lessons from the linkage, prismatic-leg, fabrication, and self-righting studies.

A reduced-size SQuIDS architecture is also proposed to consolidate these design lessons into a more compact integrated platform. This version is intended to fit within an approximately 1 cm×1 cm×2 cm envelope while retaining the core functional requirements of quadrupedal locomotion, MEMS inchworm actuation, multi-chip assembly compatibility, and self-righting capability. By reducing the overall robot size while preserving the ability to recover from an overturned state, the reduced-size design reframes self-righting not as an auxiliary feature, but as a necessary condition for practical autonomy in millimeter- to centimeter-scale walking robots. This design direction therefore serves as the chapter's culminating architecture: a smaller, more integrated MEMS walker that combines locomotion, structural robustness, and failure recovery within a manufacturable silicon microrobotic platform.

## 5.1 Introduction

### 5.1.1 Background

This work builds on the conceptualization of an autonomous walker from Hollar et al. [109] and design choices from Contreras et al. in Transducers 2017 [16]. Further, the work done here was also depicted in the Ph.D. dissertation of Dr. Hani Gomez [7], where Gomez designed and tested the hat chips for the leg chips described in this work. The general use of hat chips in these works serves the use of an electrical and mechanical connection between two opposing leg chips and houses the physical

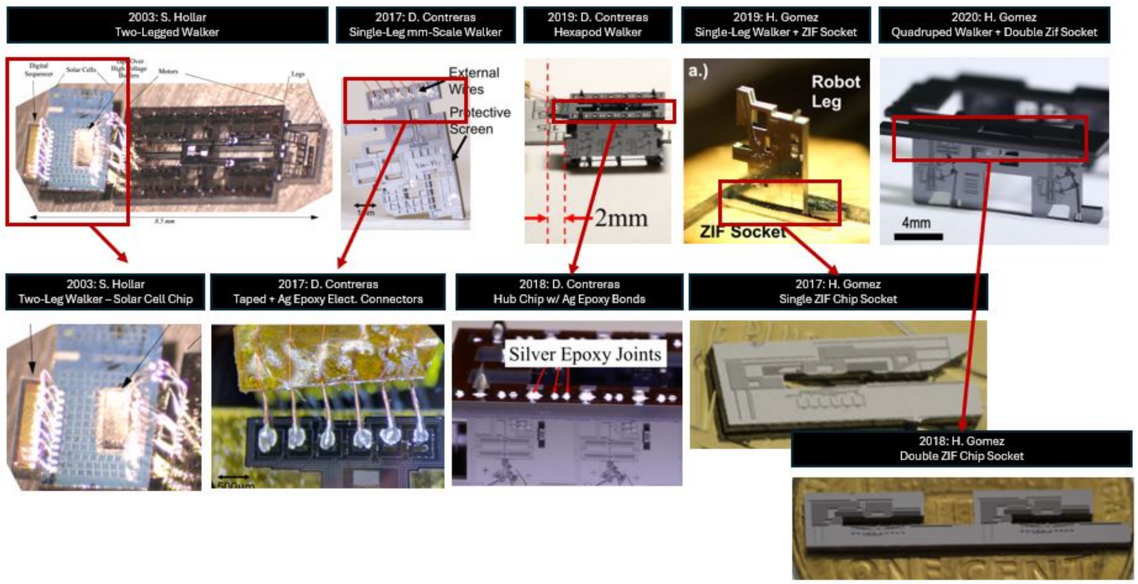


Figure 5.1: This diagram shows the progression of the walker project within the Pister group. The top row shows the walker chips themselves and the progression of the sizing as well as the locomotion method. The bottom row shows how the hat/hub chip itself has progressed. To the knowledge of the author, no previous work within the Pister group addressed the self-righting problem or attempted a similar concept.

computational and power supply units. The work builds on a fabrication process as reported by Teal et al. in Transducers 2021 [92]. The ZIF socket design and its performance analysis were detailed by Gomez et al. in MARSS 2017 [115].

Fig. 5.1 shows the progression of the walker project on which this work is based. Starting from the top-left, Hollar et al. showed the autonomous walking of a two-legged solar-powered microrobot 8.5 *mm* on a side [109]. This work demonstrated a sophisticated approach through the use of onboard power and control. However, this was accomplished with a fairly large solar cell array with wire-bonded electrical connections being dragged behind the walker itself. The legs in this first iteration were rigid folded beams that moved end-over-end in an almost army-crawl fashion.

In 2017, Contreras et al. demonstrated a tethered walker measuring 9.6 mm wide, 7 mm tall, and 13 mm long. This design extended Hollar's work by increasing the available degrees of freedom through separate motors for lifting and forward motion in a single-leg approach, while reducing the size of the robot [16]. In 2019, Contreras et al. combined these two-motor single legs to demonstrate hexapod locomotion with a wired component to the hub chip affixed by silver epoxy bonds for electrical and mechanical connection [4, 116]. The clear advantage was that the majority of the robot was no longer in contact with the walking surface.

Gomez et al. improved on the 2017 Contreras work by incorporating a socket that required negligible or nearly zero insertion force while maintaining high holding strength, introducing the zero insertion force (ZIF) chip [115]. This work allowed for electrical and mechanical connectivity and stability from orthogonal planes, reducing the reliance on wire-bonding and silver epoxy. Gomez et al. continued to improve on this method, increasing to a double ZIF chip configuration and a quadrupedal walker design, keeping the same two-motor per leg higher DOF approach [7, 111]. See Fig. 5.2 for the 2D CAD of these prior works and Table 5.1 for the actuation envelope as determined from the 2D CAD.

Table 5.1: Representative geometric parameters for the prior work (Contreras and Gomez) linkage-based leg mechanism.

| **Parameter** | **Length (mm)** | **Width (mm)** |
|---|---|---|
| Distal linkage/end effector | 3.000 | 0.120 |
| Anchor linkage | 0.995 | 0.062 |
| Vertical input linkage/shuttle | 1.380 | 0.032 |
| Vertical medial linkage | 0.496 | 0.062 |
| Horizontal input linkage/shuttle | 1.280 | 0.032 |
| Horizontal medial linkage | 1.250 | 0.062 |
| Vertical input stroke distance | 0.500 | -- |
| Horizontal input stroke distance | 0.320 | -- |
| Maximum distal-tip displacement in $-y$ direction | 0.720 | -- |
| Maximum distal-tip displacement in $-x$ direction | 1.138 | -- |

Gomez later conceptualized the hat chip/ZIF chip combination for her dissertation. This work was subsequently extended in the present dissertation.

### 5.1.2 DARPA SHRIMP as a Motivating Framework for MEMS Microrobotics

As stated above, this work builds on prior works from the Pister group.

However, a broader programmatic motivation for this work is reflected in DARPA's SHort-Range Independent Microrobotic Platforms (SHRIMP) program, which was launched to advance micro-to-milli robotic systems capable of short-range independent operation in constrained, hazardous, or disaster-response environments. DARPA framed the central challenge not merely as miniaturizing existing robots, but as devel-

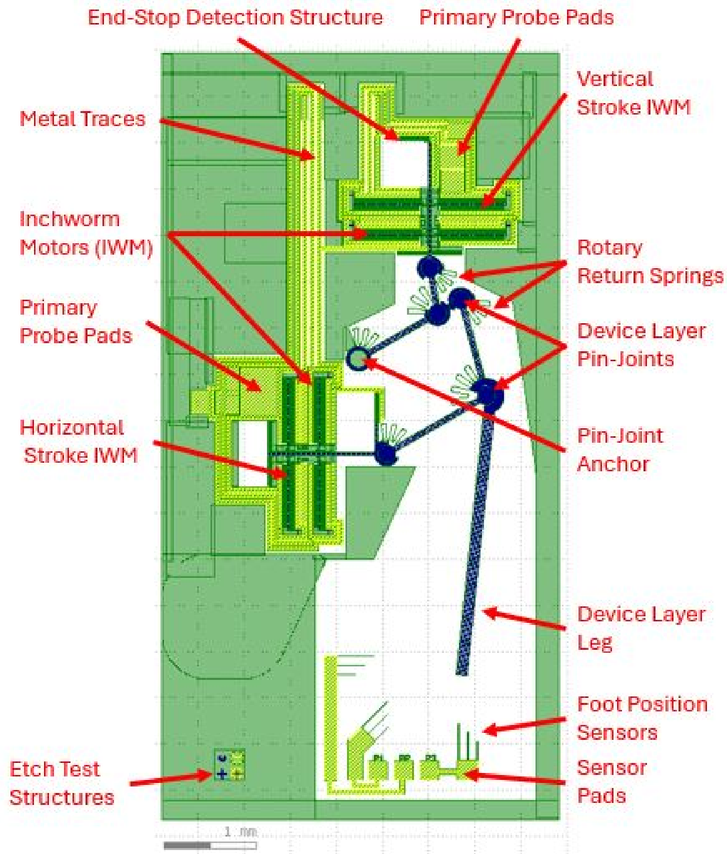


Figure 5.2: This diagram shows the 2D CAD of the prior design from Contreras et al. and Gomez et al., where the leg is controlled by two independent motors [7,16].

oping the underlying actuator, power, control, and mechanical subsystems required for useful robotic function under extreme size, weight, and power (SWaP) constraints. In particular, the program emphasized actuator force generation, efficiency, strength-to-weight ratio, work density, compact power conversion, and integrated mobility as enabling requirements for autonomous microrobotic platforms [117].

Although the microrobotic platforms developed in this dissertation are not intended to directly reproduce the SHRIMP program architecture, SHRIMP provides an important conceptual benchmark for the type of system-level capability that motivates this research. The program highlights a recurring limitation in millimeter- and centimeter-scale robotics: locomotion mechanisms, actuator technologies, onboard power, and structural transmission elements cannot be treated as independent design problems. At these scales, actuator displacement, linkage stiffness, mechanical


Figure 5.3: Diagram depicting the different event goals of the DARPA SHRIMP program. The long-term objective is to develop a microrobot capable of completing all of the listed events; demonstrating completion of one event would also satisfy a meaningful program objective.

amplification, ground interaction, and available electrical drive energy become tightly coupled. As a result, seemingly local design choices, such as leg morphology, joint compliance, shuttle stroke, or linkage geometry, directly affect the attainable gait, payload capability, robustness, and eventual autonomy of the robot.

This dissertation adopts a more focused MEMS implementation of that broader vision. Rather than attempting to realize a complete untethered robotic platform at the outset, the work emphasizes the development of manufacturable microfabricated locomotion mechanisms, mechanically robust linkage architectures, and actuator-compatible transmission schemes. In this sense, SHRIMP serves as a useful external reference point: it identifies the long-term target of independent, multifunctional microrobots, while the present work addresses several of the enabling mechanical and process-level questions that must be solved before such platforms can be reliably implemented in a MEMS-based system. The resulting research therefore contributes to the same broader design space by investigating how planar microfabricated structures can produce useful legged motion, how linkage geometry can be simplified without eliminating functional displacement, and how actuator-limited motion can be converted into repeatable locomotion-relevant trajectories. See Fig. 5.3 for a depiction of the applicable event goals for the DARPA SHRIMP Challenge and Table 5.2 for a description of the categories and their corresponding performance targets.

Table 5.2: Named DARPA SHRIMP Olympic-style event goals and associated performance emphasis. As defined by the DARPA SHRIMP documentation, the events were separated into two categories: "Actuator / Power System" (A/PS) and "Complete Microrobot" (CM).

| **Category** | **Named Event** | **Primary Performance Goal** | **Reported Target** |
|---|---|---|---|
| A/PS | High Jump | Demonstrate vertical impulse generation, actuator work density, and survivability after ballistic motion. | $>$ 5 cm vertical jump |
| A/PS | Long Jump | Demonstrate horizontal impulse generation, launch efficiency, and landing robustness. | $>$ 5 cm horizontal jump |
| A/PS | Weightlifting | Quantify lift capacity, output force, and useful mechanical work under severe mass and power constraints. | $>$ 10 g lifted mass |
| A/PS | Shotput | Evaluate the ability of the actuator or power system to transfer energy into an external payload. | $>$ 10 cm for a 1 g payload |
| A/PS | Tug of War | Measure blocking force and sustained force output against an external load. | $>$ 25 mN blocking force |
| CM | Rock Piling | Demonstrate object interaction, transport, lifting, and stacking as an integrated manipulation task. | Stack 0.5--2.0 g weights in at least two layers |
| CM | Steeplechase | Demonstrate obstacle traversal, locomotion endurance, and autonomous mobility over a fixed course. | Two obstacles over 5 m |
| CM | Biathlon | Demonstrate waypoint navigation, mobility, and guidance using external or environmental beacons. | Two beacons over 5 m |
| CM | Vertical Ascent | Demonstrate climbing or inclined-surface locomotion under challenging surface-orientation conditions. | 10 m at 10°; 1 m at 80° |

### 5.1.3 Problem Statement

The initial goals of this work were to extend the functionality of existing systems while reducing footprint, power requirements, and mass, with the broader aim of supporting DARPA SHRIMP-like microrobotic challenges.

As observed in prior systems [4, 7], the use of thinner leg models produced unexpected bending under load during actuation. These observations identified a clear opportunity to improve leg robustness.

It was also observed that prior systems used two independently controlled inchworm motors to manipulate a single leg but did not significantly change the gait or pattern of actuation in a way that clearly showed this two-DOF approach was beneficial. To extend the functionality while reducing the mass, it was surmised that there would need to be a reduction in the input signals and therefore a reduction in the number of motors controlling specific aspects of the leg motion. From here, the questions of the usefulness of both independent motion and predetermined gait became apparent. It was surmised that both questions could be answered with fewer than two motors per leg, thereby reducing a bottleneck in complexity, footprint, power input, and mass observed in prior systems.

Prior systems also showed, as noted in Table 5.1, that the overall gait displacement was not significantly larger than the motor stroke, indicating that direct drive might have sufficed without a loss of functionality.

Another goal was to increase walker functionality so that the robot could potentially complete an obstacle course or traverse walking surfaces that were less than ideally flat. In service of that goal, larger motors were incorporated to increase force output.

As motor size increases, power generation becomes more important, and reducing reliance on batteries becomes a design objective. Therefore, a power-recovery system was considered beneficial, motivating the use of the Zappy solar cells [118].

Later versions make use of the Zappy 2 as described in Moreno et al. [119] as an optically powered photovoltaic and high-voltage buffer chip that provides low-voltage supply rails for control electronics and a high-voltage rail for electrostatic MEMS actuator drive, enabling untethered high-voltage actuation in millimeter-scale robotic systems [118]. Moreno *et al.* demonstrated SARA, a $9.5 \times 31.55$ mm$^2$, 285.9 mg solar-powered wireless MEMS gripper, using the $3.26 \times 3.5$ mm$^2$ Zappy2 photovoltaic/high-voltage-buffer chip to generate three voltage domains: $V_{\mathrm{BATPV}} = 1.8$ V, $V_{\mathrm{DDIOPV}} = 3.5$ V, and $V_{\mathrm{DDHPV}} = 119$ V. At 100 mW cm$^{-2}$, these domains produced short-circuit currents of 280 $\mu$A, 16 $\mu$A, and 2.4 $\mu$A, respectively, while 200 mW cm$^{-2}$ irradiation provided 560 $\mu$A at 1.86 V for the processor/radio supply [119].

### 5.1.4 Project Goals

From these observations, the design objectives were set:

- Decrease the number of motors used for each leg.
- Increase the structural integrity of the legs.
- Integrate a spring-based energy storage or recovery system.
- Integrate a self-righting mechanism.
- Decrease the overall size of the walker.
- Increase the force output of the motors.

While other objectives were also relevant, these objectives were used to define the design paths that became the basis for this work. The work was developed through several design versions, each addressing the design objectives in a specific way.

The Cover Chip (v0) protects the critical MEMS components. These cover chips were designed for use with any of the proposed leg chips to reduce the likelihood that dust or external obstacles would interfere with locomotion by damaging the MEMS components.

The Dual Linkage Approach (v1) is a leg chip intended to provide a predetermined locomotion gait. The chip is designed to operate from a single motor input attached to two linkage systems, one for each leg on a side.

The Prismatic Linkage Approach (v2) is a leg chip intended to provide a one-DOF mechanism for locomotion. In this approach, each individual leg is operated by a single motor with no intermediate linkages.

The Self-Righting Approach (v3) is a separate chip intended as an add-on recovery mechanism for the walker. It uses a simple dual-linkage approach attached to a single motor and is similar in concept to the v1 leg chip.

The Small Approach (v4) is a redesign that incorporates lessons from the preceding approaches. It integrates a redesigned hat chip, self-righting chip, and leg chip.

All approaches incorporate the larger 15 mN force inchworm motors derived from Schindler's work [10].

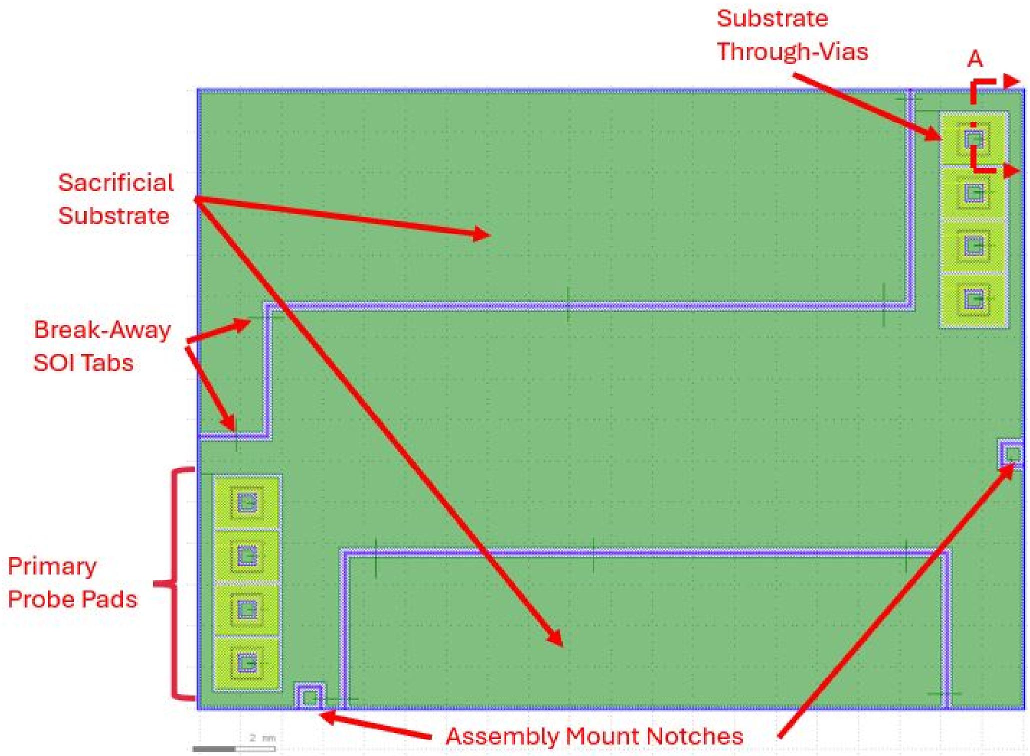


Figure 5.4: Depicted here is the 2D CAD of the Prismatic Linkage Approach cover chip. The color scheme here is the same as in the prior 2D CAD layouts. This cover chip is intended to provide through-chip electrical connection to allow for testing after assembly and prior to affixing the hat-chip by connecting to the Primary Probe Pads.

## 5.2 Cover Chip (v0)

### 5.2.1 Silicon Cover Chip (v0.1)

For each leg chip, a cover chip was produced to improve structural integrity and provide a method for aligning the legs during locomotion. See Fig. 5.4 for the 2D CAD of the cover chip. See Fig. 5.5a for an unassembled cutaway of the depicted portion of the 2D CAD. See Fig. 5.5b for the assembled depiction of the cover chip and the leg chip from the same cutaway portion of the chips. These cover chips were used for all of the leg chips and served as a standardizing feature for primary probe pad placement.

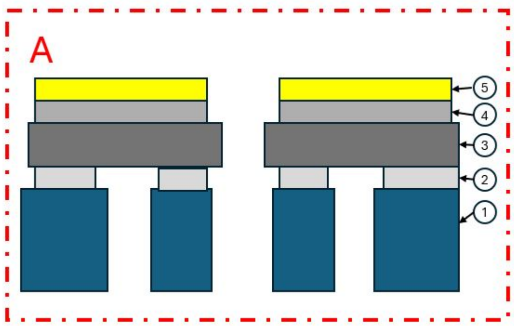


(a) Depicted here is a cutaway view of the cover chip. (1) Substrate layer: 550 $\mu$m thick, minimum feature size = 40 $\mu m$, DRIE through-layer etch; (2) Silicon Oxide layer: 2 $\mu$m thick, anhydrous Hydrogen Fluoride (HF) vapor-phase timed etch expected at 4 $\mu$m; (3) Device layer: 40 $\mu$m thick, minimum feature size 2 $\mu$m, DRIE through-layer etch; (4) Chromium layer: 0.4 $\mu$m thick, E-Beam Evaporation, minimum design line width 5 $\mu$m, offset of at least 5 $\mu$m from device layer etch edge, wet-etch lift-off process, adhesion layer prior to Gold; (5) Gold layer: 0.2 $\mu$m thick, E-Beam Evaporation, minimum feature thickness 5 $\mu$m, offset of at least 5 $\mu$m from device layer etch edge, wet-etch lift-off process, conductive layer.

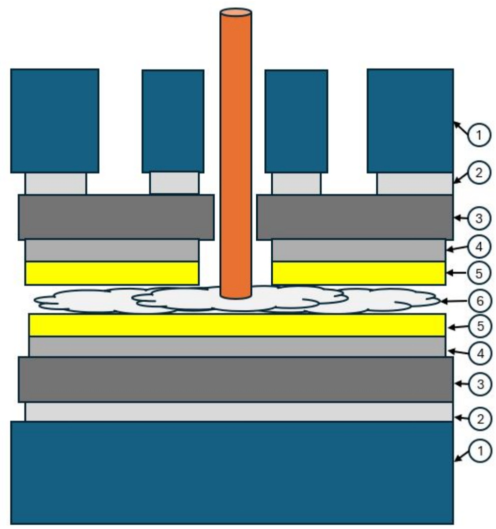


(b) Depicted here is a cutaway view of the cover chip as assembled. This diagram depicts a cutaway of both the cover chip and the leg chip showing bonding with Silver Epoxy. (1) Substrate layer, (2) Silicon Oxide layer, (3) Device layer, (4) Chromium layer, (5) Gold layer, and (6) Silver Epoxy. Additionally, the cylinder inserted represents the wire inserted for electrical testing. In the leg chip, at the Primary Probe Pads, the stack is much the same as in the corresponding cover chip with (5-1) layers. The main purpose of this diagram is to depict the method for testing after assembly should the hat chip connections not be viable.

Figure 5.5: Diagrams showing (Left) the cover chip stack cutaway and (Right) the assembled cover chip stack cutaway with the leg chip beneath it and a wire inserted.

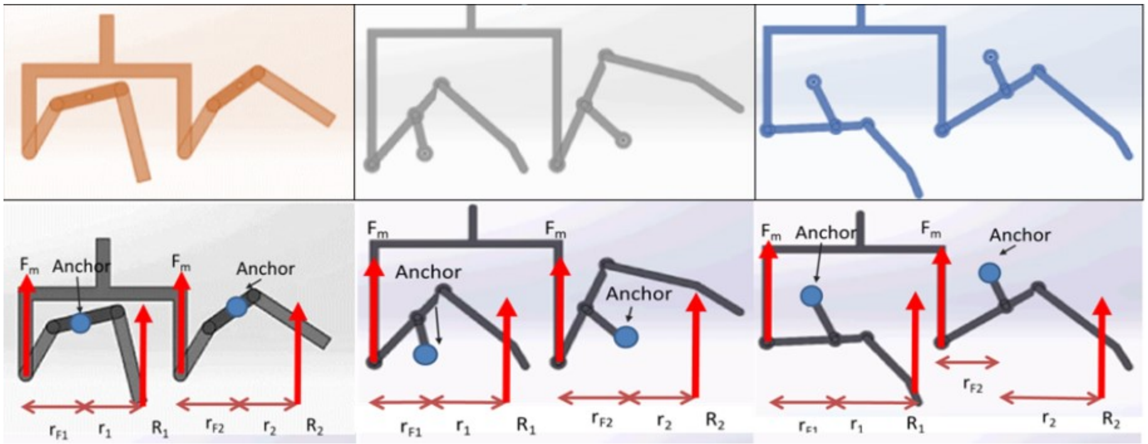


Figure 5.6: Array of SOLIDWORKS linkages depicting the relative shape and actuation flow at three stages of actuation: (Top Row) as fully retracted and (Bottom Row) showing the relative distances of each point of contact with the walking surface and the leg where it would touch. The three columns represent different linkage configurations named for their resemblances in gait or morphology to the representative names: (Left) crab, (Middle) mantis, (Right) flea. Here, $F_m$ is the input force from the motor transferred through the initial dual linkage; $r_{F1}$ is the projected distance from the vertical force vector and the anchor point of the first leg; and $r_1$ is the projected distance from the anchor to the vertical vector of the force on the walking surface $R_1$ for the first leg. Similarly, the diagram depicts the same vectors and distances for the second leg, where the distance is specific to the position that the linkage is in when it touches the walking surface during the driving stroke of the motor.

## 5.3 Dual Linkage-Based Locomotion Approach (v1)

The first-generation linkage-based designs were developed as extensions of the leg-linkage architecture introduced by Contreras et al. [16]. In addition to the previously stated design objectives, another objective was to reduce actuation and routing complexity by decreasing the number of independent input signals and motors required per leg. In the prior walker architecture, each leg required two independently driven motors: one motor generated the vertical stroke required for ground engagement and lift-off, while the second motor generated the horizontal stroke required for forward translation.

In contrast, the linkage-based variants described here were designed to approximate or expand the same functional gait envelope while using a single motor to drive a coupled pair of legs. This architecture therefore trades independent leg control for a mechanically prescribed gait trajectory, with the intended benefit of reducing motor count, electrical interconnect complexity, and signal-routing burden.

### 5.3.1 Animal-Inspired Linkage Variants

Three initial linkage geometries were developed to explore distinct design spaces and their trade-offs in quasi-static stability, stride length, foot trajectory, and gait phasing, as shown in Fig. 5.6. Each design used the same general actuation principle, but differed in linkage geometry and the resulting foot path.

- **Crab-inspired linkage (v1.1):** This design prioritized static stability by increasing the fraction of the gait cycle during which the two legs on each chip remained in contact with the walking surface. The resulting foot trajectory was intended to maintain a larger effective support polygon and reduce the likelihood of body pitching or rolling during the stance phase. This geometry was therefore best suited for stable, conservative locomotion where continuous ground contact was more important than maximizing stride length.

- **Mantis-inspired linkage (v1.2):** This design prioritized increased stride length and more clearly separated gait phases. The prescribed leg trajectory was designed to produce four distinguishable phases: (1) a relatively slow lifting phase, (2) a faster forward-swing phase, (3) a relatively slow lowering phase, and (4) a faster retraction phase. This gait structure was intended to improve forward displacement per cycle while preserving controlled ground engagement and disengagement. Compared with the crab-inspired design, the mantis-inspired geometry introduced a larger vertical excursion and a more aggressive forward stroke.

- **Flea-inspired linkage (v1.3):** This design emphasized maximizing forward displacement by producing an elongated post-lift trajectory. The foot path was designed to generate greater forward motion after the raising phase than the other two variants. Its vertical step height was lower than that of the mantis-inspired linkage, but higher than that of the crab-inspired linkage, placing it between the two designs in terms of obstacle-clearance capability. This geometry therefore represented a compromise between stride extension and vertical excursion, with an emphasis on forward progression rather than stance stability. While the previous two were named for their relative locomotion style, this design was named for the leg position image resembling a flea in flight after jumping.

The three animal-inspired linkage designs were evaluated as alternative mechanical gait generators. The crab-inspired design emphasized stability and extended ground contact, the mantis-inspired design emphasized stride length and discrete gait phasing, and the flea-inspired design emphasized forward displacement with an intermediate step height. Together, these variants provided an initial design space for comparing how linkage geometry influences foot trajectory, substrate contact timing, stride length, and locomotion stability.

For clarity, it should be noted that each of the linkage variants was selected based on their ability to maintain a holding force at any position throughout the gait such that $1 < (F_{1||} + F_{2||})/(R_{1||} + R_{2||})$, $R$ represents the weight of the robot. This relation shows that the cumulative sum of the force transferred to the linkage is greater than the cumulative sum of the force parallel to the ground transferred to the linkage from the walking surface.

At this stage of the design process, the focus was on maintaining upright locomotion and stability rather than designing directly for self-righting. Additionally, at this stage of the design the walker was intended to have a hat chip connected to the two leg chips at approximately 70--80% of the body height above the bottom of the robot. This high center of mass was the main consideration for stability being a higher concern. As such, the crab-inspired designs were favored for progression to the next stage of the design pathway.

### 5.3.2 Dual 3-Bar Linkage-Based Crab Inspired Approach (v1.1)

The crab-inspired approach is constructed from a single double-bracket structure that doubles as a shuttle and linkage and is attached to the two individual leg linkages on a single leg chip. The two leg linkages are offset.

The linkage lengths and orientations are annotated in Table 5.3, Table 5.4, and Fig. 5.8. The gait of the crab-inspired linkage design is shown in Fig. 5.7.

Each leg linkage is a combination of three device-layer pin-joints, three device-layer linkages (one of which acts as an end-effector), and a single anchor pin-joint that is adjoined to the substrate by the 2 $\mu$m oxide layer and sits between pin-joint two and three. These two leg linkage systems engage the walking surface through actuation at different times throughout the stroke of the singular motor. For this work, one stroke is defined as a full extension cycle of the inchworm-motor shuttle. See Fig. 5.20 for the design file schematic.

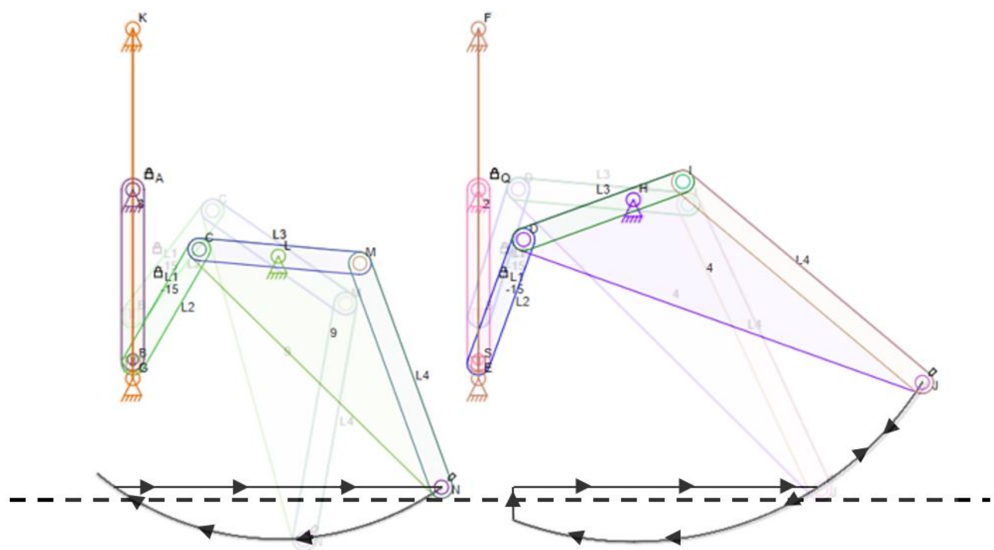

Figure 5.7: Screenshot from the Linkage 2.0 CAD software detailing the gait of the crab-inspired linkage approach, where dimensions from Table 5.3 and Table 5.4 are integrated.

Table 5.3: Linkage lengths, as designed, for the left and right leg mechanisms. Link lengths are reported in microns.

| **Linkage Desc.** | **Left Symbol** | **Len.** ($\mu$m) | **Right Symbol** | **Len.** ($\mu$m) |
|---|---|---|---|---|
| Dual connector | $L_{O,L}$ | 3300 | $L_{O,R}$ | 3300 |
| Vertical ground | $L_{1,L}$ | 3700 | $L_{1,R}$ | 3700 |
| Lower | $L_{2,L}$ | 2500 | $L_{2,R}$ | 2500 |
| Upper coupler | $L_{3,L}$ | 3000 | $L_{3,R}$ | 3200 |
| Distal leg | $L_{4,L}$ | 4500 | $L_{4,R}$ | 5900 |
| Anchor Dimension | $L_{A,L}$ | 1500 | $L_{A,R}$ | 2200 |
| Central input | $L$ | 9800 | --- | --- |

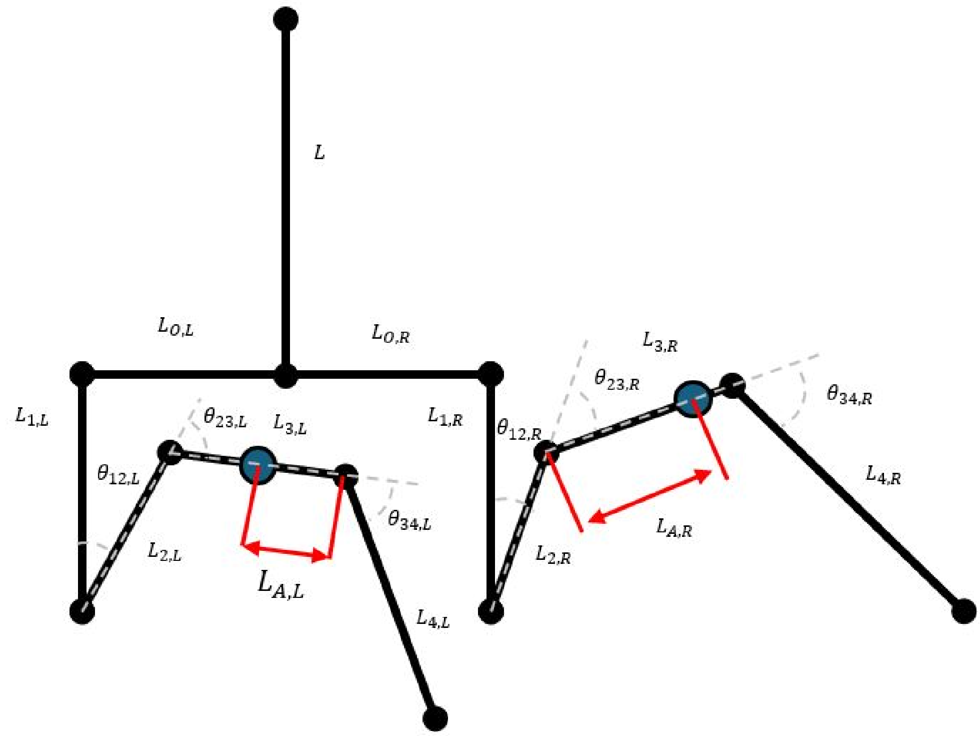


Figure 5.8: Diagram of the linkages for the crab-inspired design. All linkages are device layer with 8 $\mu$m square etch holes and 14 $\mu$m spacing, center-to-center. The $L_{O,L}$ and $L_{O,R}$ linkages are 525 $\mu$m wide, all other linkages are 40 $\mu$m depth, 300 $\mu$m width, and have had the 2 $\mu$m oxide layer etched away from beneath them.

Table 5.4: Interior linkage angles, as designed, for the left and right leg mechanisms. Angles are reported in degrees.

| **Angle Definition** | **Left Symbol** | **Angle** (°) | **Right Symbol** | **Angle** (°) |
|---|---|---|---|---|
| $\angle(L_1, L_2)$ | $\theta_{12,L}$ | 30 | $\theta_{12,R}$ | 20 |
| $\angle(L_2, L_3)$ | $\theta_{23,L}$ | 65 | $\theta_{23,R}$ | 50 |
| $\angle(L_3, L_4)$ | $\theta_{34,L}$ | 65 | $\theta_{34,R}$ | 60 |
| $\angle(L_O, L_1)$ | $\theta_{O1,L}$ | 90 | $\theta_{O1,R}$ | 90 |
| $\angle(L, L_O)$ | $\theta_{O,L}$ | 90 | $\theta_{O,R}$ | 90 |

#### 5.3.2.1 Planar Linkage Contact Model and Body-Motion Response

The crab-inspired linkage was modeled as a planar mechanism in which the internal kinematic constraints are imposed in the robot body frame. In this formulation, the shuttle, central input linkage, dual connector linkages, and vertical ground linkages are constrained to translate along the body-frame vertical direction, while the anchored and distal links rotate according to the prescribed linkage geometry. The body-frame mechanism solution is then mapped into the world frame using a rigid-body transformation that includes both translation and rotation of the robot body. This separation between the body frame and world frame is necessary because a linkage member that is constrained to translate vertically relative to the robot body is not constrained to translate vertically relative to the walking surface once the robot body rotates.

The planar body-to-world transformation is defined as

$$\mathbf{p}^W = \mathbf{r}_B^W + \mathbf{R}(\theta_B)\mathbf{p}^B, \tag{5.1}$$

where $\mathbf{p}^B$ is a point expressed in the robot body frame, $\mathbf{p}^W$ is the corresponding world-frame point, $\mathbf{r}_B^W = [x_B, y_B]^T$ is the world-frame translation of the robot body, and $\theta_B$ is the robot-body rotation relative to the world frame. The planar rotation matrix is

$$\mathbf{R}(\theta_B) = \begin{matrix} \cos\theta_B & -\sin\theta_B \\ \sin\theta_B & \cos\theta_B \end{matrix} . \tag{5.2}$$

This transformation is applied to all body-fixed points, including the robot-body outline, the center of mass, the fixed anchors, and the linkage joints.

The robot body was represented as a rectangular prism with a horizontal length of 20 mm, a vertical height of 22 mm, and a thickness of 0.592 mm. The center of mass was placed at the geometric center of the robot body, corresponding to the first-order assumption of a uniform body mass distribution. If the body rectangle is defined by horizontal bounds $x_{\min}$, $x_{\max}$ and vertical bounds $y_{\min}$, $y_{\max}$, then the body-frame center of mass is

$$\mathbf{r}_{\mathrm{COM}}^B = \begin{bmatrix} \dfrac{x_{\min} + x_{\max}}{2} \\ \dfrac{y_{\min} + y_{\max}}{2} \end{bmatrix}. \tag{5.3}$$

The world-frame center of mass is therefore

$$\mathbf{r}_{\mathrm{COM}}^W = \mathbf{r}_B^W + \mathbf{R}(\theta_B)\mathbf{r}_{\mathrm{COM}}^B. \tag{5.4}$$

A rigid walking surface was placed below the initial distal endpoint of the left leg. The walking surface is represented by the horizontal constraint

$$y = y_{\text{floor}}. \tag{5.5}$$

Contact between the distal end-effectors and the walking surface was modeled using a no-slip stance condition. If foot $s$ is the active stance foot, the no-slip constraint is

$$\mathbf{p}_s^W(q, \theta_B, \mathbf{r}_B^W) = \mathbf{p}_{s,0}^W, \tag{5.6}$$

where $q$ denotes the shuttle stroke and $\mathbf{p}_{s,0}^W$ is the world-frame foot position at the start of the stance interval. This condition is enforced only while the contact remains physically admissible; the foot is allowed to release when the estimated normal force becomes zero and/or negative.

Foot non-penetration is enforced by requiring

$$y_{e,L}^W \geq y_{\text{floor}}, \qquad y_{e,R}^W \geq y_{\text{floor}}, \tag{5.7}$$

where $y_{e,L}^W$ and $y_{e,R}^W$ are the world-frame vertical positions of the left and right distal endpoints. The corresponding foot clearances are

$$c_{e,L} = y_{e,L}^W - y_{\text{floor}}, \qquad c_{e,R} = y_{e,R}^W - y_{\text{floor}}, \tag{5.8}$$

and the residual penetrations are

$$\delta_{e,L} = \max(0, y_{\text{floor}} - y_{e,L}^W), \qquad \delta_{e,R} = \max(0, y_{\text{floor}} - y_{e,R}^W). \tag{5.9}$$

In contrast to the no-slip foot contact, contact between the robot body and the walking surface was modeled as frictionless. For a set of body vertices $\{\mathbf{v}_i^B\}$, the body non-penetration condition is

$$\min_i \;\; y_{v_i}^W \;\; \geq y_{\text{floor}}, \tag{5.10}$$

with body clearance

$$c_B = \min_i \;\; y_{v_i}^W \;\; - y_{\text{floor}}, \tag{5.11}$$

and residual body penetration

$$\delta_B = \max \;\; 0,\, y_{\text{floor}} - \min_i \;\; y_{v_i}^W \quad . \tag{5.12}$$

Because the body-floor contact is frictionless, this condition prevents vertical penetration but does not impose a tangential no-slip constraint on the body.

The joint between $L_3$ and $L_4$ was modeled as a unilateral rotational constraint. Let $\tau_{34}$ denote the moment about the $L_3$-to-$L_4$ joint, with positive moment corresponding to counter-clockwise rotation. The joint behavior was approximated as

$$\tau_{34} > 0 \quad \Rightarrow \quad \text{free rotation}, \tag{5.13}$$

$$\tau_{34} \leq 0 \quad \Rightarrow \quad \phi_4 = \phi_3 + \psi_{34}, \tag{5.14}$$

where $\phi_3$ is the orientation of $L_3$, $\phi_4$ is the orientation of $L_4$, and $\psi_{34}$ is the designed relative angle between $L_3$ and $L_4$. Thus, positive counter-clockwise loading releases the distal link, while zero or negative loading locks $L_4$ at its designed relative angle. In the free state, the distal link was assumed to transmit no moment about the joint, giving

$$(\mathbf{p}_e - \mathbf{p}_{34}) \times \mathbf{F}_e = 0, \tag{5.15}$$

where $\mathbf{p}_{34}$ is the $L_3$-to-$L_4$ joint location, $\mathbf{p}_e$ is the distal endpoint position, and $\mathbf{F}_e$ is the estimated endpoint force. This zero-moment condition prevents the model from transmitting a nonphysical resisting moment through the distal link when the joint is loaded in its release direction.

The approximate foot-force transmission was computed using the numerical end-effector Jacobian. For each distal endpoint, the world-frame Jacobian with respect to shuttle stroke $q$ is

$$\mathbf{J}_e(q) = \frac{\partial \mathbf{p}_e^W}{\partial q} \approx \frac{\Delta \mathbf{p}_e^W}{\Delta q}. \tag{5.16}$$

For a single-input mechanism, virtual work gives

$$F_m \delta q = \mathbf{F}_e^T \delta \mathbf{p}_e = \mathbf{F}_e^T \mathbf{J}_e \delta q, \tag{5.17}$$

so that

$$F_m = \mathbf{J}_e^T \mathbf{F}_e. \tag{5.18}$$

Because this relation is underdetermined for a two-dimensional endpoint force, the minimum-norm force estimate was used:

$$\mathbf{F}_e = \frac{F_m}{\mathbf{J}_e^T \mathbf{J}_e} \mathbf{J}_e. \tag{5.19}$$

This provides a first-order estimate of the force direction and magnitude transmitted to the distal endpoint.

During stance, body rotation is driven by the moment generated by the active ground reaction about the robot-body center of mass. If $\mathbf{F}_{\text{foot}}$ is interpreted as the force applied by the foot to the walking surface, then the corresponding ground reaction applied to the robot is approximated as

$$\mathbf{F}_g = -\mathbf{R}(\theta_B)\mathbf{F}^B_{\text{foot}} + \begin{matrix} 0 \\ W/n_c \end{matrix} , \tag{5.20}$$

where $W = mg$ is the robot weight and $n_c$ is the number of active contacts used in the quasi-static support approximation. The moment contribution from contact $i$ about the center of mass is

$$\tau_i = \;\; \mathbf{p}^W_{c,i} - \mathbf{r}^W_{\text{COM}} \;\; \times \mathbf{F}_{g,i}, \tag{5.21}$$

where the planar cross product denotes the out-of-plane scalar moment,

$$\mathbf{a} \times \mathbf{b} = a_x b_y - a_y b_x. \tag{5.22}$$

The net contact moment is

$$\tau_{\text{contact}} = \sum_{i=1}^{n_c} \tau_i. \tag{5.23}$$

The quasi-static rotational update was modeled using an effective rotational stiffness,

$$k_\theta \left(\theta_B - \theta_{B,\text{ref}}\right) = \tau_{\text{contact}}, \tag{5.24}$$

where $k_\theta$ is an effective rotational stiffness parameter and $\theta_{B,\text{ref}}$ is the previous or reference body angle.

The stance-foot release condition was based on the estimated normal force at the active contact. The stance normal force was approximated as the vertical component of the ground reaction,

$$N_s = \mathbf{e}_y^T \mathbf{F}_{g,s}, \tag{5.25}$$

where $\mathbf{e}_y = [0, 1]^T$. The no-slip condition is maintained only when

$$N_s > 0. \tag{5.26}$$

If $N_s \leq 0$, the contact would require the walking surface to pull on the foot, which is not physically admissible for unilateral contact. The stance foot is therefore released.

Figure 5.9 shows the linkage motion in the robot body frame. This plot verifies the internal mechanism geometry independently from robot-body translation, robot-body rotation, and floor-contact correction. Because this view is body-fixed, the shuttle-guided members retain their prescribed translational constraints.

The physically relevant motion relative to the walking surface is obtained after transforming the body-frame linkage solution into the world frame.

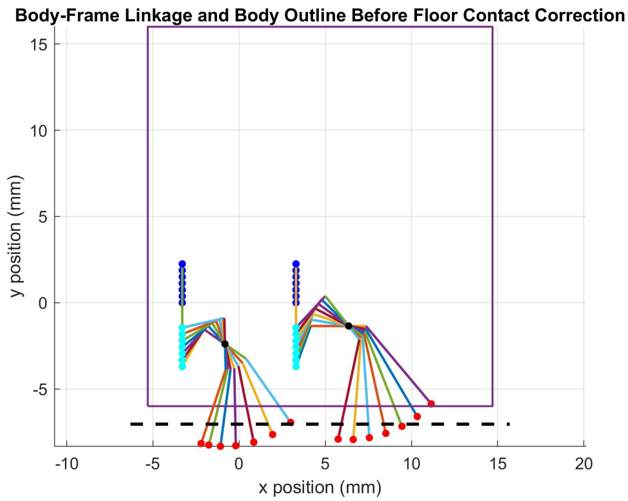


Figure 5.9: Body-frame linkage poses for the crab-inspired mechanism over the prescribed shuttle stroke. The linkage geometry is shown before transformation into the world frame, so the shuttle, input linkage, dual connector linkages, and vertical ground linkages retain their body-frame translational constraints. The rigid walking surface is included as a reference line, but contact correction has not yet been applied in this frame.

Of note, many of the figures show a discontinuity at the approx. 1 $mm$ motor displacement mark which is owed to the contact of the front leg linkage distal end with the walking surface. This is owed to the design goal of maintaining a walking gait that mimics the prior work which showed individually controlled legs. This out-of-phase linkage drive creates a walking pattern that is unique to each leg, emulating the pattern attempted in the prior works.

Figure 5.10 shows the robot body and linkage poses after applying the rigid-body transformation and the contact constraints. In this view, the shuttle-guided members are no longer constrained to move along the global vertical direction; instead, they translate and rotate with the robot body.

Figure 5.11 verifies that the center of mass remains fixed relative to the robot-body outline during the rigid-body transformation. This check is important because an incorrectly placed center of mass can introduce artificial contact moments and anomalous body rotations.

The corresponding rigid-body translation is shown in Figure 5.12. Horizontal displacement occurs when a foot acts as a no-slip stance point and the internal linkage motion moves the body relative to that fixed point. Vertical displacement is

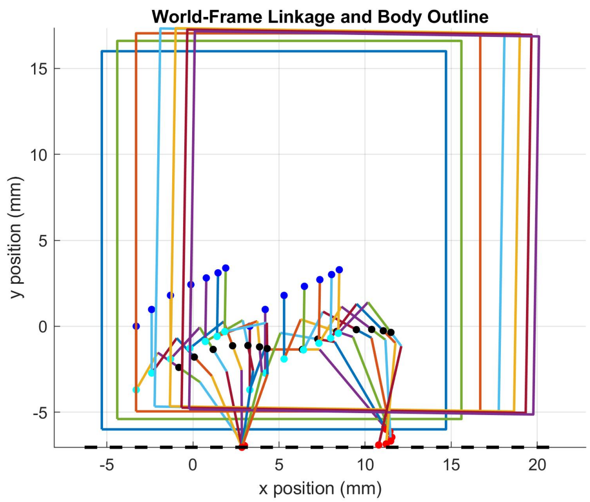


Figure 5.10: World-frame linkage poses and robot-body outline after applying the rigid-body transformation and contact constraints. The body-frame linkage solution is transformed into the world frame using the body translation and rotation generated by contact with the walking surface. The feet maintain no-slip contact only while in compressive contact, while the robot body is prevented from penetrating the walking surface under a frictionless slip condition.

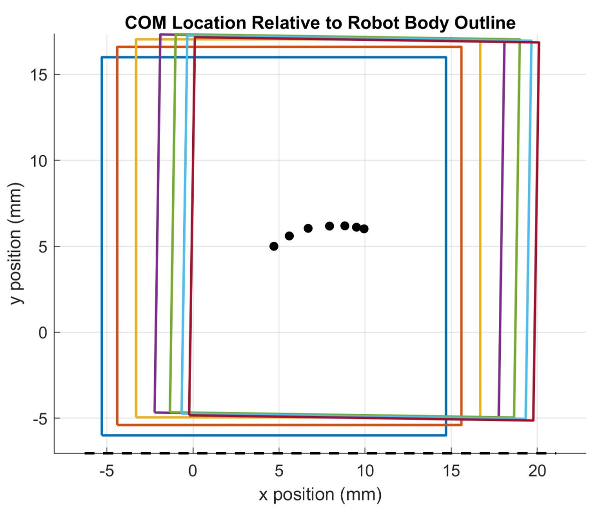


Figure 5.11: Center-of-mass location relative to the robot-body outline during the motor stroke. The center of mass is located at the geometric center of the rectangular robot body, consistent with the assumed uniform body mass distribution.

introduced to satisfy rigid non-penetration of the distal feet and the larger robot-body outline.

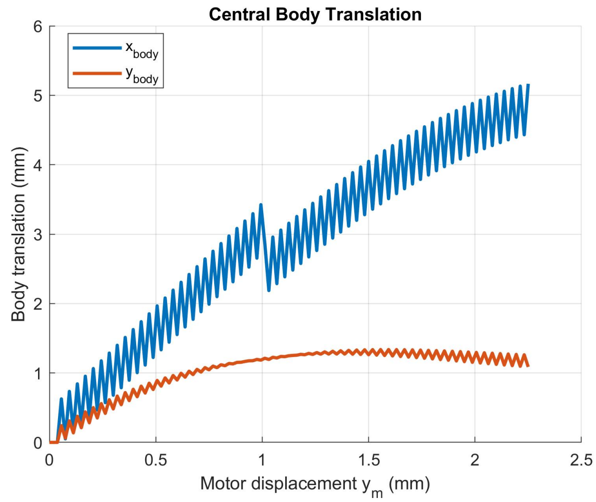


Figure 5.12: Central body translation as a function of motor stroke. The horizontal translation results from the no-slip stance-foot constraint, while the vertical translation enforces non-penetration of the feet and robot body with the walking surface.

Figure 5.13 shows the predicted robot-body rotation during the shuttle stroke. The sign and magnitude of this rotation depend on which foot is in contact, the moment arm from the contact point to the center of mass, and the direction of the estimated linkage-transmitted contact force.

The contact-state diagnostics are shown in Figure 5.14. The no-slip constraint is enforced only while the foot remains in compressive contact with the walking surface. This prevents the model from treating the stance foot as permanently attached to the floor and permits liftoff when the estimated normal force no longer supports contact.

The unilateral joint behavior is summarized in Figure 5.15. The upper subplot reports the torque about the $L_3$-to-$L_4$ joint, where positive torque corresponds to the free-rotation condition and zero or negative torque corresponds to the locked condition. The middle subplot shows the resulting joint state, and the lower subplot shows the updated distal-link orientation.

Figure 5.16 separates the center-of-mass trajectory into horizontal and vertical components. This representation is useful for evaluating whether the linkage produces net forward body motion, vertical body lift, or oscillatory motion during the motor stroke.

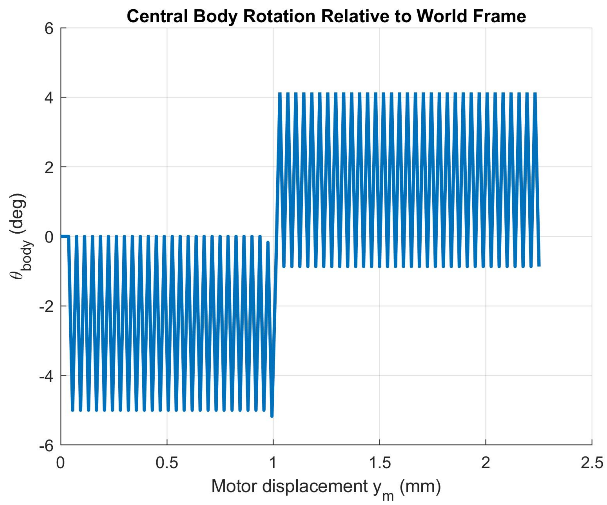


Figure 5.13: Robot-body rotation relative to the world frame as a function of motor stroke. Body rotation is driven by the moment generated by the active foot-ground reaction about the robot-body center of mass.

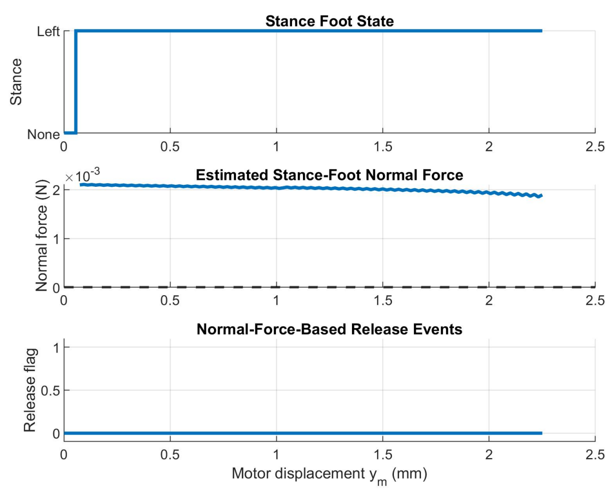


Figure 5.14: Contact-state and release diagnostics for the no-slip foot-contact model. The stance state identifies whether the left foot, right foot, or neither foot is acting as the no-slip contact point. The estimated stance-foot normal force is used to determine whether the contact remains physically admissible. When the estimated normal force becomes non-positive, the stance foot is allowed to release.

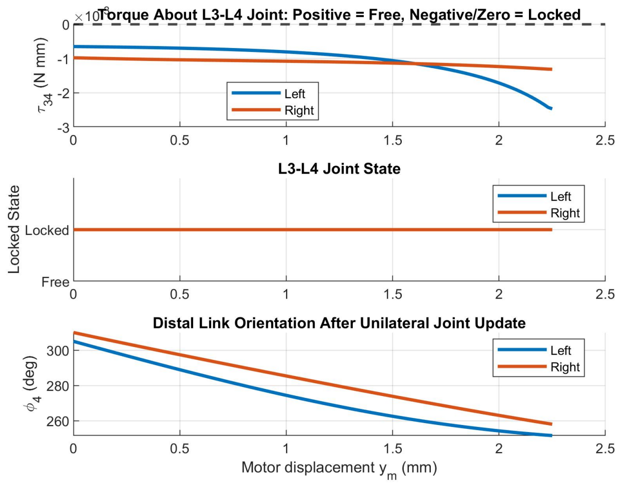


Figure 5.15: Unilateral $L_3$-to-$L_4$ joint state and torque response. Positive counter-clockwise torque about the joint releases the distal link and allows free rotation, while zero or negative torque locks $L_4$ at its designed relative angle with respect to $L_3$. The distal-link orientation is updated according to the locked or free joint state.

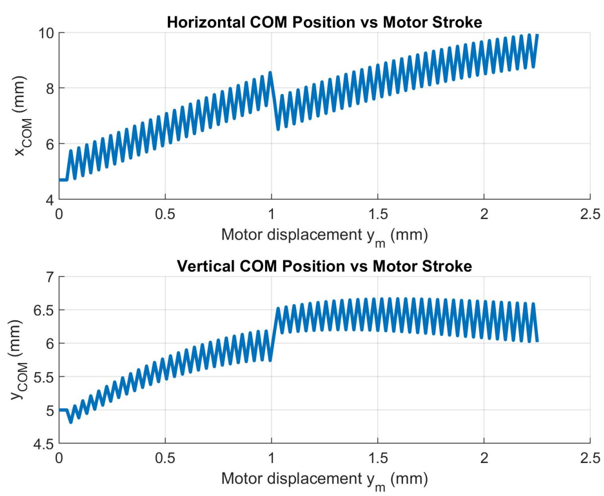


Figure 5.16: Center-of-mass trajectory components as a function of motor stroke. The center of mass is placed at the geometric center of the robot body and transformed into the world frame using the computed body translation and rotation.

The robot-body floor interaction is shown in Figure 5.17. This plot verifies that the rectangular robot-body outline does not penetrate the walking surface. Unlike the distal feet, body-floor contact is treated as frictionless, so it prevents vertical penetration without constraining tangential motion.

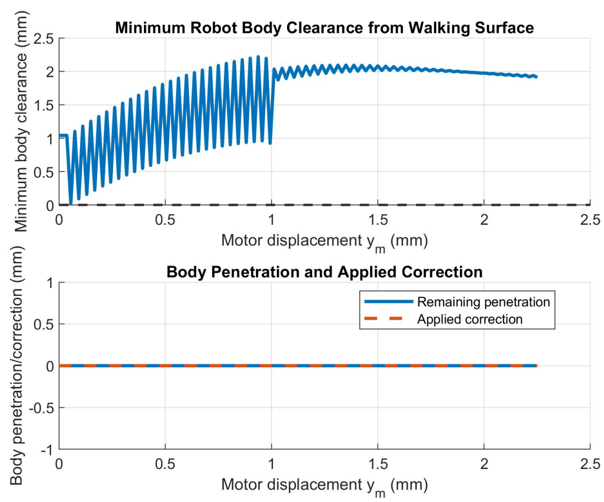


Figure 5.17: Robot-body clearance and penetration correction under the frictionless body-floor contact condition. The body is prevented from penetrating the walking surface, but body-floor contact does not impose a horizontal no-slip constraint.

The cumulative output-force components are shown in Figure 5.18. The horizontal component is associated with propulsion or resistance along the walking surface, while the vertical component is associated with support, unloading, or lift. Comparing the vertical output force with the body weight provides an approximate indication of whether the linkage can maintain compressive contact.

Finally, Figure 5.19 shows the estimated moment contribution from each distal endpoint about the robot-body center of mass. Differences between the left and right torque contributions arise from asymmetric linkage geometry, foot position, distal-joint state, and force direction. This torque is the primary quantity used to interpret contact-driven body rotation.

Together, these plots show how the body-frame linkage motion is converted into world-frame locomotion through contact with the walking surface. The body-frame plots isolate the internal mechanism geometry, while the world-frame plots include the rigid-body translation and rotation induced by no-slip foot contact. The unilateral $L_3$-to-$L_4$ joint model further allows the distal link to transition between a locked load-bearing configuration and a free-rotating release configuration depending on the

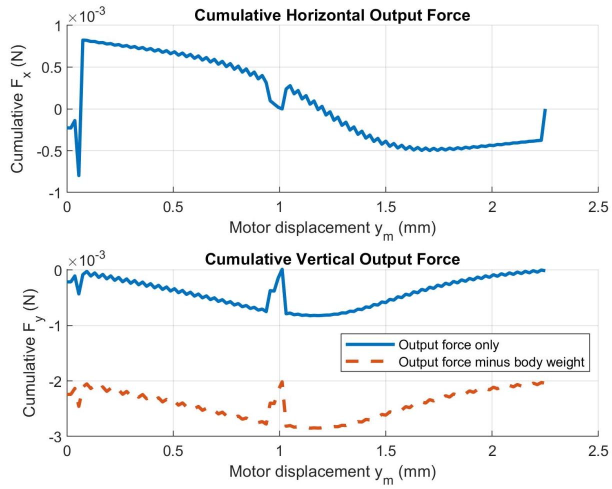


Figure 5.18: Cumulative world-frame output force components from the left and right distal endpoints. The horizontal component indicates the net fore-aft force contribution, while the vertical component indicates the net lift or loading contribution. The body weight is subtracted from the vertical force to show the approximate net vertical support margin.

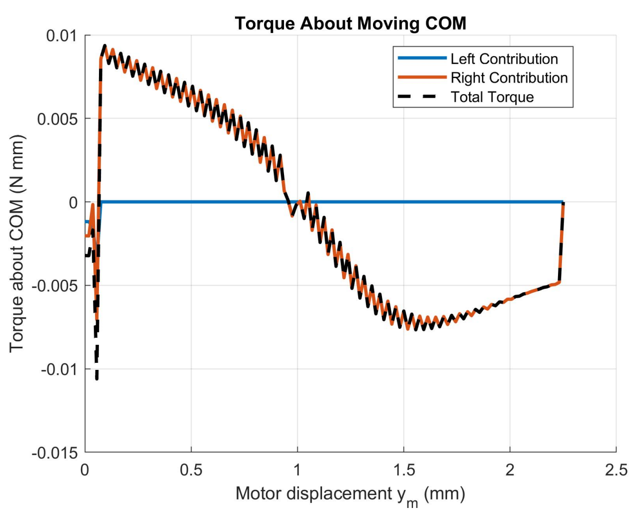


Figure 5.19: Estimated torque about the moving center of mass from the left and right distal endpoint forces. The total torque is obtained by summing the left and right moment contributions about the center of mass.

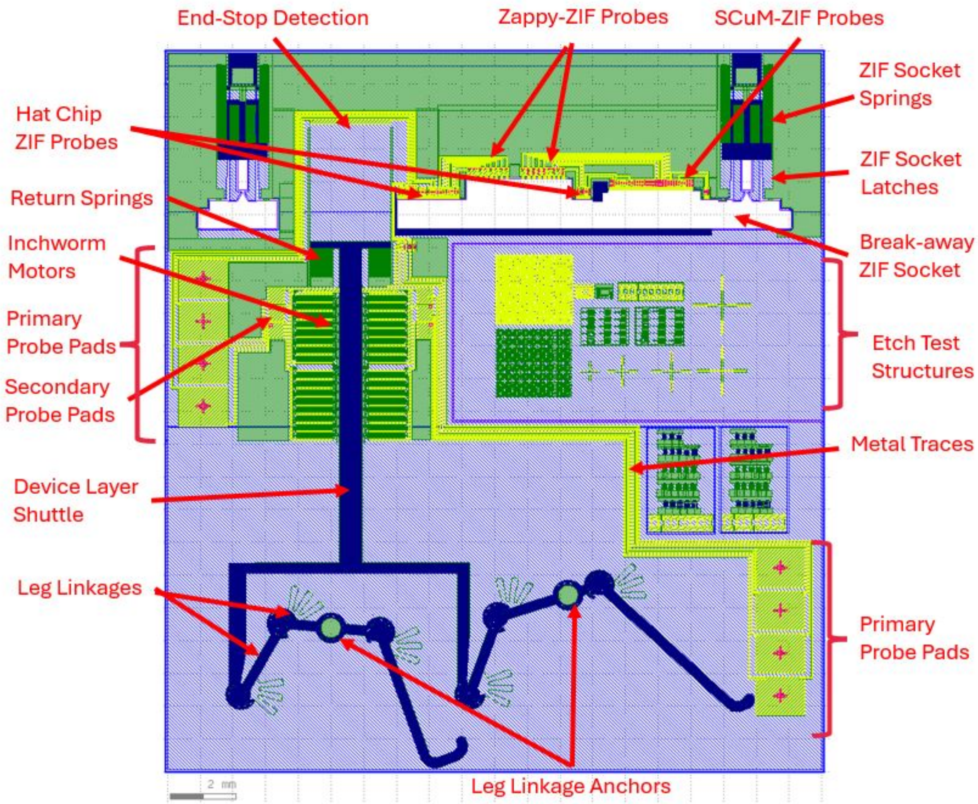


Figure 5.20: Depicted here is the 2D CAD of the crab-inspired linkage approach. The yellow is the metal layer; red is metal removal to be done computationally prior to fabrication; green is non-sacrificial SOI that is intended as anchors; dark blue is non-sacrificial SOI intended as released SOI; medium blue lines are the etched substrate layer; and the light-blue is the un-etched substrate layer. The hat chip attachments / ZIF socket connections were designed by H. Gomez.

sign of the joint torque. The contact diagnostics confirm that foot constraints are enforced only during physically admissible compressive contact, while the body-floor plots verify that the larger robot body remains non-penetrating under a frictionless slip condition. Finally, the force and torque plots provide a first-order estimate of how motor input is transmitted through the linkage into distal endpoint forces, unilateral joint states, and contact-driven body moments.

See Fig. 5.21 for the 3D CAD of the fully assembled robot.

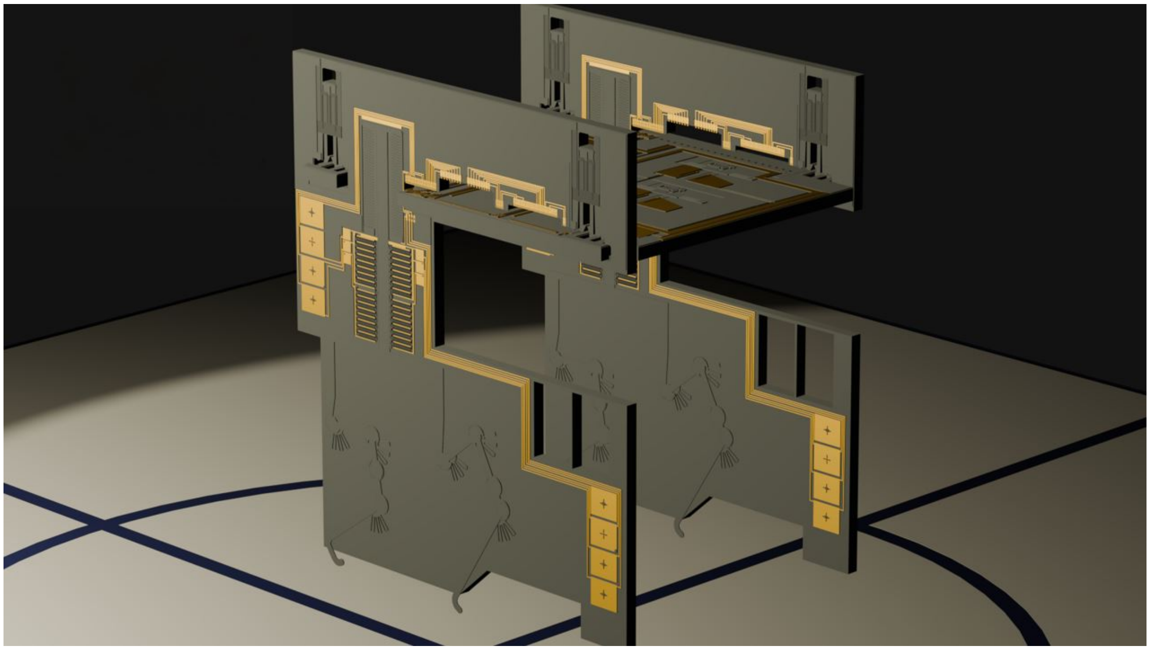

Figure 5.21: Depicted here is the 3D CAD of the crab-inspired linkage approach in full assembly with the hat chip. The radius of the circle on the walking surface is 2.5 *cm*.

#### 5.3.2.2 Fabrication Outcomes (v1.1)

In initial testing, it was observed that of the six fabricated leg chips, see Fig. 5.22, three were viable for testing. Of the three that were not viable, two had been overlapped in design with another chip's substrate layer etch during the initial fabrication file creation and the resulting etch destroyed the motor sections of these two chips. The remaining nonviable chip was dropped during fabrication and was destroyed. The three remaining chips displayed expected behavior with a pull-in voltage of $V_{PI,\text{avg}} = 90 \pm 10.1$ V; their inchworm motor speed at 10 Hz was approximately $v_{IWM} = 8.4 \pm 0.3$ $\mu$m/s.

While testing, it was observed that the pin-joint return springs on all three tested chips were either etched away or broken during handling, although at different locations. Further, the chips exhibited substantially different behavior in testing the inchworm motor actuation under power than expected and than was observed in the Prismatic Linkage Approach chips. The inchworm motors showed significant sticking, and destructive inspection revealed a significant amount of oxide still present in the peaks and valleys of the substrate beneath the SOI.

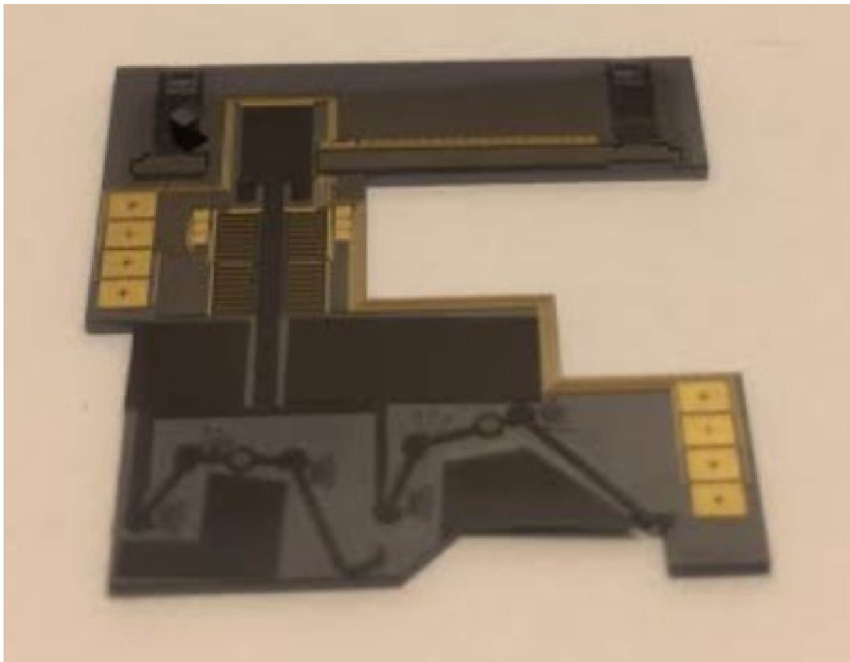

Figure 5.22: Photograph of the Crab Inspired Chip as-fabricated. Outer dimensions of the chip are 2.2 *cm* by 2.0 *cm*.

Upon assembly, the linkages for all three chips fell out of place and were destroyed prior to testing in the assembled condition.

## 5.4 Prismatic Linkage Approach (v2)

These designs were developed to simplify the leg trajectory, improve mechanical robustness, and reduce the number of actuators required per leg. Although this approach was mechanically simpler than the linkage-based alternatives, it introduced several important architectural trade-offs. The first major design decision concerned the nominal leg angle relative to the substrate and walking surface. Several candidate orientations were considered, including parallel, 30°, 45°, 60°, and perpendicular configurations relative to the walking surface (see Fig. 5.23). The perpendicular and parallel concepts were initially attractive because they represented limiting cases of the design space; however, both were rejected after practical review.

The parallel-leg configuration was rejected because it provided limited body clearance and produced a motion more closely resembling crawling or inchworm locomotion than walking. A design requirement for this system was that locomotion

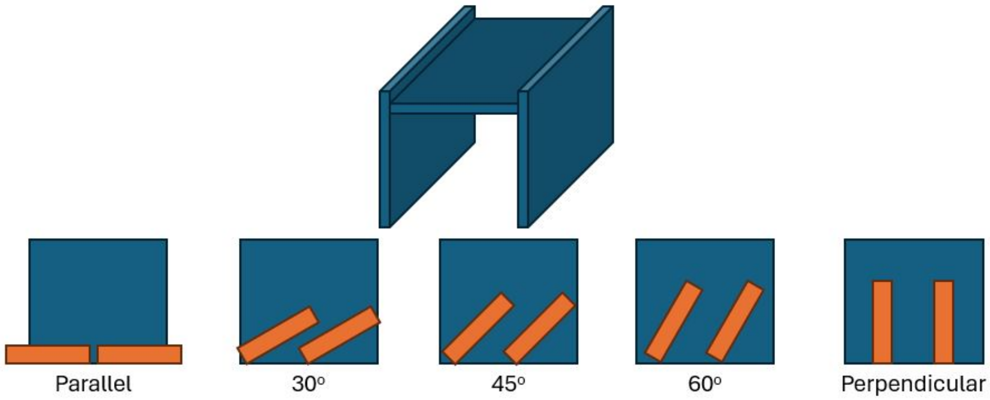


Figure 5.23: Diagram showing the straight walker approach leg angles. (Top) Simplified view of the walker robot assembly with two leg chips on either side and one hat chip connected at approximately 75% the full height of the leg chips. (Bottom) From left to right depictions of the leg orientations showing parallel, 30°, 45°, 60°, and perpendicular. Each diagram contains two legs per leg chip as simplified rectangular shapes in their respective orientations and are positioned as near to the ground as their orientation and shape allow without protruding out of the bottom of the chip. Notably, they all share similar sized legs to give an understanding that each is expected to extend the same length out of the robot, here approximately half the leg length. The leg lengths are approximately 60% of the robot height. As the leg width was deemed a non-constraining variable, they are not considered here.

should not depend on dragging the body or maintaining a large fraction of the chip surface in contact with the floor. This requirement was motivated by the desire to preserve a walking-like gait, maintain ground clearance, and enable later evaluation of obstacle clearance and graded-surface locomotion after assembly. The parallel configuration also imposed an inefficient use of chip area. The lateral travel required to generate useful forward motion consumed a large in-plane footprint relative to the displacement produced. Consequently, the parallel concept was considered poorly suited for a compact walking microrobot architecture.

The perpendicular-leg configuration was also rejected because it constrained the leg motion primarily to vertical lifting. Although such a design could potentially support a shuffling or stepping-in-place motion when combined with an appropriate actuation sequence, it did not directly satisfy the intended walking gait defined by the design objectives. In particular, the perpendicular configuration did not naturally generate the coupled lifting and forward-placement motion required for efficient locomotion.

The geometry was also restrictive from an integration standpoint. Motors oriented for predominantly vertical leg motion would require substantial structural height or extended in-plane support features, potentially exceeding the predefined design envelope. For these reasons, the perpendicular configuration was not pursued as the primary leg architecture.

To evaluate the remaining leg-angle options, the required leg-chip components were blocked out to assess spacing and layout feasibility. While the 60° option allowed for easy placement of the motors, probe pads, end-stop detection, and metal trace routing, the 45° and 30° options did not and were not considered further.

### 5.4.1 Big-Foot Substrate Legs (v2.1)

This design iteration focused on addressing undesirable leg deflection during actuation and walking, see Fig. 5.24.

The substrate was considered and implemented as a reinforcing element for the walker legs. As the pawls are designed to engage with the Device layer of the opposing shuttle, it was essential to retain this device layer on the shuttle itself. Further, the shuttle itself has no mechanism for maintaining its opposing in-plane position with the pawls and therefore requires an alignment mechanism. While the return springs at the head of the shuttle would serve as an in-plane alignment mechanism locally, it was not clear that this would be beneficial to incorporate at the base of the foot due to spacing limitations. Here, a trim around the shuttle and walker leg/foot served this purpose.

The legs themselves maintained a 50 $\mu$m trim of Device layer utilizing the sparse filling of 8 $\mu$m square perforations spaced at 14 $\mu$m, center-to-center. As these squares would allow exposure to the environment during HP vapor etch of the Oxide layer timed for a 9.5 $\mu$m etch to ensure that the diagonal space between adjacent perforations would be sufficiently reached by the HF vapor (with a 1 $\mu$m over-etch adjustment). This trim can be viewed as a blue outline around the shuttle and foot in Fig. 5.25.

A simulation similar to that in Section 5.3.2.1 was conducted with the parameters shown in Table 5.5.

#### 5.4.1.1 Substrate-Cutout Prismatic Linkage Model (v2.1)

A linkage model was also developed to evaluate a reduced-complexity leg architecture derived from the previous planar linkage contact model. The same body-frame to world-frame transformation, contact handling, no-slip stance-foot constraint, body-floor non-penetration correction, and quasi-static torque interpretation were retained

Table 5.5: Simplified prismatic linkage geometry and actuation parameters.

| **Parameter** | **Value** | **Notes** |
|---|---|---|
| Number of linkages | 2 | One linkage per leg |
| Linkage type | Single prismatic substrate cutout | Removed from substrate; contributes to COM shift |
| Linkage orientation | $-60°$ | Relative to the bottom edge of the robot body |
| Bottom edge orientation | $0°$ | Parallel to the bottom edge of the robot body |
| Top edge orientation | $30°$ | Perpendicular to the $-60°$ side edges |
| Top edge width | 4.5 mm | Width of upper linkage face |
| Right side length | 4.0 mm | Corrected dimension |
| Left side length | 6.6 mm | Longer side of the prismatic cutout |
| Left linkage lower-left corner | (1.1, 0) mm | Measured from the bottom-left corner of the robot body |
| Right linkage translation | +7.0 mm in $x$ | Center-to-center offset relative to the left linkage |
| Linkage pair spacing | 7.0 mm | Center-to-center separation |
| Linkage material role | Substrate cutout | Subtracted from the robot body area and mass |
| Linkage structural assumption | Rigid prismatic geometry | No slider-rocker kinematic chain |
| Actuator force per linkage | 15 mN | Applied independently to each leg |
| Actuator stroke | 3.5 mm | Along the linkage direction |
| Actuation direction | Parallel to linkage side direction | Downward along the $-60°$ linkage axis |
| Leg-to-leg geometry | Identical shape and orientation | Right linkage is translated from the left linkage |

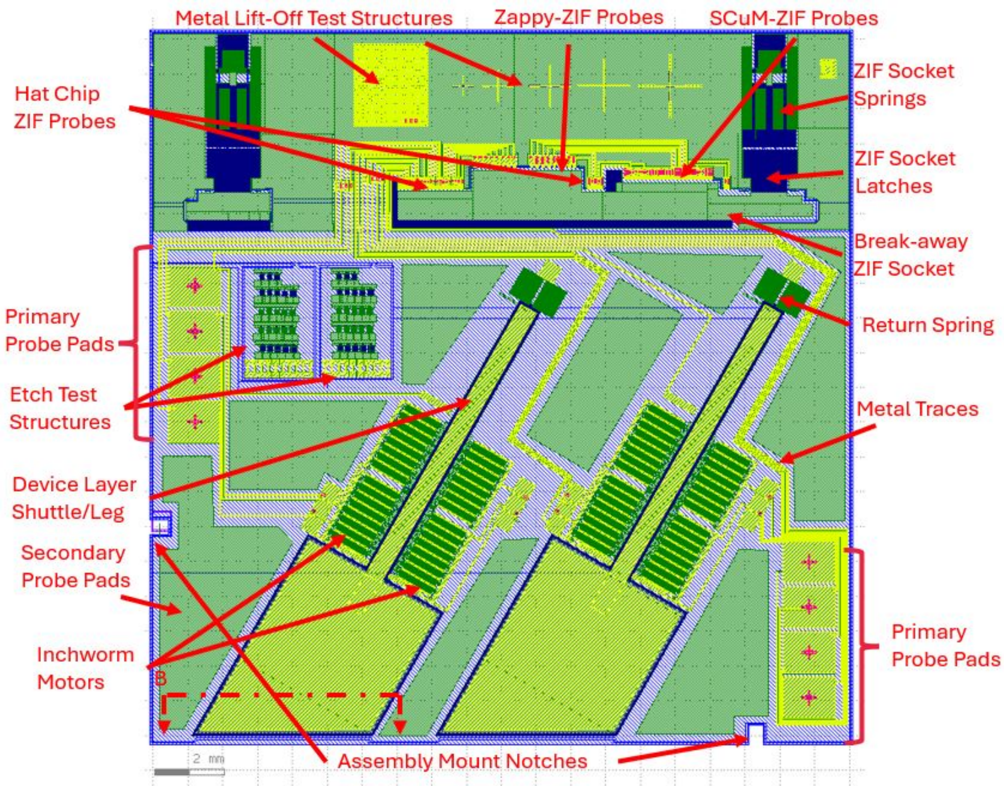


Figure 5.24: Depicted here is the 2D CAD of the Prismatic Linkage Approach, using a Big-Foot/-boot substrate leg. The yellow is the metal layer; red is metal removal to be done computationally prior to fabrication; green is non-sacrificial SOI that is intended as anchors; dark blue is non-sacrificial SOI intended as released SOI; medium blue lines are the etched substrate layer; and the light-blue is the un-etched substrate layer. The hat chip attachments / ZIF socket connections were designed by H. Gomez.

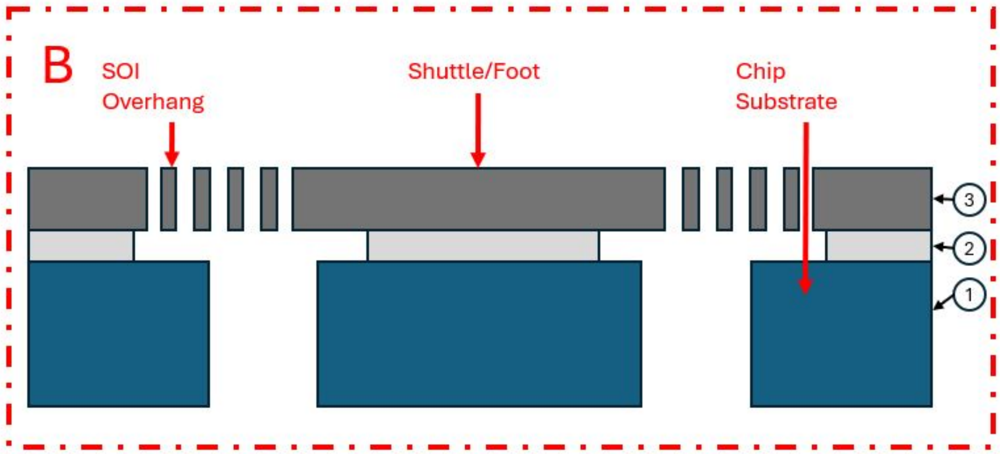


Figure 5.25: Diagram of the cutaway of the 2D CAD of the Prismatic Linkage Approach, using a Big-Foot/-boot substrate leg. The diagram shows the SOI overhang which is attached to the shuttle/foot structure and is a series of Device layer etch holes designed to allow the HP vapor etch to release the SOI from the Substrate. This allows the Substrate layer to fall away during etch and be removed. Shown here is also the chip substrate that is affixed to the SOI and for which the overhang slides across to maintain in-plane alignment with the rest of the chip device layer to within $\pm 2$ $\mu$m.

from the prior MATLAB model described in Section 5.3.2.1. However, the multi-link slider-rocker mechanism and the unilateral $L_3$-to-$L_4$ joint behavior were removed. Instead, each leg was represented as a single prismatic substrate-cutout linkage oriented at $-60°$ relative to the lower edge of the robot body.

This model isolates the effect of a simpler leg geometry while preserving the same contact-based locomotion framework used for the previous linkage study. In the prior model, the distal endpoint motion was produced by a constrained multi-body mechanism containing several rotating and translating members. In the present model, the leg geometry is prescribed directly as a rigid prismatic cutout, and the actuator stroke is applied along the linkage direction. This change removes the need to solve the internal slider-rocker kinematics, while still allowing the simulation to estimate the resulting body translation, body rotation, foot clearance, force direction, and torque about the moving center of mass.

The linkage geometry used in the model is summarized in Table 5.5. Each leg linkage has the same geometry and orientation, with the right linkage translated 7.0 mm in the $+x$-direction relative to the left linkage. The lower edge of each linkage is parallel to the lower edge of the robot body, while the side edges are aligned with the $-60°$ linkage direction. The upper edge is oriented perpendicular to the side edges, producing a prismatic cutout geometry. The left linkage is positioned such that its lower-left corner is 1.1 mm from the lower-left corner of the robot body.

A key distinction of this model is that the linkages are treated as substrate cutouts rather than separate device-layer linkage members. Consequently, the removed linkage areas contribute directly to the mass-property calculation. The body center of mass is no longer assumed to remain at the geometric center of the original rectangular body. Instead, the center of mass is recomputed from the remaining substrate area after subtracting the two linkage cutouts. If the original body area is denoted $A_B$, the cutout areas are denoted $A_{c,L}$ and $A_{c,R}$, and their centroids are denoted $\mathbf{r}^B_{c,L}$ and $\mathbf{r}^B_{c,R}$, then the modified body-frame center of mass is approximated as

$$\mathbf{r}^B_{\mathrm{COM}} = \frac{A_B\mathbf{r}^B_{B,0} - A_{c,L}\mathbf{r}^B_{c,L} - A_{c,R}\mathbf{r}^B_{c,R}}{A_B - A_{c,L} - A_{c,R}}, \tag{5.27}$$

where $\mathbf{r}^B_{B,0}$ is the centroid of the uncut rectangular robot body. This correction is important because the contact moment depends on the moment arm between the active foot contact and the moving center of mass. Treating the substrate cutouts as massless geometric features without updating the center of mass would therefore introduce an inconsistent torque estimate.

Each linkage is driven independently by a linear translation actuator that applies a force of 15 mN over a prescribed stroke of 3.5 mm. The actuator stroke is applied parallel to the linkage side direction, so the body-frame actuation direction is

$$\hat{\mathbf{u}}^B_{\mathrm{act}} = \begin{bmatrix} \cos(-60°) \\ \sin(-60°) \end{bmatrix}. \tag{5.28}$$

The resulting body-frame endpoint motion for each linkage is therefore prescribed by

$$\mathbf{p}^B_e(q) = \mathbf{p}^B_{e,0} + q\hat{\mathbf{u}}^B_{\mathrm{act}}, \tag{5.29}$$

where $q$ is the actuator stroke. This representation intentionally removes the internal linkage amplification and joint-locking behavior present in the previous model, allowing the simplified geometry to be assessed as a direct prismatic leg concept.

The same rigid-body transformation was then used to map the body-frame geometry into the world frame. Thus, the endpoint, body outline, cutout-corrected center of mass, and linkage geometry were all transformed using

$$\mathbf{p}^W = \mathbf{r}^W_B + \mathbf{R}(\theta_B)\mathbf{p}^B. \tag{5.30}$$

This preserves the original separation between the internal body-frame motion and the physically relevant world-frame motion relative to the walking surface. As in the previous model, foot contact was treated as a no-slip stance constraint while the robot-body floor interaction was treated as frictionless and non-penetrating. This allows the simulation to distinguish between foot-driven body motion and incidental body-floor support.

Figure 5.26 shows the linkage poses in the robot body frame. This figure verifies that the two prismatic substrate cutouts retain identical geometry and orientation throughout the prescribed actuator stroke. Because the plot is body-fixed, it is used primarily as a geometric verification of the linkage layout, actuator direction, and relative spacing between the two leg cutouts.

Figure 5.27 shows the corresponding world-frame linkage and robot-body poses after applying the contact correction. This plot provides the physically relevant configuration of the mechanism relative to the walking surface. The figure also shows how the apparent global motion of the linkages differs from their body-frame motion once the robot body is allowed to translate and rotate in response to contact.

The resulting rigid-body translation of the robot body is shown in Figure 5.28. As in the previous contact model, horizontal translation is generated when one of the feet acts as a no-slip stance point and the prescribed leg motion drives the body relative to that fixed point. Vertical translation is introduced by the non-penetration correction applied to the distal endpoints and the robot-body outline.

Figure 5.29 shows the predicted body rotation during the actuator stroke. The rotation is determined by the moment generated by the active contact force about the cutout-corrected center of mass. This result is especially sensitive to the revised mass distribution because the substrate cutouts shift the center of mass and therefore alter the contact moment arm.

The contact-state diagnostics are shown in Figure 5.30. These diagnostics retain the same interpretation as in the prior linkage model: a no-slip stance constraint is enforced only while the estimated normal force remains positive. When the normal force becomes non-positive, the stance condition is released to avoid imposing a nonphysical tensile contact with the walking surface.

Figure 5.31 shows the world-frame endpoint trajectories produced by the linkage motion. These trajectories represent the effective foot paths relative to the walking surface and provide the main estimate of stride behavior for the prismatic cutout design. Because the internal multi-link mechanism has been removed, the trajectories are governed primarily by the prescribed actuator direction, body rotation, stance-foot selection, and contact correction.

The center-of-mass trajectory components are shown in Figure 5.32. This plot separates the horizontal and vertical components of the cutout-corrected center-of-

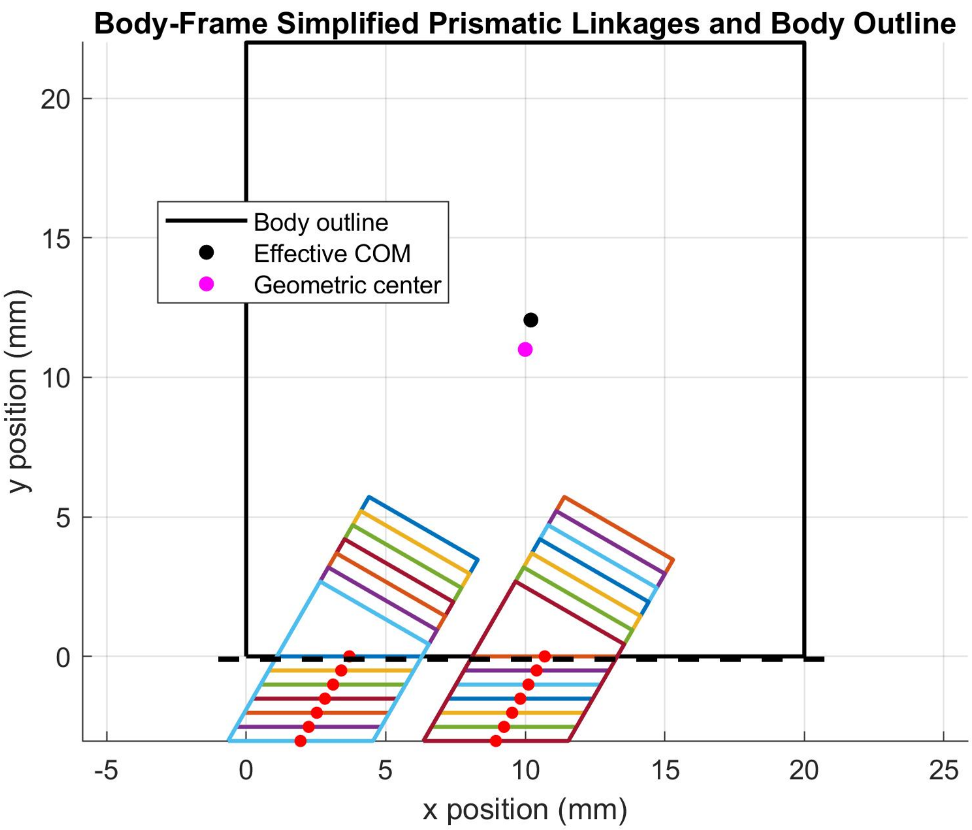


Figure 5.26: Body-frame poses of the prismatic substrate-cutout linkages over the prescribed actuator stroke. The two linkages have identical geometry and orientation, with the right linkage translated 7.0 mm in the $+x$-direction relative to the left linkage. This view verifies the prescribed linkage geometry before contact correction and transformation into the world frame.

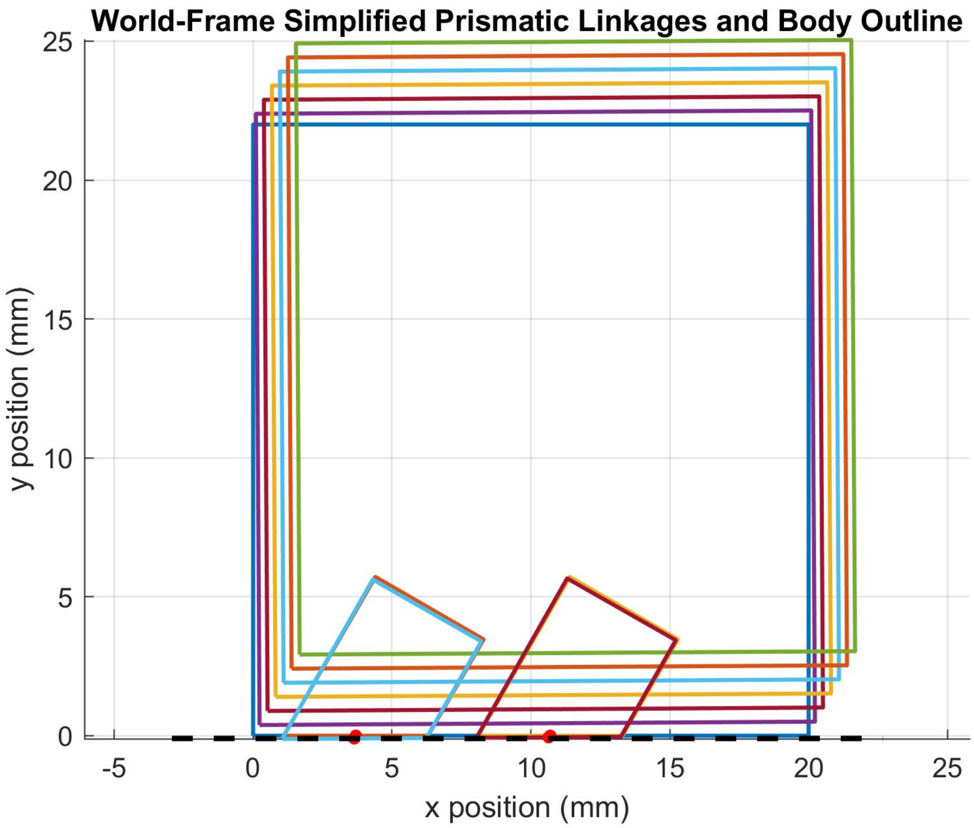


Figure 5.27: World-frame poses of the prismatic linkage model after applying the rigid-body transformation and contact constraints. The linkage motion is shown relative to the walking surface, including body translation, body rotation, no-slip foot contact, and frictionless body-floor non-penetration correction.

mass motion. It is used to evaluate whether the linkage produces useful forward translation, excessive vertical oscillation, or primarily local rocking motion during the actuator stroke.

Together, these figures show how the prismatic substrate-cutout linkage behaves within the same contact-based locomotion framework used for the earlier slider-rocker model. The main modeling difference is that the internal multi-link kinematic chain is replaced by a prescribed rigid prismatic leg motion, while the substrate cutouts are explicitly included in the center-of-mass calculation. This allows the design to be compared against the prior linkage architecture using the same output quantities: body-frame geometry, world-frame endpoint trajectories, body translation, body

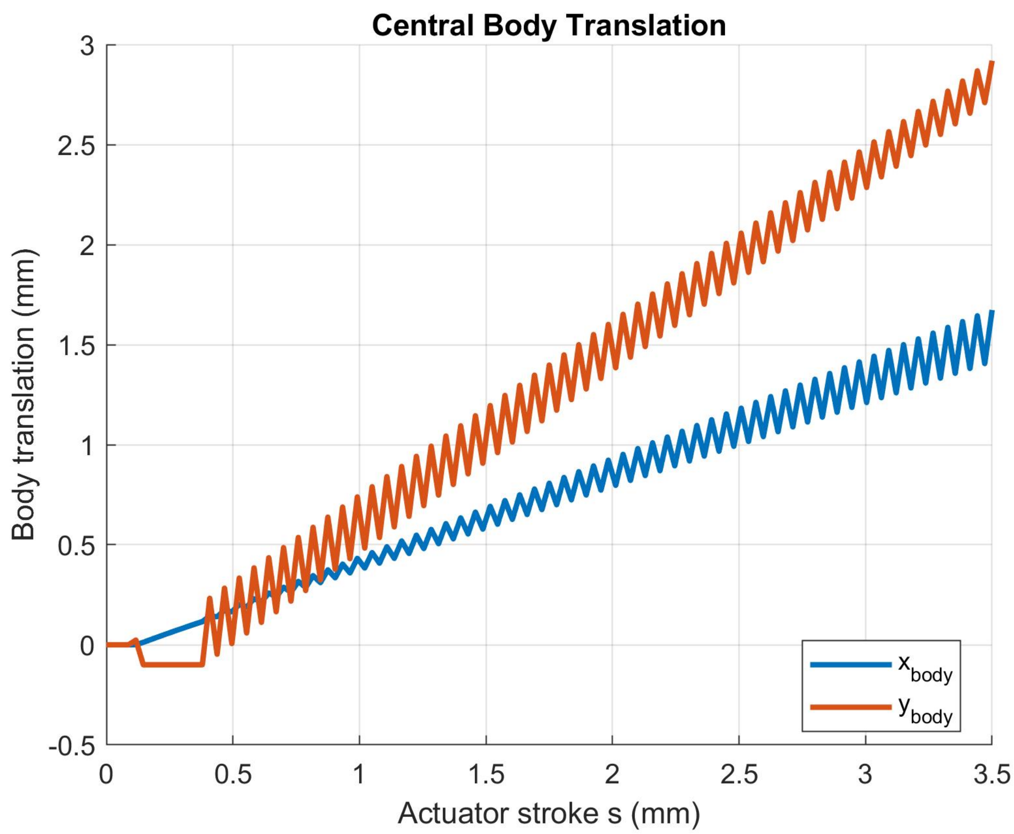


Figure 5.28: Central body translation predicted by the prismatic linkage model. Horizontal motion results from the no-slip stance-foot constraint, while vertical motion enforces non-penetration between the feet, robot body, and walking surface.

rotation, foot clearance, contact state, output-force components, and torque about the moving center of mass.

See Fig. 5.33 for the 3D CAD assembly of the big-foot substrate approach with hat chip.

#### 5.4.1.2 Fabrication Outcomes (v2.1)

The legs in this iteration were structurally robust and showed minimal deflection during assembly and motor operation. As seen in Fig. 5.34, these legs were also robust in fabrication. The legs showed few fabrication issues and seemed robust relative to other chips on the same wafers that experienced over-etch, PR bubbling, poor metal adhesion, and small spring breakage.

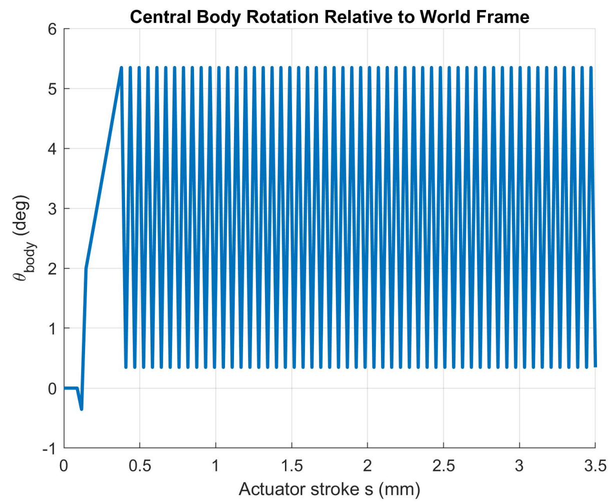


Figure 5.29: Robot-body rotation predicted by the prismatic linkage model. Body rotation is driven by the ground reaction moment about the cutout-corrected center of mass.

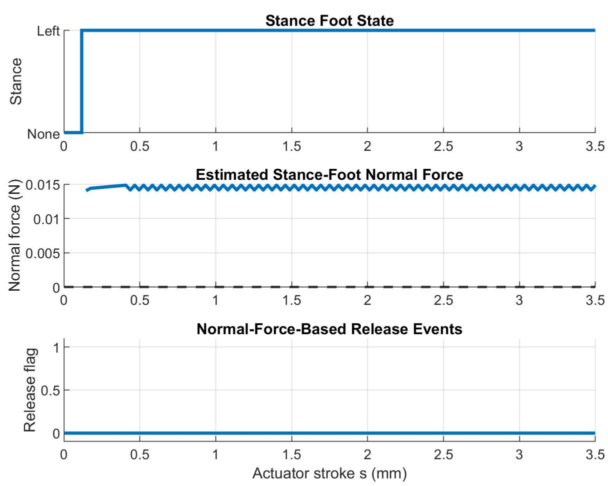


Figure 5.30: Contact-state and release diagnostics for the prismatic linkage model. The stance state identifies whether the left foot, right foot, or neither foot is enforcing the no-slip contact condition. The stance foot is released when the estimated normal force becomes non-positive.

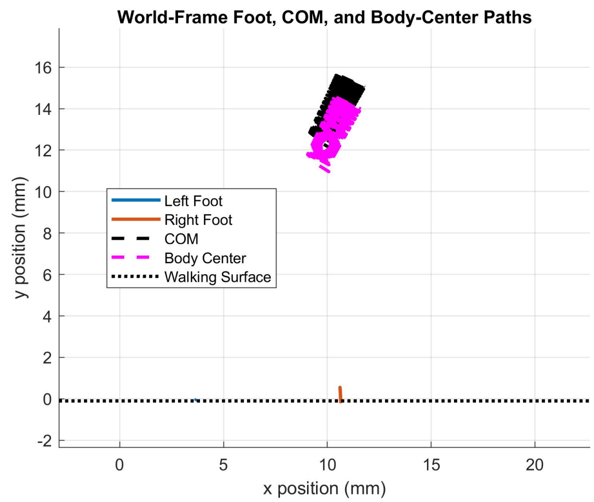


Figure 5.31: World-frame distal endpoint, center-of-mass, and body-center trajectories for the prismatic linkage model. The endpoint paths include the prescribed prismatic actuation, rigid-body transformation, no-slip stance constraint, and contact-driven body motion.

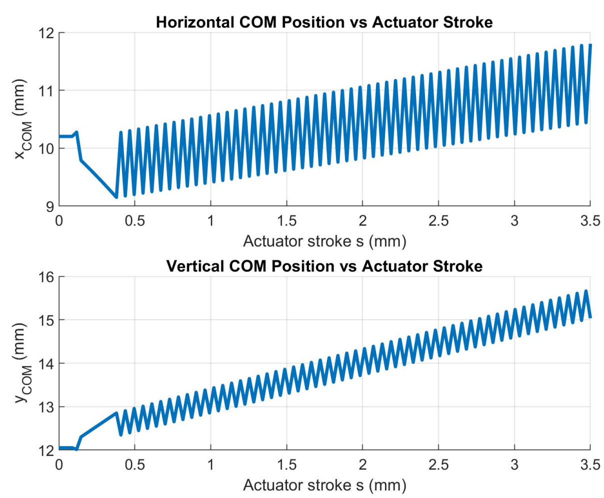


Figure 5.32: Horizontal and vertical components of the cutout-corrected center-of-mass trajectory as a function of actuator stroke. This representation separates forward body motion from vertical lift and oscillatory motion.

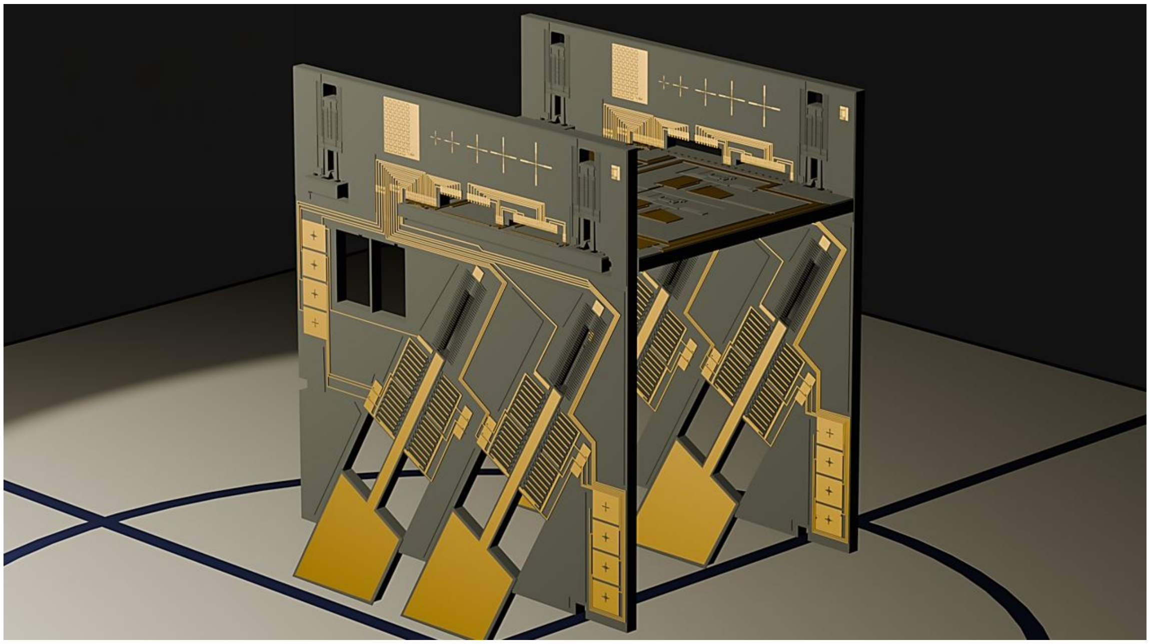

Figure 5.33: Depiction of the 3D CAD Assembly of the big-foot substrate legged walker with hat chip. The radius of the circle on the walking surface is 2.5 *cm*.

In initial testing, it was observed that of the six fabricated leg chips, four were viable for testing. The two nonviable chips had been overlapped in design with another chip's substrate layer etch during the initial fabrication file creation and the resulting etch destroyed the motor sections of these two chips. The four remaining chips displayed expected behavior with a pull-in voltage of $V_{PI,\text{avg}} = 96 \pm 4.4$ V; their inchworm motor speed at 10 Hz was approximately $v_{IWM} = 6.6 \pm 2.1$ $\mu$m/s. While testing, it was observed that near the mid-point of the shuttle extension the foot structure would fall out of the alignment gap in the surrounding chip. This occurred in three of the tested chips that were extended to this distance, the fourth was not fully extended during initial testing to reduce the occurrence of this behavior. See Fig. 5.35. Two of the three tested in this way were not testable afterward due to destruction by mishandling.

Upon assembly, the remaining two chips were destroyed beyond repair.

As the Big-Foot approach had a failure mode associated with the location of the leg/foot structure COM, subsequent versions would aim to produce a leg that was more evenly distributed, allowing the COM to remain within the surrounding chip gap and allowing the leg to be better supported by the substrate.

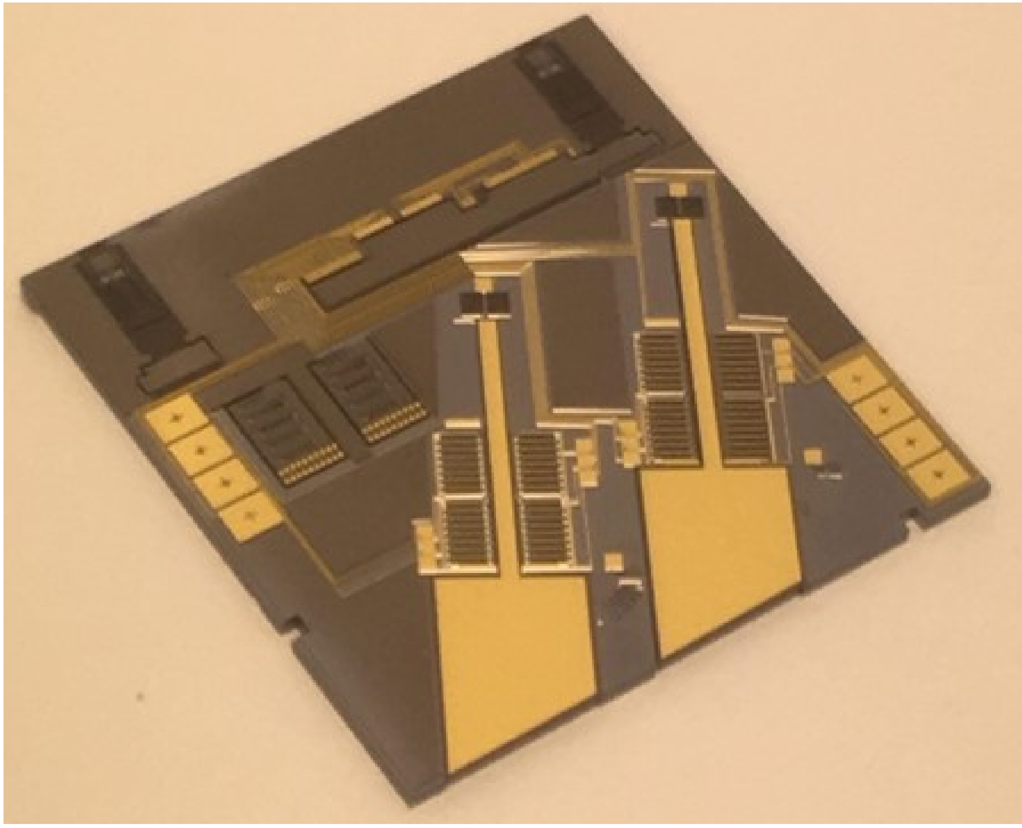

Figure 5.34: Image of the as-fabricated Big-Foot Substrate-Layer Leg Chip.

### 5.4.2 Rectangular Substrate-Layer Legs (v2.2)

This approach used a design similar to the Big-Foot approach. The major change implemented here was the shape of the substrate-layer leg. Here, the leg remains a prismatic joint with no embedded revolute joint in the actuation mechanism, and it retains positioning similar to v2.1. However, in this iteration the approach was aimed at allowing the full length of the leg to act as a shuttle. Similarly, since the leg itself was a substrate structure, the COM shift would have to be considered. See Fig. 5.36 for the 2D CAD and Fig. 5.37 for the 3D CAD of the assembly.

Eight of these chips were fabricated, of which two were viable for testing. The six that were nonviable were thought to be nonviable because of handling issues and poor etching quality in and around the motors. This poor etching quality was thought to be due to poorly developed or poorly baked PR at the onset of the frontside SOI etch which propagated liquid and gas phase pockets of PR.

However, after much investigation and characterization, it was determined that

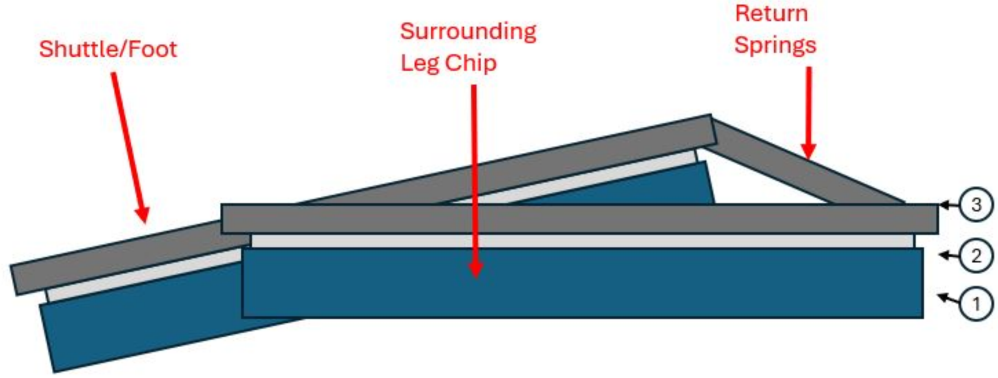


Figure 5.35: Diagram of the Prismatic Linkage Approach, using a Big-Foot/-boot substrate leg showing the out-of-plane motion. The diagram shows the shuttle/foot structure falling towards the floor or into the surrounding chip structure gap when being tested in a flat chip-face-up position because gravity acted on an off-center leg/foot center of mass. The diagram also shows the return springs acting as a stabilizing structure to keep the shuttle from completely losing alignment.

there were other contributing factors that are further discussed in Appendix A.

The remaining two chips were evaluated and tested; however, motor function was atypical and would cease after 4--5 tests. Additionally, the author was unable to access the laboratory for an extended period, which contributed to further sample contamination because the samples were not safely returned to the cleanroom before the author's absence from the lab.

See Fig. 5.37 for the 3D CAD assembly of the big-foot substrate approach with hat chip.

### 5.4.3 Rectangular Device-Layer Legs (v2.3)

This iteration used device-layer structures instead of substrate-layer structures as the prismatic linkage for the legs. It retained the shape and outline of v2.2 while reducing reliance on the substrate as structural support. The design hypothesis was that the substrate could act as a better guide for the leg itself rather than acting as the leg. This would improve assembly, and although it would reduce the structural rigidity of the leg, it would still provide a valuable increase in structural support relative to the prior work legs.

Table 5.6 summarizes the perforation geometry used for the perforated cantilever approximation. The perforations are modeled as square through-holes arranged

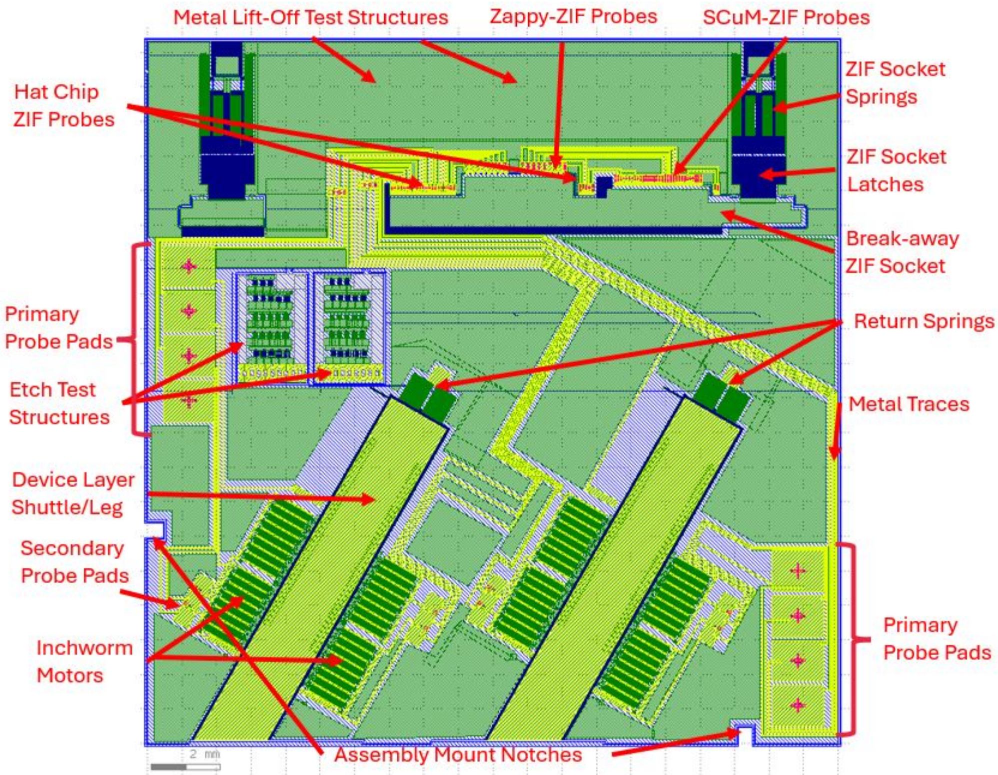


Figure 5.36: Depicted here is the 2D CAD of the Prismatic Linkage Approach, using a rectangular substrate leg.

on a square pitch. The local ligament width, defined as the difference between the pitch and the hole side length, is a critical dimension because it governs the local compliance between adjacent perforations and determines the mesh refinement required for explicit perforated-geometry simulations. The removed-area fraction provides a first-order estimate of the reduction in effective bending rigidity, while the large number of periods along the beam length and width supports the use of a homogenized stiffness correction as an initial approximation. However, because the bending strain energy is largest near the fixed boundary, the actual perforation layout near the anchor should be preserved or explicitly documented in any reduced-domain finite element model.

#### 5.4.3.1 Analytical Estimation of Perforated Beam Bending

The analytical estimate was used to frame the proposed SOI device-layer leg as a relative compliance comparison against the distal linkage/end-effector geometry

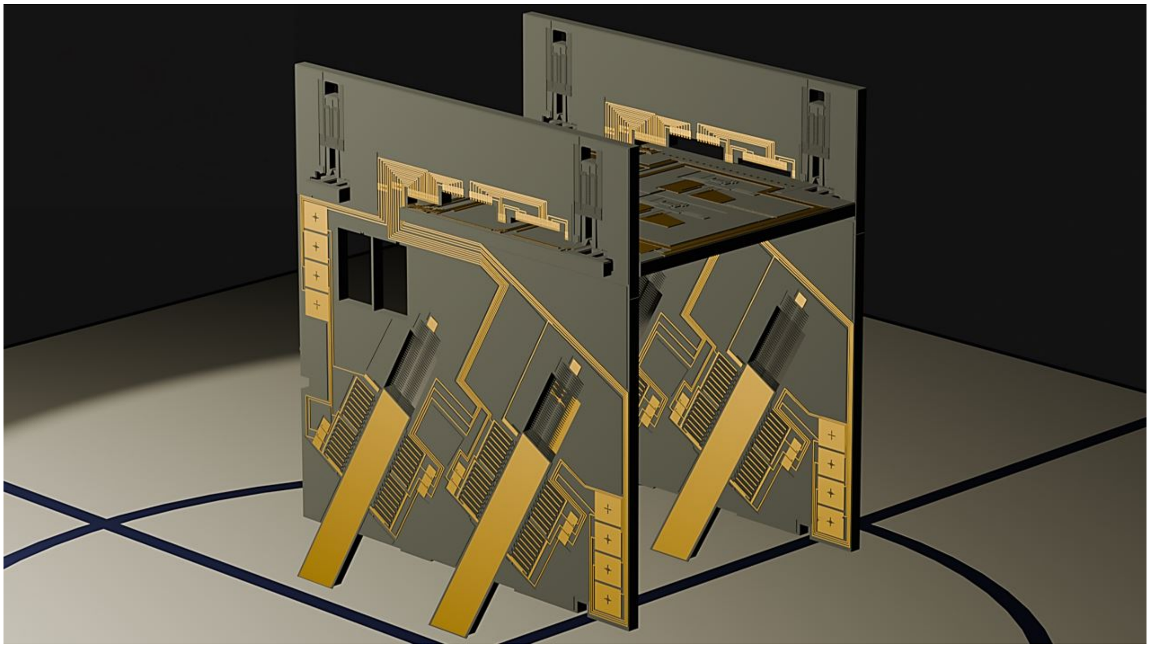

Figure 5.37: Depiction of the 3D CAD assembly of the rectangular substrate-layer legged walker with hat chip. The radius of the circle on the walking surface is 2.5 *cm*.

reported in prior linkage-based leg work. The objective of this analysis is to determine whether the current 3 mm long, 2 mm wide device-layer leg remains within the same millimeter-scale compliance regime as the distal linkage/end-effector structure from the prior work [7, 16].

The prior work comparison is restricted to the distal linkage/end-effector element, which had a length of 3.000 mm and a width of 0.120 mm, as summarized in Table 5.1. This is the most appropriate comparison feature because it represents the output linkage responsible for transmitting distal motion. The present model is therefore evaluated using a nominal 3 mm leg length so that the comparison is not dominated by length scaling.

For a rectangular fixed--free beam loaded in bending, the small-deflection tip displacement is given by

$$\delta = \frac{FL^3}{3EI}, \tag{5.31}$$

where $F$ is the applied transverse load, $L$ is the beam length, $E$ is the elastic modulus, and $I$ is the second moment of area about the bending axis. For thickness-direction bending of a rectangular SOI device layer,

Table 5.6: Perforation geometry details for the perforated SOI cantilever model.

| **Perforation Characteristic** | **Value** | **Units** | **Notes** |
|---|---|---|---|
| Perforation shape | Square | -- | Square through-hole pattern. |
| Perforation side length ($a$) | 8 | $\mu$m | Each perforation is 8 $\mu$m $\times$ 8 $\mu$m. |
| Perforation pitch ($p$) | 14 | $\mu$m | Center-to-center spacing between adjacent holes. |
| Ligament width | 6 | $\mu$m | Calculated as $p - a$. |
| Perforation depth | 40 | $\mu$m | Through the full SOI device-layer thickness. |
| Unit-cell area ($A_{unit}$) | 196 | $\mu$m$^2$ | Calculated as $p \times p$. |
| Removed area per unit cell ($A_{unit,\ rem}$) | 64 | $\mu$m$^2$ | Calculated as $a \times a$. |
| Removed-area fraction ($\phi$) | 0.327 | -- | $\phi = A_{unit,\ rem}/A_{unit}$. |
| Remaining silicon area fraction ($\eta_A$) | 0.673 | -- | $\eta_A = 1 - \phi$. |
| Approximate periods along full beam length | 250 | periods | 3500 $\mu$m/14 $\mu$m. |
| Approximate periods across full beam width | 143 | periods | 2000 $\mu$m/14 $\mu$m. |

$$I = \frac{bt^3}{12}, \tag{5.32}$$

where $b$ is the in-plane leg width and $t$ is the SOI device-layer thickness. Substituting Eq. 5.32 into Eq. 5.31 shows that, for fixed material, thickness, loading condition, and boundary condition,

$$\delta \propto \frac{FL^3}{bt^3}. \tag{5.33}$$

Because the current comparison uses a 3 mm current leg and the 3.000 mm prior distal linkage/end effector, the length term is approximately the same for both structures,

$$L_{\text{current}} \approx L_{\text{prior}} = 3.000 \text{ mm}. \tag{5.34}$$

Thus, the cubic length term is approximately unity, and the first-order geometric comparison is governed primarily by the width ratio. For two beams of the same material, thickness, length, loading mode, and boundary condition, the relative deflection may be approximated as

$$\frac{\delta_{\text{current}}}{\delta_{\text{prior}}} \approx \frac{F_{\text{current}}}{F_{\text{prior}}} \quad \frac{b_{\text{prior}}}{b_{\text{current}}} \quad , \tag{5.35}$$

and the corresponding relative stiffness may be approximated as

$$\frac{k_{\text{current}}}{k_{\text{prior}}} \approx \frac{b_{\text{current}}}{b_{\text{prior}}}. \tag{5.36}$$

This indicates that if the current leg is wider than the prior distal linkage, the current solid leg would be expected to be proportionally stiffer before accounting for perforations. However, this width-based estimate is only a first-order approximation. It does not include local ligament compliance, stress concentrations near perforation corners, geometric nonlinearity, or differences in the actual loading and support conditions.

The perforation pattern modifies this comparison because the perforated SOI leg does not retain the full stiffness of the corresponding solid silicon structure. For square through-holes with side length

$$a = 8\ \mu\text{m} \tag{5.37}$$

arranged on a square center-to-center pitch of

$$p = 14\ \mu\text{m}, \tag{5.38}$$

the removed-area fraction of a periodic unit cell is

$$\phi = \frac{a^2}{p^2} = \frac{(8\ \mu\text{m})^2}{(14\ \mu\text{m})^2} \approx 0.327. \tag{5.39}$$

The corresponding remaining silicon area fraction is

$$\eta_A = 1 - \phi \approx 0.673. \tag{5.40}$$

As a first-order homogenized estimate, the perforated stiffness may therefore be approximated as

$$k_{\text{perforated}} \approx \eta_A k_{\text{solid}}, \tag{5.41}$$

or, equivalently, the perforated deflection under the same load may be estimated as

$$\delta_{\text{perforated}} \approx \frac{\delta_{\text{solid}}}{\eta_A}. \tag{5.42}$$

Using the area-fraction correction alone, the perforated structure is therefore expected to be approximately

$$\frac{1}{\eta_A} = \frac{1}{0.673} \approx 1.49 \tag{5.43}$$

times as compliant as the corresponding solid structure. This correction does not represent a complete mechanical model of the perforated beam because it neglects local ligament bending, corner stress concentration, and spatial variations in strain energy. Nevertheless, it provides a useful first-order estimate of the stiffness penalty introduced by the perforation pattern.

The analytical comparison therefore supports the following interpretation: the current 3 mm device-layer leg should be assessed relative to the prior 3.000 mm distal linkage/end-effector geometry, not relative to an arbitrary displacement threshold. Beam theory provides the expected stiffness trends, while the perforation area fraction provides a preliminary correction for the reduced effective stiffness of the perforated SOI layer.

#### 5.4.3.2 Finite Element Estimation of Device-Layer Leg Deflection

Finite element analysis was used to estimate the bending response of the current 3 mm SOI device-layer leg under representative loading and to compare the result against the displacement scale reported for the prior distal linkage/end-effector design. The simulation was performed in SolidWorks using a nonlinear static analysis, as shown in Fig. 5.38. The current full-size model was loaded with a transverse force of

$$F = 10 \text{ mN}. \tag{5.44}$$

Under this loading condition, the distal end deflected

$$\delta_{\text{FEA}} = 0.7269 \text{ mm}. \tag{5.45}$$

The corresponding effective secant stiffness is

$$k_{\text{FEA}} = \frac{F}{\delta_{\text{FEA}}}. \tag{5.46}$$

Substituting the applied load and simulated displacement gives

$$k_{\text{FEA}} = \frac{0.010 \text{ N}}{0.0007269 \text{ m}} \approx 13.76 \text{ N/m}. \tag{5.47}$$

Equivalently,

$$k_{\text{FEA}} \approx 0.01376 \text{ N/mm}. \tag{5.48}$$

The corresponding compliance is

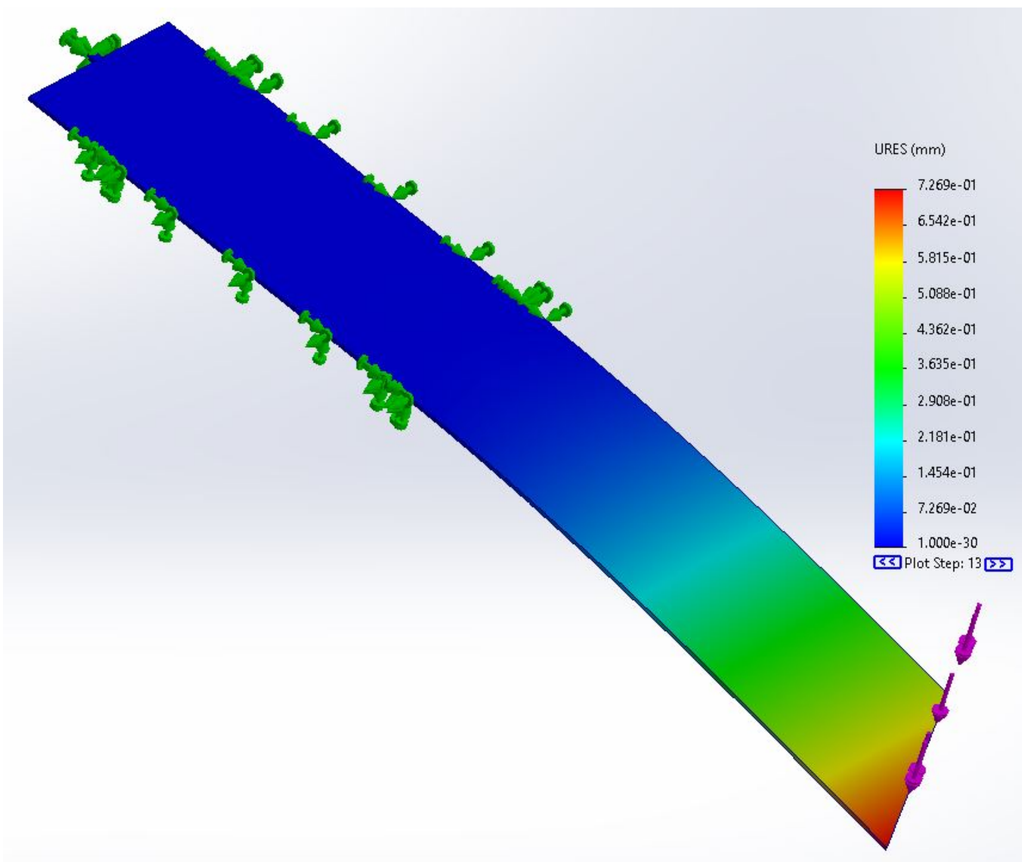


Figure 5.38: Depicted here is the screenshot of the resultant deflection heatmap of the nonlinear static analysis from the SolidWorks 3D CAD of the non-perforated device-layer leg. The colorbar shows a maximum deflection of 0.7269 mm and a minimum of $1 \times 10^{-3}$ mm where the colors correspond to the distal end and the fixed end, respectively.

$$C_{\text{FEA}} = \frac{\delta_{\text{FEA}}}{F} = \frac{0.7269 \text{ mm}}{10 \text{ mN}} \approx 0.07269 \text{ mm/mN}. \tag{5.49}$$

This result is directly relevant to the comparison with the prior distal linkage/end-effector mechanism. The prior work distal linkage/end effector had an estimated distal-tip flexure of

$$\delta_{\text{prior},-z} = 2.5 \text{ mm} \tag{5.50}$$

in the $-z$ direction and

$$\delta_{\text{prior},+x} = 0.5 \text{ mm} \tag{5.51}$$

in the $+x$ direction as observed from video footage [120]. The current finite element result of 0.7269 mm under a 10 mN transverse load is therefore within the same order of magnitude as the prior $-z$-direction distal-tip displacement.

The ratio between the current simulated deflection and the prior $-z$-direction displacement is

$$\frac{\delta_{\text{FEA}}}{\delta_{\text{prior},-z}} = \frac{0.7269 \text{ mm}}{2.5 \text{ mm}} \approx 0.29. \tag{5.52}$$

Thus, the simulated current leg deflection is approximately 70% smaller than the prior reported $-z$-direction displacement.

This places the current leg within the same millimeter-scale compliance regime as the prior distal linkage/end-effector design. This comparison is significant because it is made against the distal linkage geometry alone rather than the entire prior linkage mechanism. The finite element result therefore suggests that the current 3 mm SOI device-layer leg is capable of reaching displacement magnitudes comparable to those demonstrated in the previous perforated linkage-based leg work.

If the finite element result in Eq. 5.45 corresponds to the non-perforated current geometry, then the perforated version would be expected to deflect more under the same load. Using the first-order area-fraction correction from Eq. 5.40, the estimated perforated deflection is

$$\delta_{\text{perforated,est.}} \approx \frac{\delta_{\text{FEA}}}{\eta_A} = \frac{0.7269 \text{ mm}}{0.673} \approx 1.08 \text{ mm}. \tag{5.53}$$

Thus, the perforated version of the current leg is preliminarily estimated to deflect approximately 1.08 mm under the same 10 mN load. This estimated value lies between the prior estimated $-z$-direction and $+x$-direction distal-tip flexure.

The finite element result therefore supports the central design argument: the current 3 mm SOI device-layer leg is not being evaluated against an arbitrary displacement threshold, but against the displacement regime demonstrated by the prior distal linkage/end-effector. The simulated non-perforated deflection of 0.7269 mm, together with the estimated perforated deflection of approximately 1.08 mm, suggests that the current leg geometry remains mechanically compatible with millimeter-scale motion.

See Fig. 5.39 for the 3D CAD assembly of the rectangular device-layer approach with hat chip.

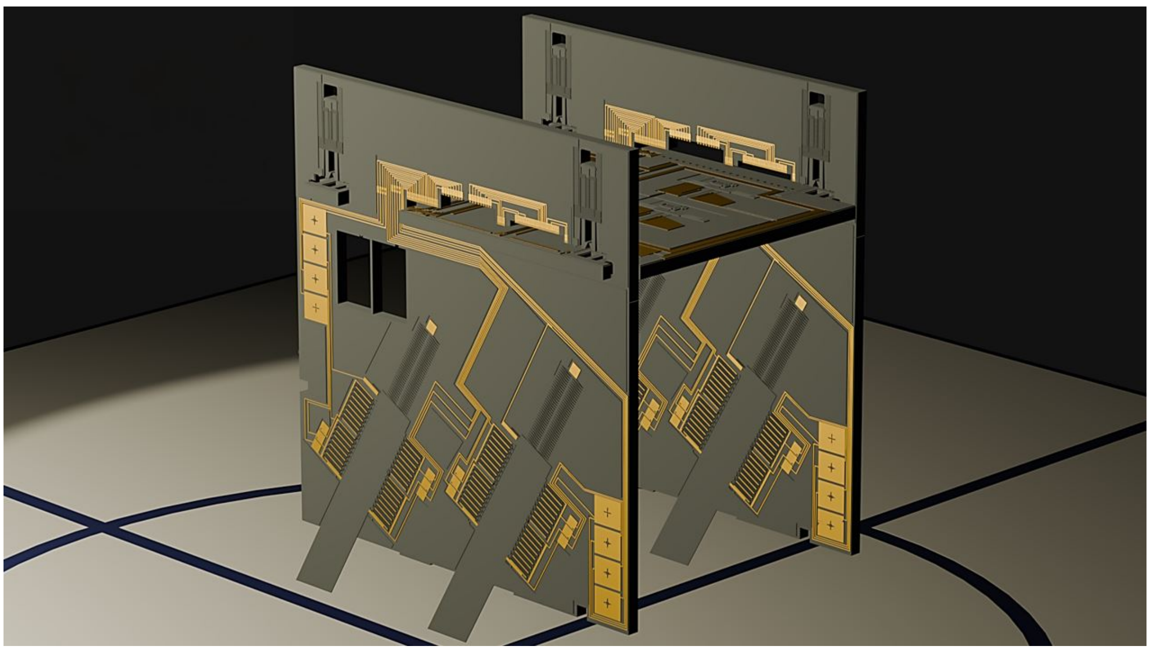

Figure 5.39: Depiction of the 3D CAD assembly of the rectangular device-layer legged walker with hat chip. The circle on the walking surface has radius 2.5 *cm*.

#### 5.4.3.3 Fabrication Outcomes

During this fabrication cycle, approximately eight chips were produced using the same fabrication approach as the prior designs. However, due to unforeseen circumstances, this author was unable to test, validate, or characterize the chips in person.

## 5.5 Self-Righting Approach (v3)

### 5.5.1 Motivation

This work began as a separate project aimed at producing locomotion through controlled flipping of a cubic robot while retaining self-righting capability. This work was also inspired by the DARPA SHRIMP initiative in the ways described in Table 5.7 and further by the work of the Lin Lab [121] and the Full Lab [122], as well as other works on robotic self-righting [123, 124].

### 5.5.2 Problem Statement

The DARPA SHRIMP Challenge designated the robot envelope as less than 1 $cm^3$ with a mass below 1 g while maintaining power and autonomy.

Here, the primary focus was not autonomy or power, but the mechanical capability required for the robot to overturn, or self-right, within the prescribed envelope.

First, the initial design considerations assumed a simple cubic structure with the COM at the geometric center of the robot body and negligible COM change during actuation. To accomplish this, the robot would be restricted to actuation via the device layer SOI because it represented a significantly smaller fraction of the total mass than the substrate layer, making it reasonable to neglect actuator-induced COM shifts under a quasi-static, non-inertial assumption.

Second, it was assumed that given the mass of 1 g as the upper limit, larger 15 mN motors would be used. This confined the design space significantly as the motor itself has minimum dimensions of 3 mm by 4.765 mm, not including probe pads, secondary metal traces, silicon buffer stand-offs, or the shuttle. This reduces the usable design space by approximately 1/8.

Third, concern existed that the 3D structure would tip onto its face if an asymmetric approach was taken. As such, a simplified approach using multiple chips with symmetric self-righting mechanisms was selected.

Depicted in Fig. 5.40 is the simplified concept for self-righting using an end-effector. See Fig. 5.41 for the 3D model of the SRA robot and Fig. 5.42 for the conceptualized final robot design as a self-rolling die.

### 5.5.3 Mechanical Design

The self-righting robot utilizes a linkage-based design. The linkage layout is shown in Fig. 5.43, with the corresponding linkage parameters summarized in Table 5.8 and the angle definitions summarized in Table 5.9.

Table 5.7: Relationship between self-righting capability and DARPA SHRIMP microrobotic performance goals.

| **SHRIMP Capability Area** | **Relevance of Self-Righting** |
|---|---|
| Survivability after jumps | High-jump and long-jump maneuvers require landing after impulsive motion. If the robot lands inverted or in an unusable posture, self-righting enables recovery without external reset. |
| Obstacle traversal | Steeplechase-style locomotion can induce rollovers, pitch instabilities, or partial inversion when the robot contacts obstacles. Self-righting improves robustness after failed traversal attempts. |
| Vertical ascent | Climbing or inclined locomotion increases the probability of falling, slipping, or rotating into an unfavorable body orientation. Self-righting provides a recovery mode after such failures. |
| Untethered autonomy | A core feature of SHRIMP-scale systems is operation without human intervention. Self-righting supports this objective by allowing the robot to resume locomotion after inversion. |
| Field robustness | Disaster-recovery and confined-environment applications involve irregular terrain, rubble, and unpredictable contact conditions. Self-righting helps preserve mission continuity in these unstructured environments. |
| Object interaction and manipulation | Tasks such as rock piling require repeated contact with external objects. These interactions can destabilize the robot, making self-righting useful as a secondary recovery behavior. |

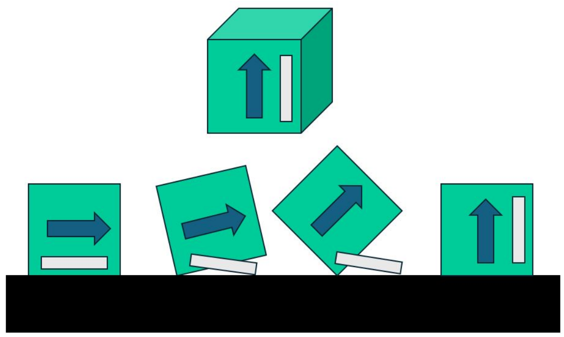

Figure 5.40: Diagram showing the conceptual progression of the self-righting robot showing simplified versions of the required motion. The diagrams show (Top) the robot upright with arrow depicting the direction of the top/head of the robot and a rectangle representing the end effector. (Bottom Row) Four diagrams showing the progression of the self-righting mechanism as seen from the front of the robot. From left to right the depictions start from the robot being overturned on its side, the next showing initiation of self-righting by rotating out the end-effector linkage, then showing the robot at approximately 45° angle with the end-effector still engaging the ground surface, and on the far-right, showing the robot fully returned to its right-side-up position with end-effector linkage returned to its resting position.

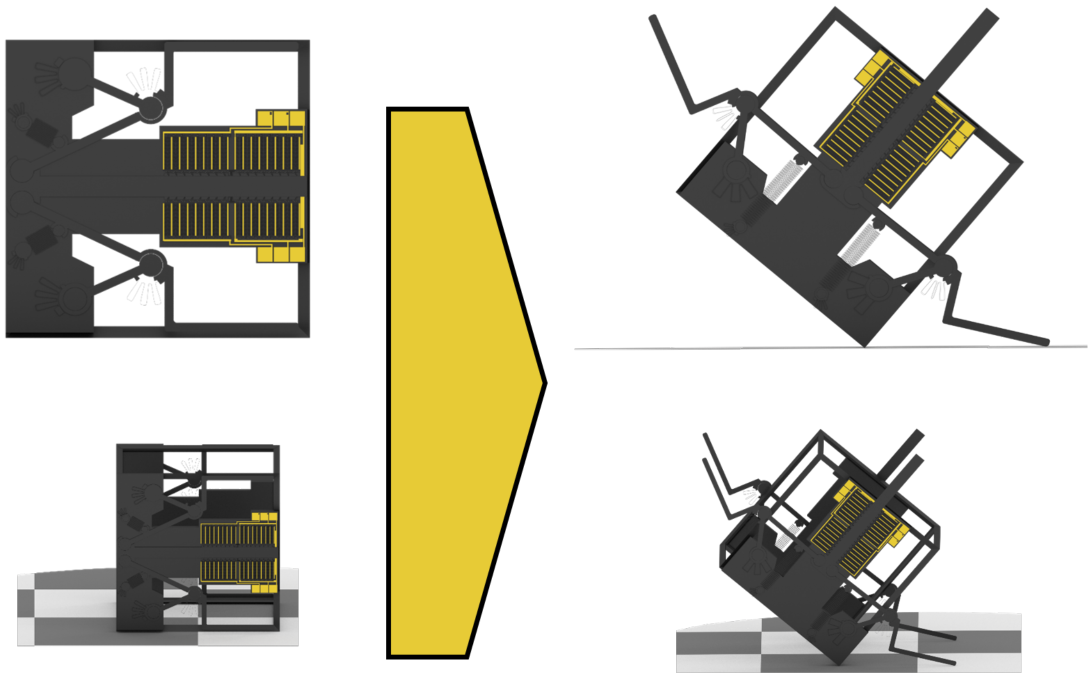

Figure 5.41: Image of 3D CAD Blender showing the self-righting device overturned on the left and self-righting on the right. Top row shows front-facing perspective and bottom row shows a perspective view.

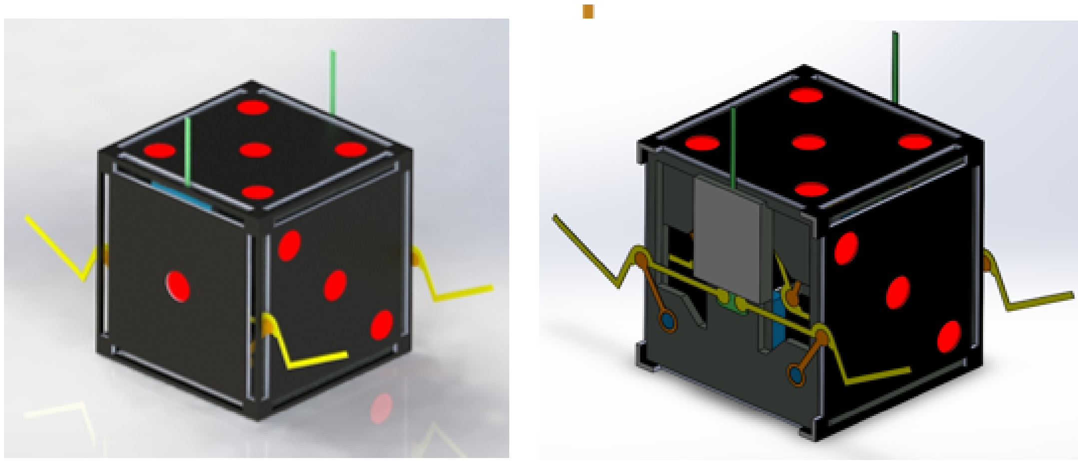

Figure 5.42: Depiction of the 3D CAD of an assembled self-righting actuator within a die. (Left) Actuators extended with the die face cover on. (Right) Actuators extended with die face cover removed.

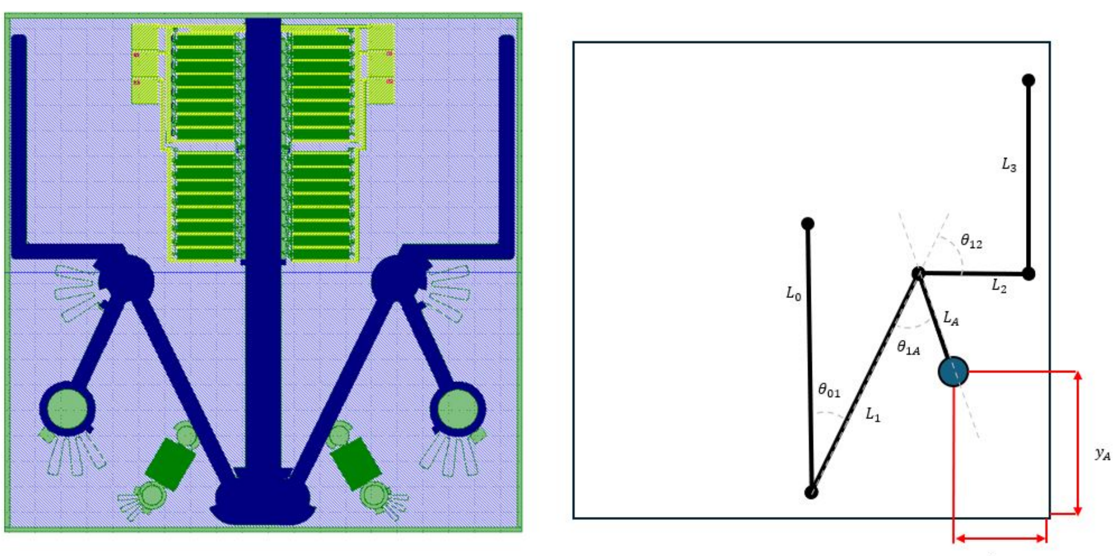


Figure 5.43: Depicted here is an overlay of the linkage structure on the 2D CAD KLayout screenshot. This image corresponds to Table 5.8.

Table 5.8: Self-righting linkage model parameters used in the MATLAB simulation.

| **Parameter** | **Value** | **Description** |
|---|---|---|
| $L_0$ | 5.000 mm | Vertical actuator/shuttle linkage |
| $x_{L_0}$ | 5.000 mm | Fixed body-frame $x$ position of $L_0$ |
| Initial bottom of $L_0$ | 0.250 mm | Initial $y$ position of the $L_0$--$L_1$ joint |
| Initial top of $L_0$ | 5.250 mm | Initial $y$ position of the top of $L_0$ |
| Actuator stroke | 4.000 mm | Imposed upward shuttle stroke |
| $L_1$ | 5.130 mm | Main linkage from bottom of $L_0$ to central joint |
| $L_{\text{anchor}}$ | 2.542 mm | Linkage from fixed body anchor to central joint |
| $L_2$ | 2.100 mm | Distal linkage rigidly coupled to $L_1$ |
| $L_3$ | 5.000 mm | End-effector linkage with frictionless floor contact |
| Linkage width | 0.300 mm | Common linkage width |
| Initial anchor position in world frame | $(2.235, 1.528)$ mm | Prescribed initial anchor coordinate before body-floor correction |
| Body contact condition | No slip | Body contact point fixed in the world frame |
| $L_3$ contact condition | Frictionless | Vertical floor constraint with horizontal sliding allowed |
| Non-contacting members | $L_0$, $L_1$, $L_{\text{anchor}}$, $L_2$ | Ignored for floor-contact interaction |
| Number of stroke steps | 151 | Number of evaluated actuator-stroke configurations |
| Body-angle search window | 35.0° | Search window used in the contact solve |

Table 5.9: Self-righting linkage angle definitions. Angles are measured counter-clockwise from the positive horizontal axis of the robot body frame unless otherwise stated.

| **Angle** | **Symbol** | **Value** | **Description** |
|---|---|---|---|
| Input linkage orientation | $\theta_0$ | 90.0° | $L_0$ remains parallel to the body-frame $y$ axis |
| Main linkage orientation | $\theta_1$ | 64.3° | Orientation of $L_1$ relative to the body-frame horizontal axis |
| Anchor linkage orientation | $\theta_A$ | 114.4° | Orientation of $L_A$ relative to the body-frame horizontal axis |
| Horizontal distal linkage orientation | $\theta_3$ | 0.0° | $L_3$ remains parallel to the body-frame horizontal axis |
| End-effector relative angle | $\theta_{34}$ | 90.0° | Nominal rigid angle between $L_3$ and $L_4$, assuming $L_4$ is vertical |
| End-effector absolute orientation | $\theta_4$ | 90.0° | Nominal absolute orientation of $L_4$ in the body frame |
| Body-frame to world-frame rotation | $\theta_{\text{body},0}$ | 90.0° | Initial condition placing the robot side parallel to the ground |

### 5.5.4 Self-Righting Linkage Model

A planar linkage model was developed to evaluate the first-stage self-righting motion of the robot during the imposed actuator stroke. The model intentionally reduces the mechanism to the minimum set of geometric constraints needed to study whether the linkage sweep can generate a favorable body rotation while preserving the experimentally relevant contact assumptions. The robot body is modeled as a rigid square body with a fixed center of mass at the geometric center. The linkage assembly is represented by a set of rigid line segments connected through ideal revolute or rigidly coupled joints. This abstraction omits elastic deformation, joint compliance, and out-of-plane effects, but it provides a useful first-order visualization of the body-linkage geometry during the self-righting stroke.

The coordinate transformation used in the simulation maps the robot-frame positive $y$-axis into the world-frame positive $x$-axis, while the robot-frame positive

$x$-axis maps into the world-frame negative $y$-axis. This orientation corresponds to the robot initially resting on its side in the world frame. The lower body contact point is treated as a no-slip contact with the ground, while the distal end of $L_3$ is treated as a frictionless contact point. Thus, the body contact point remains fixed in the world frame, whereas the $L_3$ end-effector is constrained vertically by the floor but is allowed to slide horizontally. All other linkage elements are excluded from ground contact in the model. This contact structure was selected to isolate the intended self-righting interaction between the body and the distal end-effector while avoiding artificial reaction forces from intermediate links.

The actuator linkage $L_0$ is constrained to remain on the robot-frame centerline at $x = 5.000$ mm. The $L_1$ linkage is connected to the bottom of $L_0$, and the initial bottom point of $L_0$ is shifted upward to match the current linkage layout. The imposed input is a vertical stroke of $L_0$, which drives the $L_0$--$L_1$ joint upward in the body frame. The central joint location is then solved using the geometric closure between $L_1$ and the fixed body-anchor linkage. The distal links $L_2$ and $L_3$ are treated as a rigidly coupled output chain: $L_2$ rotates with $L_1$, and $L_3$ rotates with $L_2$. This representation captures the current design intent that the distal linkage assembly behaves as a single rigid output member after the main rocker motion is established.

The simulation output is presented as static sweep plots rather than as an animation. Each sweep overlays a finite set of configurations sampled across the actuator stroke, allowing the evolution of the linkage and body pose to be inspected directly. The robot-frame sweep in Fig. 5.44 shows the internal linkage motion relative to the body. This plot is useful for verifying that the prescribed $L_0$ centerline constraint, the bottom connection between $L_0$ and $L_1$, and the rigid coupling between $L_1$, $L_2$, and $L_3$ are represented consistently in the body frame.

The corresponding world-frame sweep is shown in Fig. 5.45. In this view, the ground line, no-slip body contact point, and frictionless $L_3$ contact samples are shown together with the transformed body and linkage configurations. This plot provides the clearest visual interpretation of the modeled self-righting interaction: the body remains constrained at its no-slip floor contact while the distal $L_3$ tip maintains a vertical floor constraint and is allowed to slide horizontally. The overlay also shows how the imposed body-frame linkage stroke translates into world-frame body rotation and center-of-mass motion.

The center-of-mass trajectory is isolated in Fig. 5.46. This plot is used to assess whether the actuator stroke moves the body center of mass in a direction favorable for self-righting. Since the model is restricted to the actuator-driven stroke and does not include a second gravity-driven phase, the trajectory should be interpreted as the kinematic and contact-constrained motion produced directly by the linkage actuation. A useful design outcome is indicated when the COM is displaced toward

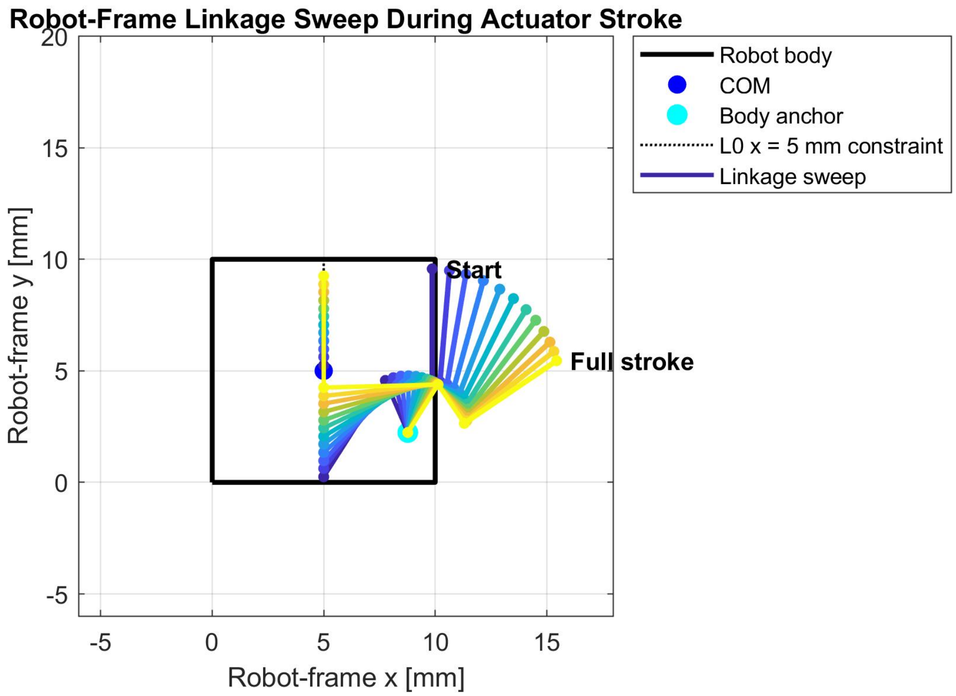


Figure 5.44: Robot-frame linkage sweep for the self-righting model. The body outline, fixed body anchor, center of mass, $L_0$ centerline constraint, and sampled linkage configurations are shown in the robot frame. The plot verifies the imposed actuator path and the rigid distal-link coupling during the prescribed stroke.

a configuration in which gravity can continue the turnover or reduce the required additional actuation.

The coordinate history in Fig. 5.47 separates the world-frame $x$- and $y$-components of the COM displacement as functions of actuator stroke. This representation is useful for comparing future linkage variants because it converts the sweep into a more quantitative measure of body motion. In particular, the world-frame vertical COM coordinate indicates whether the linkage raises or lowers the body mass during the stroke, while the horizontal coordinate indicates the corresponding lateral shift caused by the no-slip body contact and frictionless $L_3$ contact constraints.

Finally, Fig. 5.48 summarizes the body rotation, estimated angular velocity, and gravity-torque measures over the actuator stroke. These plots should be treated as diagnostic outputs rather than a complete dynamic prediction, because the model uses geometric contact constraints and a pseudo-time stroke parameter rather than a fully

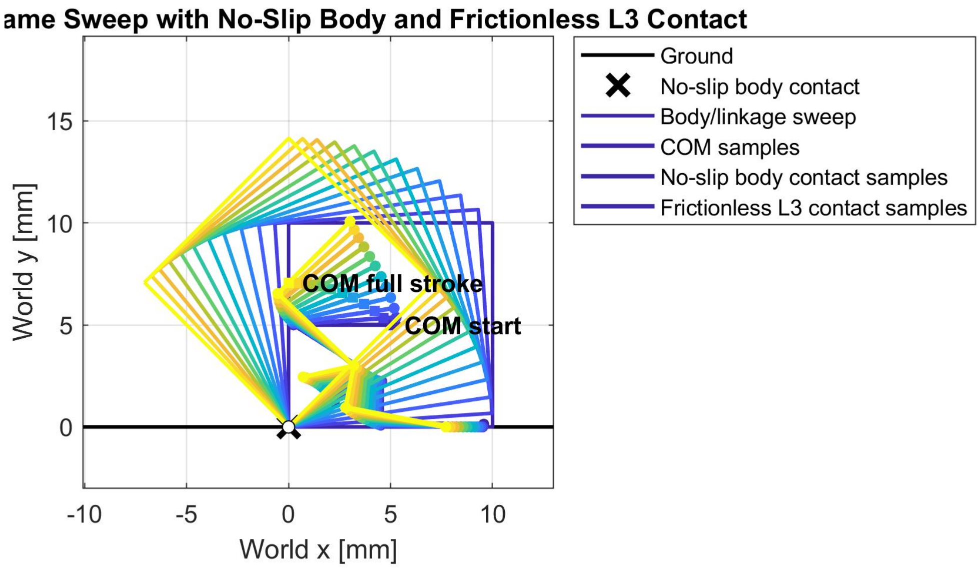


Figure 5.45: World-frame sweep of the robot body and linkage assembly during the actuator stroke. The body has no-slip contact with the ground, while the distal $L_3$ end-effector is modeled as a frictionless ground contact. The overlay illustrates the body rotation and linkage-ground interaction generated by the full actuator stroke.

resolved multibody contact simulation. Nevertheless, the summary provides a compact way to evaluate whether the linkage stroke produces monotonic or discontinuous body rotation, whether the contact solve remains smooth, and how the gravity moment changes relative to the no-slip body contact and the instantaneous frictionless $L_3$ contact.

Overall, this model provides a compact design-screening tool for comparing self-righting linkage geometries before higher-fidelity dynamic simulation or fabrication. Its primary value is not in predicting exact transient dynamics, but in revealing whether a proposed linkage architecture produces the desired contact-constrained body motion over the available actuator stroke.

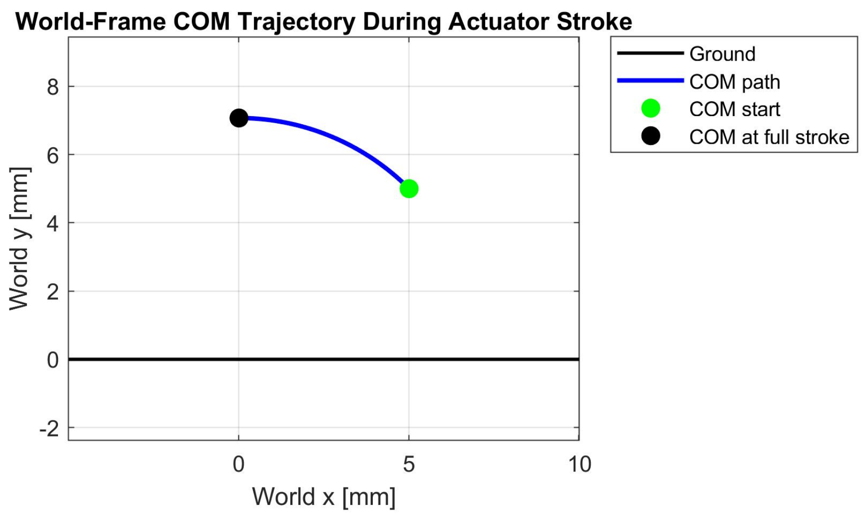


Figure 5.46: World-frame center-of-mass trajectory during the actuator stroke. The start and full-stroke COM positions are marked to show the net displacement generated by the self-righting linkage under the specified body and $L_3$ contact constraints.

### 5.5.5 Fabrication Outcomes

Of the sixteen fabricated devices, six were viable for initial testing. The ten chips which were not viable had varying issues: two had over-etched the motors and four were dropped, destroying the devices and the rest had an incomplete oxide etch beneath the shuttle. The remaining six showed varying degrees of functionality with some of the linkages contorting out of the plane in various cycles of the run. Of these only two were capable of running the full sweep of their linkage folding capability. During an attempted repositioning for improved microscope visibility, the devices were accidentally dropped and destroyed. See Fig. 5.49 and Fig. 5.50.

## 5.6 Small Approach (v4) and Future Work

While the above work was a systematic approach developed as multiple different experiments to test and solve for interconnected issues, here the overall approach was

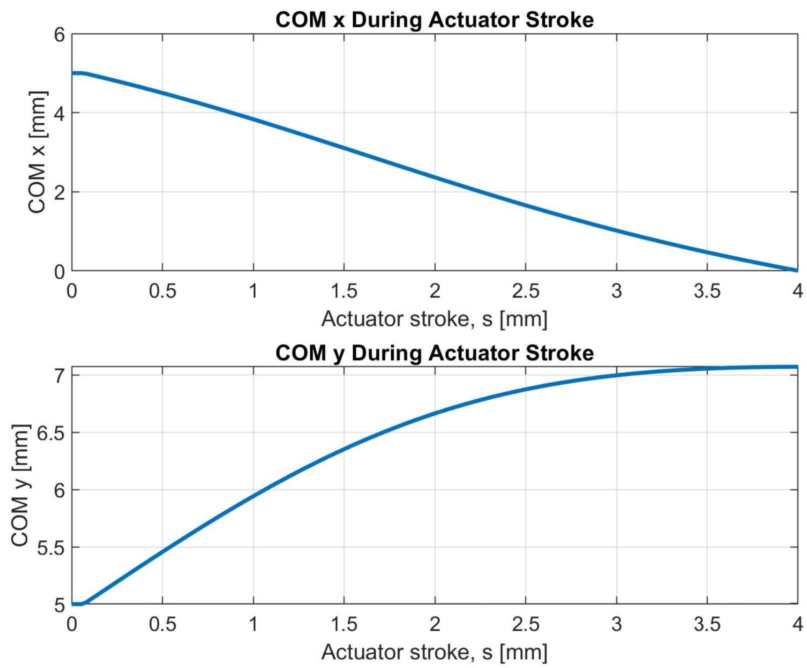


Figure 5.47: World-frame center-of-mass coordinate histories during the actuator stroke. The upper and lower plots show the COM $x$- and $y$-positions, respectively, as functions of the imposed $L_0$ stroke.

to start from a more centralized theme. The centralized theme is an overall reduction in size while maintaining benefits of prior designs. As no clear better design won out with respect to the linkage approach vs the straight-legged approach, it was decided that both would be kept.

From lessons learned on the previous set of Quadrupedal Walkers from simulation, experimentation, fabrication, and hand calculations it was clear that the chips were too large and too tall overall for a nimble and robust walker robot and to be stowed aboard the BLISS spacecraft as a rover.

As such, the small approach was employed.

As shown in Fig. 5.51, the reduced size architecture includes smaller versions of all components: hat chip, with ZIF chip integration for the two side leg chips and the two front and aft self-righting chips. While this work does not sufficiently show that this work fully addresses the need for a smaller robot/rover, as full simulation and experimentation are still necessary, this does serve as a motivation for future work.

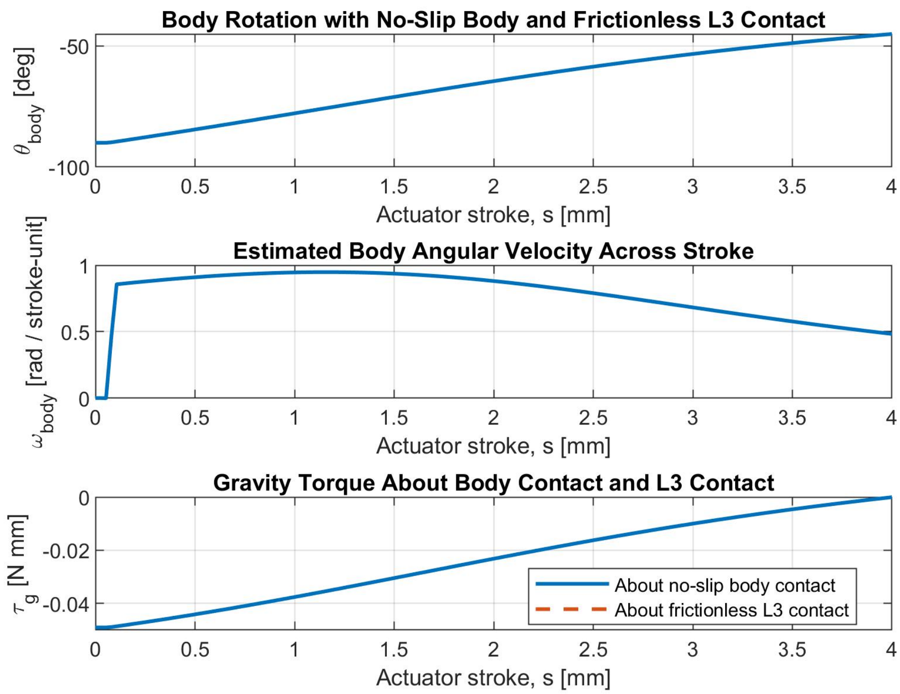


Figure 5.48: Summary of the actuator-driven self-righting stroke. The plots show body rotation, estimated angular velocity across the stroke, and gravity-torque measures about the no-slip body contact and the frictionless $L_3$ contact.

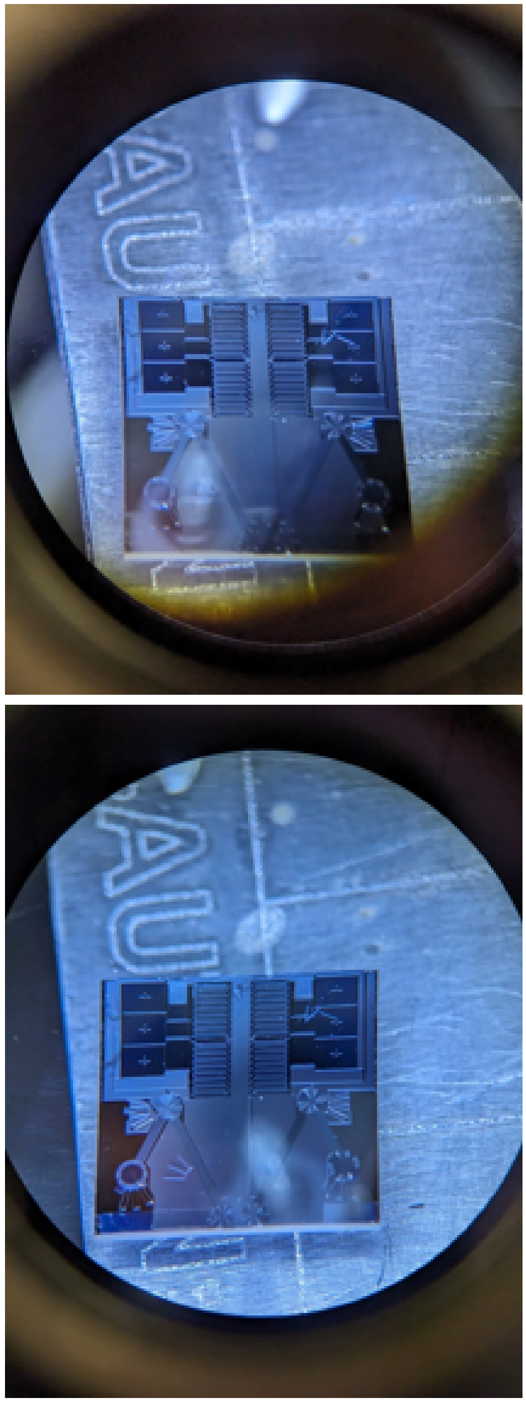

Figure 5.49: Photograph of the SRA device in the vacuum pick and place station through microscope taken with phone camera during removal of sacrificial SOI. (Top) Left eyepiece and (Bottom) right eyepiece.

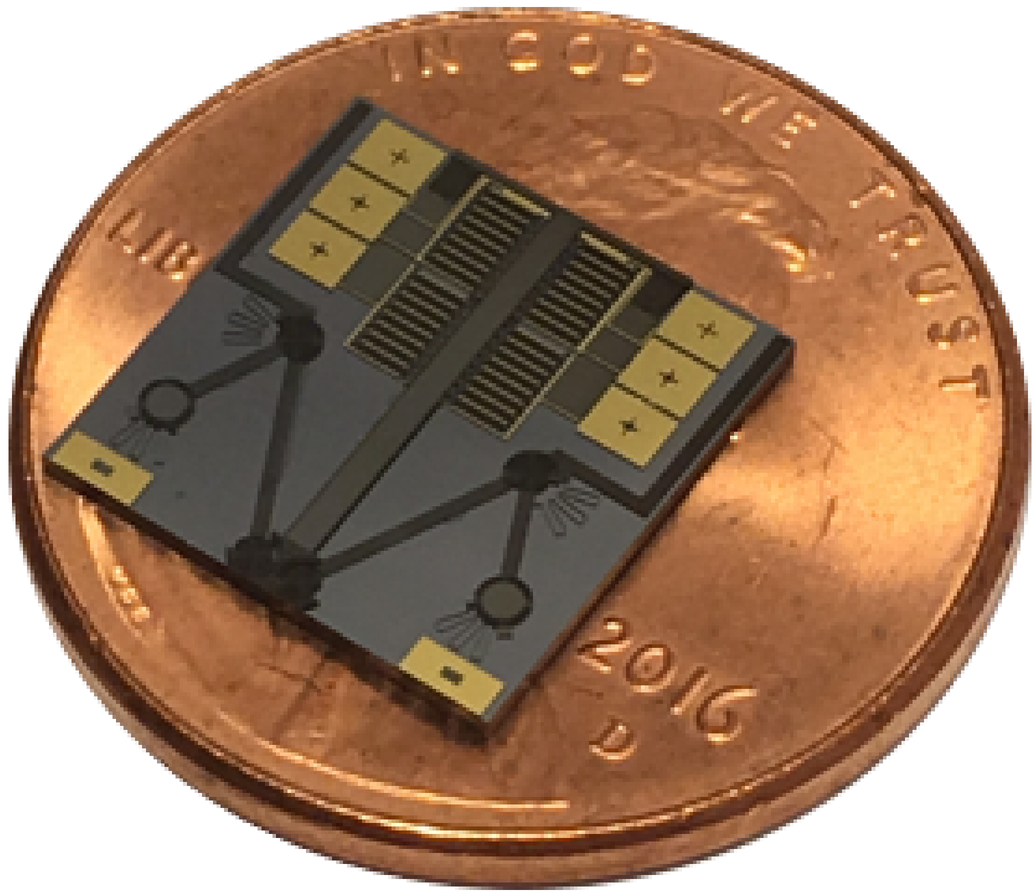


Figure 5.50: SRA on a penny.

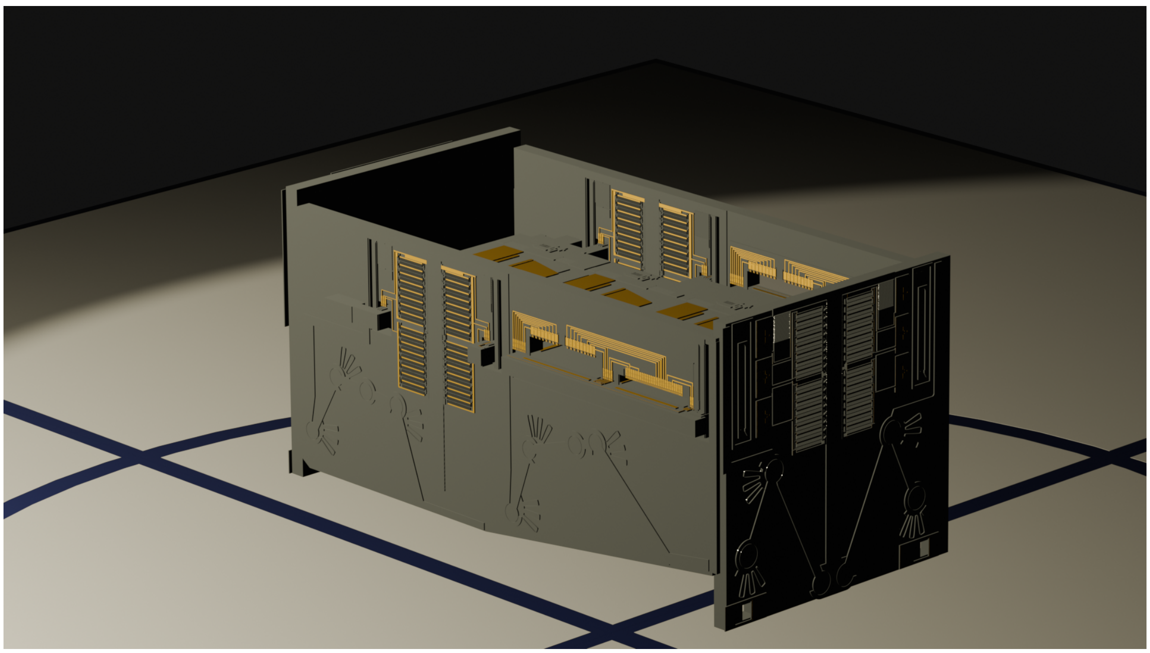

Figure 5.51: Image of the 3D CAD Blender model for the small approach. Of note, the smaller hat chip shown here is not sufficiently mapped out and only contains placeholders for the necessary components, as laid out by Gomez [7], and a reduced size version of the ZIF architecture.

# Chapter 6

# The Helm: MEMS for Actuation and Control of Small Solar Sail Tethers (MAST)

## 6.1 Introduction

The objective of this chapter is to develop and evaluate a microelectromechanical-system (MEMS) actuation approach for direct mechanical control of small solar-sail tethers. The broader spacecraft architecture motivating this work is the Berkeley Low-cost Interplanetary Solar Sail (BLISS), in which a lightweight sail, carbon-fiber support structure, and miniature spacecraft payload are integrated into a compact propellantless spacecraft concept [2,125]. In that architecture, small changes in tether length or tether position can be used to alter the geometry of the sail-frame system and thereby provide a mechanism for shape control, trim, or steering authority without conventional reaction wheels, cold-gas thrusters, or other macroscopic attitude-control hardware.

The device developed in this chapter is referred to as MEMS for Actuation and Control of Small Solar Sail Tethers (MAST). The MAST concept uses MEMS inchworm motors to produce controlled, incremental, bidirectional linear motion of a silicon shuttle. The shuttle mechanically interfaces with a carbon-fiber tether connected to the solar-sail frame. In this configuration, tether displacement is produced directly by the MEMS device rather than through an intermediate macro-scale transmission. This approach is attractive for small solar-sail spacecraft because MEMS actuators provide high lithographic repeatability, compact form factor, batch fabrication, and the possibility of direct integration with on-chip electrical routing, end-stop sensing, and shuttle-position control.

This work builds on three prior technical foundations. First, Zoll et al. demonstrated MEMS-actuated carbon-fiber manipulation, establishing a precedent for using MEMS motors to control filament-like structural elements [126]. Second, Teal et al. developed related silicon MEMS inchworm-motor fabrication processes and robot-scale implementations [92]. Third, Rauf et al. modeled and experimentally characterized the nonlinear dynamics of gap-closing actuators (GCAs) and MEMS inchworm motors in different fluidic environments [113]. The present work differs from those prior demonstrations in the intended application, shuttle geometry, loading condition, and environmental objective. Here, the actuator is designed as a tether-control mechanism for a solar-sail spacecraft, with emphasis on loaded actuation and eventual operation under reduced-pressure, space-analogous conditions.

The chapter proceeds as follows. Section 6.2 defines the tether-actuation requirements that motivate the MAST device. Section 6.3 summarizes the relevant GCA and inchworm-motor operating principles. Section 6.4 describes the mechanical evolution from the substrate-shuttle design to the SOI-shuttle design. Section 6.5 introduces the pull-in/pull-out and inchworm-speed test structures used to evaluate actuator behavior. Section 6.6 describes the vacuum and Earth-analog testing approaches. Section 6.8 summarizes the experimental observations and design lessons. Section 6.9 concludes the chapter.

## 6.2 Design Requirements and System Role

### 6.2.1 Solar-Sail Tether-Control Objective

The MAST device is intended to provide linear actuation of carbon-fiber tethers connected to the perimeter structure of a thin-film solar sail. In the motivating spacecraft concept, the sail is supported by a carbon-fiber ring, while the sail membrane is made from a thin polymer film such as colorless polyimide (CP1). The tether-control problem is therefore mechanically simple in its local form: a tether must be advanced or retracted along a single axis with sufficient force, resolution, and repeatability to modify the boundary condition imposed on the sail-frame system.

At the device level, this requirement leads to a linear shuttle architecture. A carbon-fiber tether is placed on or mechanically coupled to the shuttle, and the shuttle is displaced by MEMS inchworm motors. The desired output motion is bidirectional, quasi-static or low-speed, and compatible with electrical probing during laboratory characterization. Because the sail-scale structure is orders of magnitude larger than the MEMS actuator, the tether interface must also be tolerant of modest alignment errors, local friction, and mechanical compliance in the carbon fiber.

### 6.2.2 Actuator-Level Requirements

The principal actuator-level requirements are:

1. **Bidirectional linear motion:** the device must push or pull the tether along the axis of the carbon fiber.
2. **Incremental displacement control:** the inchworm architecture should allow displacement to be accumulated in discrete steps.
3. **Tether compatibility:** the shuttle must provide a mechanically robust interface to the carbon fiber without causing premature fracture, slipping, or excessive parasitic rotation.
4. **Electrical accessibility:** probe pads must be available for GCA drive signals, locking-tab actuation, shuttle drive signals, and end-stop detection.
5. **Reduced-pressure compatibility:** the actuator should be testable under vacuum conditions relevant to the reduction of gas damping and eventual spacecraft operation.
6. **Fabrication compatibility:** the geometry must remain compatible with the available SOI MEMS fabrication process, release process, metallization, and probing constraints.

These requirements motivate a design in which opposing MEMS motor banks are arranged around a central shuttle. The motor banks provide push--hold--push--hold actuation in opposite directions, allowing tether displacement to be accumulated in either direction along the shuttle axis.

## 6.3 Operating Principle

### 6.3.1 Gap-Closing Actuator Behavior

The primary force-generating elements in the MAST device are electrostatic gap-closing actuators. A GCA consists of interdigitated or adjacent silicon fingers separated by a lithographically defined gap. When a voltage is applied between the moving and fixed electrodes, electrostatic attraction reduces the gap and produces lateral motion of the moving structure. The resulting force depends on the electrode geometry, the applied voltage, the instantaneous gap, and the mechanical restoring stiffness of the suspension.

In the MAST implementation, the GCA does not directly drive the spacecraft tether over the full travel range. Instead, each GCA is used as a local actuator within an inchworm motor. This arrangement converts small, repeatable GCA strokes into a larger accumulated shuttle displacement. The GCA pull-in voltage, pull-out behavior, and dynamic response are therefore critical because they determine the voltage range over which the motor can be reliably stepped.

### 6.3.2 Inchworm Motor Stepping Sequence

The inchworm motor architecture uses a sequence of clamp and drive actions to produce net shuttle displacement. In a simplified forward step, one locking or holding element constrains the shuttle while another actuator advances the shuttle by one stroke. The first holding element is then released, the second element holds position, and the drive actuator resets. Repetition of this sequence produces net translation. Reversing the order of the holding and drive sequence produces motion in the opposite direction.

For MAST, the motor banks are arranged in opposing configurations so that the shuttle can be driven bidirectionally along the tether axis. This architecture is beneficial for solar-sail tether control because it provides a mechanically direct means of increasing or decreasing tether displacement. In the present design, the actuation concept targets approximately micrometer-scale incremental control, with the intended shuttle step size set by the inchworm-motor geometry and the local pawl/shuttle engagement behavior.

## 6.4 Mechanical Design

### 6.4.1 Overall Device Architecture

The MAST device consists of a central shuttle, opposing GCA-driven inchworm motor arrays, probe pads, return springs, end-stop structures, and carbon-fiber mounting or tether-interface regions. The central shuttle forms the mechanical output of the chip. GCA arrays are placed adjacent to the shuttle, and their motion is rectified by pawl-like or locking features that engage the shuttle during the inchworm stepping sequence. Return springs restore moving elements after actuation, while end stops limit travel and provide a potential electrical trigger for end-of-travel detection.

The design evolved through two main device generations. The first generation used a substrate-shuttle architecture intended to maximize structural stiffness. The second generation used an SOI-shuttle architecture that improved integration with the released silicon device layer and reduced the alignment and fragility issues observed in the first implementation.

### 6.4.2 Substrate-Shuttle MAST Design (v1)

The first MAST implementation used a substrate-based shuttle, see Fig. 6.1 for the 2D CAD and Fig. 6.2 for the 3D CAD. This design was initially selected because a substrate-supported shuttle provides high bending stiffness and a mechanically robust platform for coupling to the carbon-fiber tether. The high stiffness was expected to reduce shuttle deformation during tether loading and probing.

However, initial testing revealed important practical limitations. The return springs were susceptible to fracture, and once the springs failed the shuttle could become misaligned. After misalignment, attempts to restore the shuttle position frequently damaged the motor pawls, limiting the ability to continue testing the same die. Thus, although the substrate-shuttle design provided desirable structural rigidity, it was mechanically unforgiving during handling, probing, and post-failure recovery.

Twelve substrate-shuttle MAST chips were fabricated, see Fig. 6.3. Of these, eight were viable for testing. At a drive frequency of 10 Hz, the measured inchworm-motor speed was approximately $v_{\mathrm{IWM}} = 5 \pm 2\ \mu\mathrm{m/s}$ with pull-in voltages ranging from 84 V to 98 V. The large uncertainty in the measured speed indicates that device-to-device variability, intermittent stepping, stiction, or test-fixture limitations likely dominated the measured response. These observations motivated the transition to the SOI-shuttle design described in Section 6.4.3.

### 6.4.3 SOI-Shuttle MAST Design (v2)

The second MAST implementation replaced the substrate-shuttle approach with an SOI-shuttle architecture. This redesign was motivated by the failure modes observed in the v1 devices. By placing the shuttle and compliant suspension features within the SOI device layer, the v2 design reduced the dependence on substrate-level realignment and improved compatibility with the released MEMS structures, see Fig. 6.4 for the 2D CAD and Fig. 6.5 for the 3D CAD.

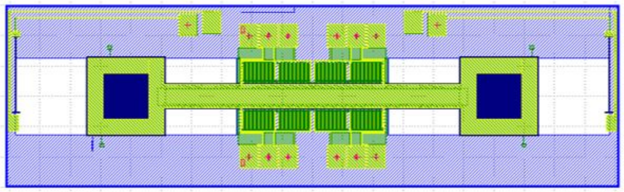

Figure 6.1: Two-dimensional KLayout layout of the substrate-shuttle MAST v1 design. The design uses a stiff shuttle structure intended to interface with a carbon-fiber tether while opposing MEMS inchworm motor banks provide bidirectional linear actuation.

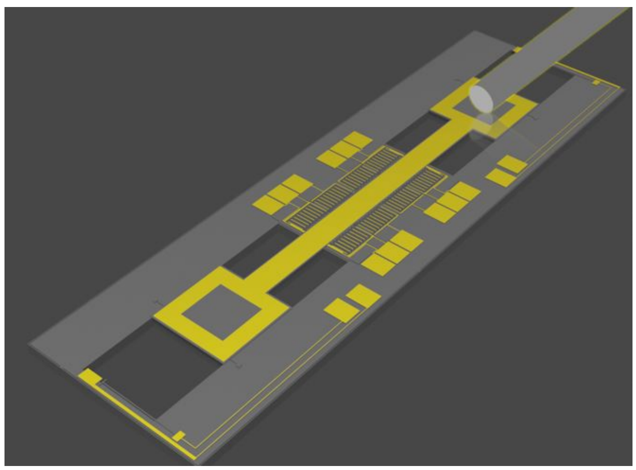

Figure 6.2: Three-dimensional rendering of the substrate-shuttle MAST v1 design. The rendering illustrates the intended mechanical relationship between the shuttle, actuator banks, probe regions, and tether-interface geometry.

The SOI-shuttle design retains the same functional objective as the v1 device: bidirectional linear displacement of a carbon-fiber tether. However, the mechanical layout is better matched to the MEMS fabrication process and the expected motion of the released structures. The shuttle is positioned between opposing GCA arrays, with probe pads and metal traces routed to support electrical actuation. Carbon-fiber mounting regions are included so that a tether can be positioned along the shuttle axis.

In the v2 design, the motors are arranged as two opposing groups of four motors each. This arrangement enables push--hold--push--hold stepping in both the forward and reverse directions. End-stop detectors are placed near the travel limits of the shuttle so that the device can, in principle, provide an electrical indication when

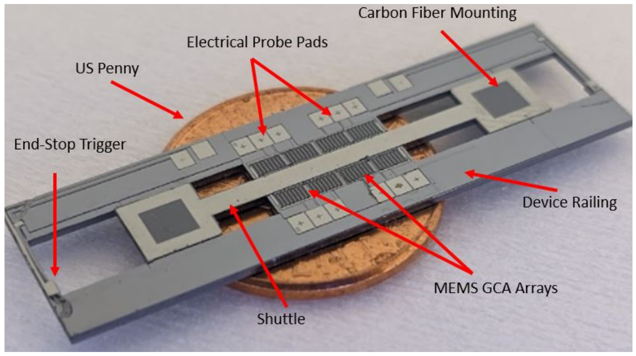


Figure 6.3: As-fabricated substrate-shuttle MAST v1 device shown on a U.S. penny for scale. The image highlights the chip-scale footprint of the actuator relative to a common macroscopic reference object.

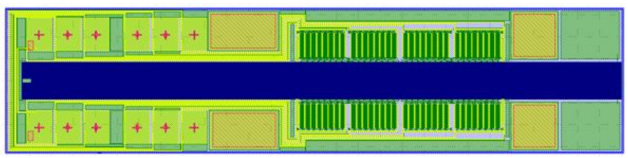

Figure 6.4: Two-dimensional KLayout layout of the SOI-shuttle MAST v2 design. The design places the shuttle and actuation features in the SOI device layer and arranges opposing motor banks around the tether-actuation axis.

the shuttle reaches the end of its available stroke. This feature is important for automated or semi-automated operation because it provides a direct mechanism for terminating motor drive before mechanical over-travel occurs. See Fig. 6.6 for the as-fabricated device.

## 6.5 Test Structures

### 6.5.1 Pull-In and Pull-Out Test Chips

Pull-in and pull-out (PIPO) test chips were designed to characterize GCA behavior independently of the full MAST shuttle. These structures are conceptually similar to the test devices used by Rauf et al. for GCA and inchworm-motor dynamic characterization [113]. The purpose of the PIPO chips was to evaluate how GCA pull-in voltage depends on finger geometry, particularly finger overlap length.

The PIPO array contains GCA test structures with varying finger lengths. The layout arranges the test cells so that the finger length increases across the array,

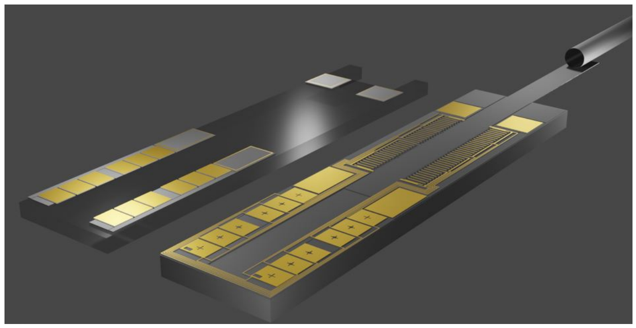

Figure 6.5: Three-dimensional rendering of the SOI-shuttle MAST v2 design with a carbon-fiber tether positioned on the shuttle. The rendering illustrates the intended tether-routing path and the mechanical interface between the fiber and the MEMS output stage.

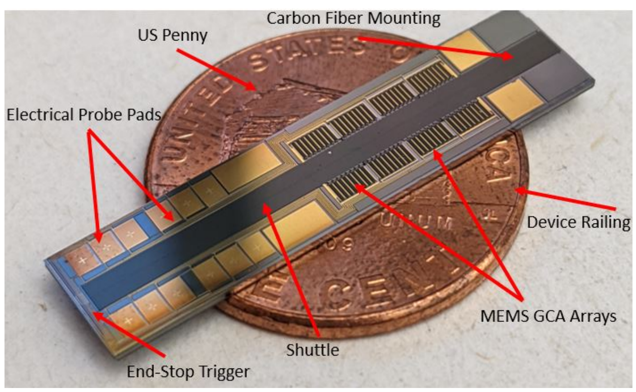


Figure 6.6: As-fabricated SOI-shuttle MAST v2 device shown on a U.S. penny for scale. The device includes a central shuttle, opposing MEMS GCA arrays, probe pads, carbon-fiber mounting regions, and mechanical rails that guide the shuttle motion.

allowing multiple geometries to be fabricated and inspected on a single die. This approach provides an efficient means of identifying voltage ranges and geometries that are compatible with the available probing equipment and desired actuation behavior.

The fabricated PIPO structures included arrays of GCA fingers with nominal finger lengths spanning approximately 25--100 $\mu$m, see Fig. 6.7. In the fabricated structures, pull-in voltage decreased as the finger overlap length increased, consistent with the expected increase in electrostatic actuation authority for longer engaged electrode geometries. The measured trend is shown in Fig. 6.11. The data indicate that shorter finger overlaps required pull-in voltages in the approximate range of 70--76 V, while longer overlaps produced pull-in near the mid-30 V to low-40 V range.

Metallization was also considered because the released silicon structures require sufficient electrical conductivity for reliable electrostatic actuation. TiN coatings with varying nominal thicknesses were investigated; however, the tested samples did not demonstrate the desired improvement in conductivity. As a result, further PIPO testing with that coating approach was not completed. This outcome suggests that future test structures should include a more systematic metallization study, including sheet resistance measurement, contact resistance measurement, and verification of coating continuity across released GCA fingers.

The PIPO structures require an electrical readout from the two end-stop structures. In this design, the corresponding readout nodes are routed to the top and bottom probe pads, as shown in Fig. 6.8. Because the end-stop structures must remain mechanically separated prior to actuation, they cannot be fabricated as permanently connected electrical nodes without eliminating the intended switching function or relying on a destructive release process. A post-fabrication connection mechanism was therefore incorporated into the layout. This function is provided by the wedge and locking-tab structure.

After fabrication and release, the locking tab is displaced laterally using a probe-station micromanipulator. In the orientation shown in Fig. 6.8, the locking tab is pushed to the left until it drives the wedge downward and the two features mechanically interlock. Once engaged, the wedge and locking tab form a mechanically stable contact path. Because the wedge is electrically connected to the upper probe pad, shown in yellow in Fig. 6.8, this post-fabrication engagement establishes an electrically conductive connection between the upper end-stop structure and the upper readout pad. This approach allows the end-stop and probe-pad structures to remain electrically isolated during fabrication while enabling a stable electrical connection to be formed during device preparation. The as-fabricated PIPO devices can be seen in Fig. 6.9 and Fig. 6.10

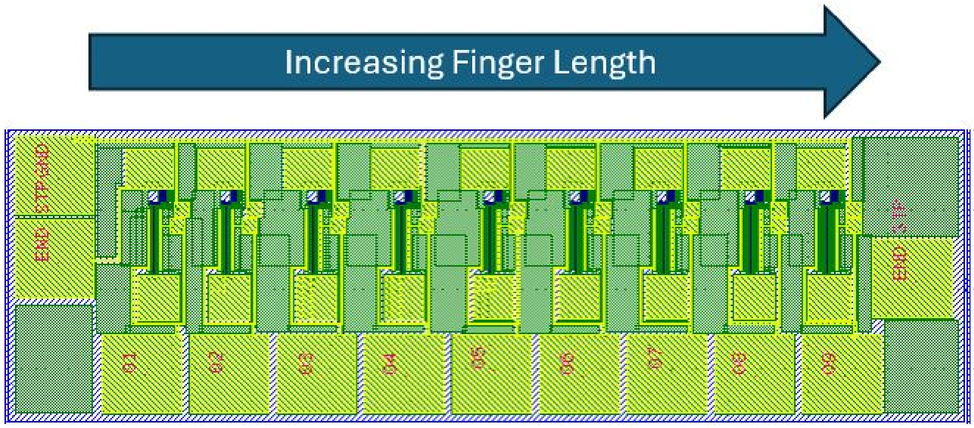


Figure 6.7: KLayout layout of the PIPO GCA test-chip array. The array contains multiple GCA cells with increasing finger length, enabling pull-in and pull-out behavior to be compared across geometries on a common die.

### 6.5.2 Inchworm Motor Speed Test Chips

In addition to the PIPO structures, inchworm motor speed test (IWMST) chips were designed to evaluate complete motor stepping behavior. Whereas the PIPO devices isolate GCA pull-in and pull-out behavior, the IWMST structures incorporate the shuttle, pawls, return springs, GCA fingers, probe pads, metal traces, and end-stop features needed to evaluate motor-level displacement, see Fig. 6.12.

The IWMST chips were designed with an end-stop detection feature at the end of travel, see Fig. 6.13. Two testing modes were considered. In the first mode, an electrical feedback loop would use the end-stop signal to terminate actuation when the shuttle reached the end of travel. This approach would require integration with a microcontroller or data-acquisition system, such as an Arduino-based trigger loop. In the second mode, the motor would be driven feedforward for a specified number of steps at a specified frequency, and the final shuttle position would be measured optically. The feedforward method is experimentally simpler, while the feedback method is more representative of an autonomous or instrumented device.

Although these IWMST devices were designed and fabricated (see Fig. 6.14), the full speed-characterization sequence was not completed in the present work. Nevertheless, the structures provide a useful design bridge between isolated GCA characterization and full MAST tether-control testing. They also identify the required infrastructure for future testing: synchronized high-voltage actuation, end-stop detection, optical displacement measurement, and automated image-based tracking

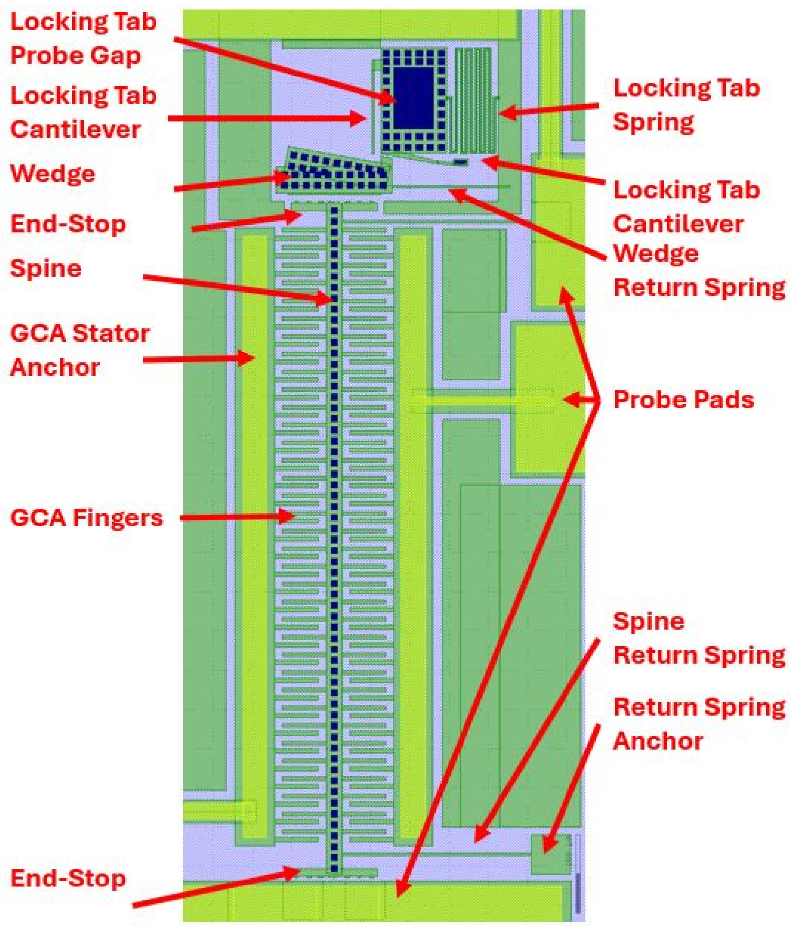


Figure 6.8: Zoomed KLayout layout of a single PIPO test cell. The labeled features include the locking-tab probe gap, locking-tab cantilever, wedge, end stop, spine, GCA stator anchor, GCA fingers, probe pads, return springs, and return-spring anchor.

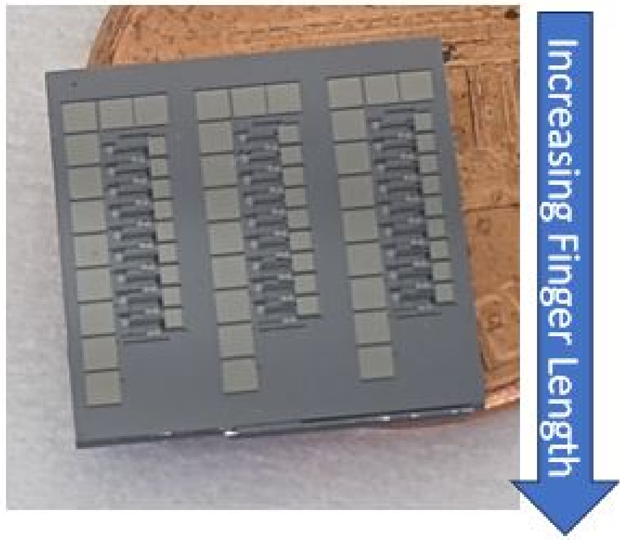


Figure 6.9: As-fabricated PIPO test chips shown before full separation from the break-away tabs. The array layout permits multiple GCA geometries to be inspected and tested from a single fabricated chip.

of shuttle travel.

## 6.6 Experimental Setup

### 6.6.1 Vacuum Test Motivation

The experimental validation strategy was motivated by prior work on GCA and inchworm-motor dynamics in different environments [113]. For the present application, the relevant environmental question is whether MEMS inchworm motors can operate under reduced-pressure conditions appropriate for a space-analogous test environment. Vacuum testing is particularly important for MEMS because gas damping, squeeze-film damping, surface adhesion, and electrical breakdown behavior may differ substantially between ambient laboratory conditions and reduced pressure.

The vacuum objective in this work is not to reproduce the full radiative, thermal, plasma, and contamination environment of deep space. Instead, the near-term objective is to reduce gas damping and demonstrate that the MEMS actuator can be driven in an environment more representative of spacecraft operation than ambient air. This distinction is important because different spacecraft qualification objectives require different pressure ranges. Thermal-vacuum testing, outgassing evaluation,

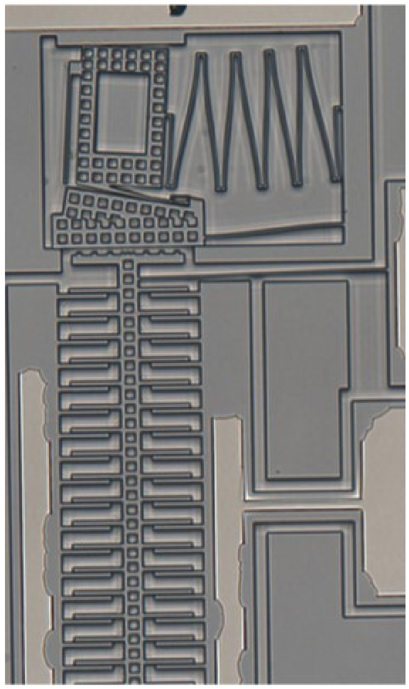

Figure 6.10: Optical micrograph of an as-fabricated PIPO test structure. A single GCA PIPO cell is visible within the array. The etch-hole spacing is approximately 14 $\mu$m center-to-center, providing a scale reference for the released silicon features. Also shown is the engaged wedge and lock tab structures.

aerodynamic damping studies, and deep-space environmental simulation do not impose identical vacuum requirements (see Tab. 6.1.

Table 6.1: NASA Space-Like Vacuum Requirements by Component Test Category

| **Test Category** | **Pressure (torr)** | **Primary Physical Effect** |
|---|---|---|
| Thermal Considerations | $10^{-5}$ to $10^{-6}$ | Elimination of air convection [127] |
| Electronics / Outgassing | $< 10^{-5}$ | Corona arcing & material loss [128] |
| Aerodynamic Damping | $10^{-2}$ to $10^{-4}$ | Structural damping dominance [129] |
| MEMS / Microscale | $10^{-1}$ to $10^{-3}$ | Squeeze-film damp. reduction [130] |
| Deep Space Fidelity | $10^{-7}$ | Full radiative environment [131] |

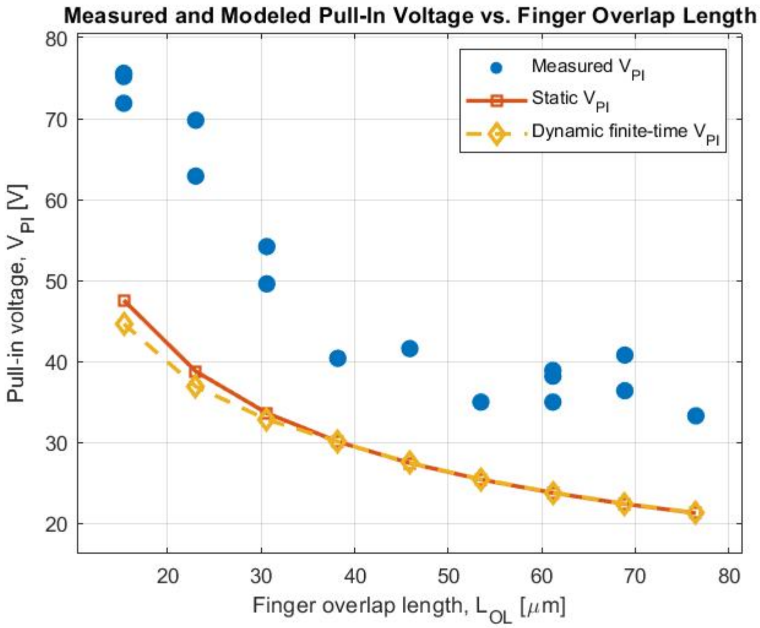


Figure 6.11: Measured pull-in voltage, $V_{\mathrm{PI}}$, as a function of finger overlap length, $L_{\mathrm{OL}}$, for the GCA PIPO test structures. The data show a general reduction in pull-in voltage with increasing finger overlap, consistent with increased electrostatic force for longer active electrode engagement. Also depicted is the static and dynamic finite time pull in voltage for the same finger overlap lengths. Possible explanations for the deviation from theoretical calculations are differences in undercut not accounted for or the presence of oxidized surfaces.

### 6.6.2 Vacuum Chamber and Electrical Interface

The vacuum chamber used for these tests consists of an aluminum chamber body, an acrylic viewing cover, electrical feedthroughs, and a pump capable of reaching approximately 10 mTorr. This chamber is similar to the system described in Teal's dissertation [11]. A standoff adapter and printed-circuit board were used to mount the MEMS devices and route electrical signals from the chamber feedthroughs to the probe or bond-pad interface.

The experimental configuration must satisfy three constraints simultaneously. First, the chip must be mechanically secured without constraining the shuttle or tether interface. Second, high-voltage signals must be routed to the GCA and locking structures with low leakage and sufficient isolation. Third, the device must remain optically visible so that shuttle displacement, pull-in events, and failure modes can

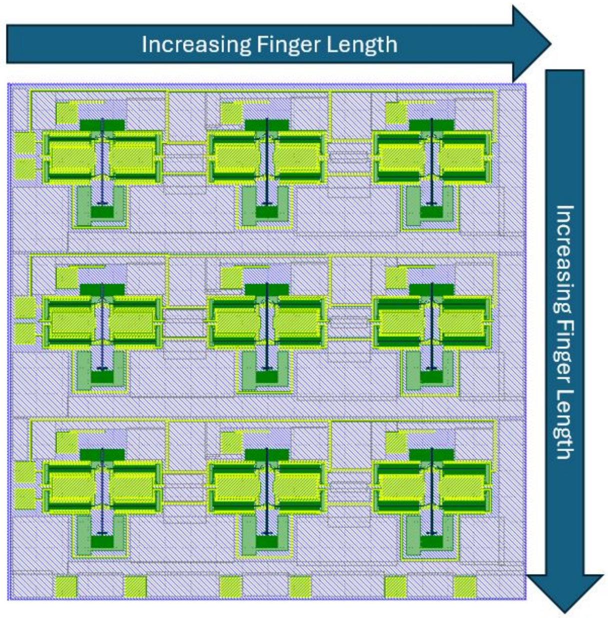


Figure 6.12: KLayout layout of the IWMST array. The test cells are arranged so that the finger length varies across the array, enabling motor-level performance to be compared as a function of GCA geometry.

be observed during testing.

While the vacuum chamber (see Fig. 6.15) was assembled, pressure checked, and electrically verified for the use under the described conditions to test the chips in space-like conditions, no chips were tested.

## 6.7 Earth-Analog Tether-Loading Setup

Earth-analog testing was performed to evaluate whether the MAST v2 device could actuate a tether connected to a full-scale sail-like structure. In the initial configuration, one end of a carbon-fiber tether was attached to the SOI shuttle, and the other end was attached to the side of a circular aluminized Mylar sail at approximately half-height. The test used a full-size circular sail with area

$$A_{\mathrm{SS}} = 1 \text{ m}^2,$$

and a carbon-fiber tether of length

$$L_{\mathrm{CF}} = 2 \text{ m}$$

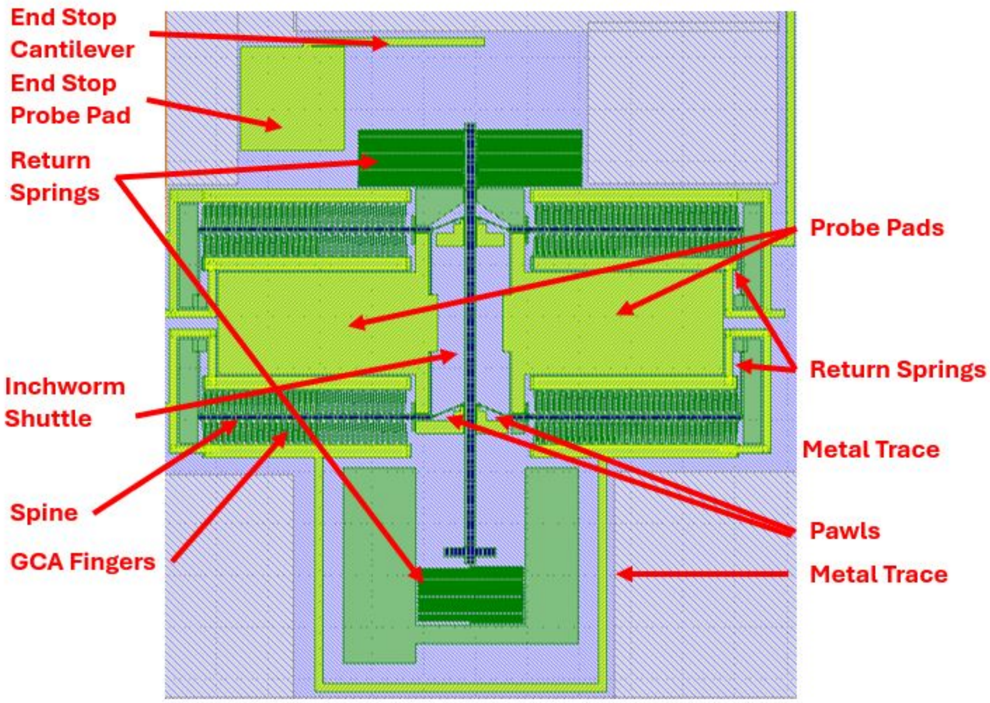


Figure 6.13: Zoomed KLayout layout of a single IWMST device. The labeled features include the inchworm shuttle, spine, GCA fingers, pawls, return springs, metal traces, probe pads, and end-stop probe pad.

and diameter

$$D_{\mathrm{CF}} = 300\ \mu\mathrm{m}.$$

Because the tether applied a load to the MAST device, the chip was suspended by a fishing line with radius approximately 0.14 mm and length approximately 10 in, equivalent to 0.254 m. The fishing line was tied to a metal rod approximately 2.2 m long, affixed above the probe station and oriented horizontally using external clamps and supports.

The initial ambient-air test revealed that the full-scale sail was highly sensitive to environmental disturbances. Motion caused by nearby personnel, breathing, and room-scale airflow produced sail displacements on the order of centimeters. Tarp separators were then placed around the setup, and a camera was used to monitor the residual swaying motion. Although this reduced the disturbance amplitude, HVAC-induced airflow still caused millimeter-scale motion even after long settling periods. This residual motion was large compared with the intended MEMS-scale

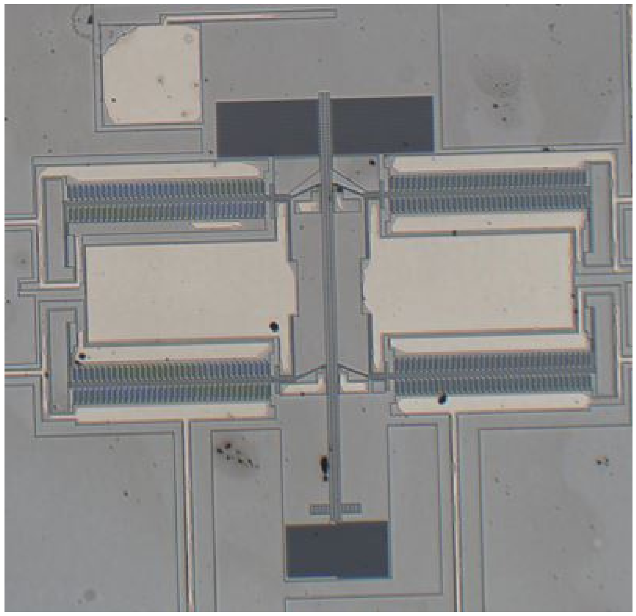

Figure 6.14: Optical image of an as-fabricated IWMST die. The device provides a compact test platform for measuring inchworm stepping behavior independently from the full tether-control assembly.

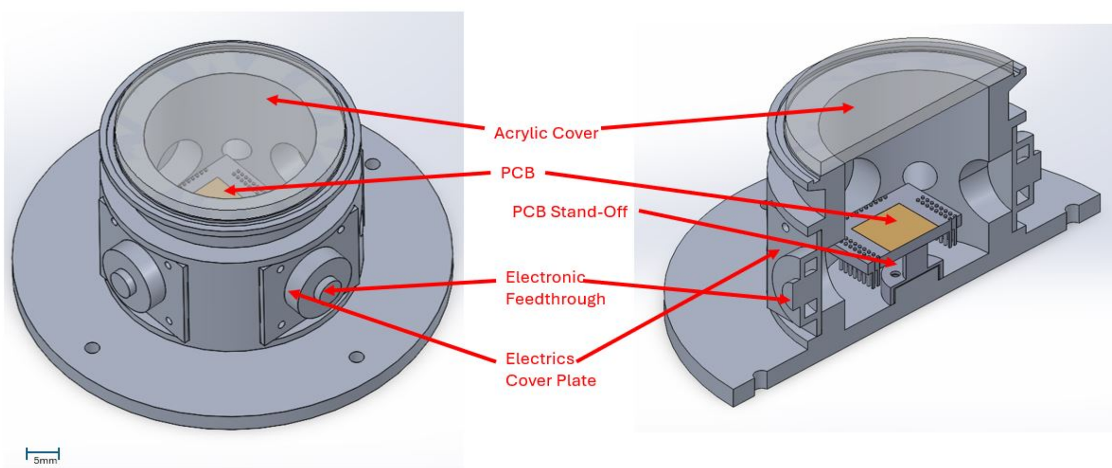


Figure 6.15: Vacuum-chamber test configuration for MAST device evaluation. The chamber provides reduced-pressure operation, electrical feedthroughs, and optical access for observing MEMS shuttle displacement during actuation.

tether displacement.

For this reason, the full sail was not an ideal first test article for tether-actuation validation in ambient air. A more appropriate intermediate test article is a full-size ring with a moment of inertia matched to the sail-frame system but with substantially reduced aerodynamic area. Such a ring preserves the inertial loading relevant to low-frequency rotational response while suppressing the dominant ambient-air disturbance mechanism. This approach provides a more controlled path toward evaluating MAST-driven tether manipulation before returning to full-sail testing in vacuum or a more isolated environment.

## 6.8 Results and Discussion

### 6.8.1 Substrate-Shuttle Device Performance

The substrate-shuttle MAST v1 devices demonstrated that the basic inchworm actuation concept could be implemented in the MAST geometry, but they also exposed several practical weaknesses. The measured pull-in voltage range of 84--98 V was compatible with high-voltage MEMS probing but higher than desirable for spacecraft integration. The measured motor speed at 10 Hz,

$$v_{\mathrm{IWM}} = 5 \pm 2\ \mu\mathrm{m/s},$$

indicates that the tested devices did not yet provide robust or repeatable shuttle translation.

The dominant limitation was mechanical reliability. Spring fracture and shuttle misalignment frequently prevented continued testing. Once the shuttle moved out of its intended alignment, the pawls were vulnerable to damage during attempts to reset the device. This failure mode is especially important for space-oriented MEMS actuators because a tether-control system must tolerate handling, packaging, and launch-induced mechanical uncertainty. The v1 results therefore motivated a design shift away from substrate-dominated shuttle mechanics and toward an SOI-shuttle architecture with improved compatibility between the released device layer and the moving shuttle.

### 6.8.2 SOI-Shuttle Device Assessment

The SOI-shuttle MAST v2 design addressed several of the mechanical integration concerns observed in v1. By moving the shuttle architecture into the SOI device layer, the device became more consistent with the released MEMS structures and less dependent on recovering a misaligned substrate-supported shuttle. The optical images in Figs. 6.6 and related callout figures show the key functional regions: electrical probe pads, MEMS GCA arrays, shuttle, carbon-fiber mounting region, device railings, and end-stop trigger.

The v2 architecture is also more appropriate for tether experiments because the carbon fiber can be routed along the shuttle axis while the opposing motor banks remain accessible for probing. This layout improves the separation between mechanical tether handling and electrical actuation. However, the design still requires further work before it can be considered a complete spacecraft actuator. In particular, future iterations should quantify shuttle displacement per step, maximum tether load, hold force, reverse stepping reliability, electrical leakage, lifetime under repeated cycling, and vacuum-dependent changes in pull-in and pull-out behavior.

### 6.8.3 GCA Pull-In Voltage Scaling

The PIPO test data provide the clearest quantitative trend observed in this chapter. As shown in Fig. 6.11, the measured pull-in voltage decreases with increasing finger overlap length. This trend is consistent with the expected scaling of electrostatic actuation: longer active finger overlap increases the electrostatic force contribution for a given voltage and therefore reduces the voltage needed to reach pull-in.

The measured data also show scatter, particularly at intermediate and long finger overlaps. This scatter may arise from fabrication variation, release variation, local stiction, probe contact differences, metallization nonuniformity, or geometric differences in finger bending. The data nevertheless provide a useful design rule for subsequent MAST devices: increasing finger overlap can reduce the required drive voltage, but the geometry must be selected while also considering finger stability, pull-out reliability, lateral compliance, and the possibility of unintended finger contact.

### 6.8.4 Limitations of Ambient Full-Sail Testing

The Earth-analog testing effort showed that a full-scale 1 $m^2$ sail is not a well-conditioned ambient-air test article for MEMS-scale tether actuation. The sail area is large enough that small air currents produce displacements much larger than the MEMS shuttle stroke. Even after the setup was partially isolated using tarp barriers, residual airflow produced millimeter-scale motion. This made it difficult to attribute observed sail motion to MEMS actuation rather than environmental disturbance.

This limitation does not invalidate the tether-control concept; rather, it identifies a mismatch between the first ambient-air test article and the actuator scale. A staged validation sequence is more appropriate. First, isolated GCA and IWM test structures should be characterized under microscope observation. Second, the MAST shuttle should be tested with known micro- to milli-newton-scale tether loads. Third, a reduced-aerodynamic-area inertial surrogate should be used to represent the full sail's rotational inertia. Finally, full-sail testing should be performed in a controlled airflow or vacuum environment where aerodynamic disturbances are sufficiently reduced.

## 6.9 Conclusions

This chapter presented the design and preliminary evaluation of MAST, a MEMS inchworm-motor architecture for direct actuation of small solar-sail tethers. The motivating application is the BLISS spacecraft concept, in which tether displacement can provide a compact mechanism for sail-shape control or steering authority. The MAST approach uses lithographically defined MEMS GCA arrays and inchworm motor sequences to produce bidirectional linear motion of a silicon shuttle mechanically coupled to a carbon-fiber tether.

Two MAST device generations were developed. The v1 substrate-shuttle design provided high structural stiffness but suffered from return-spring fracture, shuttle misalignment, and pawl damage during testing. Eight of twelve fabricated v1 devices were viable for testing, with measured pull-in voltages of 84--98 V and an approximate motor speed of $5 \pm 2$ $\mu$m/s at 10 Hz. These results demonstrated the feasibility of the layout but also showed that the substrate-shuttle architecture was not sufficiently robust for repeatable tether-actuation experiments.

The v2 SOI-shuttle design was introduced to improve mechanical compatibility with the released MEMS structures and to provide a better tether-interface geometry. The SOI-shuttle architecture places the central shuttle, motor banks, return springs, probe pads, and end-stop structures in a configuration more suitable for bidirectional tether actuation. This design is better aligned with future vacuum and loaded-tether experiments, although additional characterization is still required to quantify step size, hold force, lifetime, and vacuum-dependent behavior.

Dedicated PIPO and IWMST test structures were also developed. The PIPO devices showed that GCA pull-in voltage decreases with increasing finger overlap length, with longer-overlap structures pulling in near the mid-30 V to low-40 V range. This result provides a useful design direction for lowering MAST drive voltage in future revisions. The IWMST devices provide a motor-level test platform for future speed, displacement, and end-stop-feedback characterization.

Finally, preliminary Earth-analog testing with a full-scale 1 m$^2$ sail showed that ambient-air disturbances dominate the motion of large-area sail test articles. The observed centimeter- to millimeter-scale environmental motion was too large relative to the intended MEMS-scale actuation. A more suitable intermediate validation article is therefore a moment-of-inertia-matched ring with lower aerodynamic area. This surrogate would preserve the relevant inertial loading while reducing airflow sensitivity, allowing the MAST device to be evaluated under more controlled conditions before returning to full-sail testing.

The main conclusion is that MEMS inchworm motors remain a promising actuation mechanism for small solar-sail tether control, but reliable system-level operation requires careful co-design of actuator geometry, shuttle mechanics, tether interface, electrical routing, test environment, and inertial loading. The results in this chapter establish the first design path and experimental framework for MAST while identifying the key improvements needed for future flight-relevant tether-control demonstrations.

# Chapter 7

# Conclusion

This dissertation has presented a framework for femtoscale, MEMS-controlled solar-sail spacecraft intended for low-cost interplanetary exploration, asteroidal imaging, and cometary sample capture. The central spacecraft architecture developed in this work is the Berkeley Low-cost Interplanetary Solar Sail (BLISS), a gram-scale solar-sail spacecraft that uses solar radiation pressure as its primary source of propulsion and MEMS-based mechanical actuation as its steering authority. Rather than treating miniaturization as only a reduction in spacecraft mass, this dissertation has treated miniaturization as a system-level design problem in which propulsion, steering, sensing, computation, surface mobility, and fabrication must be co-designed around the constraints of gram-scale spacecraft.

The BLISS concept demonstrates how a small spacecraft can use a thin-film solar sail, carbon-fiber structural members, commercial-off-the-shelf electronics, and MEMS actuation to form a plausible architecture for distributed interplanetary science. The spacecraft is designed to exploit the high area-to-mass ratio of a lightweight sail while using low-mass onboard systems for computation, imaging, communications, and attitude control. The trajectory and control analyses presented in Chapter 3 show that a spacecraft in the BLISS mass regime can, in principle, execute Earth-escape spiral trajectories and interplanetary transfers relevant to near-Earth asteroid imaging and small-body reconnaissance. These analyses do not by themselves constitute a flight-qualified spacecraft, but they establish the physical and architectural basis for using femtoscale solar sails as a serious platform for future planetary-science missions.

The actuation architecture developed in this dissertation is equally central to the overall concept. BLISS is not simply a passive sailcraft; it requires controlled steering through relative motion between the spacecraft body, carbon-fiber support structure, and solar-sail surface. The MEMS Actuators for control of Solar-sail Tethers (MAST), presented in Chapter 6, are the intended steering mechanism for this spacecraft. In the BLISS architecture, MAST functions as the tether-control system: it displaces carbon-fiber tethers connected to the sail-frame system and thereby changes the relative geometry of the sail and spacecraft body. This enables the center-of-pressure and center-of-mass relationship to be modified for attitude control and steering under solar radiation pressure. In this sense, MAST is the helm of the BLISS spacecraft. It provides the direct mechanical interface between MEMS-scale motion and spacecraft-scale steering.

The second major extension of the BLISS architecture is the Self-righting Quadrupedal Inchworm Driven Spacewalker (SQuIDS), presented in Chapter 5. SQuIDS is intended as a MEMS-based rover payload that could be carried by a BLISS-class spacecraft for on-asteroid or small-body surface exploration. The motivation for SQuIDS is that asteroid and comet environments present mobility challenges that differ fundamentally from terrestrial locomotion. Low gravity, uncertain surface contact, and unpredictable orientation after deployment require a rover architecture that can tolerate tumbling, recover from overturned states, and use small controlled motions to interact with a surface. The SQuIDS designs, linkage models, and self-righting concepts presented here provide a first step toward that capability. As with BLISS and MAST, the SQuIDS work is not presented as a completed flight rover, but rather as a mechanical and analytical foundation for a future MEMS microrover that could extend the BLISS mission concept from flyby imaging to in-situ surface exploration.

The Transmission Gap Closing Actuator (TGCA) work in Chapter 4 provides a third enabling technology and a longer-term path toward unifying the actuation strategy across the spacecraft, steering mechanism, and rover. Conventional MEMS inchworm motors are effective but are often specialized for a narrow range of motion, directionality, or output force. The TGCA and $\mu\Delta$ motor concepts developed here address that limitation by introducing a transmission-capable MEMS actuator architecture with bidirectional and variable-output behavior. The TGCA is therefore not only a standalone motor contribution; it is a proposed future replacement for the more conventional inchworm motors used in BLISS, MAST, and SQuIDS. Once further matured, TGCA-based motors could provide a common actuator family for sail steering, tether control, rover locomotion, self-righting, sample interaction, and other MEMS-driven spacecraft functions. This would reduce architectural complexity while increasing mechanical versatility across the broader femtospacecraft platform.

Taken together, the four technical thrusts of this dissertation form a linked system rather than a set of unrelated projects (see Fig. 7.1). BLISS defines the spacecraft and mission architecture. MAST provides the steering and tether-control mechanism needed for BLISS to maneuver as an active solar sail. SQuIDS provides the conceptual rover payload that a BLISS-class spacecraft could deliver for small-body surface exploration. TGCA provides the next-generation actuator technology that could eventually replace the motors throughout the BLISS, MAST, and SQuIDS systems. The long-term vision is therefore a MEMS-enabled exploration architecture in which a low-cost solar-sail spacecraft carries and deploys microrobotic instruments, with both spacecraft steering and surface mobility powered by related families of lithographically fabricated actuators.

A central outcome of this work is the identification of what remains incomplete. The dissertation establishes feasibility arguments, mechanical designs, simulations, fabrication outcomes, and preliminary experimental demonstrations, but it does not complete the full integrated system. The BLISS architecture requires additional work in integrated flight packaging, closed-loop attitude determination and control, communications, radiation tolerance, and environmental qualification. The MAST devices require further testing under controlled tether loads, reduced-pressure environments, and closed-loop end-stop or position feedback. The SQuIDS rover requires continued mechanical refinement, assembly validation, locomotion testing, and integration with a realistic deployment and payload interface. The TGCA motors require additional design iterations to improve repeatability, manufacturability, lifetime, and compatibility with autonomous electrical control. These limitations are not incidental; they define the natural boundary between the foundational work completed here and the next stage of the research program.

For this reason, the work presented in this dissertation should be understood as both a contribution and a roadmap. It establishes a set of designs, models, and experimental lessons that make a larger program possible, but the resulting systems remain open for substantial continuation. A future student could productively advance this work by treating BLISS, MAST, SQuIDS, and TGCA as an integrated platform rather than as separate devices. A particularly valuable next phase would be to redesign the MAST and SQuIDS motor banks around TGCA-based actuators, fabricate a unified generation of test chips, and evaluate the resulting devices under realistic mechanical loads and vacuum conditions. Such a project would directly connect the actuator-level advances of the $\mu\Delta$ motor to the spacecraft-level goals of BLISS and the surface-mobility goals of SQuIDS.

The broader implication of this dissertation is that MEMS can do more for spacecraft than provide sensors. MEMS mechanisms can become primary spacecraft actuators, steering elements, transmission systems, deployment mechanisms, and mobility platforms. At the femtoscale, where conventional spacecraft hardware becomes too massive, too power-intensive, or too mechanically complex, MEMS offers a path toward integrated mechanical intelligence. The same fabrication methods that produce small, repeatable, low-mass structures can also produce the mechanisms needed to steer a sail, manipulate a tether, drive a rover, or reconfigure a spacecraft. This is the central technological argument of the dissertation: that MEMS actuation can extend the reach of small spacecraft by giving them controlled mechanical interaction with their own structures and with their surrounding environment.

Ultimately, this dissertation has advanced the concept of a MEMS-controlled femtoscale solar-sail exploration platform. It has shown that BLISS is a plausible spacecraft architecture for low-cost interplanetary exploration, that MAST provides a direct MEMS tether-control approach for steering such a spacecraft, that SQuIDS offers a path toward carried microrobotic surface exploration, and that TGCA motors provide a future actuator architecture capable of replacing and improving the motors across these systems. The work is necessarily incomplete because the vision is larger than any single dissertation-scale demonstration. Nevertheless, the designs, models, fabrication results, and experiments presented here provide a coherent foundation for the next generation of MEMS-enabled spacecraft and microrobotic explorers.

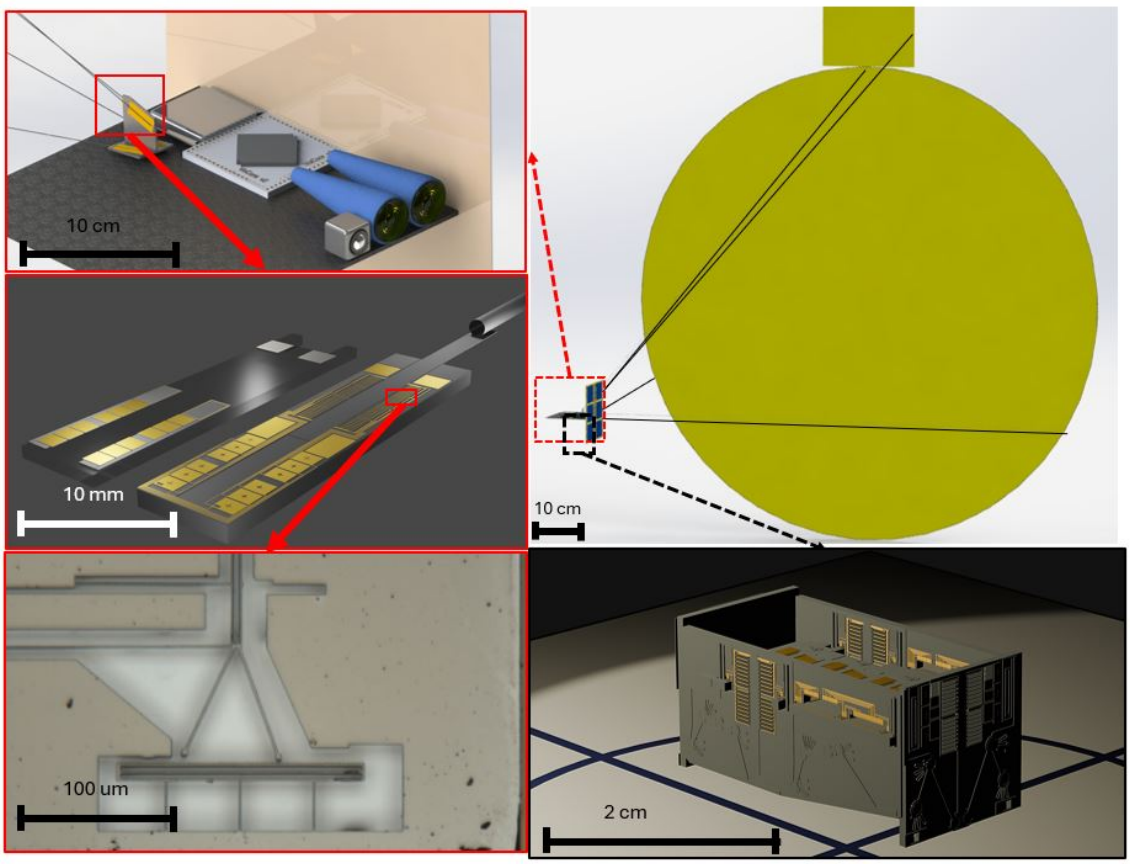


Figure 7.1: Image showing the combined project starting from upper right in the counterclockwise direction: full BLISS 3D CAD, zoomed in 3D CAD of the BLISS components, 3D CAD of the MAST device, image of the TGCA test chip, and 3D CAD of the small approach SQuIDS. Here the SQuIDS robot is depicted as being attached to the underside of the BLISS main body.

# Bibliography


[1] C. R. McInnes, *Solar Sailing: Technology, Dynamics, and Mission Applications*. Chichester: Springer-Praxis, 1999.

[2] A. N. Alvara, L. Lee, E. Sin, N. Lambert, A. J. Westphal, and K. S. J. Pister, ‘‘BLISS: Interplanetary exploration with swarms of low-cost spacecraft,’’ *Acta Astronautica*, vol. 215, pp. 348--361, feb 2024. [Online]. Available: https://doi.org/10.1016/j.actaastro.2023.11.027

[3] J. Greenspun, ‘‘Mechanical Energy Storage for Self-Destructing Motes and Jumping Microrobots,’’ p. 113, 2018. [Online]. Available: http://www2.eecs.berkeley.edu/Pubs/TechRpts/2018/EECS-2018-112.html

[4] D. Contreras, ‘‘Walking silicon: Actuators and legs for small-scale terrestrial robots,’’ Ph.D. dissertation, EECS Department, University of California, Berkeley, may 2019. [Online]. Available: http://www2.eecs.berkeley.edu/Pubs/TechRpts/2019/EECS-2019-18.html

[5] D. Drew, ‘‘The ionocraft: Flying microrobots with no moving parts,’’ Ph.D. dissertation, EECS Department, University of California, Berkeley, dec 2018, advisor: Kristofer Pister. [Online]. Available: http://www2.eecs.berkeley.edu/Pubs/TechRpts/2018/EECS-2018-164.html

[6] O. Chen, ‘‘Hydrogel actuated carbon fiber microelectrode array,’’ Ph.D. dissertation, EECS Department, University of California, Berkeley, may 2023, committee: Michel Maharbiz, Kristofer Pister, and Michael DeWeese. [Online]. Available: http://www2.eecs.berkeley.edu/Pubs/TechRpts/2023/EECS-2023-59.html

[7] H. C. Gomez, ‘‘Design, fabrication, and assembly of multi-chip walking silicon microrobots,’’ PhD Dissertation, EECS Department, University of California, Berkeley, dec 2020, committee chair: Kristofer S.J. Pister. [Online]. Available: http://www2.eecs.berkeley.edu/Pubs/TechRpts/2020/EECS-2020-229.pdf

[8] M. Bustamante Eguiguren, ‘‘Rotary inchworm motor for underwater microrobot propulsion,’’ Ph.D. dissertation, EECS Department, University of California, Berkeley, aug 2024, advisors: Kristofer Pister and Michel Maharbiz. [Online]. Available: http://www2.eecs.berkeley.edu/Pubs/TechRpts/2024/EECS-2024-175.html

[9] A. Moreno, ‘‘Integrated low-power wireless systems for the next generation of iot, sensors and microrobots,’’ Ph.D. dissertation, EECS Department, University of California, Berkeley, dec 2023, advisors: Kristofer Pister and Ali Niknejad. [Online]. Available: http://www2.eecs.berkeley.edu/Pubs/TechRpts/2023/EECS-2023-262.html

[10] C. Schindler, ‘‘Jumping silicon microrobots with electrostatic inchworm motors and energy storing substrate springs,’’ PhD Dissertation, EECS Department, University of California, Berkeley, may 2020, advisor: Kristofer Pister. [Online]. Available: http://www2.eecs.berkeley.edu/Pubs/TechRpts/2020/EECS-2020-73.html

[11] D. Teal, ‘‘Multimaterial nanoscale printing via charged nanoparticle deposition,’’ Ph.D. dissertation, EECS Department, University of California, Berkeley, dec 2024, advisor: Kristofer Pister. [Online]. Available: http://www2.eecs.berkeley.edu/Pubs/TechRpts/2024/EECS-2024-233.html

[12] D. Acker-James, ‘‘Pcb-less integration of a robust wireless MEMS tactile package,’’ Master’s thesis, EECS Department, University of California, Berkeley, jan 2023, advisor: Kristofer Pister. [Online]. Available: http://www2.eecs.berkeley.edu/Pubs/TechRpts/2023/EECS-2023-1.html

[13] B. Kilberg, ‘‘Actuation and localization of resource-constrained autonomous microrobotic systems,’’ PhD Dissertation, EECS Department, University of California, Berkeley, may 2021, advisor: Kristofer Pister. [Online]. Available: http://www2.eecs.berkeley.edu/Pubs/TechRpts/2021/EECS-2021-20.html

[14] N. Deka, ‘‘Design, development and applications of portable field emission devices,’’ PhD Dissertation, EECS Department, University of California, Berkeley, dec 2021, advisors: Kristofer Pister and Vivek Subramanian. [Online]. Available: http://www2.eecs.berkeley.edu/Pubs/TechRpts/2021/EECS-2021-224.html

[15] Y. Liu, D. Lovell, T. Yuan, and K. S. J. Pister, ‘‘Toward a self-powered mm-scale MEMS sensor platform through heterogeneous integration of SCuM and

HV SOI CMOS,'' in *2025 23rd International Conference on Solid-State Sensors, Actuators and Microsystems (Transducers)*, jun 2025.

[16] D. Contreras, D. S. Drew, and K. Pister, ''First steps of a millimeter-scale walking silicon robot,'' *2017 19th International Conference on Solid-State Sensors, Actuators and Microsystems (TRANSDUCERS)*, vol. null, pp. 910--913, 2017. [Online]. Available: https://www.semanticscholar.org/paper/bdb032f0bea75d3f3f8ec26b17ac65e42859ffd7

[17] J. Puig-Suari, C. Turner, and W. Ahlgren, ''Development of the standard CubeSat deployer and a CubeSat class PicoSatellite,'' in *Proceedings of the 2001 IEEE Aerospace Conference*, vol. 1, Big Sky, MT, USA, 2001, pp. 347--353.

[18] J. Janicik and J. Wolff, ''ChipSat spacecraft design -- Significant science on a low budget,'' in *Proc. SPIE 5164, Optical Science and Technology, SPIE's 48th Annual Meeting*, 2003. [Online]. Available: https://www.spiedigitallibrary.org/conference-proceedings-of-spie/5164/0000/CHIPSat-spacecraft-design-significant-science-on-a-low-budget/10.1117/12.512521.short

[19] Z. Manchester, M. A. Peck, and A. Filo, ''KickSat: A crowd-funded mission to demonstrate the world's smallest spacecraft,'' in *27th Annual AIAA/USU Conference on Small Satellites*, Logan, UT, USA, 2013. [Online]. Available: https://digitalcommons.usu.edu/smallsat/2013/all2013/111/

[20] R. P. Feynman, ''There's plenty of room at the bottom,'' *Engineering and Science*, vol. 23, no. 5, pp. 22--36, feb 1960.

[21] C. Sagan, *Pale Blue Dot: A Vision of the Human Future in Space*. New York: Random House, 1994.

[22] National Aeronautics and Space Administration, ''State of the Art of Small Spacecraft Technology, 2024 Edition,'' NASA Small Spacecraft Systems Virtual Institute (S3VI), Tech. Rep., feb 2025. [Online]. Available: https://www.nasa.gov/smallsat-institute/sst-soa

[23] United Nations Office for Outer Space Affairs and Our World in Data, ''Cumulative number of objects launched into space,'' https://ourworldindata.org/grapher/cumulative-number-of-objects-launched-into-outer-space, 2025, data compiled from the UNOOSA Online Index of Objects Launched into Outer Space. Accessed: July 22, 2025.

[24] Wikipedia contributors, ‘‘List of human spaceflights --- wikipedia, the free encyclopedia,’’ https://en.wikipedia.org/wiki/List_of_human_spaceflights, 2025, accessed: July 22, 2025.

[25] ------, ‘‘List of spacewalks since 1965 --- wikipedia, the free encyclopedia,’’ https://en.wikipedia.org/wiki/List_of_spacewalks_since_1965, 2025, accessed: July 22, 2025.

[26] ------, ‘‘Sample-return mission --- wikipedia, the free encyclopedia,’’ https://en.wikipedia.org/wiki/Sample-return_mission, 2025, accessed: July 22, 2025.

[27] D. R. Wibben, A. Levine, S. Rieger, J. V. McAdams, P. G. Antreasian, J. M. Leonard, M. C. Moreau, and D. S. Lauretta, ‘‘Osiris-rex frozen orbit design and flight experience,’’ in *AAS/AIAA Astrodynamics Specialist Conference, 2019*. Univelt Inc., 2020, pp. 2959--2971.

[28] T. Nakamura, T. Noguchi, M. Tanaka, M. E. Zolensky, M. Kimura, A. Tsuchiyama, A. Nakato, T. Ogami, H. Ishida, M. Uesugi, T. Yada, K. Shirai, A. Fujimura, R. Okazaki, S. A. Sandford, K. Nagao, H. Kagi, and H. Yurimoto, ‘‘Itokawa dust particles: A direct link between s-type asteroids and ordinary chondrites,’’ *Science*, vol. 333, no. 6046, pp. 1113--1116, 2011.

[29] T. Yokoyama, K. Nagashima, I. Nakai, E. D. Young, Y. Abe, J. Aléon, Y. Amelin, K. Amma, T. Arai, M. Bizzarro, A. Bouvier, J. C. Bridges, L. Bonal, C. M. O. Alexander, R. Fukai, K. Fukuda, E. Furi, J. Han, D. Harries, M. Hashiguchi, K. Hatakeyama, H. Hidaka, H. Homma, P. Hoppe, W. Hsu, T. Iizuka, T. R. Ireland, A. Ishikawa, M. Ito, S. Itoh, N. Kawasaki, M. Kikuiri, M. Kimura, Y. Kimura, N. T. Kita, H. Kitagawa, S. Kobayashi, K. Koga, H. Komatani, B. K. Kruger, M. Lee, Z. Martins, Y. Masuda, M. Matsuoka, K. A. McCain, H. L. Mclain, T. Nagai, T. Naoya, H. Naraoka, L. R. Nittler, T. Nogi, M. Nomura, R. Okai, R. Okazaki, C. Park, L. Piani, L. Qin, S. S. Russell, N. Sakamoto, M. Schönbächler, M. Shigenaka, R. M. Stroud, K. Sugiura, T. Sugiyama, S. R. Sutton, Y. Takaesu, A. Takigawa, K. Tanimoto, K. Torii, Y. Tsuda, K. Uesugi, E. M. M. E. van Kooten, J. Villeneuve, L. E. Webb, A. Yamakawa, M. Yamanaka, D. Yamamoto, K. Yamashita, M. Yoshikawa, and H. Yurimoto, ‘‘Samples returned from the asteroid ryugu are similar to ivuna-type carbonaceous meteorites,’’ *Science*, vol. 379, no. 6634, p. eabn7850, 2022.

[30] D. Brownlee, P. Tsou, J. Aléon, C. M. O. Alexander, T. Araki, S. Bajt, G. A. Baratta, R. Bastien, P. Bland, P. Bleuet, J. Borg, J. P. Bradley, A. Brearley,

F. Brenker, S. Brennan, J. C. Bridges, N. D. Browning, J. R. Brucato, E. Bullock, M. J. Burchell, H. Busemann, A. Butterworth, N. Chaoui, M. Chi, M. J. Cintala, B. C. Clark, S. J. Clemett, G. Cody, L. Colangeli, M. Collier, J. Cuzzi, Z. R. Dai, L. D'Hendecourt, Z. Djouadi, G. Dominguez, T. Duxbury, J. P. Dworkin, D. S. Ebel, T. E. Economou, S. Fakra, S. A. J. Fairey, S. Fallon, G. Ferrini, T. Ferroir, H. Fleckenstein, C. Floss, G. Flynn, I. A. Franchi, M. Fries, Z. Gainsforth, J.-P. Gallien, M. Genge, M. K. Gilles, P. Gillet, D. P. Glavin, M. Gounelle, M. M. Grady, G. A. Graham, P. G. Grant, S. F. Green, F. Grossemy, L. Grossman, J. N. Grossman, Y. Guan, K. Hagiya, R. Harvey, P. Heck, G. F. Herzog, P. Hoppe, F. Hörz, J. Huth, I. D. Hutcheon, K. Ignatyev, H. Ishii, M. Ito, D. Jacob, C. Jacobsen, S. Jacobsen, S. Jones, D. Joswiak, A. Jurewicz, A. T. Kearsley, L. P. Keller, H. Khodja, A. L. D. Kilcoyne, J. Kissel, A. Krot, F. Langenhorst, A. Lanzirotti, L. Le, L. L., L. A. Leshin, J. Leitner, L. Lemelle, H. Leroux, M.-C. Liu, K. Luening, I. Lyon, G. MacPherson, M. A. Marcus, K. Marhas, B. Marty, G. Matrajt, K. McKeegan, A. Meibom, V. Mennella, K. Messenger, S. Messenger, T. Mikouchi, S. Mostefaoui, T. Nakamura, T. Nakano, M. Newville, L. R. Nittler, I. Ohnishi, K. Ohsumi, K. Okudaira, D. A. Papanastassiou, R. Palma, M. E. Palumbo, R. O. Pepin, D. Perkins, M. Perronnet, P. Pianetta, W. Rao, F. J. M. Rietmeijer, F. Robert, D. Rost, A. Rotundi, R. Ryan, S. A. Sandford, C. S. Schwandt, T. H. See, D. Schlutter, J. Sheffield-Parker, A. Simionovici, S. Simon, I. Sitnitsky, C. J. Snead, M. K. Spencer, F. J. Stadermann, A. Steele, T. Stephan, R. Stroud, J. Susini, S. R. Sutton, Y. Suzuki, M. Taheri, S. Taylor, N. Teslich, K. Tomeoka, N. Tomioka, A. Toppani, J. M. Trigo-Rodríguez, D. Troadec, A. Tsuchiyama, T. Tyliszczak, K. Uesugi, M. Velbel, J. Vellenga, E. Vicenzi, L. Vincze, J. Warren, I. Weber, M. Weisberg, A. J. Westphal, S. Wirick, D. Wooden, B. Wopenka, P. Wozniakiewicz, I. Wright, H. Yabuta, T. Yada, H. Yano, E. D. Young, R. N. Zare, T. Zega, K. Ziegler, E. Zinner, M. Zolensky, and V. Zyla, ''Comet 81p/wild 2 under a microscope,'' *Science*, vol. 314, no. 5806, pp. 1711--1716, 2006.

[31] R. L. Garwin, ''Solar sailing-a practical method of propulsion within the solar system,'' *Jet Propulsion*, vol. 28, no. 3, pp. 188--190, 1958.

[32] C. Jack and C. Welch, ''Solar kites: Small solar sails with no moving parts,'' *Acta Astronautica*, vol. 40, no. 2-8, pp. 137--142, 1997.

[33] C. Jack, R. Wall, and C. Welch, ''Spacefarer solar kites for solar system exploration,'' *Journal of the British Interplanetary Society*, vol. 58, no. 5-6, pp. 155--166, 2005.

[34] C. Sauer, ‘‘Solar sail trajectories for solar polar and interstellar probe missions,’’ 1999.

[35] B. Dachwald, ‘‘Optimal solar sail trajectories for missions to the outer solar system,’’ *Journal of Guidance, Control, and Dynamics*, vol. 28, no. 6, pp. 1187--1193, 2005.

[36] S. A. Stern, ‘‘The new horizons pluto kuiper belt mission: An overview with historical context,’’ *Space Science Reviews*, vol. 140, no. 1, pp. 3--21, 2008.

[37] National Academies of Sciences, Engineering, and Medicine, *Origins, Worlds, and Life: A Decadal Strategy for Planetary Science and Astrobiology 2023-2032*. Washington, DC: The National Academies Press, 2022.

[38] S. W. Squyres, A. G. Hayes, M. Arakawa, M. Bailey, R. P. Binzel, J. P. Bradley, N. L. Chabot, H. C. Connolly, N. Dello Russo, P. D. Feldman, Y. Furukawa, S. Gulkis, J. Hartwig, H. Ishii, M. Josset, L. Kaltenegger, D. S. Lauretta, N. McLoughlin, T. Nakamura, S. A. Sandford, S. A. Stern, T. D. Swindle, K. Uesugi, T. Usui, and D. Wooden, ‘‘The caesar new frontiers comet sample return mission,’’ Japan Geoscience Union Meeting, 2018, meeting abstract and presentation.

[39] T. R. Perez and K. Subbarao, ‘‘A survey of current femtosatellite designs, technologies, and mission concepts,’’ *Journal of Small Satellites*, vol. 5, no. 1, pp. 437--462, 2016.

[40] B. P. de Paula, E. C. da Silva, and J. A. F. da Costa, ‘‘A unified taxonomy of satellite classes,’’ *Journal of Aerospace Technology and Management*, vol. 11, 2019.

[41] NASA, ‘‘What are SmallSats and CubeSats?’’ https://www.{NASA}.gov/what-are-{SmallSats}-and-{CubeSats}/, 2024, accessed: July 30, 2025.

[42] B. Stuurman and K. Kumar, ‘‘Ryefemsat: Ryerson university femtosatellite design and testing,’’ in *AIAA SPACE 2010 Conference & Exposition*, 2010.

[43] Z. Manchester and M. A. Peck, ‘‘Sprite: A chip-sized spacecraft,’’ in *Proceedings of the 2011 IEEE Aerospace Conference*, 2011, pp. 1--10.

[44] A. M. Hein, N. Perakis, T. M. Eubanks, M. Lingam, A. Loeb, A. Hibberd, W. Noyes, and A. Tziolas, ‘‘Breakthrough Starshot: A roadmap to interstellar flight,’’ 2016.

[45] ESA, ‘‘Kicksat nanosatellite mission,’’ https://www.eoportal.org/satellite-missions/kicksat, 2014, accessed: July 30, 2025.

[46] D. J. Barnhart, T. Vladimirova, and M. N. Sweeting, ‘‘Enabling space sensor networks with pcbsat,’’ *Journal of Spacecraft and Rockets*, vol. 46, no. 4, pp. 856--867, 2009.

[47] P. H. Krisko, ‘‘The predicted growth of the low-earth orbit space debris environment — an assessment of future risk for spacecraft,’’ *Proceedings of the Institution of Mechanical Engineers, Part G: Journal of Aerospace Engineering*, vol. 221, no. 12, pp. 975--985, 2007.

[48] F. Letizia, C. Colombo, and H. G. Lewis, ‘‘Analytical model for the propagation of small-debris-object clouds after fragmentations,’’ *Journal of Guidance, Control, and Dynamics*, vol. 38, no. 8, pp. 1478--1491, 2015.

[49] D. Krejci, F. Mier-Hicks, R. Thomas, T. Haag, and P. Lozano, ‘‘Emission characteristics of passively fed electrospray microthrusters with propellant reservoirs,’’ *Journal of Spacecraft and Rockets*, vol. 54, no. 2, pp. 447--458, 2017.

[50] Y. Wen, Z. Yu, L. He, Q. Wang, and X. He, ‘‘Collision probability prediction and orbit maneuvering probability determination of non-cooperative space object orbit,’’ *Remote Sensing*, vol. 12, no. 20, p. 3310, 2020.

[51] National Aeronautics and Space Administration, ‘‘Announcement of opportunity: Small explorer program,’’ *NASA Headquarters, Office of Space Science and Applications*, 1988, established the first formal NASA classification for small satellites, defining the category as spacecraft with masses typically under 250 kg. [Online]. Available: https://ntrs.nasa.gov/

[52] J. Gaspar, S. Spangelo, A. Klesh, and B. Yost, ‘‘Small spacecraft technology state of the art,’’ *NASA Ames Research Center, Small Spacecraft Systems Virtual Institute (S3VI)*, pp. 1--160, 2013, first comprehensive NASA classification of ultra-small satellites, defining Nanosatellites (1--10 kg), Picosatellites (0.1--1 kg), and Femtosatellites (<0.1 kg).

[53] Y. Zhang, E. Lagunas, S. Chatzinotas, and B. Ottersten, ‘‘Laser intersatellite links in a Starlink constellation: A classification and analysis,’’ *IEEE Vehicular Technology Magazine*, vol. 16, no. 2, pp. 48--56, 2021.

[54] I. del Portillo, B. G. Cameron, and E. F. Crawley, ‘‘A technical comparison of three low Earth orbit satellite constellation systems to provide global broadband,’’ *Acta Astronautica*, vol. 159, pp. 123--135, 2019.

[55] M. Safyan, *The PlanetScope Constellation*. Springer, Cham, 2020.

[56] A. Poghosyan and A. Golkar, ‘‘CubeSat evolution: Analyzing CubeSat capabilities for conducting science missions,’’ *Progress in Aerospace Sciences*, vol. 88, pp. 59--83, 2017.

[57] S. Speretta, J. Bouwmeester, and E. Gill, ‘‘CubeSats to PocketQubes: opportunities and challenges,’’ in *Proceedings of the 67th International Astronautical Congress (IAC)*, 2016. [Online]. Available: https://repository.tudelft.nl/islandora/object/uuid:a5823577-96a1-438c-8797-2917711904e9

[58] R. Twiggs, A. Zucherman, E. Bujold, and N. Counts, ‘‘The ThinSat program: Flight opportunities for education, research and industry,’’ in *32nd Annual AIAA/USU Conference on Small Satellites*, 2018. [Online]. Available: https://digitalcommons.usu.edu/smallsat/2018/all2018/409/

[59] J. A. Atchison, ‘‘Monarch: An r-selected spacecraft,’’ Cornell University Dissertation, 2020. [Online]. Available: https://ecommons.cornell.edu/items/8160f6cd-c4f3-4b5b-8898-7ed5b0f5f8bd

[60] SnT University of Luxembourg, ‘‘Launching a pioneering and distributed satellite network,’’ https://snt-highlights.uni.lu/2023/02/27/launching-a-pioneering-and-distributed-satellite-network/, 2023, accessed: July 30, 2025.

[61] K. Kanavouras, A. M. Hein, and M. Sachidanand, ‘‘AttoSats: ChipSats, other Gram-Scale spacecraft, and beyond,’’ *Journal of the British Interplanetary Society*, vol. 72, 2019. [Online]. Available: https://www.researchgate.net/publication/336869820

[62] NASA, ‘‘CubeSat technology roadmap,’’ NASA SMD, Tech. Rep., 2014.

[63] C. Francisco, R. Henriques, and S. Barbosa, ‘‘A review on CubeSat missions for ionospheric science,’’ *Aerospace*, vol. 10, no. 7, p. 622, 2023. [Online]. Available: https://doi.org/10.3390/aerospace10070622

[64] C. Bottiglieri, F. Piccolo, C. Giordano, F. Ferrari, and F. Topputo, ‘‘Applied trajectory design for CubeSat close-proximity operations around asteroids: The

milani case,'' *Aerospace*, vol. 10, no. 5, p. 464, 2023. [Online]. Available: https://doi.org/10.3390/aerospace10050464

[65] S. M. Tieze, L. C. Liddell, S. R. Santa Maria, and S. Bhattacharya, ''Biosentinel: A biological CubeSat for deep space exploration,'' *Astrobiology*, vol. 23, no. 6, pp. 631--636, 2023. [Online]. Available: https://doi.org/10.1089/ast.2019.2068

[66] L. Mazzarella, C. Lowe, D. Lowndes, S. K. Joshi, S. Greenland, D. McNeil, C. Mercury, M. Macdonald, J. Rarity, and D. K. L. Oi, ''QUARC: Quantum research CubeSat---a constellation for quantum communication,'' *Cryptography*, vol. 4, no. 1, p. 7, 2020. [Online]. Available: https://doi.org/10.3390/cryptography4010007

[67] L. Huang, J. Luo, Z. Lin, F. Niu, and L. Liu, ''Using deep learning to map retrogressive thaw slumps in the tibetan plateau using CubeSat imagery,'' *Remote Sensing of Environment*, vol. 237, p. 111534, 2020. [Online]. Available: https://doi.org/10.1016/j.rse.2019.111534

[68] T. Villela, C. A. Costa, A. M. B. ao, F. T. Bueno, and R. Leonardi, ''Towards the thousandth CubeSat: A statistical overview,'' *International Journal of Aerospace Engineering*, vol. 2019, pp. 1--13, 2019. [Online]. Available: https://doi.org/10.1155/2019/5063145

[69] Cornell University, ''ChipSats,'' https://alphacubesat.cornell.edu/{ChipSats}.html, 2020, accessed: July 30, 2025.

[70] H. Gong and S. Gong, ''Design of foldable pcbsat enabling three-axis attitude control,'' *Acta Astronautica*, vol. 192, pp. 193--202, 2022.

[71] K. S. J. Pister, ''Smart Dust: Baa97-43 proposal summary,'' University of California, Berkeley, Research Report, 1997, foundational DARPA proposal for the Smart Dust project.

[72] S. Seager, J. J. Petkowski, C. E. Carr, D. H. Grinspoon, B. L. Ehlmann, S. J. Saikia, R. Agrawal, W. P. Buchanan, M. U. Weber, R. French, P. Klupar, S. P. Worden, and D. Baumgardner, ''Venus life finder missions motivation and summary,'' p. 385, 2022.

[73] B. Warneke, M. Last, B. Liebowitz, and K. S. J. Pister, ''Smart Dust: Communicating with a cubic-millimeter computer,'' *Computer*, vol. 34, no. 1, pp. 44--51, 2001.

[74] J. R. Barker and F. Rodriguez-Salazar, ''Self-organizing Smart Dust sensors for planetary exploration,'' in *Third International Conference on Nano-Networks (Nano-Net 2008)*. ICST/Springer, 2008.

[75] J. M. Kahn, R. H. Katz, and K. S. J. Pister, ''Next century challenges: Mobile networking for Smart Dust,'' in *Proceedings of the 5th Annual ACM/IEEE International Conference on Mobile Computing and Networking (MobiCom '99)*, 1999, pp. 271--278.

[76] B. Warneke, M. Scott, B. Leibowitz, L. Zhou, C. Bellew, J. Chediak, J. Kahn, B. Boser, and K. Pister, ''An autonomous 16 mm3 solar-powered node for distributed wireless sensor networks,'' in *Sensors, 2002. Proceedings of IEEE*, vol. 2, 2002, pp. 1510--1515 vol.2.

[77] Y. Tsuda, O. Mori, R. Funase, and H. Sawada, ''Flight status of IKAROS deep space solar sail demonstrator,'' in *21st AAS/AIAA Space Flight Mechanics Meeting*. AIAA, 2011.

[78] J. Block and J. Straub, ''Solar sail propulsion for CubeSats: A review,'' in *AIAA Space 2016*. AIAA, 2016.

[79] R. Ridenoure, R. Munakata, A. Diaz, and D. Spencer, ''Testing the lightsail 2 flight unit,'' in *AIAA Space 2018 Conference and Exposition*. AIAA, 2018.

[80] A. Heaton *et al.*, ''NEA Scout solar sail propulsion system,'' in *AIAA Space 2014 Conference and Exposition*. AIAA, 2014.

[81] H. A. Atwater *et al.*, ''Materials challenges for the Starshot lightsail,'' *Nature Materials*, 2016.

[82] J. Banik and T. W. Murphey, ''High strain composite booms for solar sails,'' in *AIAA SciTech 2020 Forum*. AIAA, 2020.

[83] L. Nguyen, K. Medina, Z. McConnel, and M. S. Lake, ''Solar cruiser trac boom development,'' in *AIAA SciTech 2023 Forum*. AIAA, 2022.

[84] T. W. Murphey and T. Meink, ''High strain composites for space applications,'' in *58th AIAA/ASCE/AHS/ASC Structures, Structural Dynamics, and Materials Conference*. AIAA, 2017.

[85] W. K. Wilkie, J. Warren, and M. Thom, ''The heliogyro reloaded,'' in *52nd AIAA/ASME/ASCE/AHS/ASC Structures, Structural Dynamics and Materials Conference*. AIAA, 2011.

[86] P. Daukantas, ‘‘Breakthrough Starshot,’’ *Optics & Photonics News*, vol. 28, no. 5, pp. 26--33, 2017. [Online]. Available: https://opg.optica.org/opn/abstract.cfm?uri=opn-28-5-26

[87] L. Niccolai, M. Bassetto, A. A. Quarta, and G. Mengali, ‘‘A review of Smart Dust architecture, dynamics, and mission concepts,’’ *Progress in Aerospace Sciences*, vol. 106, pp. 1--14, 2019. [Online]. Available: https://www.sciencedirect.com/science/article/abs/pii/S0376042118301544

[88] D. Krejci and P. Lozano, ‘‘Space propulsion technology for small spacecraft,’’ *Proceedings of the IEEE*, vol. 106, no. 3, pp. 362--378, 2018.

[89] D. Krejci, F. Mier-Hicks, C. Fucetola, and P. Lozano, ‘‘Design and characterization of a scalable ion electrospray propulsion system,’’ in *34th International Electric Propulsion Conference (IEPC)*. Kobe, Japan: Electric Rocket Propulsion Society (ERPS), 2015.

[90] A. Toorian, K. Diaz, and S. Lee, ‘‘The CubeSat approach to space access,’’ in *2008 IEEE Aerospace Conference*. IEEE, 2008, pp. 1--14.

[91] R. S. Zoll, C. B. Schindler, T. L. Massey, D. S. Drew, M. M. Maharbiz, and K. S. Pister, ‘‘MEMS-actuated carbon fiber microelectrode for neural recording,’’ *IEEE Transactions on Nanobioscience*, vol. 18, no. 2, pp. 234--239, 2019.

[92] D. Teal, H. C. Gomez, C. B. Schindler, and K. S. J. Pister, ‘‘Robust electrostatic inchworm motors for macroscopic manipulation and movement,’’ *2021 21st International Conference on Solid-State Sensors, Actuators and Microsystems (Transducers)*, 2021.

[93] J. E. Rogers, P. M. Ozmun, J. Y. Hung, and R. N. Dean, ‘‘Bi-directional gap closing MEMS actuator using timing and control techniques,’’ in *IECON 2006-32nd Annual Conference on IEEE Industrial Electronics*. IEEE, 2006, pp. 3149--3154.

[94] P. D. Fieseler, ‘‘A method for solar sailing in a low earth orbit,’’ *Acta Astronautica*, vol. 43, no. 9-10, pp. 531--541, 1998. [Online]. Available: https://doi.org/10.1016/S0094-5765(98)00175-1

[95] C. C. Liebe, ‘‘Pattern recognition of star constellations for spacecraft applications,’’ *IEEE Aerospace and Electronic Systems Magazine*, vol. 8, no. 1, pp. 31--39, 1993.

[96] P. Chodas, “Overview of the JPL center for neo studies (cneos),” in *AAS/Division for Planetary Sciences Meeting Abstracts# 47*, 2015, pp. 214--09.

[97] M. Sedky, M. Horii, T. Hosmer, K. Pister, and T. Zohdi, “Multi-objective mission planning for solar sails and swarm networks,” *Computer Methods in Applied Mechanics and Engineering*, vol. 446, p. 118247, 2025.

[98] A. Chamberlin and D. Yeomans, “JPL small-body database browser,” *Jet Propulsion Laboratory: Solar System Dynamics.< Http://Ssd. JPL. NASA. Gov/Sbdb. Cgi# Top*, 2010.

[99] J. R. Samson, “Small, light-weight, low-power, low-cost, high performance computing for CubeSats,” in *2014 IEEE Aerospace Conference*. IEEE, 2014.

[100] ------, “Implementation of a dependable multiprocessor CubeSat,” in *2011 Aerospace Conference*. IEEE, 2011.

[101] V. Studio, “Vocore2: The coin-sized linux computer,” p. 1, 2020.

[102] Y. Su and L. Lin, “A water-powered micro drug delivery system,” *IEEE/ASME Journal of Microelectromechanical Systems*, vol. 13, pp. 75--82, 2004.

[103] B. L. Smarr, D. C. Burnett, S. M. Mesri, K. S. J. Pister, and L. J. Kriegsfeld, “A Wearable Sensor System with Circadian Rhythm Stability Estimation for Prototyping Biomedical Studies,” *IEEE Transactions on Affective Computing*, vol. 7, no. 3, pp. 220--230, jul 2016.

[104] S. Kim and S. Roy, “Microelectromechanical systems and nephrology: the next frontier in renal replacement technology,” *Adv Chronic Kidney Dis*, vol. 20, no. 6, pp. 516--535, 2013.

[105] S. Roy, L. Ferrara, A. Fleischman, and E. Benzel, “Microelectromechanical systems and neurosurgery: a new era in a new millennium,” *Neurosurgery*, vol. 49, no. 4, pp. 779--797; discussion 797--778, 2001.

[106] F. Pirmoradi, K. Iwai, K. Lee, T. Brubaker, and L. Lin, “Microcapsules with magnetic nanoparticle-based shell and aqueous core via selective polymerization for therapeutic delivery applications,” 2013.

[107] M. Nems, *MEMS/NEMS*, 2006.

[108] R. Yeh, S. Hollar, and K. S. J. Pister, “Single mask, large force and large displacement electrostatic linear inchworm motors,” *Journal of Microelectromechanical Systems*, vol. 11, no. 4, pp. 330--336, 2002.

[109] S. Hollar, S. Bergbreiter, and K. S. J. Pister, ‘‘Bidirectional inchworm motors and two-DOF robot leg operation,’’ in *Proceedings of the International Conference on Solid-State Sensors, Actuators, and Microsystems (Transducers)*, vol. 1, 2003, pp. 262--267.

[110] I. Penskiy and S. Bergbreiter, ‘‘Optimized electrostatic inchworm motors using a flexible driving arm,’’ *Journal of Micromechanics and Microengineering*, vol. 23, no. 1, 2012.

[111] H. C. Gomez, C. B. Schindler, H. L. Clark, J. T. Greenspun, and K. S. J. Pister, ‘‘Zero insertion force MEMS socket: 3d multi-chip assembly for microrobotics,’’ in *2019 20th International Conference on Solid-State Sensors, Actuators and Microsystems (TRANSDUCERS EUROSENSORS XXXIII)*, jun 2019, pp. 1732--1735.

[112] C. B. Schindler, H. C. Gomez, and K. S. J. Pister, ‘‘First jumps of a silicon microrobot with an energy-storing substrate spring,’’ in *Proceedings of the International Conference on Solid-State Sensors, Actuators, and Microsystems (Transducers)*, vol. 1, 2021, pp. 349--352.

[113] A. Rauf, D. S. Contreras, R. M. Shih, C. B. Schindler, and K. S. J. Pister, ‘‘Nonlinear dynamics of lateral electrostatic gap-closing actuators for applications in inchworm motors,’’ *Journal of Microelectromechanical Systems*, vol. 31, no. 1, p. 1, 2022.

[114] C. B. Schindler, J. T. Greenspun, H. C. Gomez, and K. S. J. Pister, ‘‘A jumping silicon microrobot with electrostatic inchworm motors and energy storing substrate springs,’’ in *2019 20th International Conference on Solid-State Sensors, Actuators and Microsystems (TRANSDUCERS EUROSENSORS XXXIII)*, jun 2019, pp. 88--91.

[115] H. Gomez, D. Contreras, J. Greenspun, and K. S. J. Pister, ‘‘Zero insertion force MEMS socket for microrobotics assembly,’’ in *2017 International Conference on Manipulation, Automation and Robotics at Small Scales (MARSS)*. IEEE, 2017, cited in later Berkeley microrobotics publications as a MARSS 2017 conference paper.

[116] Daniel S. Contreras, D. S. Contreras, D.S. Contreras, K.S.J. Pister, K.S.J. Pister, Kristofer S. J. Pister, and K. S. J. Pister, ‘‘A SIX-LEGGED MEMS SILICON ROBOT USING MULTICHIP ASSEMBLY,’’ may 2018, mAG ID: 2911260301.

[117] Defense Advanced Research Projects Agency, ‘‘Developing microrobotics for disaster recovery and high-risk environments,’’ jul 2018, DARPA SHort-Range Independent Microrobotic Platforms (SHRIMP) program announcement. [Online]. Available: https://www.darpa.mil/news/2018/microrobotics-disaster-recovery

[118] J. S. Rentmeister, M. H. Kiani, K. S. J. Pister, and J. T. Stauth, ‘‘A 120--330v, sub-$\mu$a, 4-channel driver for microrobotic actuators with wireless-optical power delivery and over 99% current efficiency,’’ in *2020 IEEE Symposium on VLSI Circuits*. Honolulu, HI, USA: IEEE, 2020, pp. 1--2.

[119] Moreno, A. Patel, D. Teal, H. C. Gomez, A. Fearing, J. S. Rentmeister, J. T. Stauth, and K. S. J. Pister, ‘‘Small autonomous robot actuator (SARA): A solar-powered wireless MEMS gripper,’’ in *2021 IEEE International Conference on Robotics and Automation (ICRA)*, 2021.

[120] D. S. Contreras and K. S. J. Pister, ‘‘Hexapod actuation montage,’’ YouTube video, 2018, supplementary video associated with ‘‘A Six-Legged MEMS Silicon Robot Using Multichip Assembly,’’ Proc. 2018 Solid-State Sensors, Actuators and Microsystems Workshop, Hilton Head ’18. [Online]. Available: https://www.youtube.com/watch?v=Ocxz7f7t4e4

[121] Y. Wu, Justin K. Yim, J. K. Yim, J. Nellie Liang, J. Liang, Zhichun Shao, Z. Shao, Mingjing Qi, M. Qi, Junwen Zhong, J. Zhong, Zihao Luo, Z. Luo, Xiangqiao Yan, X. Yan, Min Zhang, M. Zhang, M. Zhang, M. Zhang, Xiaohao Wang, X. Wang, Ronald S. Fearing, R. S. Fearing, Robert J. Full, R. J. Full, Lin Liu, and L. Lin, ‘‘Insect-scale fast moving and ultrarobust soft robot,’’ vol. 4, no. 32, jul 2019, mAG ID: 2966665557.

[122] C. Li, T. Wöhrl, H. K. Lam, and R. J. Full, ‘‘Cockroaches use diverse strategies to self-right on the ground,’’ *Journal of Experimental Biology*, vol. 222, no. 15, p. jeb186080, 2019. [Online]. Available: https://doi.org/10.1242/jeb.186080

[123] U. Saranli, A. A. Rizzi, and D. E. Koditschek, ‘‘Model-based dynamic self-righting maneuvers for a hexapedal robot,’’ *The International Journal of Robotics Research*, vol. 23, no. 9, pp. 903--918, sep 2004. [Online]. Available: https://doi.org/10.1177/0278364904045594

[124] C. C. Kessens, D. C. Smith, and P. R. Osteen, ‘‘A framework for autonomous self-righting of a generic robot on sloped planar surfaces,’’ in *2012 IEEE International Conference on Robotics and Automation*. Saint

Paul, MN, USA: IEEE, may 2012, pp. 4724--4729. [Online]. Available: https://doi.org/10.1109/ICRA.2012.6224770

[125] A. N. Alvara and K. S. J. Pister, ‘‘Low-level control of MEMS driven femto-scale small solar sail spacecraft for earth escape trajectories,’’ in *Small Satellites Systems and Services Symposium (4S 2024)*, ser. Proceedings of SPIE, vol. 13546, Palma de Mallorca, Spain, mar 2025, p. 135464E. [Online]. Available: https://doi.org/10.1117/12.3062792

[126] R. S. Zoll, C. B. Schindler, T. L. Massey, D. S. Drew, M. M. Maharbiz, and K. S. J. Pister, ‘‘MEMS-actuated carbon fiber microelectrode for neural recording,’’ *IEEE Transactions on NanoBioscience*, vol. 18, no. 2, 2019.

[127] NASA, ‘‘Payload test requirements,’’ National Aeronautics and Space Administration, Tech. Rep. NASA-STD-7002B, 2018. [Online]. Available: https://nasa.gov

[128] NASA Goddard Space Flight Center, ‘‘General environmental verification standard (gevs) for gsfc flight programs and projects,’’ NASA GSFC, Tech. Rep. GSFC-STD-7000B, 2021.

[129] E. F. Crawley and D. G. Mohr, ‘‘Experimental measurement of material damping for space structures,’’ *Journal of Guidance, Control, and Dynamics*, vol. 9, no. 1, pp. 87--93, 1986.

[130] T. J. O’Donnell, ‘‘MEMS applications in spacecraft thermal control,’’ NASA Goddard Space Flight Center, Tech. Rep. 20050147478, 2005.

[131] NASA Johnson Space Center, ‘‘Thermal vacuum chamber a facility overview,’’ https://{NASA}.gov, 2023.

[132] TASS (Soviet News Agency), ‘‘Announcement of the first satellite (sputnik) in *Pravda*,’’ Pravda, October 5, 1957 (translated and archived by NASA History Office), 1957, text of original press release issued by TASS, published in Pravda on October 5, 1957, marking the first public disclosure of Sputnik-1’s successful launch. [Online]. Available: https://www.nasa.gov/history/sputnik/14.html

[133] Y. A. Gagarin, ‘‘Report of the flight on satellite-spacecraft vostok 1, 12 april 1961,’’ Federation Aéronautique Internationale Records File (original typescript, Russian), apr 1961, signed typescript flight report submitted 15 April 1961, documenting the first human orbital spaceflight. Submitted for official record validation by the USSR Central Aero Club. [Online]. Available: https://www.wilsoncenter.org/blog-post/declassified-sources-gagarin

[134] N. Aeronautics and S. Administration, ‘‘Apollo 11 mission press kit,’’ NASA Press Release / Press Kit, 8 July 1969, 1969, first publicly released technical summary and crew information prior to launch, documenting mission parameters, objectives, spacecraft systems, and crew biographies.

[135] TASS (Soviet News Agency), ‘‘Announcement of valentina tereshkova as first woman in space in *Pravda*,’’ Pravda, June 16, 1963 (translated from TASS press release), 1963, first public communiqué announcing Soviet cosmonaut Valentina Tereshkova’s flight aboard Vostok 6, marking history as the first woman in space.

[136] A. T. Méndez, ‘‘Soyuz 38 flight: First person of african descent in space,’’ Soviet Intercosmos Program Communiqué, September 1980, 1980, first person of African heritage (and first Latin American) to orbit Earth aboard Soyuz38.

[137] N. . G. S. B. Jr., ‘‘Sts-8 mission specialist guion s. bluford jr. becomes first african-american in space,’’ NASA Press Release, August 30, 1983, 1983, first African-American astronaut to fly in space aboard Space Shuttle Challenger.

[138] R. N. Vela, ‘‘Sts-61-b mission specialist: First mexican citizen in space,’’ NASA / Mexican Government Joint Announcement, December 1985, 1985, neri Vela flew as payload specialist aboard Space Shuttle Atlantis (STS-61-B), becoming the first Mexican citizen in orbit.

[139] J. M. Acabá, ‘‘Soyuz tma-04m / expedition 31/32 crew: First person of puerto rican descent in space,’’ NASA News Release, May 15, 2012, 2012, acabá, of Puerto Rican heritage, became the first person of Puerto Rican descent to travel to space.

[140] NASA, ‘‘Astronaut anne mcclain’s career and public acknowledgment of lgbtq+ identity,’’ NASA Biography and News, 2019, 2019, anne McClain became publicly known as LGBTQ+ following a legal dispute in 2019. [Online]. Available: https://en.wikipedia.org/wiki/Anne_McClain

[141] J. Herrington, ‘‘Sts-113 mission: First native american astronaut,’’ NASA Press Release, November 2002, 2002, john Herrington, Chickasaw Nation member, flew aboard Space Shuttle Endeavour on STS-113. [Online]. Available: https://www.nasa.gov/mission_pages/shuttle/shuttlemissions/sts113/mission-overview.html

[142] M. Jemison, ‘‘Sts-47 mission: First female african-american astronaut,’’ NASA Press Release, September 1992, 1992, flew aboard Space Shuttle Endeavour on

STS-47. [Online]. Available: https://www.nasa.gov/audience/forstudents/5-8/features/nasa-knows/who-was-mae-jemison-58.html

[143] P. S. bin Salman Al Saud, ‘‘Sts-51-g mission: First muslim astronaut and first arab in space,’’ NASA Press Release, June 1985, 1985, flew aboard Space Shuttle Discovery on STS-51-G, first Muslim and Arab in space. [Online]. Available: https://www.nasa.gov/mission_pages/shuttle/shuttlemissions/sts51g/index.html

[144] M. H. Jones, J. Smith, and L. K. Brown, ‘‘Spacesuit development for women astronauts,’’ *Acta Astronautica*, vol. 69, no. 11--12, pp. 1066--1076, 2011, discusses ergonomic improvements in spacesuit design to accommodate female astronauts.

[145] NASA, ‘‘Artemis spacesuit designs to support diverse astronauts,’’ NASA Technical Report, Tech. Rep., 2022, details modular and inclusive design for Artemis spacesuits. [Online]. Available: https://www.nasa.gov/specials/artemis-spacesuit/

[146] R. M. Schneider and K. L. Huang, ‘‘Sex differences in radiation risk for spaceflight,’’ *Radiation Research*, vol. 188, no. 5, pp. 543--555, 2017, evaluates differential radiation sensitivity between sexes.

[147] L. L. Gernhardt, P. W. Smith, and R. J. Patel, ‘‘Physiological considerations for female astronauts,’’ *Journal of Space Medicine*, vol. 15, no. 2, pp. 55--62, 2017, addresses health and fitness requirements for women in microgravity.

[148] M. A. Jones and E. Petrova, ‘‘Cross-cultural communication in international space missions,’’ *Acta Astronautica*, vol. 70, no. 1, pp. 108--116, 2012, discusses language and cultural adaptation in multinational crews.

[149] A. Salas and D. E. Maurino, ‘‘Team training in spaceflight operations: The importance of cultural competence,’’ *Human Factors*, vol. 57, no. 5, pp. 857--866, 2015, examines cultural competence training for diverse astronaut crews.

[150] NASA, ‘‘Incorporating religious practices into space missions: Lessons from the iss,’’ NASA Internal Report, Tech. Rep., 2018, addresses religious accommodations for astronauts on long-duration missions.

[151] S. Ride, ‘‘NASA engineers packed 100 tampons in legendary astronaut sally ride’s toiletry kit for just one week in space,’’ 2025, accessed: 2025-07-22. [Online]. Available: https://people.com/nasa-engineers-packed-100-tampons-for-sally-ride-for-one-week-in-space-8781804

[152] Presidential Commission on the Space Shuttle Challenger Accident, ‘‘Report of the presidential commission on the space shuttle challenger accident, volume 1,’’ U.S. Government Publishing Office, Washington, DC, Tech. Rep. AD-A171402, jun 1986. [Online]. Available: https://ntrs.nasa.gov/archive/nasa/casi.ntrs.nasa.gov/19860015255.pdf

[153] E. N. Satinsky, T. Kimura, M. V. Kiang, R. Abebe, S. Cunningham, H. Lee, X. Lin, C. H. Liu, I. Rudan, S. Sen, M. Tomlinson, M. Yaver, and A. C. Tsai, ‘‘Systematic review and meta-analysis of depression, anxiety, and suicidal ideation among Ph.D. students,’’ *Scientific Reports*, vol. 11, no. 1, p. 14370, 2021. [Online]. Available: https://doi.org/10.1038/s41598-021-93687-7

[154] A. G. Garcia-Williams, L. Moffitt, and N. J. Kaslow, ‘‘Mental health and suicidal behavior among graduate students,’’ *Academic Psychiatry*, vol. 38, no. 5, pp. 554--560, 2014. [Online]. Available: https://doi.org/10.1007/s40596-014-0041-y

[155] E. A. Jach and A. P. Rinaldi, ‘‘Applying theory and research toward reducing suicidality among graduate students and postdoctoral scholars,’’ *Studies in Graduate and Postdoctoral Education*, vol. 15, no. 1, pp. 49--64, 2024. [Online]. Available: https://doi.org/10.1108/SGPE-12-2022-0084

[156] L. Zhang, ‘‘Why is suicide incidence among doctoral students so high? a study of china’s doctoral tutorial system,’’ *Heliyon*, vol. 9, no. 8, p. e18382, 2023. [Online]. Available: https://doi.org/10.1016/j.heliyon.2023.e18382

[157] T. Marutani, K. Yasumi, K. Saito, T. Ibaraki, and J.-y. Takayama, ‘‘Suicide among national university graduate students in japan from 2002 to 2021,’’ *Psychiatry and Clinical Neurosciences Reports*, vol. 3, no. 1, p. e180, 2024. [Online]. Available: https://doi.org/10.1002/pcn5.180

[158] J. A. Cox, C. Driver, B. T. Hutchinson, J. E. Bragg, and G. J. M. Read, ‘‘Experiences of suicidality in PhD students: A mixed methods study,’’ *Counselling Psychology Quarterly*, pp. 1--25, 2025, advance online publication. [Online]. Available: https://doi.org/10.1080/09515070.2025.2572565

[159] M. Kogien, S. R. Marcon, A. F. d. Oliveira, V. F. Leite, C. F. Modena, and F. C. d. S. Nascimento, ‘‘Factors associated with suicidal behavior in graduate students: A scoping review,’’ *Revista De Enfermagem Da UFPI*, vol. 11, no. 1, p. e2731, 2022. [Online]. Available: https://doi.org/10.26694/reufpi.v11i1.2731

[160] C. M. Hazell. (2022) ‘‘You Have to Suffer for Your PhD’’: Poor mental health among doctoral researchers -- new research. The Conversation.

[161] V. B. Meyer-Rochow and J. Gal, ‘‘Pressures produced when penguins pooh---calculations on avian defaecation,’’ *Polar Biology*, vol. 27, pp. 56--58, 2003.

# Appendix A

# MEMS Fabrication

## A.1 SOI Fabrication Stack and Process Rationale

The primary fabrication sequence was developed around a silicon-on-insulator (SOI) wafer consisting of a 550 $\mu$m thick single-crystal $\langle 100 \rangle$ silicon handle layer, a 2 $\mu$m buried silicon dioxide layer, and a 40 $\mu$m thick single-crystal $\langle 100 \rangle$ silicon device layer. The device layer defined the released mechanical structures, while the handle layer provided wafer-level mechanical support during frontside lithography, metal patterning, and device-layer etching. The buried oxide served both as an etch-stop layer during silicon DRIE and as the sacrificial release layer during the final HF vapor etch.

The fabrication process is broken up into specific structure layers: Metal (MET), Device layer (SOI), Buried Oxide (BOX), and Substrate (SUB). Each of these layers has its own set of fabrication steps and in addition there are Chip Removal, Nitride Layer, and Glass Cover Layer processes that have their own fabrication steps. While Nitride Layer and Glass Cover Layer steps are not usually done for all processes here, the rest are what is considered the normative process workflow.

The frontside device and metal lithography steps used 2 $\mu$m MiR701 without edge-bead removal. This choice preserved resist coverage near the patterned wafer perimeter, but it also required care during subsequent handling because edge-bead retention can increase local topography and may affect contact during lithography or bonding. The metal layer was deposited by e-beam evaporation using chromium followed by gold. Chromium was used as an adhesion layer to the silicon surface, while gold provided the conductive layer for electrical routing and actuator contact pads. Following deposition, the excess metal was removed using a lift-off process.

Table A.1: Nominal SOI wafer stack and process materials used in the fabrication sequence.

| **Layer or material** | **Nominal thickness** | **Function in process** |
|---|---|---|
| ⟨100⟩ Si handle layer | 550 $\mu$m | Mechanical support layer; removed locally by backside DRIE. |
| Buried $SiO_2$ layer | 2 $\mu$m | DRIE etch stop and sacrificial release layer. |
| ⟨100⟩ Si device layer | 40 $\mu$m | Structural layer for actuators, linkages, and released micromechanical components. |
| MiR701 photoresist | 2 $\mu$m | Frontside device-layer etch mask and metal lift-off lithography resist. |
| AZ 12XT photoresist | 10 $\mu$m | Thick backside photoresist mask for handle-layer silicon DRIE. |
| Cr/Au metallization | 0.04 $\mu$m/0.02 $\mu$m | Chromium adhesion layer and gold conductive layer deposited by e-beam evaporation. |

## A.2 Process Notes

Step 1 (picotrack1) uses the picotrack1 tool to perform Spin PR. The specific recipe employed is 'T1 _OiR906_1.2um'. Key operational notes include: Disable TEBR.

Step 2 (mla150) uses the mla150 tool to perform Expose PR. The specific recipe employed is 'Approx 210mJ/cm2, defocus of -2. Use defoc +4 for pneumatic.'. Alignment marks are needed here and should be taken from the MLA150 standard manual.

Step 3 (picotrack2) uses the picotrack2 tool to perform Develop PR. Step 4 (axcelis UV bake) uses the axcelis UV bake tool to perform Hardbake. The specific recipe employed is 'program J'.

Step 4 (cha) uses the cha tool to perform Evaporate Cr and Au.

Step 5 (asap liftoff) uses the asap liftoff tool to perform Lift off excess Au. The specific recipe employed is 'Recipe 17'.

Step 6 (picotrack1) uses the picotrack1 tool to perform Spin PR.

Step 7 (mla150) uses the mla150 tool to perform Expose PR. The specific recipe employed is 'Approx 210mJ/cm2, defocus of -2. Alignment mode here. Use defoc +4

Table A.2: Itemized representation of approximate normative tool usage and timing. Shows the process flow and reservation system requirements. Each tool requires passing a required quiz and some others like primaxx, ptherm, cha, sts-2/-oxide, picotract 1/2, mla150, and all sinks require in-person training and qualification verification by a process engineer.

| | Step | Duration (mins) | Duration (hours) | Tool | Needs RSVP? | Process |
|---|---|---|---|---|---|---|
| Metal | 1 | 5.00 | 0.08 | picotrack1 | N | Spin PR |
| | 2 | 90 | 1.50 | mla150 | Y | Expose PR |
| | 3 | 5 | 0.08 | picotrack2 | N | Develop PR |
| | 4 | 10 | 0.17 | axcelis UV bake | N | Hardbake PR |
| | 4 | 180 | 3.00 | cha | Y | Evaporate Metal |
| | 5 | 15 | 0.25 | asap liftoff | N | Lift-off |
| Frontside | 6 | 5 | 0.08 | picotrack1 | N | Spin PR |
| | 7 | 90 | 1.50 | mla150 | Y | Expose PR |
| | 8 | 5 | 0.08 | picotrack2 | N | Develop PR |
| | 9 | 5 | 0.08 | axcelis UV bake | N | Hardbake PR |
| | 10 | 60 | 1.00 | sts2 | Y | DRIE $Si$ |
| | 11 | 10 | 0.17 | msink18 | Y | Strip PR |
| Backside | 12 | 5.00 | 0.08 | picotrack1 | N | Spin PR |
| | 13 | 120 | 2.00 | mla150 | Y | Expose PR |
| | 14 | 5 | 0.08 | picotrack2 | N | Develop PR |
| | 15 | 60 | 1.00 | oven | N | Hardbake PR |
| | 16 | 5 | 0.08 | cool-grease | N | Bonding Wafers |
| | 17 | 20 | 0.33 | hotplate | N | Cure Cool-Grease |
| | 18 | 300 | 5.00 | sts-oxide | Y | |
| DRIE $SiO_2$ | 19 | 180 | 3.00 | sts2 | Y | DRIE $Si$ |
| | 20 | 20 | 0.33 | msink18 | N | Strip PR |
| | 21 | 5 | 0.08 | coolgrease | N | Wafer De-Bonding |
| | 22 | 60 | 1.00 | primaxx | Y | Vapor HF Etch $SiO_2$ |
| | Total | 1260 | 21.00 | | | |

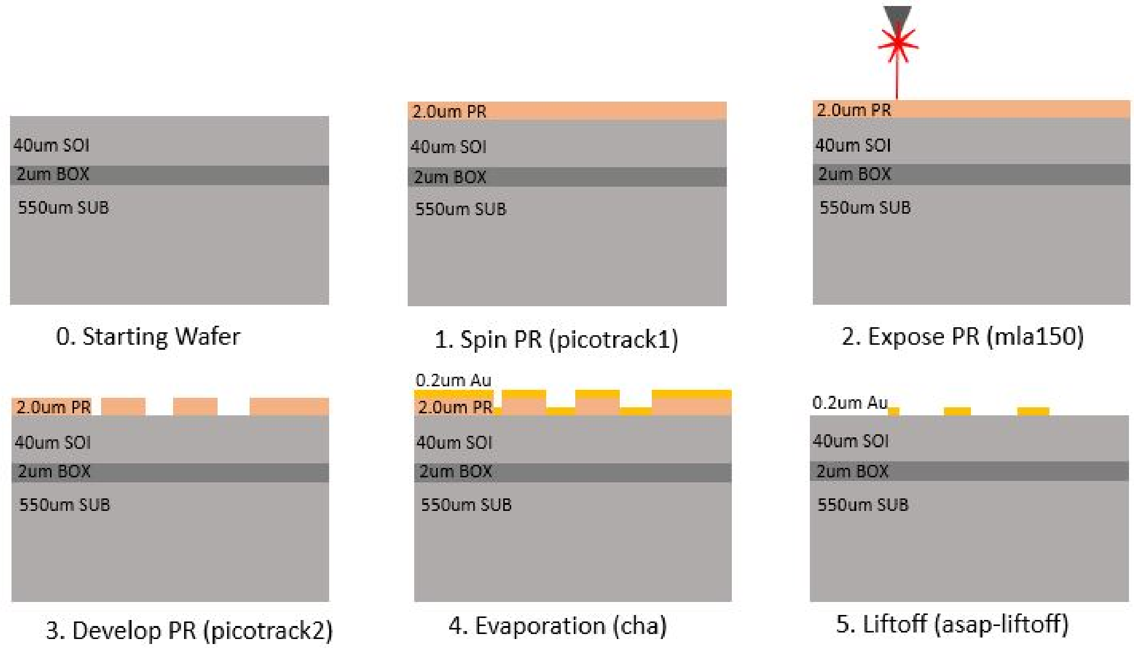


Figure A.1: Diagram showing the metal layer fabrication process. Displayed here are six sub-figures: (0) Starting wafer with SOI, BOX, and SUB layers at 40/2/550 $\mu m$

for pneumatic.'.

Step 8 (picotrack2) uses the picotrack2 tool to perform Develop PR.

Step 9 (axcelis UV bake) uses the axcelis UV bake tool to perform Hardbake PR. The specific recipe employed is 'recipe U (it takes 5 minutes to run). This is the same as in the NanoLabś example MiR701 process'.

Step 10 (sts2) uses the sts2 tool to perform DRIE.

Step 11 (msink18) uses the msink18 tool to perform Strip PR if picotrack1/2 is down. Key operational notes include: Email Joanna to see if she can help..

Step 12 (picotrack1) uses the picotrack1 tool to perform Spin PR. Key operational notes include: Disable TEBR.

Step 13 (mla150) uses the mla150 tool to perform Expose PR (immediately after soft bake). The specific recipe employed is 'Approx 1200mJ/cm2, defocus of -2. Alignment mode here. HA Mode. Use defoc +4 for pneumatic.'.

Step 14 (picotrack2) uses the picotrack2 tool to perform Develop PR.

Step 15 (oven) uses the oven tool to perform Hardbake PR. The specific recipe employed is '120C for 1 hour'. Key operational notes include: This step is bad because it re-flows the resist. Might need to find alternative in future..

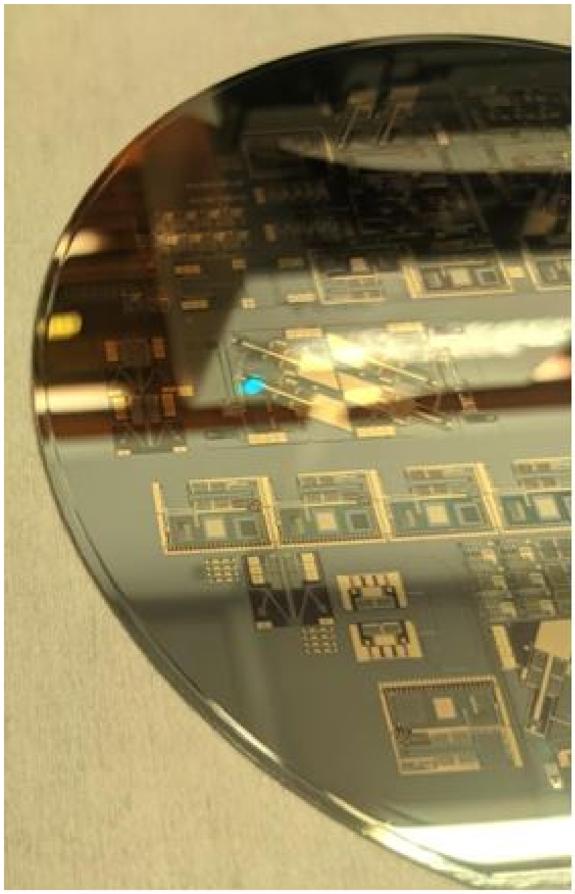

Figure A.2: Image of the wafer as fabricated after completing the metal layer phase. Image shows the metal structures with PR removed after metal liftoff.

Step 16 (countertop) uses the countertop tool to perform Bond to Oxidized Handle Wafer. The specific recipe employed is 'bond wafers with Cool Grease dollops'. Key operational notes include: Be careful with where we put the cool grease, it kills motors and deposits film.

Step 17 (Hotplate) uses the Hotplate tool to perform Cure cool grease. The specific recipe employed is '50C for 20 mins with weight on top'.

Step 18 (sts-oxide) uses the sts-oxide tool to perform etch of oxide.

Step 19 (sts2) uses the sts2 tool to perform DRIE.

Step 20 (msink18) uses the msink18 tool to perform Strip PR.

Step 21 (countertop) uses the countertop tool to perform Wafer de-bonding.

Step 22 (primaxx) uses the primaxx tool to perform Vapor HF Release. The

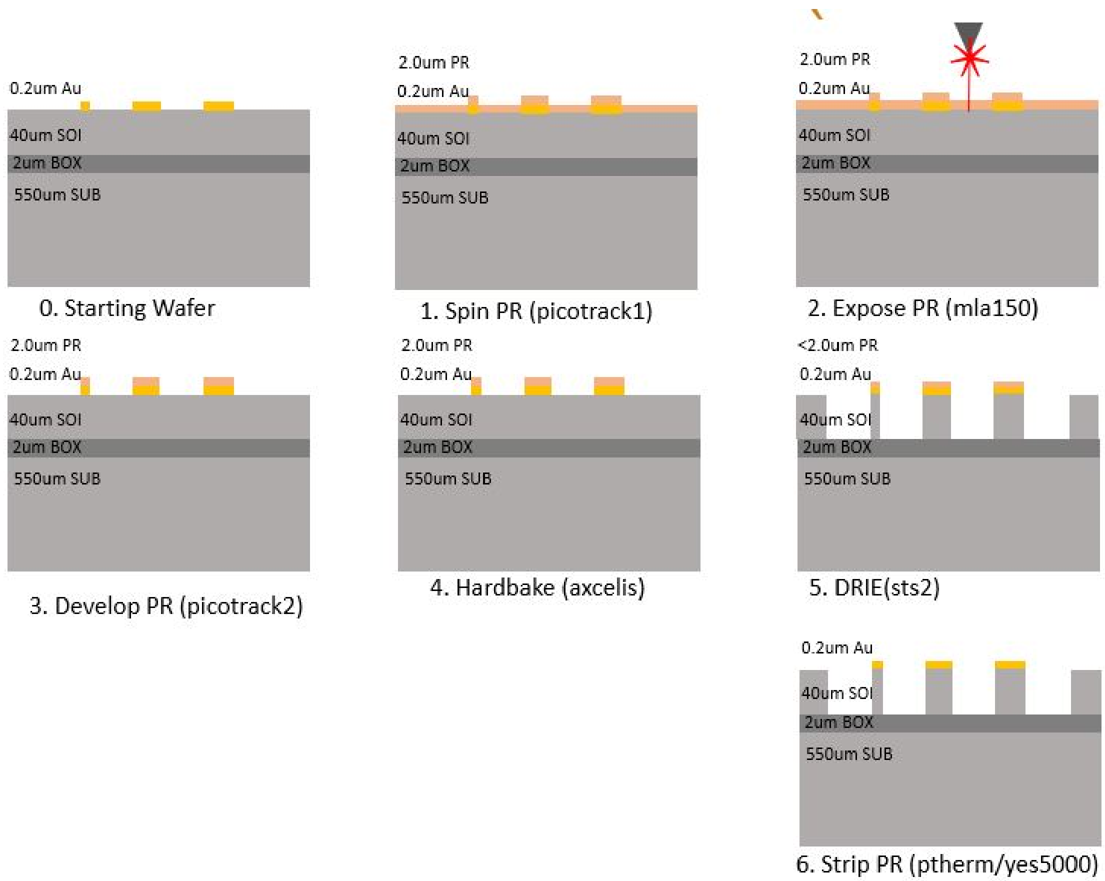


Figure A.3: Layout showing the device layer process with seven sub-figures: (0) Starting Wafer with metal already deposited; (1) Spin PR step showing 2 $\mu m$ PR layer; (2) Expose PR step showing the laser raster exposing the photoresist; (3) Develop PR; (4) Evaporation of metal; (5) Metal Lift-offwet-etch.

specific recipe employed is Recipe 3, 8 cycles.

Tools used in this process include: picotrack1, mla150, picotrack2, axcelis UV bake, cha, asap liftoff, sts2, msink18, oven, countertop, Hotplate, sts-oxide, primaxx. Each of these tools plays a vital role in the overall fabrication sequence and would not be possible without the maintenance, training, upkeep, troubleshooting, detailed instruction, safety, and general ambiance of the Marvell Nanolab Staff, Technicians, and Interns.

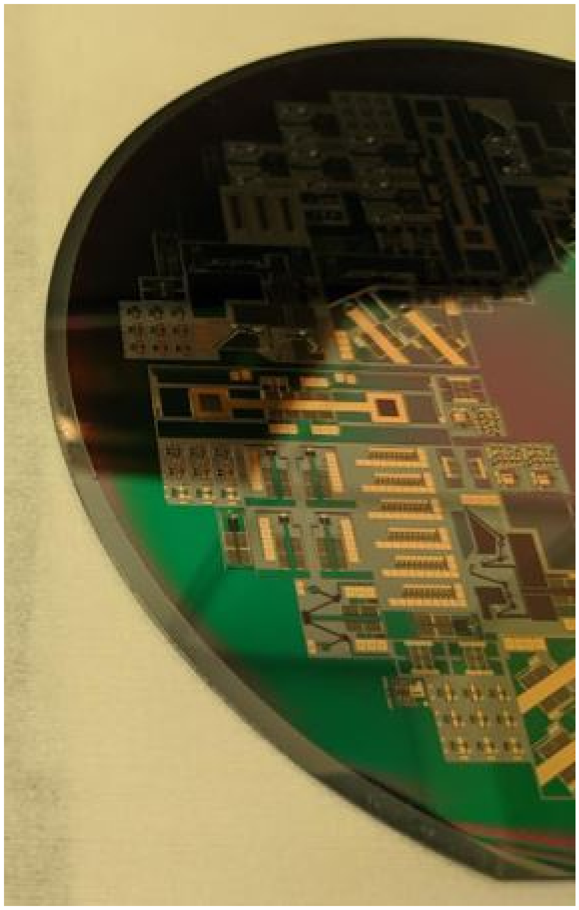

Figure A.4: Image of a pre-etched frontside wafer showing the metal and SOI structures.

## A.3 Buried-Oxide Vapor HF Release

After silicon DRIE and photoresist removal, the exposed buried oxide was etched using the Primaxx vapor HF release process. Vapor HF was selected because it reduces liquid-water exposure during release and therefore reduces the probability of stiction in released MEMS structures. This was particularly important for compliant micromechanical structures with narrow gaps and suspended members.

The required oxide undercut was set by the square access geometry. For a 6 $\mu$m $\times$ 6 $\mu$m opening, the minimum lateral etch distance needed to reach the center

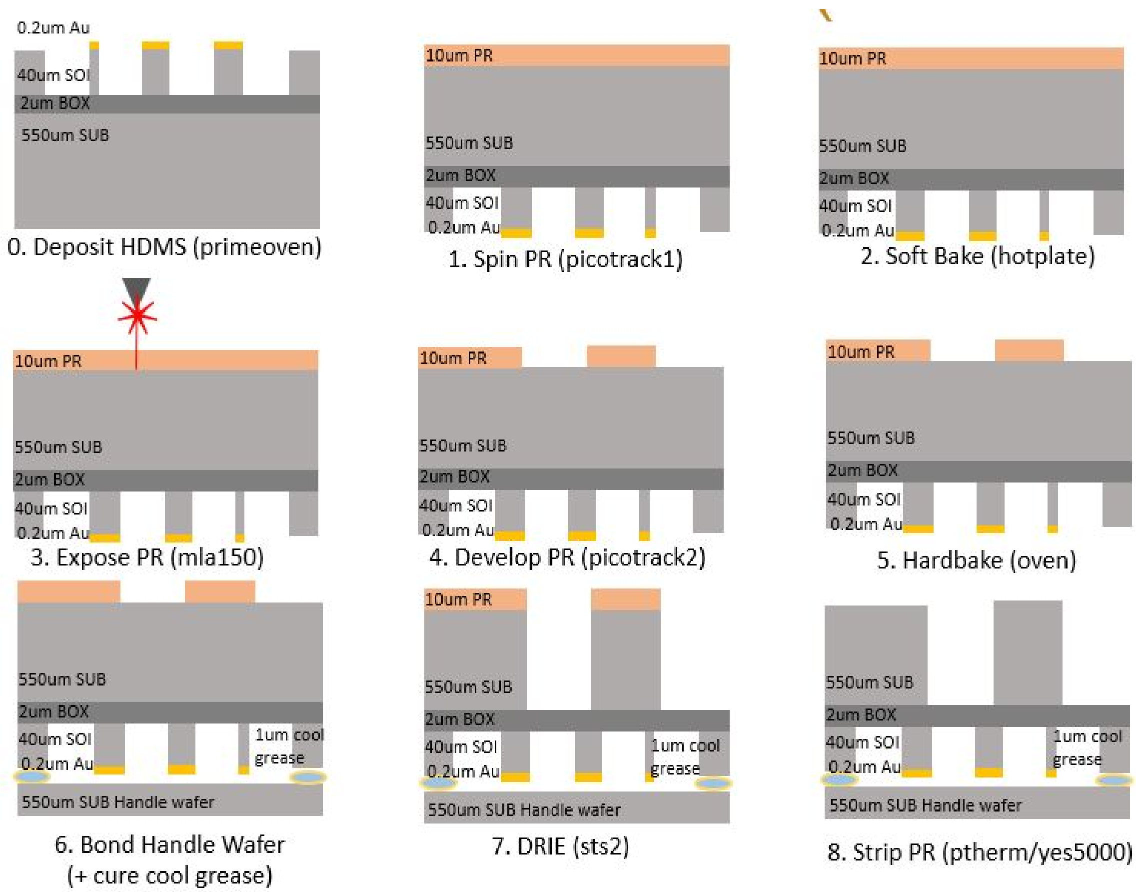


Figure A.5: diagrams of nine sub-figures showing the backside etch process: (0) Deposit Hexamethyldisilazane (HMDS, $(CH_3)_3SiNHSi(CH_3)_3$); (1) Spin PR to the backside; (2) Soft Bake PR on the hotplate; (3) Expose PR, shown here as the raster of a laser in mla150 tool; (4) Develop PR; (5) Hardbake wafer in the oven; (6) Bond handle wafer to frontside using cool grease; (7) DRIE using the specified recipe; (8) Strip PR.

of the square is one half of the diagonal:

$$\frac{\sqrt{(6\ \mu\text{m})^2 + (6\ \mu\text{m})^2}}{2} = 3\sqrt{2}\ \mu\text{m} \approx 4.24\ \mu\text{m}.$$

An additional 1.5 $\mu$m over-etch was included to account for process variation and ensure complete oxide removal under the intended square feature. The target lateral


Figure A.6: Image of the backside etch process through the view port of the STS-2 tool showing the wafer on the chuck within the vacuum chamber as plasma is active (blue color).

oxide etch distance was therefore

$$x_{\mathrm{HF,target}} = 3\sqrt{2}\ \mu\mathrm{m} + 1.5\ \mu\mathrm{m} \approx 5.74\ \mu\mathrm{m}.$$

Using the nominal Primaxx Recipe 3 thermal-oxide etch rate of approximately 900 Å/min, or 0.09 $\mu$m/min, this target undercut corresponds to an estimated process time of approximately 64 min. The final recipe time was therefore selected to be on the order of one hour, with the understanding that oxide etch rate, exposed interface area, and local release geometry can modify the effective undercut rate.

Because photoresist is not a reliable masking material for vapor HF release and can contaminate the chamber, the HF vapor release step was performed only after the lithographic masks used for DRIE had been removed. This sequencing ensured that the final release chemistry acted primarily on the exposed buried oxide and not on residual polymer masking layers.

## A.4 Deep Reactive Ion Etching

Deep reactive ion etching (DRIE) was used for both the frontside device-layer etch and the backside handle-layer etch. In the STS2 process, silicon etching is performed using an alternating-cycle advanced silicon etch (ASE) process. Each cycle alternates between a passivation step, in which a fluorocarbon polymer protects exposed sidewalls, and an etch step, in which the exposed silicon is directionally removed. This cyclic passivation--etch sequence enables high-aspect-ratio silicon trenches with near-vertical sidewalls, provided that the etch mask, thermal contact, loading, and etch depth are controlled.

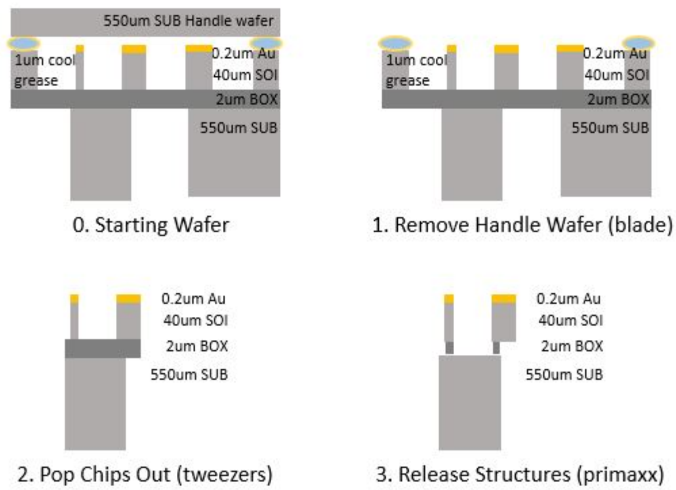


Figure A.7: Figure showing the chip release and removal process steps in four subfigures: (0) Starting wafer with handle wafer epoxied to the frontside; (1) using a straight blade, apply pressure between the handle wafer and the frontside of the fabrication wafer at the point of epoxy application; (2) use tweezers to carefully remove chips that have already fallen out and apply pressure at edges of wafer near chip attachment to pop the chips out; and (3) place chips in HF-gas chamber for the set recipe.

For the frontside etch, the 40 $\mu$m device layer was patterned using the MiR701 mask and etched until the buried oxide was reached. For the backside etch the tool requires vacuum sealing through the wafer, and as such the frontside having already been etched an additional handle wafer was bonded to the frontside using a cool grease. This bonding process was messy and difficult to manage, often ending in epoxy causing contamination of the frontside structures.

Additionally, the process requirement was substantially more demanding because the 550 $\mu$m silicon substrate layer had to be etched through locally from the backside. In this case, the backside mask was not a thin frontside resist, but a 8 $\mu$m AZ 12XT thick-photoresist layer. The backside process therefore required explicit characterization of the effective silicon-to-photoresist etch ratio under the intended layout and etch conditions. The etch process was treated in terms of cycle count rather than only total etch time. This is important because DRIE depth is more directly tied to etch depth per cycle, while total time can obscure changes in cycle structure, loading, platen conditions, or local feature density. The backside etch was also expected to be more sensitive to wafer-scale spatial effects because the etch depth approached

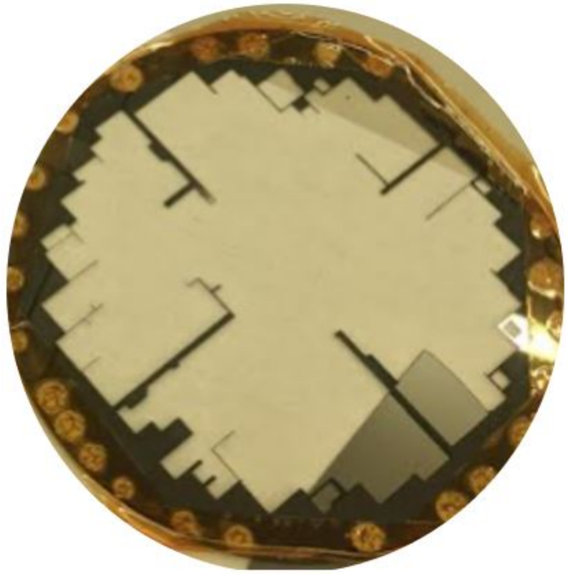

Figure A.8: Image of wafer after all chips are popped out.

the full handle-layer thickness. Consequently, backside PR survival was evaluated experimentally before committing to the full device process, as described in Section A.5.

## A.5 Thick Photoresist Use Case: AZ 12XT

A 10 $\mu$m AZ 12XT backside photoresist mask was selected for the handle-layer DRIE because the backside silicon etch required hundreds of micrometers of silicon removal. Although tool-level DRIE selectivity values provide a useful first-order estimate, the relevant process margin depends on the actual resist, exposure mode, hardbake, feature geometry, wafer position, and etch depth used in the device process. Because this AZ 12XT use case had not been fully characterized for the specific backside release geometry, a dedicated photoresist-consumption study was performed.

As shown in Fig. A.9, the 150 $\mu$m etch condition left approximately 5.6--6.1 $\mu$m of residual AZ 12XT across the measured wafer markers. The 350 $\mu$m condition reduced the remaining PR thickness to approximately 2.6--3.6 $\mu$m, while the 450 $\mu$m condition produced the lowest residual mask thickness, with several measured locations approaching or falling below 1 $\mu$m. This result indicated that a 10 $\mu$m AZ 12XT mask could support deep backside etching, but that the process margin became narrow for etches approaching the full 550 $\mu$m SOI handle thickness.

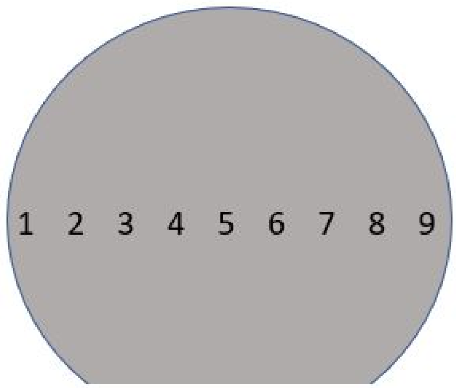


(a) Schematic of the AZ 12XT backside photoresist characterization sample. The test structure was used to measure residual photoresist thickness after silicon DRIE at multiple wafer locations and etch depths.

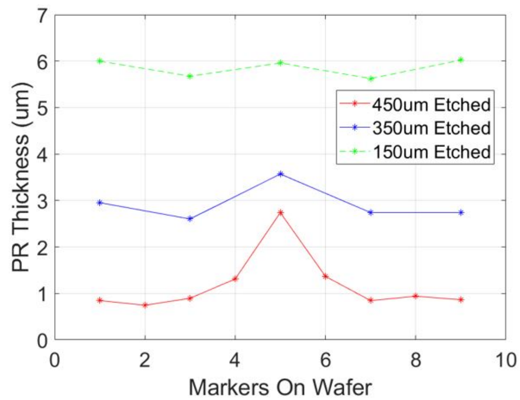


(b) Measured AZ 12XT photoresist thickness at selected wafer markers after silicon etch depths of approximately 150 $\mu$m, 350 $\mu$m, and 450 $\mu$m. The residual PR thickness was highest for the shallow etch and decreased with increasing silicon etch depth, as expected.

Figure A.9: Characterization of photoresist erosion during deep reactive ion etching (DRIE).

To separate wafer-position effects from feature-geometry effects, additional measurements were taken on center-ring and outer-ring test structures. This comparison is important because backside DRIE can exhibit spatial nonuniformity, local loading effects, and geometry-dependent etch behavior. The outer ring represents a more conservative process region because edge-adjacent features and larger exposed areas can experience different ion, neutral-species, and thermal histories than central features.

The ring-structure measurements, shown in Fig. A.10, revealed a clear divergence between the center-ring and outer-ring regions. At approximately 150 $\mu$m of silicon etch depth, both regions consumed roughly 2 $\mu$m of AZ 12XT. At approximately 350 $\mu$m, the center-ring structure consumed approximately 4.4 $\mu$m of PR, while the outer-ring structure consumed approximately 5.0 $\mu$m. At approximately 450 $\mu$m, this difference increased further, with the center-ring consuming approximately 5.3 $\mu$m and the outer-ring consuming approximately 7.1 $\mu$m. The corresponding effective silicon-to-photoresist selectivity was therefore approximately 85:1 for the center-ring region and approximately 63:1 for the outer-ring region at the deepest characterized condition.

These results show that the backside AZ 12XT mask cannot be evaluated using a single global selectivity value. Instead, the conservative design case is governed by the lowest measured effective selectivity and the thinnest residual PR region. For a


(a) Ring-based characterization layout.

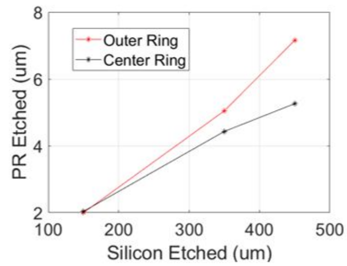


(b) PR removed vs. Si etch depth.

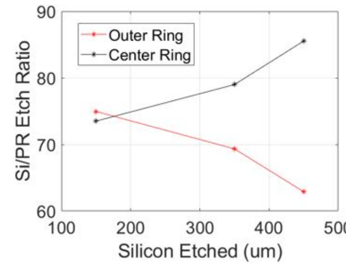


(c) Effective Si-to-PR etch ratio.

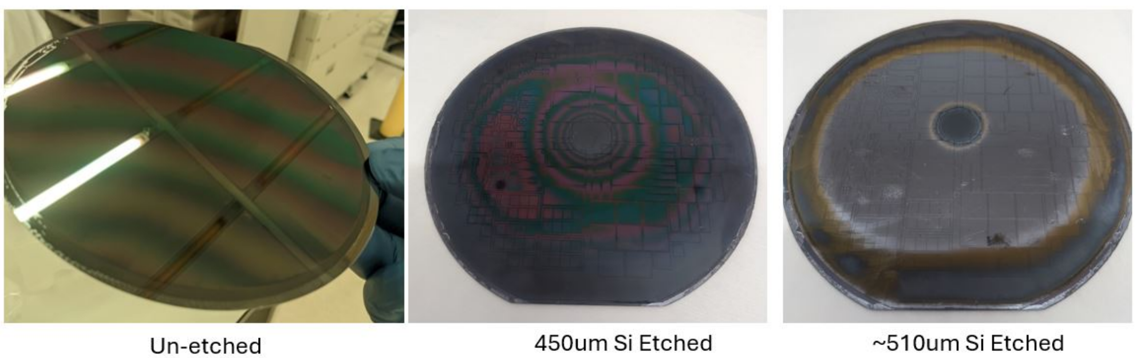


(d) Backside wafer images: (Left) after PR hard bake; (Middle) after 450 $\mu$m Si etch; and (Right) after $\sim 510$ $\mu$m Si etch.

Figure A.10: Comprehensive characterization of spatial variation in AZ 12XT photoresist consumption and etch selectivity during backside silicon DRIE.

full 550 $\mu$m handle-layer etch, a 63:1 selectivity would consume approximately

$$\frac{550\ \mu\text{m}}{63} \approx 8.7\ \mu\text{m}$$

of AZ 12XT, leaving only about 1.3 $\mu$m of nominal resist from an initial 10 $\mu$m film. This remaining margin is small when wafer-scale nonuniformity, local PR thinning, and endpoint uncertainty are included. Therefore, the outer-ring measurements were treated as the conservative mask-budget condition for backside etch planning.

## A.6 MLA Use Cases

As I was one of the Marvell Nanolab's first users on the Heidelberg Maskless Aligner (MLA150), a set of previously undiscovered errors were discovered.

During exposure of PR on wafers while using the MLA150 tool, it was observed that the samples would exit the tool with varying strips of unexposed PR along the entirety of the wafer. These strips were neither regular nor uniform in width of periodicity of occurrence. They were however occurring across the entirety of the wafer where they did occur. See Figs. A.11, A.12, A.13, A.14, A.15, and A.16 for images of the lines.

Inspection confirmed that these lines were in fact undeveloped or underdeveloped sections of PR, as ellipsometry after exposure, development, and before hard bake confirmed the height to be approximately 2 $\mu m$. Further, profilometry after exposure and hard bake confirmed the height of the PR structures to be uniformly approximately 1.7 $\mu m$, as expected.

After an attempt to reproduce the lines for a review of exposure and dosage parameters, it was observed that a variation in dosage, exposure, or tolerance parameters did not sufficiently reproduce these lines in a consistent manner, nor did it reduce them in a meaningful way.

Upon inspecting wafers for bowing, it was also confirmed that these wafers were well within the 70 $\mu m$ bowing height tolerance set by the Marvell Nanolab process engineers ($10 - 40$ $\mu m$). There was no observed correlation between wafer bowing height and the presence of the lines.

It was also observed that the presence of the lines did not occur on all wafers and would not occur with all designs uploaded to the MLA system. Upon inspection, the anomalous lines would only occur when using a specific design file.

After inspecting the suspected design file, it was confirmed that these lines were not in the file itself nor did they appear in computational postprocessing as viewed in the adjoined computer housing the Heidelberg system. This was already suspected as the lines were not consistent in their placement from wafer to wafer although the same design file would be used.

After confirming that these lines only occurred when using the specified design file, the orientation of the design was changed by a range of angles ($15^o$, $45^o$, and $60^o$) all showing presence of the lines in the same direction, though again in non-regular spacing and thickness. Upon inquiry with Nanolab engineers, Heidelberg engineers, and inspection of the tool itself, it was determined that these lines were in fact in the direction of the laser raster motion. It was further posited that the file itself might be somehow interfering with the control mechanism. As such, the file was sent to Heidelberg for inspection and no indication that the file itself caused the issue was

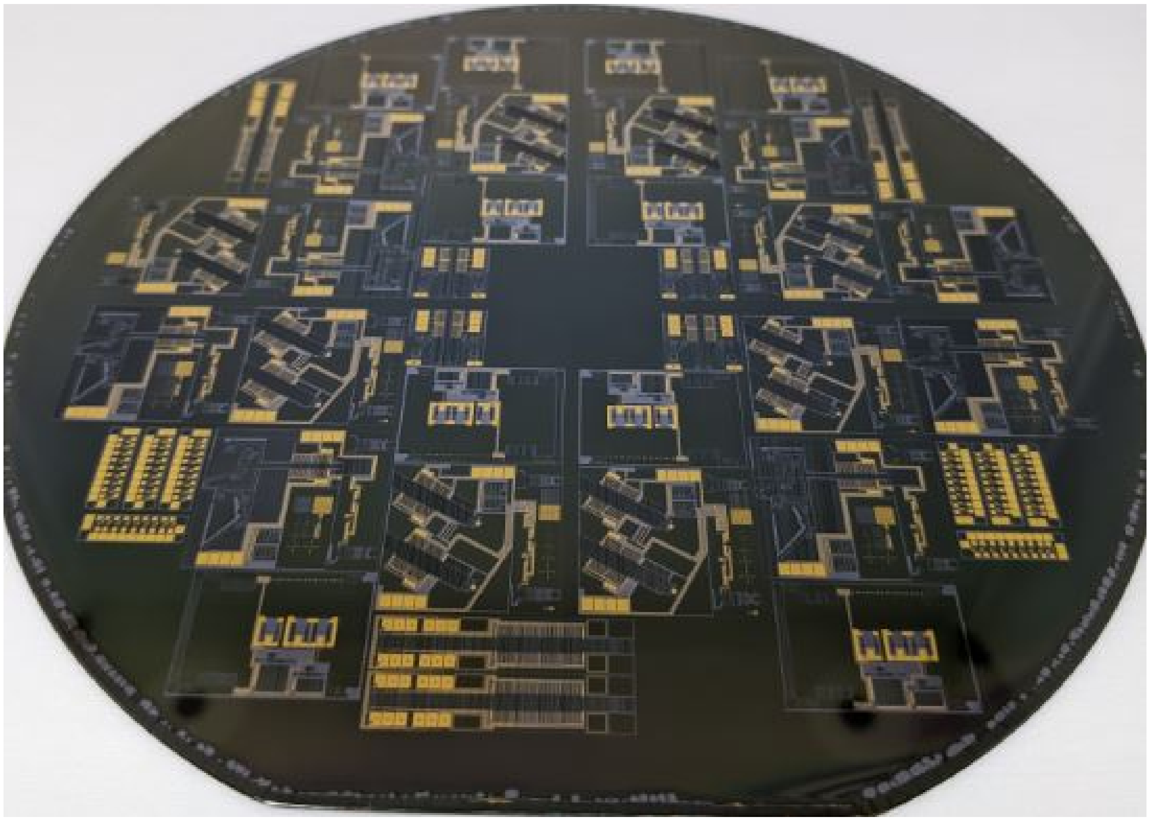

Figure A.11: Image of the wafer post-PR development after frontside designs were exposed in MLA150.

stated. Similarly the file was recreated with only specific structures present (though from the same file) and the lines would not present under these circumstances.

To further inquire here, the file was augmented to have varying fractions of the design present on the file to test if the control processor was somehow being overloaded by the number of instructions per line. It was verified that for this specific design file, approximately 1/4 showed no presence of lines, above this fraction the lines occurred and angular changes did not adequately affect the presence or frequency of the lines, nor the periodicity of them.

An inspection of the wafers that presented with the lines showed a varying spacing of 5 $\mu m$ to 1 $cm$; varying width of 4 $\mu m$ to 0.9 $mm$; and varying number of lines 8 to 42 per wafer.

A solution that was found was to expose 1/4 of the design file at a time in four successive exposures. This proved successful. No further analysis on this problem has been done by the author and no feedback from Heidelberg or Marvell Nanolab

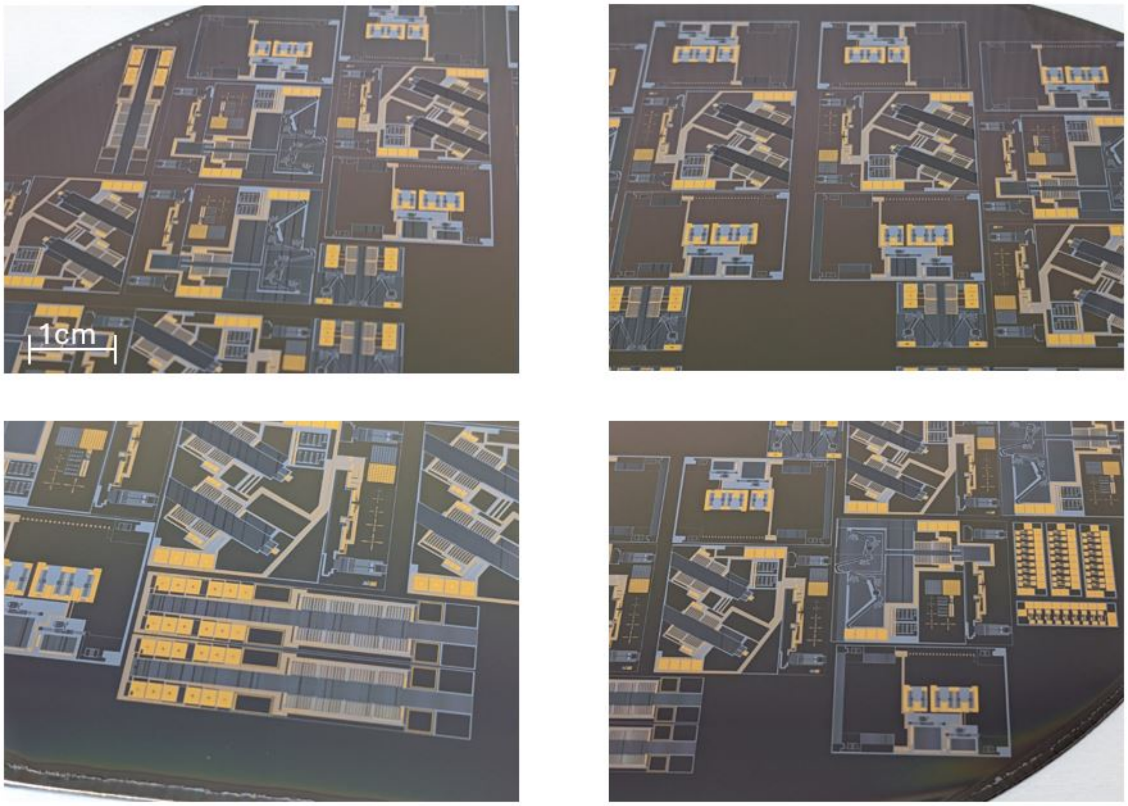


Figure A.12: Zoomed in images of the wafer post-PR development after frontside designs were exposed in MLA150.

was offered on the root cause of the problem.

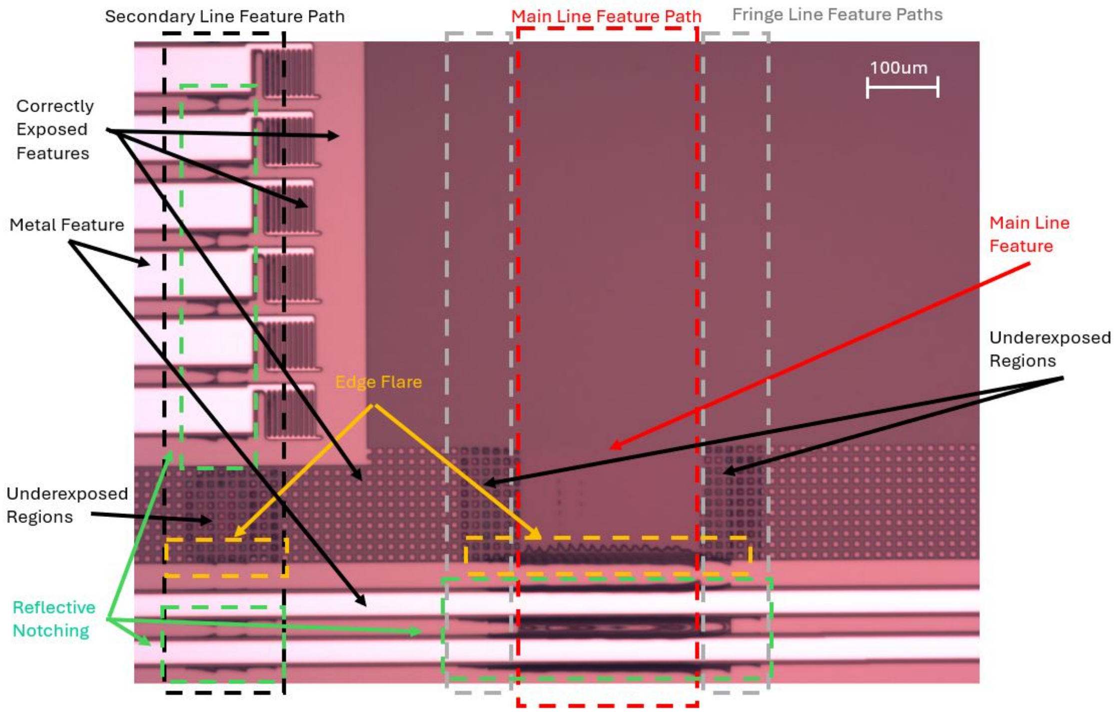


Figure A.13: Image of the wafer post-PR development after frontside designs were exposed in MLA150. Showing the main line feature which is the feature that is visible in Fig. A.12; the fringe line features which are accompanied with every main line; the secondary line features which are features that have underexposed areas but do not have the main line style feature that represents what can only be described as a continuous lack of exposure; the edge flare regions that have notching style shapes that are more prominent the closer to a main line or secondary line path; as well as the reflection notching regions that were only present on or around the metallicized features.

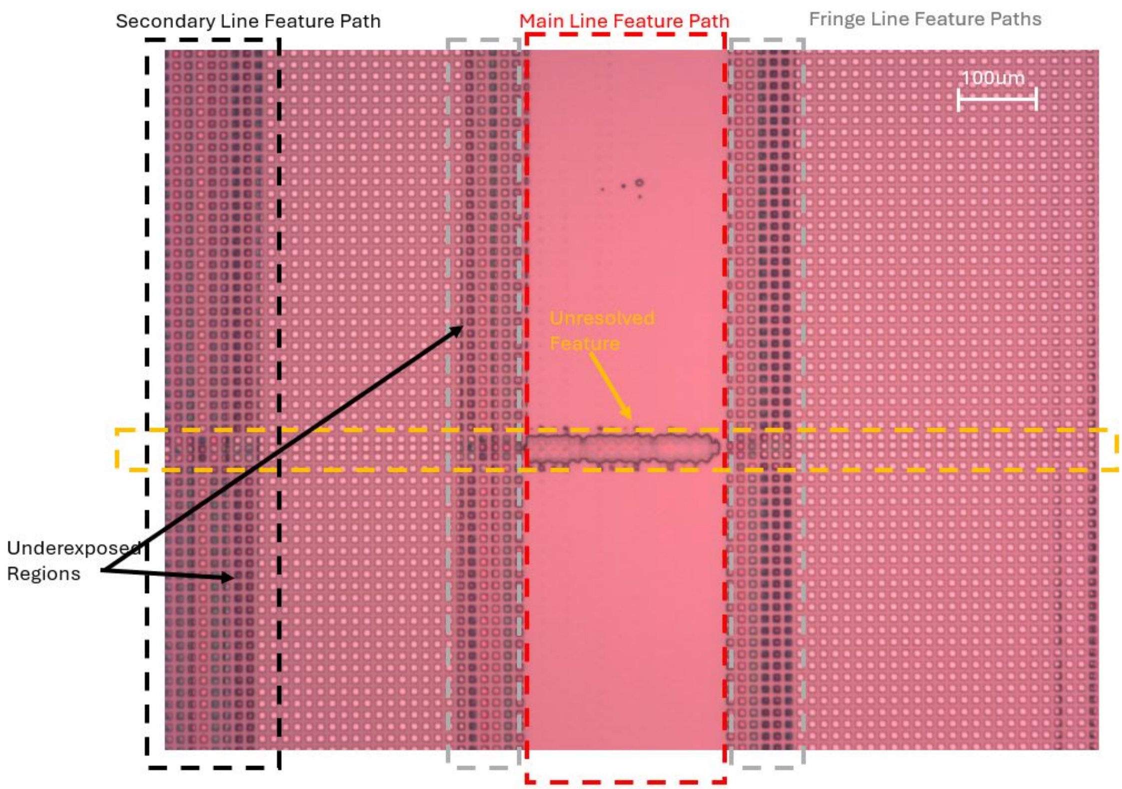


Figure A.14: Zoomed in image of the wafer post-PR development after frontside designs were exposed in MLA150. The image depicts the etch hole region and shows the most prominent areas where the MLA150 failed to expose entire lines of the wafer. Shows the main line feature paths, the fringe line feature path, and the secondary line feature paths together with the presence of a lateral line feature.

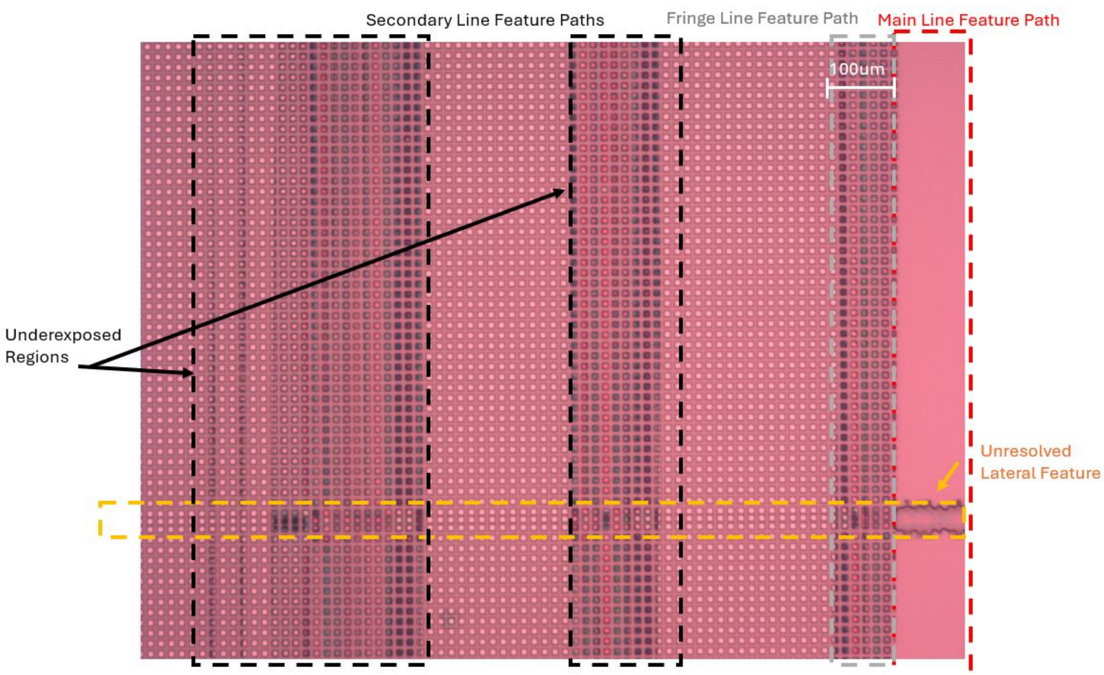


Figure A.15: Image of the wafer post-PR development after frontside designs were exposed in MLA150. Shows the continuation of a main line feature that was severely underexposed as well as a lateral feature for which the cause is currently unresolved. It was originally thought that this lateral feature was caused by the presence of some reflective features along the same lateral line that created a consistent error in the control system, however this theory has not been tested or adequately understood.

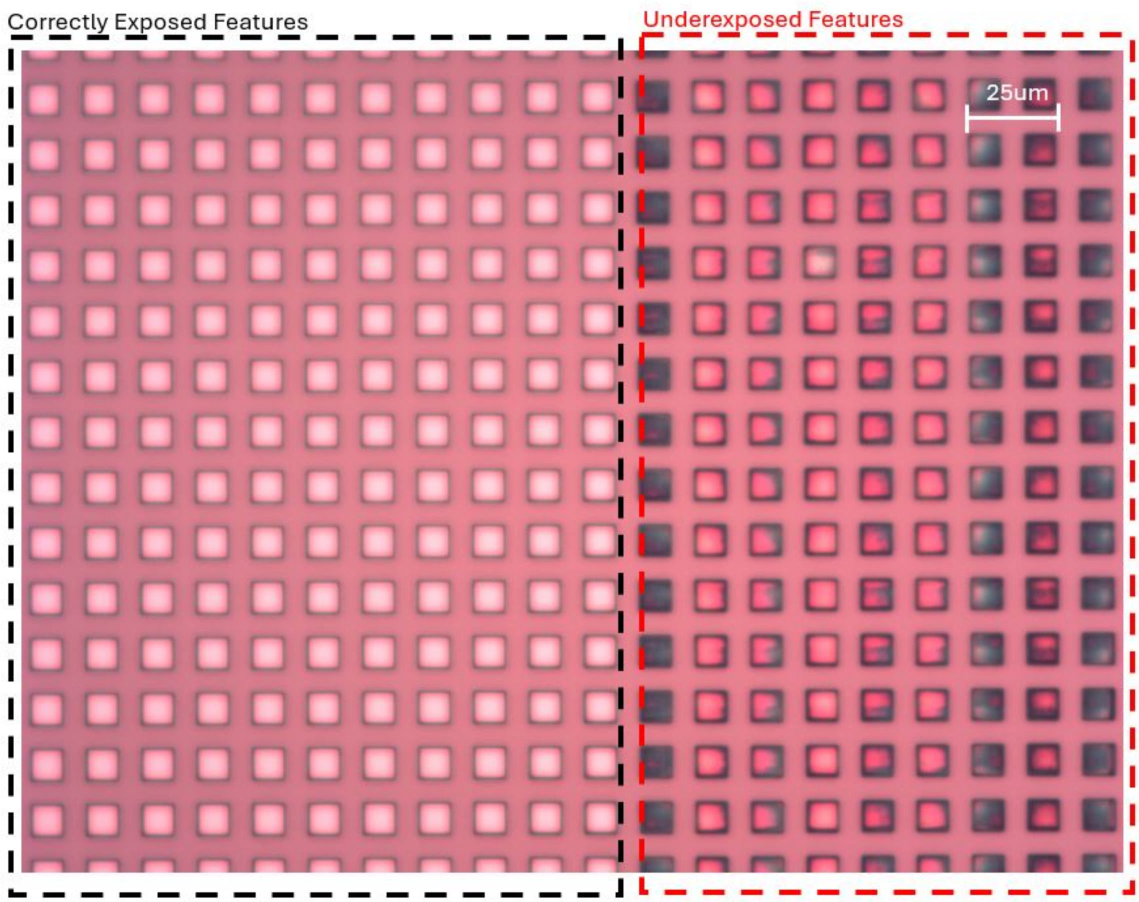


Figure A.16: Zoomed in image of the wafer post-PR development after frontside designs were exposed in MLA150. Shows partially exposed regions within the etch hole squares, indicating that full exposure was occurring in regions outside of where the lines occurred near to areas where underexposure was occurring, again in the direction of the laser raster.

# Appendix B

# General lab advice

**MEMS (Micro-Electro-Mechanical Systems)**

- **Hands Off:** Never touch the active area; air guns are destructive weapons to suspended structures.
- **Routing Taboos:** Do not place metal traces or vias directly under LGA/MEMS packages to avoid parasitic capacitance.
- **Symmetry:** Ensure PCB pad layouts are perfectly symmetric to prevent uneven solder reflow tilting.
- **Buffer Zones:** Keep stress-inducing components (screws, connectors) at least away from sensors.
- **Purity:** Particles invisible to the naked eye are catastrophic "boulders" for moving micro-parts.

**Mechanics of Materials**

- **Stiffness Scaling:** Remember that beam stiffness scales with the power of dimension. Small changes = big impact.
- **Verify Libraries:** Assume CAD material defaults are wrong. Cross-reference with MatWeb data sheets.
- **Understand the Curve:** Know the difference between yield and ultimate strength for your specific alloy.
- **Standardize:** Follow ASTM procedures for tensile/fatigue testing to ensure your data is defensible.

### Electrical Probe Station

- **Sacrificial Chips:** Always practice on "trash" dies before touching a functional wafer.
- **Vertical Approach:** Lower the tip vertically, then move forward slightly to "scrub" without dragging.
- **Contamination:** Organic oils (fingerprints) are the primary cause of low-leakage measurement errors.
- **Voltage First:** Always zero your bias supplies before lifting or landing your probes.

### Wire Bonder

- **Cleanliness:** Wear finger cots; even microscopic skin oil prevents a successful bond.
- **Plasma Power:** If bonds aren't sticking, use a vacuum plasma cleaner to remove organic residue.
- **Ball Size:** Ensure the free air ball (FAB) is approx $3x$ the wire diameter.
- **Rotation:** Wedge bonders are unidirectional; plan your pad orientation before you start.

### Simulations (FEA/CFD)

- **KISS Rule:** Keep It Simple, Stupid. Start with 2D linear static before going 3D non-linear.
- **Check Constraints:** Bad boundary conditions are the #1 cause of "pretty but useless" plots.
- **Mesh Convergence:** If doubling the mesh density changes the result by $> 5\%$, your mesh is too coarse.
- **Sanity Check:** If it doesn't match a back-of-the-envelope calculation, the software is probably lying.

### The Real World

- **The First-Try Tax:** If you are the first person in the lab, you will break the first probe tip you touch.

- **Patience:** If a wire bonder breaks your spirit, take a walk. It can smell your fear.
- **The Assembly Paradox:** Taking it apart and putting it back together fixes 50% of mechanical issues for no reason.
- **Famous Last Words:** "But it worked perfectly in the simulation!"
- **Default Blame:** If the results look weird, it's definitely the mesh (or the intern).

**General Lab Advice**

- Every time an array is appended to in Matlab, it allocates a new portion of memory the size of the new array, copies the old into the new, then deletes the old one. This can mean a 10x slowdown when dealing with arrays larger than a few tens of thousands of elements. Heed Matlab's recommendation to "preallocate for speed" by allocating the whole array up front. (This could've made my work in Chapter 3 take days instead of weeks.)
- USB3 is 10x faster than USB2 but only if the underlying device can run that fast. Flash drive write speeds can also differ by 10x − what a cheap flash drive does in over a half hour, a fast one can do in 4 minutes.
- Explore output file options. A 1GB CSV can be represented as an 84MB HDF5.

# Appendix C

# Acknowledgments cont'd.

As stated above, everyone I have encountered has contributed to me in ways I am sure you did not perceive. To those I have missed because of my poor memory, know you are not forgotten. So... again, thank you all very very much.

## Collaborators and Fellow Graduate Students

To my collaborators, fellow graduate students, and dear friends who were there with me those long hours:

- Anthony Salazar for his insight, communications, calculations, and keen eye. Your expertise in and out of your field of interest still surprises me. I am very impressed in every conversation that you have maintained who you are at your core and still built so much around that as part of who you will become. I am forever in your debt professionally and personally.

- Humberto Batiz Guerrero for being what I didn't know a friend could be. I am sincerely overwhelmed everytime I see how good a person you and how I wish I could be more like you. Thank you for being there for me in the ways I never knew I needed.

- Yichen "Alex" Liu for his high degree and volume of discussions around conceptualization and design, simulations in Ansys, simulations troubleshooting, and help in processing the devices.

- Alex Moreno for his great knowledge of the interconnectedness of the work and the process. Your insight and advice was a great help and lifted my eyes to keep working every time we conversed.

- Lydia Lee for her collaboration, insight, and technical contributions to the BLISS work. Your perspective helped strengthen the connection between the mission concept, spacecraft-scale constraints, and the larger scientific purpose of low-cost interplanetary exploration. I am grateful for the care and thoughtfulness you brought to the work. May your impact and plush live on in all the labs you visit.

- Hani Gomez for her insight into fabrication, process development, and the many details surrounding the quadrupedal-walking projects. Your lessons continue to shape how I think about devices, processing, and experimental judgment, and I remain grateful for the care and expertise you brought to the work.

- Lisa Anne Torres for the many long hours of working together in our volunteer capacity and for the greatly personal connection we were able to maintain. I continue to value all your insight and advice.

- Daniel Teal for his initiation of the first drafts of the trapezoidal finger GCAs and his conceptualization that higher stiffness should reduce parasitic capacitance. Your insights into MEMS and other parallel works and your initiative as an engineer are still very impressive.

- Dillon Acker-James for your thoughtful insight into human--robot interaction and for your ability to explain complex concepts with clarity and care. Your perspective helped me think more carefully about how robotic systems are understood, interpreted, and designed around the people who interact with them.

- Ahad Rauf for his insight into the computational modeling of MEMS devices and gap-closing actuators. Your perspective on simulation, numerical methods, and actuator behavior helped me better understand the limits and possibilities of the models used throughout this work.

- Emmanuel Sin for his collaboration, calculations, and sustained engagement with the BLISS project. Your contributions helped shape the technical foundation of the mission analysis and supported the development of the ideas that became central to the spacecraft and trajectory portions of this work.

- Nathan Lambert for his collaboration, technical discussions, and contributions to the BLISS mission concept. Your insight helped connect computation, autonomy, and mission-level thinking in ways that strengthened the broader framing of distributed small-spacecraft exploration.

- Neil Ramirez for his deep care and amazing vibes that helped me through all of my graduate student hurdles and issues. I wish we stayed in contact.
- Gabriel Lopez for being such a wonderful peer mentor. Your steady hand and clear ability to maintain your cool under clearly difficult situations has always been an inspiration. May your prosperity only be overwhelmed by your gratitude and satisfaction with your life.
- Gabriela Arango for being the leader I wish I could have always been. Your clear sight through tangled and difficult to navigate paths has always been a wonder to behold. I cannot wait to see your lab blossom into its own. Thank you for always being such a good mentee and mentor.
- Jesse Garcia-Castillo for bring such a smart and open minded person, while maintaining such a fun perspective even in the face of difficult duty. I would have liked to learn more from you, given the chance. May your lab be the best that even your high standards can think up and may your life be easier than it has been, so that you do not always have to be the bravest one in the room.
- Laura Cristal Magaña for always being there for me, even when I was a crybaby. Your leadership and strength at every step of our journey has and will continue to be a masterclass to behold. I will always look up to you and I will always lookd down to you also (shorty). May your toxica mentality never waver and your grace never be mistaken for weakness. I look forward to seeing all your accomplishments and what your future lab will blossom into.
- Ronald Rodriguez for being such a great person to work alongside. I am always amazed how you've maintained so much of yourself throughout the years I have known you. I am forever grateful for our time together and for your solidarity that never failed.
- Robin D. López for your optimistic outlook and all our real talk. You continue to amaze me, Dr. Mayor López.
- Beyazit Yalcinkaya for being my brother from another mother. I wish we could have stayed in contact and my apologies for all the part I had in our separation. You truly are a good man and one of the smartest people I have ever met (in all ways). May your big heart not overwhelm what your big brain has created and may your big brain learn to work with your heart.
- Nikita Lukhanin for the conversations on graduate-school advice, academic planning, and navigating the transition into advanced research. I am grateful

for the understanding we shared around family, responsibility, and the quiet discipline learned from work done with one's hands before entering graduate school. It was a privilege to support your path and to speak with someone who understood that persistence, care, and endurance are forms of preparation too often left unnamed.

## Mentees and Junior Collaborators

To my mentees, students, and junior collaborators, who trusted me with their questions, ambitions, uncertainty, and growth during our research together:

- Jasmine Bitanga for the thoughtful conversations on graduate school, research direction, and the many hidden steps involved in building a path through engineering and computing. I am proud to have played even a small part in your academic journey.

- Yuqi Nie for the opportunity to mentor you through optical-physics research. Your curiosity, care, and precision reminded me how much good research depends on asking careful questions before rushing toward answers.

- Emily Concepcion for your interest in mission planning and trajectory design, including how small changes in control decisions can accumulate into large changes in where a spacecraft goes.

- Siqin Yu for the opportunity to discuss soft-robotic engineering and research development. Your technical perspective and willingness to engage across disciplines strengthened the way I thought about mechanism design.

- Ezekiel Ayala for your curiosity around small-spacecraft mission design and the early questions that helped make the BLISS architecture easier to explain to younger students and non-specialist audiences.

- Maya Concepcion for your curiosity about autonomy and decision-making, especially how small robots and spacecraft might respond to uncertainty without constant human intervention.

- Heya Kaakeh for years of research conversations, technical development, and academic growth. Watching you develop as a mechanical engineer and researcher has been one of the great privileges of my time at UC Berkeley.

- Ethan Lee for your work, questions, and persistence as an undergraduate researcher. Your engagement helped shape the way I learned to explain research problems clearly and support students as they build confidence.

- Albert Lorenzana for the conversations on graduate-school applications, academic preparation, and finding a path forward in mechanical engineering. I am grateful to have been part of your transition toward the next stage of your career.

- Lizzette Corrales for the many conversations on graduate school, academic development, and persistence in engineering. Your growth, focus, and determination have been deeply meaningful to witness.

- Abigail Concepcion for your interest in communication systems and for helping me think about how tiny spacecraft might share information across large distances.

- Kole Makinde--Odusola for your work as an undergraduate researcher and for the opportunity to mentor you through academic-year research. Your questions and effort helped make the research environment stronger.

- Sam Phillips, Jason Xu, Benson Peng, and Pranit Mohnot for your work on ion and electrospray propulsion concepts. Your efforts helped move early-stage propulsion ideas from broad technical possibilities toward concrete research directions.

- Dylan Potter and Trevor Zinky for your work on directional propulsion. Your contributions helped clarify how small propulsion architectures could be organized, compared, and developed within a larger spacecraft-systems context.

- Jeremy Gong, Tyler Adkison, and Eliot Foss for your work on solid-propulsion concepts. Your efforts helped broaden the design space and strengthened the comparative framing of small-scale propulsion approaches.

- Jadesola Aderibigbe for the academic conversations, encouragement, and continued commitment to growth in mechanical engineering. It has been a privilege to support your path and to see your persistence in graduate study.

- Betty Concepcion for your curiosity about thermal behavior and energy management, including how small systems must carefully balance sunlight, heat, power, and survival.

- Yichen "Alex" Liu for your academic and research growth, your design discussions, your simulation work, and your sustained engagement with the technical details of this research. Your contributions became part of the intellectual structure of this dissertation, and I am grateful for the care you brought to the work.

- Carson Spoo for your work on machine-learning approaches for asteroid-approach trajectories. Your efforts helped connect computational methods to mission-design questions that are central to this dissertation.

- Mahit Namburu for your work on machine-learning methods for trajectory collection and mission analysis. Your curiosity and technical engagement helped expand the computational direction of the project.

- Cezar Carvajal for your work on commercial-off-the-shelf components and space-characterization concepts. Your contributions helped ground the spacecraft work in practical implementation constraints.

- Zachariah Ayala for your interest in microrobot motion and for helping me think about how small robotic systems can be described through simple walking, crawling, and self-righting examples.

- Lucas Concepcion for your interest in mechanical design and structural behavior, especially how small beams, springs, and linkages can produce useful motion when designed carefully.

- Yash Jain for your work on machine-learning approaches for microrobot space-walking concepts. Your efforts helped connect microrobotic motion, autonomy, and space-environment considerations.

- Charles Paxson for your work on the vacuum-chamber miniature probe-station effort. Your contributions supported the experimental infrastructure needed to move from design toward testable devices.

- Atreus Ayala for your engagement with solar-sail concepts and for reminding me that even highly technical spacecraft ideas should be explainable through clear physical intuition.

- Ronan Castro for your curiosity about imaging and sensing, especially in the context of how very small spacecraft might observe asteroids, comets, and other distant objects.

- Tobias Montoya for your questions around actuation and motion, which helped me think about how MEMS motors, inchworm stepping, and mechanical transmission could be described more clearly.
- Leah Payan for your determination, thoughtfulness, and willingness to keep moving forward as you considered your own goals. It was a privilege to offer advice, encouragement, and support along the way. I am grateful for the trust you placed in me and for the reminder that mentorship can matter most when it helps someone feel capable of taking the next step.
- Penelope Ziranda for your curiosity about fabrication and small-device construction, especially the idea that large engineering systems can begin as tiny patterned structures.
- Timothy Concepcion for your curiosity about computational modeling and simulation, especially the role that simple models can play in understanding complex spacecraft and microrobot behavior.
- Eduardo Gonzalez for your work on small-body characterization. Your engagement helped connect the engineering work to the planetary-science questions that motivate small-spacecraft exploration.
- Xiaomei Song for your work on language-model approaches for small-body selection. Your contributions helped explore how emerging computational tools could assist in mission-target identification and research organization.
- Isela Sosa for the academic conversations, planning, and persistence you brought to engineering. I am grateful to have supported your development and to have been part of your path forward.
- Oliver Aceves for your curiosity, effort, and technical contributions to the work on additive manufacturing, MEMS motors, and robust millimeter-scale mechanisms. Your engagement helped broaden the practical direction of the project, and it was a privilege to support your development as an engineer and researcher.
- Jacob Crouse for your energetic approach and intuition around all things mechanical. Your consistency and many conversations brought about many future works that I wish you could have stayed to work on.
- Delilah Castro for your interest in the materials side of the work, including thin films, flexible structures, and the way small changes in materials can shape the behavior of a larger system.

- Melody Ziranda for your interest in experimental testing and observation, including the careful process of watching devices move, fail, recover, and teach us what the design still needs.
- Leyla Payan for your curiosity, kindness, and the perspective you brought to our conversations. I am grateful for the opportunity to support you, encourage you, and be part of even a small piece of your academic journey. Your questions and openness reminded me that mentorship is often built through simple conversations, patient listening, and belief in someone before they fully see the path for themselves.
- Emmalyn Montoya for your curiosity about robotics and mechanism design, especially the relationship between linkages, motion paths, and the ability of a small system to interact with its environment.
- Matthew Hernandez for your interest in propulsion concepts and for helping me think about how ion, electrospray, solar-sail, and solid-propulsion ideas can be compared at small scales.
- Lisa Crouse for your deep understanding of the fundamentals and great willingness to start from scratch on many approaches. The conversations and iterations on our designs were greatly helpful.
- Isabella Concepcion for your curiosity about science targets and discovery, especially how small spacecraft could help us learn more about asteroids, comets, and the material history of the solar system.

## Cal Staff and Student Advisors

To the staff members, advisers, and student-support professionals at UC Berkeley, who helped me navigate the parts of graduate school that rarely appear in a dissertation:

- Meltem Erol for her guidance, advocacy, and steady support through the College of Engineering. Your work helped make the administrative, funding, and policy dimensions of graduate education feel more navigable during moments when the path forward was not always clear.
- Tiffany Reardon for her long-standing commitment to student support, transfer pathways, and engineering excellence. Your work has shaped a more humane and accessible version of engineering education, and your support reminded me that institutional care is built through people who choose to see students fully.

- Audrey Sillers for her support, guidance, and care through the EECS Department. Thank you for the administrative clarity, student-centered help, and steady presence that made difficult parts of graduate school easier to navigate. I am grateful for the time and attention you gave to helping students move through complicated systems while still feeling seen as people.

- Yawo Dagbevi Akpawu for his support within the Mechanical Engineering Department and for the many forms of advising and administrative guidance that helped me continue moving through the program. I am grateful for the patience, clarity, and care that staff labor requires, especially when students arrive with complicated questions and urgent needs.

- Isabel Blanco for her support within the ME Department and for helping maintain the departmental structures that graduate students rely on. The completion of this dissertation depended not only on research, but also on the many forms of coordination, advising, and administrative care that make research possible.

- Ricky Vides from the ME Department for his never ending support and warmth. You always made me feel more at home when I passed through the halls or saw your emails. I will sincerely miss you and your direct approach to care and knowledge. May your future be brighter than the stars in our eyes.

- William from the ME Department for his support, encouragement, and presence within a community that helped students like me feel that we belonged in STEM. Your work contributed to the kind of student-centered environment that made persistence possible.

- Diana Lizarraga for her vision, leadership, and care through Cal NERDS and STEM equity work at UC Berkeley. Your commitment to mentoring, advising, and building systems of belonging has had a profound impact on students navigating STEM from the margins toward the center. I am grateful for the community you helped build and for the example you set in making institutional support both practical and deeply human.

- Marcia Breslin-Cantillana for your work with the COE and with transfers, I am inspired by how much you are continuously able to contribute to those who sorely need it even in the face of great sorrow. I truly look up to you and hope that each of your days from here out is significantly easier and happier.

# BSAC and Staff

I would like to thank the Berkeley Sensor and Actuator Center (BSAC) for continued support. Specifically, a great thanks to Dalene Schwartz Corey. My many thanks for being so patient with me every semester, being so welcoming to me each time I saw you, and for being a bright spot in the hallways and throughout the days.

# Marvell Nanolab and Staff

Each of the tools in the Marvell Nanolab plays a vital role in the overall fabrication sequence and would not be possible without the maintenance, training, upkeep, troubleshooting, detailed instruction, safety, and general ambiance of the Marvell Nanolab Staff, Technicians, and Interns. Special appreciation goes out to:

- David K. Taosaka, for being there as a friendly face and a calm voice when I was wracked with stress and worry. Without your steady hand and broader perspective, I might not have made it through my first round of mistakes;

- Ryan Rivers, for his process-engineering expertise, especially in etching, wafer handling, temporary bonding, tool compatibility, and the practical details that determine whether a fabrication process succeeds or fails. Without your careful questions and direct answers, I might have made serious and costly mistakes. Your kind, patient, and matter-of-fact approach helped me nearly every time I came into the lab, and I am deeply grateful for the way you made difficult processing decisions feel manageable.

- Allison Dove, for her process-engineering expertise in lithography, e-beam lithography, wafer-level process compatibility, and the many practical details surrounding what my wafers could safely touch, enter, survive, or become. Your willingness to help, your direct answers, and your ability to translate complicated tool and process constraints into clear guidance were exactly what I needed at each step. I am grateful for the care and clarity you brought to so many parts of my fabrication work.

- Joanna Strongson Bettinger, for her process-engineering guidance, especially in lithography, maskless/direct-write processing, cleanroom practice, and the broader flow of my fabrication work. Thank you for the clear direction, practical judgment, and steady help you gave me throughout the process. Your ability to see both the immediate tool-level issue and the larger process-flow consequence helped keep my work moving when the fabrication path felt uncertain.

- Anthony Bielecki, for your equipment expertise, practical tool knowledge, and steady help with the realities of working inside the Marvell NanoLab. Your guidance helped me understand not only what a tool was supposed to do, but what it could safely and reliably do in practice.

- Sam Tsitrin, for your R&D engineering expertise and your guidance on deposition, coating, and process-development questions. Your direct technical advice helped me make better decisions at several important points in my fabrication work.

- Daniel Martinez, for your R&D engineering support, process guidance, and practical insight into NanoLab tools and fabrication workflows. Thank you for the clear answers, careful help, and steady presence you provided in the lab.

- Stone, without whom I would be completely lost in the codeswitch of it all. Thank you for your practical help, steady guidance, and generosity with your time in the Marvell NanoLab. Thank you for helping me navigate the lab, the tools, and the many small details that made fabrication work possible. Your support helped me avoid mistakes, understand the process more clearly, and feel less alone in the cleanroom when the next step was not obvious.

- To the fellow scientists working within the Nanolab, Sean Cheung and Jeff without whom I might have had multiple breakdowns and without whom I would have been lost in the thick of it. Your generosity with your time and thoughtful words had a great impact on my mental health as well as my job performance. I wish you two the greatest of luck and the easiest that life has to offer.

## Spaceflight Inspiration

To the first spaceflight, Sputnik [132], to the first human launched into space, Vostok 1 [133], to the first moon landing, Apollo 11 [134] many technologies have changed. Indeed many firsts have been accomplished in the spaceflight realm including the first: cis-het woman in space Valentina Tereshkova [135]; African heritage and Cuban descent, Arnaldo T. Mendez [136]; African-decended American, Guion S. Bluford Jr. [137]; Mexican, Rodolfo N. Vela [138]; Puerto Rican, Joseph M Acaba [139]; LGBTQ+, Anne McClain [140]; Native American, John Herrington [141]; African cis-het woman from America, Mae Jemison [142]; Muslim, Prince Sultan bin Salman Al Saud [143]. Indeed some of these have come with technical changes related to their specific differences to allow them the same safety and capabilities that previous

spacefaring astronauts have enjoyed, including gender [144--147]; culture [148, 149]; religious [150], with some changes having laughable outcomes [151]. To those who did not make it back from their journey, [152], and to those with whom I almost left it [153--160].

Also, this: In the spirit of research that first makes one laugh and then think, I also remain grateful for work such as Meyer--Rochow and Gal's calculation of penguin defecation pressures, which reminds us that serious mechanics can emerge from wonderfully unserious questions [161].